
Submarine mass movement processes on the North Sea Fan as interpreted from the 3D seismic data

Joana Gafeira



A thesis submitted for the degree of Doctor of Philosophy.
The University of Edinburgh.
November 2009

Abstract

This research has been focused on the characterisation and analysis of the deposits of large-scale mass movement events that shaped the North Sea Fan since the Mid-Pleistocene. Located at the mouth of the cross-shelf trough Norwegian Channel, the North Sea Fan is one of the largest through-mouth fans in the glaciated European margin with an area of approximately 142,000 km². Submarine mass movement processes have occurred intermittently throughout the Quaternary history of the North Sea Fan, related to recurrent climate-related episodes of growth and retreat of the ice sheets. These processes can transport large amounts of sediment from the upper shelf up to the abyssal basins, playing an important role on the evolution of continental margins and can also represent major geological hazards.

This thesis uses mainly 3D seismic data to investigate the external geometry and internal structure of large-scale mass movement deposits. The high spatial resolution provided by the 3D seismic data has allowed a detailed geomorphological analysis of these deposits. This study involved the interpretation of the seismic data and the detailed picking of key reflectors followed by the extraction of both horizon and window-based seismic attributes. Digital elevation models of the key reflectors and their seismic attribute maps were then transferred to a geographical information system (GIS) where they were interactively interpreted using spatial analysis tools and the full visualisation potential of the software.

The outcomes of this study highlight the importance of detailed horizon picking and interactive interpretation followed by spatial analysis and visualisation in GIS environment. The identification of acoustic patterns within deposits that are normally described from 2D seismic as chaotic or acoustically transparent emphasizes the potential of detailed analysis of 3D seismic data. It gives an example of how this type of data can provide new insights into the mechanisms and processes associated with mass movements. In particular, amplitude and RMS amplitude maps provided remarkable detailed information of internal deformation structures whereas slope, shaded-relief and thickness maps allowed detailed characterisation of the external geometry. Various types of kinematic indicators can be recognized within the mass movement deposits through combined seismic analysis and detailed morphological mapping.

Declaration of originality

I hereby declare that the research recorded in this thesis and the thesis itself has been conducted and written entirely by myself, unless otherwise stated. The work has not been submitted in any previous application for a degree.

Joana Gafeira

November 2009

Acknowledgements

First of all, I would like to acknowledge the two identities that provided the basics for this thesis. StatoilHydro is thanked for providing the 3D seismic and bathymetric data and for allowing their use for publication. The Portuguese Foundation for Science and Technology for providing the founding required for my PhD.

Dan Evans, Roger Scutton, Luis Pinheiro and more recently Roger Hipkin were my supervisors through this project. At different stages of the project, all of them had crucial roles and I will be always grateful for their help and support. Dan Evans was the one that followed my progress through the entire PhD. There are many things I have to thank him for: the freedom he granted me throughout my PhD, especially in regard to the research routes I wanted to follow; his support towards attending conferences and courses; his constructive insightful observations; and, more than any thing, his flexibility and patience.

Although not officially my supervisors, Joe Bulat and David Long were for me as if they were so. I am extremely grateful for their generosity, patience and ability to share their knowledge, shown the countless times I pass by their offices and asked *Do you have a 'minute'?*

Since I joined the Murchison House, I have been receiving the help, support and encouragement of many of BGS staff. Not being able to name all, I would like to highlight the help of Bob Gatliff, Angela Morando, Phil Richards, Derek Ritchie, Kevin Smith, Alan Stevenson, Heather Stewart, and Martin Stoker, among others.

In the Murchison House I also count with the friendship of other PhD students. Isabel, Adrian, Steve, Baerbel and Sonia, shared with me their doubts and problems and made me see that there is no such thing as a perfect PhD without problems.

I am also thankful for the friendship of the long term *residents* of the port cabin (Gareth, Greg, Jorge). To whom, I still not certain if I should thank or curse them for having convinced me to use Latex to write this thesis.

I am extremely grateful to the friend I gain in Edinburgh. My ex-flatmates, key players to made Edinburgh my home, Bruno, Eleni, Stef, Inger and Claire. The Portuguese speakers (with or without brazilian accent): Nuno, Andreia and Luiz. And all the others that have been part of

Acknowledgements

my Scottish experience.

To my great friends back in Portugal: Inês, Manuela, Rita, Joana M., Joana V. and Juliana, for never forgetting about me and for having kept thinking, caring and calling me despite the distances.

The marine geology group from the now *LNEG* (previously *INETI* and before *IGM*). For their encouragement and support to embark in the adventure that is doing research in marine geology. It was especially thanks to Pedro Terrinha that I found myself for the first time on a research vessel.

To my parents, Anabela and Francisco, my brother, Luis, my two nieces, Inês and Raquel and the rest of my family: I would like to express my deep debt of gratitude for forgiving me for my absence and the impossibility to share with them the good and bad moments.

Finally, to Remy. His love, daily support, cooking and infinite patience have not only made last years of my PhD much easier but my life far more enjoyable. I will be always grateful to him and I hope that my love will express that better than I would ever be able to do by words.

Contents

Abstract	ii
Declaration of originality	iii
Acknowledgements	iv
Contents	vi
List of figures	viii
List of tables	xiv
1 Introduction	1
1.1 Introduction to thesis	1
1.2 Submarine mass movements: processes and products	2
1.2.1 Classification and terminology	3
1.2.2 Triggering mechanisms	5
1.3 Rationale	8
1.4 Aims and objectives	11
1.5 Outline of thesis	12
2 Geological Setting	14
2.1 Introduction	14
2.2 Glaciated european margin	14
2.3 Stratigraphic framework	22
2.4 North Sea Fan	26
2.4.1 Morphology	27
2.4.2 Fan evolution and slope instability	29
2.5 Storegga Slide	34
3 Data and methodology	38
3.1 Introduction	38
3.2 Type and source of the data	38
3.3 3D seismic data	41
3.3.1 From data visualisation to seismic attributes extraction	42
3.3.2 Data handling and integration	49
3.3.3 Recognition and characterisation of submarine mass movement deposits on 3D seismic data	53
4 Seabed and shallow subsurface geomorphology	55
4.1 Introduction	55
4.2 Detailed geomorphological characterisation	55
4.2.1 Zone S	56
4.2.2 Zone Ch	59
4.2.3 Zone Cl	67
4.2.4 Zone B	71
4.2.5 Zone U	74
4.3 Summary of Events that shaped the present day seabed	76

5	Geomorphology of the middle and upper pleistocene slide deposits	79
5.1	Introduction	79
5.2	Tampen Slide	81
5.2.1	Description	81
5.2.2	Interpretation	92
5.3	Møre slide	98
5.3.1	Description	98
5.3.2	Interpretation	112
5.4	Slide U	121
5.4.1	Description	121
5.4.2	Interpretation	137
6	Deposit geometry and internal deformation	142
6.1	Introduction	142
6.2	Collapse of the sidewall	142
6.3	Sliding surface	144
6.3.1	Sliding surface ramps	145
6.3.2	Islands of undisturbed material	150
6.4	Structures of Internal deformation	155
6.4.1	Compression structures	156
6.4.2	Longitudinal Shear Structures	160
6.5	Implications of slide deposit's external geometry and internal structures	163
7	Summary and Conclusions	167
7.1	Key points of the thesis	167
7.2	Further work	169
A	Tulipan Survey Header	172

List of figures

1.1	Classification of different type of submarine mass movement modified from the Varnes' classification by Coleman et al. (1993).	4
1.2	Classification of mass movement deposits applied by Moscardelli and Wood (2008).	4
1.3	Diagram explaining the relative importance of the trigger mechanism compare to the preconditions.	8
2.1	Distribution and extent of prograding wedges along the glaciated NW European margin. Modified from Dahlgren et al. (2005).	15
2.2	Late Jurassic, mid-Cretaceous, Paleocene-Early Eocene and Oligocene-Miocene plate reconstructions by Doré et al. (1999).	17
2.3	Last Glacial Maximum (28-22~ka) extent of the Fennoscandian, UK, and western Barents ice sheets (Sejrup et al., 2000).	19
2.4	Location of the main mass movement deposits adjacent or within the North Sea Fan. Modified from Hjelstuen et al. (2007)	20
2.5	Diagram correlating the used stratigraphic scheme defined by the Norwegian Deepwater Programme (unpublished, 2004)with the SW Norwegian Schematic Glacial (Sejrup et al., 2005) and the Mid and Upper Pleistocene stratigraphy (Funder et al., 1998).	23
2.6	Isopach maps o the the Naust Formation and the Naust sequences with a geoprofile across Haltenbanken.	24
2.7	Correlation between stratigraphy and seismic units used in this study and the ones on previous studies done by King et al. (1996) and Nygård et al. (2005).	25
2.8	Bathymetry and main structural elements of the SE Nordic Seas margin.	26
2.9	Sketch showing the main dimensions of the North Sea Fan. After Vorren and Laberg (1997)	27
2.10	Profile of the North Sea Fan, reaching from the continental shelf to the Ægir Ridge in the Norway Basin (Nygård et al., 2005).	28
2.11	Shaded-relief map of the North Sea Fan present-day seabed, from the SEA4 swath bathymetric data	30
2.12	Volume measurements and estimates for the Quaternary (< 1.1Myr) North Sea Fan sequences.	31
2.13	Conceptual model illustrating the bipartite development of the North Sea Fan by (Nygård et al., 2005).	32
2.14	Isopach maps for the Nygård's units P10-1 (correspondent to the seismic unit I-VII used in this study). Modified from (Nygård et al., 2005)	33
2.15	Shaded-relief map of the boundary between the North Sea Fan and the Storegga Slide, showing the study area location.	35

2.16	Map of the distribution of mass-movement types, headwalls, and other geomorphological features within the Holocene Storegga Slide. The names of the headwalls are derived from the sediment units in which failure took place (Bryn et al., 2005a). Modified from (Micallef et al., 2007)	36
2.17	Conceptual model illustrating the cyclic deposition and slide processes in the Storegga region. Extracted from Rise et al. (2005).	37
3.1	Data coverage overlain on Gebco bathymetry.	39
3.2	Sketch of a simple autopicking algorithm (Dorn, 1998).	43
3.3	Sketch of a seismic trace showing the onsets (-/+ zero, maximum +/- zero and minimum) that can be used for autopicking.	43
3.4	Example of the extraction of multiple amplitude map from a key horizon. . . .	46
3.5	Example of a combined map obtained by coupling the seismic amplitude map with the confidence map	47
3.6	The effect of amplitude clipping on the automatic picking and the generated terracing artefact.	48
3.7	3D image of the DEM of the Tampen Slide deposits' top and base, cutting through two time-slices 100 ms apart.	50
3.8	Flow-chart summarising multi-stage generation of the surface maps gathered within the GIS environment from a given seismic unit.	52
4.1	Shaded-relief map of the seabed and distribution map of the identified zones . .	56
4.2	Three-dimensional perspective view from East showing Zone S, the area largely remoulded by the Storegga deep failure at the foreground.	57
4.3	Seismic line through Zone S showing upslope progressive loss of coherence and succession of graben-and-horst blocks followed by a succession of pop-up blocks closer to the edge of Zone S.	58
4.4	Model of development of the Zone S pop-up faults associated with the Storegga deep failure in the Ormen Lange area.	59
4.5	Morphology and internal structure of the compression zones Ch ¹ and Ch ² . . .	61
4.6	3D perspective view of the present-day seabed cutting through Ch ² looking towards NE and seismic profile across the toe region of the zone Ch ²	62
4.7	Seismic reflection amplitude map of the seabed showing Zone Ch.	63
4.8	The deformation pattern on the compression zone Ch derived from the interpretation of several seabed maps obtained from the 3D seismic data.	64
4.9	Schematic representation of the compression structures at the toe region of Zone Ch and gradual loss of internal structure upslope.	65
4.10	Overview from undisturbed area between the two lobes Ch ¹ and Ch ² , and the Ch ¹ internal boundary between compressional and chaotic facies.	66
4.11	Shaded-relief map of the boundary between the North Sea Fan and the Storegga and detail image showing zone Cl.	69
4.12	Seismic profile through Zone Cl showing the succession of pop-up blocks and enlarged view of a part of this succession.	70
4.13	Seismic profile cutting through Zone Cl, its interpretation and schematic illustration of the development of the Cl ridges.	71
4.14	Shaded-relief and amplitude maps of Zone B.	73

4.15	Schematic illustration of the spatial extent of Zone B, and the localisation of the seismic sections displayed.	74
4.16	Shaded-relief map of the seabed showing GDF's deposits in the area adjacent to the Ch ² zone.	75
4.18	Sketch representation of chronological reconstitution the main events that shaped the seabed in the proximities of Zone Ch ¹	78
5.1	Schematic representation of the relative stratigraphic position of the megaslides. The top surfaces of the slides mark their age in terms of the seismic stratigraphy of the Naust Formation. Vertical extent gives indication of erosion by the slides, whereas the horizontal extent gives a sense of their lateral extension.	79
5.2	Map of the spatial extent of the main buried slides on the North Sea Fan and Storegga region.	80
5.3	3D seismic profile through the MTH showing the Tampen Slide deposits at the contact between the top of Unit III and the top of the MTH.	82
5.4	Three-dimensional perspective view of the <i>TNS</i> reflector's DEM from south-southeast.	82
5.5	Shaded-relief map of the <i>TNS</i> reflector with artificial illumination from northwest at 45° and seismic line 3500 across the MTH with the Tampen Slide deposits.	83
5.6	Tampen Slide deposits time-thickness map calculated from <i>TNS</i> and <i>TTS</i> reflectors depth values.	84
5.7	Detail of the amplitude map extract from the key reflector <i>TNS</i> , that correspond to the interphase between the Tampen Slide deposits and the underlying material.	85
5.8	This display shows both the overall pattern distribution on amplitude map of the horizon <i>TNS-12ms</i> and detail aspects of each main fabric	86
5.9	Shaded-relief map of the top of the Tampen Slide deposits obtain from the DEM of the <i>TTS</i> reflector, with artificial illumination from northwest at 45°.	87
5.10	Gradient and depth map of the top of Tampen Slide deposits (<i>TTS</i>)	88
5.11	Fabric classification used in this study to describe the patterns observed on the Tampen Slide deposits.	89
5.12	Distribution map of the types of fabric recognised on the Tampen Slide deposits. It was identified seven fabric regions (A1, A2, B, C1, C2, D1 and D2) dominated by one of the four main types of fabric, surrounded by areas of complex or undefined fabric.	89
5.13	Internal structure of the Tampen Slide deposits displayed on RMS amplitude map above the Top of the Naust S, reflector (<i>TNS</i>), and seismic section.	90
5.15	Model of compressive and extending flow in a glacier. Compressive flow takes place where the bed flattens, and extending flow takes place where the bed steepens. After Nye (1952).	94
5.16	Graphic representation of the relation between the fabrics observed on the Tampen Slide deposits and the inferred mass flow behaviour across the MTH.	96
5.17	Interpretative map of the Tampen Slide deposits showing the main direction transport inferred from the recognised fabrics.	97
5.18	Shaded-relief map of the post-Møre surface DEM in ms (TWT) and 3D seismic profile across the study area.	99
5.19	Amplitude map of the post-Møre slide surface.	101

5.20	RMS amplitude map for the 20 ms window centred 30 ms below the post-Møre surface. This map shows the flow patterns on the remoulded material.	102
5.21	3D view of the Post-Møre surface looking north-northeast providing a good perspective towards the side scar that characterise Zone C.	103
5.22	Detail of the RMS amplitude map (see Fig. 5.20) showing Zone C area and seismic profile across slide scarp cutting through the southern part of the headwall, the internal depositional area and Zone M ²	105
5.23	Detail of the post-Møre surface shaded-relief map (see Fig. 5.18) focused on Zone C area, showing both internal depositional areas (A and B) and the main slide scarp headwall area and seismic profile across the two internal depositional areas and location map.	106
5.24	Time-slice at 2100 ms TWT showing the contact of Unit VI with: Tampen Slide deposits (upper part), Unit III (central part) and Unit IV (bottom part), and Time-slice at 2300 ms TWT showing the deeper area remoulded within the slide scars A and B, and their location map	107
5.25	Schematic representation of the south-eastern edge of the MTH and segments of seismic profiles across it.	109
5.26	Block of undisturbed material within Zone R display on 2000 ms TWT time-slice, post-Møre surface shaded-relief and seismic trace 800	110
5.27	a) Detail of the RMS amplitude map (see Fig. 5.20) through part of Zone R - Zone M ¹ boundary, showing mass movement flow lineations. b) Schematic representation of the main flow lineations observed on the RMS amplitude map (a) and the direction of transport inferred from these lineations. Note how the flow lineations are deflected on the boundary between Zone R and Zone M ¹ (brown dashed line). c) Segment of seismic trace 2000 centred on the boundary between Zone R and Zone M ¹ , where a stratigraphic step in the sliding surface is observed. d) Location map.	111
5.28	Interpretative map of the Zone C, showing the distribution of sediment pathways inferred from the post-Møre surface amplitude maps.	113
5.29	Conceptual model of the Zone C main slide scar development. <i>I</i> - Main Møre Slide collapse. <i>II</i> - Collapse of the Møre Slide sidewall. <i>III</i> - Retrogressive collapses. <i>IV</i> - Post-Møre surface final stage.	114
5.30	3D diagram of the deflection effect on the flow of remoulded material caused by the presence of a block standing out of the sliding surface.	116
5.31	Interpretation map of the shear zone on the north-western edge of Zone R, based on acoustic maps.	117
5.32	Model of development of the shear zone on the north-western edge of Zone R. I - Schematic diagram showing the geometry, characteristics and main shear sense of the shear zone. II - Early development of dextral Riedel faults across the brittle shear zone. III - Further development led to the propagation of the Riedel faults behind the shear zone.	118
5.33	Interpretative map of the Slide U deposits showing main direction transport inferred from the material remoulded and the location of the ramps that characterise the sliding surface.	120
5.34	Gradient and depth map of the top of Slide U deposits (<i>TSU</i>).	122
5.35	Segment of seismic trace 1500 showing the boundary between undisturbed sequence of the North Sea Fan and the Storegga Slide deep failure.	124

5.36	3D view of the top of Slide U looking southward.	125
5.37	Geometry and orientation of the ramps identified at the base of Slide U.	126
5.38	Schematic diagram illustrating possible slide deposits profiles across a sliding surface ramp.	127
5.39	Thickness map of the Slide U deposits, with the location of the sliding surface ramps.	129
5.40	RMS amplitude map for the time window between the horizon <i>TSU+20ms</i> and the horizon <i>BSU-15ms</i>	130
5.41	Diagram illustrating the main characteristics of the three types of seismic signature of Slide U deposits	131
5.42	Distribution map of the three main types of seismic record observed on the Slide U deposits: Type I, Type II and Type III.	131
5.43	Transition from seismic signature Type I to Type II. a) Location map. b) Segment of the seismic trace 3500, showing Slide U deposits between <i>TSU</i> and <i>BSU</i> reflectors. c) Swath from the RMS map displayed on Fig. 5.40 centred at trace 3500.	133
5.44	Transition from seismic signature Type II to Type III across Ramp E.	134
5.45	Spatial distribution of the three types of Slide U deposits' seismic signature overlying the deposits thickness map.	135
5.46	Details of the morphology of the boundary b , between Type I and Type II Slide U seismic signature. a) Location map. b) RMS amplitude map enlarged view of boundary b showing a bay-shaped segment. c) Detail of RMS amplitude map showing Type II deposits enclosed within deposits Type I.	136
5.47	Interpretation map of detailed view of the RMS amplitude map displayed on Fig. 5.44, showing the changes on the direction of transport upslope Ramp E.	138
5.48	Two models of development of Type II deposits' enclosure within the Type I deposits shown on Figure 5.46.	140
5.49	Interpretative map of the Slide U deposits showing the distribution of the different types of seismic signatures, the location of the sliding surface ramps and both the inferred directions of transport and the material deformation features. The sizes of the arrows that show direction of transport reflect its relative velocity.	141
6.1	Schematic diagram of the decomposing the sliding surface into its basic four components, from the headwall to the toe of the mass movement.	145
6.2	Seismic lines showing the down-cutting ramps between the main Møre Slide and, respectively, Zone C and Zone R	147
6.3	Backstripped image extracted from Moscardelli et al. (2006) showing several geomorphological elements in base of a mass movement deposit (MTC1), including a major megascour	149
6.4	Schematic diagram showing the main location of <i>detached</i> , <i>rafted</i> or <i>outrunner</i> blocks relatively to a slide deposit.	150
6.5	Coherency image and seismic lines across a erosional shadow remnant presented by Moscardelli et al. (2006).	151

6.6	Morphology of adjacent headscars on Zone C of the Møre Slide complex. Above) Location map. Left) Time-slice at 2300 ms TWT cutting through the western edge of the MTH and the Møre Slide remoulded material. Right) Distribution map of undisturbed and remoulded material, from the 2300 ms time-slice, showing the promontory of undisturbed material (<i>p</i>) between the two retrogressive headscars (1 and 2).	153
6.7	Conceptual model of development of isolated block as result of adjacent retrogressive failures. a) Retrogressive evolution of two simultaneous and adjacent cauliflower-shaped headwall, resulting of sidewall collapse (stage I), and joining into a single headwall at a final stage (stage IV). Note: the isolated block left by this process (<i>i</i>). b) Detail view of the evolution of the isolated block (<i>i</i>) marked by a stage of evolution, shown in 1 and 2, and stage 3 where that lateral support by the material. Brown arrows show main direction of transport.	154
6.8	Example of main structural patterns in an accretionary prism and a fold-and-thrust belt, extracted from Bonini (2007). a) Cascadia margin. b) Sulaiman thrust belt, Pakistan.	158
6.9	Comparison between shear zones recognised in a hand specimen from the Peñalba landslide (Yenes et al., 2009) and in the study 3D dataset.	162
6.10	The outline of the Palaeo-Afen Slide mimics that of the Afen Slide on the seabed (Long et al., 2003).	164
6.11	Seismic line showing up-pulling and disruption of the INS and TNS reflectors due to fluid migration.	166
7.1	Amplitude maps of the base and top of the glaciogenic debris-flow deposits of Unit III.	170

List of tables

1.1	Trigger mechanism classification relatively to their effect and their origin Locat and Lee (2002).	6
1.2	List of main triggering mechanisms and associated examples	7
2.1	Glaciated European Margin slides. From Leynaud et al. (2009). The references present in this table are to be found in the original article	21
5.1	Description of the main characteristic of the three ramps observed at the sliding surface of Slide U. It presents aspect of both the geometry of Ramp W, Ramp N and Ramp E and the overlying deposits thickness.	127

Chapter 1

Introduction

1.1 Introduction to thesis

Development in recent decades of side-scan sonar and multibeam swath-bathymetry systems has offered exciting information from the previously hidden landscape and allowed detailed studies of seabed morphological characteristics worldwide. The increase of knowledge of the seabed has revealed an unexpected abundance of submarine mass movement deposits. This type of deposits can be found in almost all geological settings, from volcanic islands (e.g. Moore et al., 1994; Labazuy, 1996; Masson, 1996; Deplus et al., 2001) to both active and passive continental margins (e.g. Dowdeswell et al., 1996; Goldfinger et al., 2000; McAdoo et al., 2000; Evans et al., 2005). Since the early 1980s, the study of submarine mass movements has been the focus of major national and international research projects sponsored by the industry, governmental organizations and granting agencies (Locat and Mienert, 2003). Financial support from industry for these projects reflect that, to some extent, the increased interest in submarine mass movements have been related to the development of large-scale projects in areas of known slope instability (e.g. Ormen Lange Field, located in the scar of the Storegga Slide), whereas the involvement of governmental agencies reflect, to some extent, the increased awareness of the geohazards associated to these processes, which can represent a threat to highly populated coastlines (as it was sadly proved by the Papua New Guinea's 1997 Tsunami).

The redistribution of the material remoulded during a submarine mass movement leads to the development upslope of 1) a main *zone of depletion*, characterised by extensional deformation, and downslope of 2) a main *zone of accumulation*, characterised by compressional deformation. This has been describe in studies of both modern and ancient deposits (e.g. Martinsen and Bakken, 1990; Booth et al., 1993; Lindberg et al., 2004; Dykstra, 2005; Greene et al., 2006; Yenes et al., 2009). In some cases, an intermediate zone can be also identified characterised mainly by simple shear and translation and referred to as *zone of propagation* (e.g. Trincardi and Argnani, 1990). While the geometry and processes taking place on the zone of depletion, are

rather well studied particularly around the headscar, the processes taking place further downslope along the propagation and the accumulation zones remain poorly understood. However, the increasing number and type of datasets acquired from areas affected by submarine mass movement can provide new insights into the processes.

The presented PhD project uses 3D seismic data to characterise slide deposits within the North Sea Fan. The data available, covering an area of 1618 km² of the northern flank of this trough-mouth fan, is well suited for such analysis. The good quality of this data is enhanced by a stratigraphic sequence that allowed the unequivocal identification of the slide deposits, easily distinguishable from the remaining type of deposits (mainly hemipelagic and glaciogenic debris flow deposits), and by the absence of any subsequent process of major deformation of the deposits. Special emphasis has been given to the characterisation and understanding of the morphology and internal structure of slide deposits. To this end, seismic analysis has been combined with spacial analysis of the DEM generated from key seismic reflectors. The detailed reflector-picking applied during the project coupled with the extraction of different attribute maps and effective visualization tools has allowed a better understanding of these deposits.

1.2 Submarine mass movements: processes and products

Mass movement deposits include a vast spectrum of deposits which resulted from downslope transport *en mass* driven by gravity. The gravity-induced mass movement processes are also referred to in the literature as: *gravitational collapse*, *mass-wasting*, *slope failure* and more often *mass-transport*. These processes can occur on both subaerial and submarine environments, and even deposits seen on images from other planets (e.g. Lucchitta, 1978; Malin, 1992, Mars and Venus respectively) and satellites (e.g. Howard, 1973; Moore et al., 1999, Moon and satellites of Jupiter) have been interpreted as resultant of mass movement processes.

There is an extensive literature dedicated to subaerial mass movement processes, reflecting the intensive effort to study these processes which play an important role on land erosion and can represent a threat to human activities, infrastructure and lives. Extended literature reviews on these processes are offered by vary authors, including Brunsdon and Prior (1984); Schwab et al. (1993); Hampton et al. (1996); Erismann and Abele (2001); Locat and Lee (2002); Dykstra (2004). Although more limited than its subaerial counterpart, literature dedicated to submarine mass movement increased markedly in the last 20 years, reflecting improvement on marine

geophysical techniques that allowed detailed morphological characterisation of a large number of mass movement deposits on continental margins and inner seas.

1.2.1 Classification and terminology

The classification of submarine mass movements has been the object of continuing debate since the earlier papers, such as Dott (1963), describing offshore deposits of gravity-driven processes. This unsettled debate is partly due to the fact that these processes occur in very distinctive geological settings, at different scales, and the remoulded material can be transported by a wide variety of mechanisms (from rigid block motion to turbulent flow) and, therefore, generate a huge spectrum of deposits. Additionally, in one given event a continuum of different types of transport processes can occur and a single deposit may contain imprints of more than one process (Nardin et al., 1979). Another factor that contributes to keep the debate alive is not related to the processes nature, but to the fact that many geological and geotechnical researchers and applied research engineers studying these processes have been using terminology influenced by their diverse backgrounds (Nardin et al., 1979; Shanmugam, 2000; Mulder and Alexander, 2001). It is also virtual impossible to find a consensual classification that can be applied to both modern and ancient deposits, and to studies based on 1) remote-sense geophysical data, 2) direct observation of the resulting deposits (either with coring techniques or study of ancient deepwater systems exposed outcrop), or 3) laboratory experiential work.

Most of the used classifications of submarine mass movements are inherited from the terminology applied to subaerial mass movements and based on Varnes (1978) classification (Fig. 1.1). Middleton and Hampton (1973) presented a first classification for submarine mass movement and highlighted two fundamental dynamic boundaries distinguishing elastic, plastic, and fluid behaviours. Rockfalls, slides and slumps represent elastic transport mechanisms. Mass flows that move plastically are represented by debris flows, mud-flows and inertial grain flows. Viscous fluid behaviour includes viscous grain flows, liquefied flows, fluidized flows, and turbidity currents. Nardin et al. (1979) compiled a system that incorporates both sedimentary features of the deposits, such as size distribution and sedimentary fabric, and the mechanical behaviour inferred from the deposits. This classification is synthesized into three groups in which the major transport and grain support processes can be grouped according to mechanical behaviour. However, as recognised by Mulder and Cochonat (1996), these are static classifications and do not adequately account for the continuous changes in shape and dynamics that may occur

in a mass movement between its initiation and final deposition. These authors proposed the use of both a static and a dynamic classification, based for the first time on geophysical techniques such as swath bathymetry and deep-tow side scan sonar (Canals et al., 2004). Since then, alternative classifications have been presented using factors like: mechanical behaviour, particle-support mechanisms, sediment concentration by volume, and geometry of the remaining deposits. Some classifications are focused only one group of mass movement, as Normark and Piper (1991) while others are focused only on the processes found on a specific geographic site, as the classification recently presented for the area offshore Trinidad by Moscardelli and Wood (2008) (Fig. 1.2).

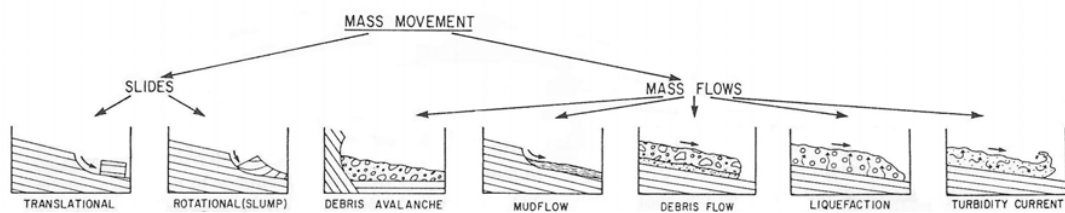


Figure 1.1: Classification of different type of submarine mass movement modified from the Varnes' classification by Coleman et al. (1993).

GRAVITY INDUCED DEPOSITS		Genetic Classification Transport Mechanism	Descriptive Classification Sedimentary Structures	Seismically Recognizable Features
Mass Transport Complex	Slide	Shear failure along discrete shear planes with little or no internal deformation or rotation	Essentially undeformed, continuous bedding	Continuous blocks without apparent internal deformation. High-amplitude, continuous reflections.
	Slump	Shear failure accompanied by rotation along discrete shear surfaces with various degrees of internal deformation	Plastic deformation particularly at the toe or base. Flow structures, folds, tension faults, joints, slickensides, grooves, rotational blocks	Compressional ridges, imbricate slides, irregular upper bedding contacts, duplex structures, contorted layers. Low- and high-amplitude reflections geometrically arranged as though deformed through compressive stresses.
	Debris Flow	Shear distributed throughout the sediment mass. Strength is principally from cohesion due to clay content. Additional matrix support may come from buoyancy, Plastic rheology and laminar state.	Matrix supported, random fabric, clast size variable, matrix variable. Rip ups, rafts, inverse grading and flow structures possible.	Mega rafted and/or detached blocks, irregular upper bedding contacts, lateral pinch-out geometries, oriented ridges and scours. Low-amplitude, semitransparent chaotic reflections.
Turbidity Current	Turbidite	Supported by fluid turbulence (newtonian rheology)	Normal size grading, sharp basal contacts, gradational upper contacts.	Lobate features Laterally continuous

Figure 1.2: Classification of mass movement deposits used by Moscardelli and Wood (2008) for their study of 3D seismic data from offshore Trinidad. Compiled from Dott (1963) and Nardin et al. (1979), and adapt to both the study area and the use of seismic data.

Additional to the multiplicity of classification systems used to categorize mass movement, the terminology used is a source of uncertainty and confusion in itself. The terminology used to describe the mechanisms and different sedimentological aspects of the resulting deposits

presents a multiplicity of equivalent terms in use. For instance, *Landslide Shear Surface* and *Gliding Surface* are considered as equivalent terms to *Slip Surface*. Furthermore, the use in the literature of some of the terms is unclear. Canals et al. (2004) draw attention to the example of the term *Slip Surface* that can mean 1) a stratigraphical or mechanic plane defining the base of failed deposits, or 2) the older seabed over which the failed material was transported.

The term *slide deposit* is used in this thesis as a general term for almost any type of submarine mass movement deposit, rather than exclusively used for deposits generated by this specific type of transport, in order to set a quick distinction with the glaciogenic debris flow deposits.

1.2.2 Triggering mechanisms

Sediments are deposited in a stable state where their shear strength exceeds shear stressed oriented downslope. Nonetheless, any modification of this state, through either a decrease in sediment shear strength (resisting strength), an increase in shear stress (driving shear stress) operating on that sediment, or a combination of both, can lead to slope failure (Hampton et al., 1996). The shear strength of the slope-forming material is generally described by the Mohr-Coulomb failure criterion:

$$\tau_f = c' + (\sigma - u)\tan\phi'$$

where τ_f is the shear strength, c' is the effective cohesion, σ is the stress acting normal to the failure surface, u is the pore water pressure and ϕ' is the friction angle. The term $(\sigma - u)$ is the effective normal stress and is normally condensed to σ' . A slope failure can also occur when the overall resisting forces are exceeded by the gravitational forces or when the resisting forces are reduced to a point below which they are less than the gravitational forces.

The term *triggering mechanisms* is commonly used in the study of slope instability processes to refer to the external stimulus capable of inducing slope failure (Sultan et al., 2004). According to Locat and Lee (2002) these mechanisms can be grouped into two broad classes: (1) mechanisms that reduce the shear strength and, thus, decrease the resisting forces and (2) mechanisms that increase the driving shear stress on the slope. These two classes are not mutually exclusive, *i.e.* mechanisms of both classes can occur simultaneously in a given slope. Furthermore, a given mechanism can be included in both classes. Several triggering mechanisms, some specific to the marine environment, are presented in the literature (e.g. Hampton et al., 1996) and include 1) earthquakes, 2) wave loading, 3) tides, 4) rapid sediment accumulation, 5)

gas charging, 6) gas hydrate dissociation, 7) glacial loading, 8) erosion, 9) salt diapirism, 10) volcanic processes, 11) water seepage, 12) mud volcanoes 13) sea-level fluctuations and 14) human activity. Table 1.1 modified from Locat and Lee (2002) separates the referred mechanisms in natural triggers or induced by human activity and places the mechanisms according to their potential to reduce the resisting strength and increase the driving shear stress, whereas table 1.2 presents examples of known slope failure events that have been attributed to one specific triggering mechanisms.

Reducing the Strength	Increasing the Stresses
<i>Natural Triggers</i>	
Earthquakes	Earthquakes
Wave Loading	Wave Loading
Tides	Tides
Sedimentation	Sedimentation
Gas and Gas Hydrates	-
Groundwater Seepage	-
Glaciation	Glaciation
-	Erosion
-	Diapirs
<i>Man-made Triggers</i>	
Gas-hydrates and reservoir depletion	Excavation Loading Subsidence

Table 1.1: Trigger mechanism classification relatively to their effect, reducing the strength or increasing the stresses, and their origin, natural or anthropogenic after Locat and Lee (2002).

In many of the above mentioned cases, the triggering mechanisms are considered as the ultimate and determining factors capable of inducing the slope failure. However, there is an increasing awareness of the need to understand the relative importance of triggers mechanisms as the fulfilment of a set of essential preconditions can be the enabling factor of the failure event. In the situation where the ratio between resisting forces and gravitational forces defined by the preconditions is low, the nature of the triggering mechanism can be considered as almost secondary, and a poor representation of the causes of the event (Ayers, 2007). This is graphically explained by figure 1.3 where in the first scenario the trigger mechanism plays a determinant role whereas in the second scenario it is of little significance compared to the initial conditions. Therefore the attempt to determine retrospectively the nature of the trigger mechanism may not be as important as understanding the precondition factors in the cases better represented by the second scenario.

Triggering Mechanisms	Examples
Earthquakes	Grand Banks, Piper et al. (1988); Papua New Guinea Tappin et al. (2001); North Aegean Trough, Lykousis et al. (2002)
Wave loading	Mississippi Fan (Hurricane Camille), Bea et al. (1983)
Tides	Terzaghi (1956); Fraser River delta (Canada), Atigh and Byrne (2003)
Rapid sediment accumulation	Mississippi Fan, Coleman et al. (1993); offshore Mauritania Krastel et al. (2006)
Gas charging	Caspian Sea, Newton et al. (1980)
Gas hydrate dissociation	Beaufort Sea Kayen and Lee (1993); North Atlantic, Maslin et al. (2004)
Glacial loading	Scotian Shelf, Mulder and Moran (1995); Laurentian Channel, Piper and Macdonald (2001); Nyk Slide, Lindberg et al. (2004)
Erosion	California canyons, McAdoo et al. (2000)
Salt diapirism	Off North Carolina, Cashman and Popenoe (1985); Gulf of Mexico, Prior and Hooper (1999)
Volcanic processes	Canary Islands, Watts and Masson (1995) & Gee et al. (2001); Hawaiian, Moore et al. (2008)
Water seepage	New Jersey, Dugan and Flemings (2000)
Mud volcanoes	Gulf of Mexico, Prior and Doyle (1993); Offshore Trinidad, Moscardelli and Wood (2008)
Sea-level fluctuations	Madeira Abyssal Plain, Weaver and Kuijpers (1983)
Human activity	Nice, Assier-Rzadkiewicz et al. (2000)

Table 1.2: List of main triggering mechanisms and associated examples

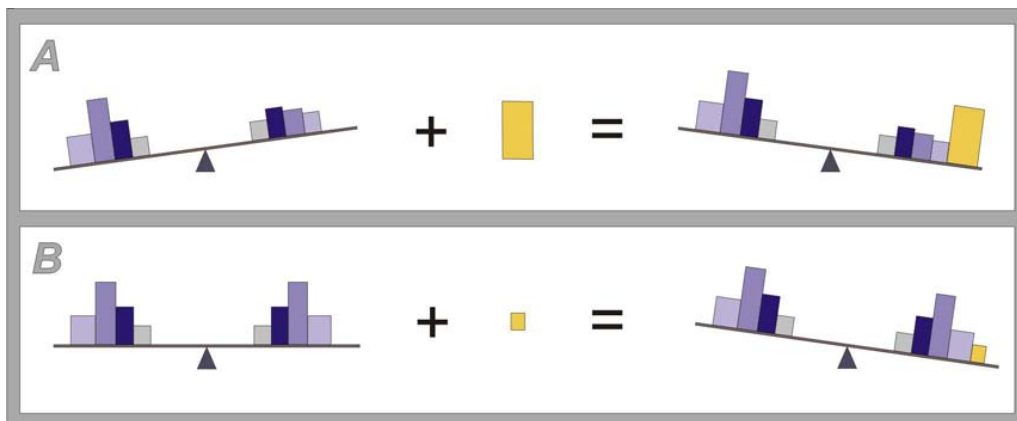


Figure 1.3: Diagram explaining the relative importance of the trigger mechanism compared to the preconditions. The schematic scales represent the balance between resisting and gravitational forces. This representation has been previously presented by A. Camerlenghi in oral communications.

1.3 Rationale

Importance of submarine mass movements

The greatest mass movement events have occurred on the seabed however, although until recently it was thought that these types of events were rare and limited to areas of high slope, areas of rapid deposition or areas of high seismic activity. The increasing knowledge of seabed and subsurface have uncovered that these events have been far more common than previously believed and can occur in many environments such as fjords, active river deltas, submarine canyons, oceanic volcanic islands or ridges and open continental margin slopes, as shown by Lee et al. (1991).

Their frequency, their widespread occurrence and the fact that mass movement processes can cause massive erosion, sediment re-distribution and change in depositional patterns, makes them important processes in continental margins evolution. They can even be in some margins the main mechanism of sediment transport, capable of transferring volumes of sediment that vary from tens to thousands of cubic kilometres, over slopes of less than 1° (e.g. Locat, 2001; Locat and Lee, 2002; Canals et al., 2004). Additionally, submarine mass movement deposits can represent a significant stratigraphic component of many ancient and modern continental margins. Newton et al. (2004) recognized that locally up to 94% of the Quaternary sedimentary column of the Nile Fan can be comprised of submarine mass movement deposits. Consequently, and additional to the scientific interest on the understanding of these processes, there is an

economic aspect to it as the hydrocarbon industry also shows a particular interest in these processes and their importance on hydrocarbon reservoir characterisation (e.g. Frey-Martinez, 2005).

Geohazards associated to submarine mass movements

As early as 1929, when an earthquake-related failure broke several submarine telecommunication cables off Newfoundland (Piper et al., 1988), the destructive power of submarine mass movements was demonstrated. This event not only exemplified the existence of fast-moving, long-distance sediment flows across the ocean floor as the impact that such events could have on the marine infrastructure. Nowadays, due to the marked increase of the use of the marine environment, such type of events could threaten not just submarine cables but also a vast number of oil platforms, transportation corridors, coastal structures, wind farms and other seabed installations (e.g. Nadim, 2006).

However, the destructive impact of submarine mass movements can extend beyond the marine environment. It has been recognized that they can generate locally damaging tsunamis. Worldwide, tsunamis generated by submarine slope failure have damaged coastal structures and caused casualties, e.g.: Corinth Gulf - Greece, 1963 (Papadopoulos et al., 2007); Aleutian forearc - Alaska, 1964 (Fryer et al., 2004); Nice Airport - France, 1979 (Dan et al., 2007); Papua New Guinea, 1998 (Tappin et al., 2001). The devastation scale and the number of lives lost (estimated to over than 2200) as result of to the 1998 Papua New Guinea's Tsunami in particular, led to a major re-evaluation of the potential threat of this source to coastal communities worldwide.

Since then, a significant effort has been made to try to assess the risk associated with landslide-generated tsunamis and to develop prediction and mitigation tools to better constrain the main parameters that define wave height of a landslide-generated tsunami. Mainly from numerical modelling work, as recently presented by Brune (2009), it is known that the magnitude of the generated tsunami will be affected by the following factors: slide volume and thickness (positive feedback), velocity and acceleration, water depth (negative feedback), slide proximity to shore, slide density and slide evolution.

Although submarine mass movements are mainly seen as a threat, they actually could be used as an alert system for earthquakes, since small submarine landslides seem to occur before major

seismic events. These small-scale collapses could be identified as precursory signals and be detected by hydrophones on the seabed. Though such type of alert system may be still far from becoming a reality, earthquake triggered turbidites have been already proven to be a source of valid data to address the recurrence interval of earthquake (Adams, 1990).

Study of the European glaciated margin

Sedimentary processes vary considerably along European continental margin, mainly due to the distribution of extensive ice sheets during the Northern Hemisphere glaciations (Weaver et al., 2000). The formerly glaciated margins, north of 52°N (Leynaud et al., 2009) were particularly affected by recurrent glacial-interglacial cycles and heavily shaped by glaciomarine processes that supplied huge volume of sediments. These margins present unique stratigraphic characteristics, marked by (1) lateral variation resulting from the different sedimentation rate controlled by the location and dynamics of *ice streams* and *ice sheets*, and (2) vertical variation related with glacial-interglacial cycles. As a result of their particular development, formerly glaciated margins present marked lateral changes in slope stability and recurrent development of preconditions to failure due to: 1) the presence of weak layers related to contourite drifts and 2) the presence of excess pore pressure due to the rapid loading by glacial sediments. High-magnitude earthquakes due to isostatic rebound during major ice sheet decay could act as final triggering mechanisms (Leynaud et al., 2009).

It is in the Glaciated European Margin that one of the largest landslides of the world can be found, the Holocene Storegga Slide that is the most recent of several major slides in the Storegga Slide Complex. This large-scale slide occurred 8200 years ago as a response to climatic variability, at the end of a glaciation or soon after the deglaciation (Bryn et al., 2005a). This event is a good example of the geohazard associated with glaciated margins during periods of ice sheets retreat. Understanding better the mass movement processes that shaped formerly glaciated margins will provide better chances of assessing the geohazard potential of present day glaciated margins and their sensitivity to climatic variability. In the context of the current climate changes, such understanding is extremely relevant as the occurrence of an event of scale comparable to the Storegga Slide would have dramatic consequences.

3D seismic data from Norwegian margin

The Mid-Norwegian margin has been extensively surveyed due to the presence of hydrocarbons. Since the 1970s, a large amount of data has been acquired and studied, making it today

one of the best investigated margins in the world. The study of 3D seismic data from this margin offers excellent conditions for the study of the seismic geomorphology of its mass movement deposits by coupling the potential provided by this type of data to the background knowledge of the margin evolution.

1.4 Aims and objectives

The main goal of this project is to better understand the large-scale mass movement events that shaped the North Sea Fan from the Mid-Pleistocene to the present day. The second aim of this thesis is to explore the full potential of the use of 3D seismic for the study of mass movement deposits, by developing and exploring new approaches and techniques to obtain and display data from 3D seismic volumes. For that purpose, the following objectives were set:

- To analyse in detail the seismic data available for this study and carefully extract the surface of key surface and seismic attribute maps from the 3D seismic volume.

- To couple seismic interpretation with geomorphological analysis on a Geographic Information System (GIS) environment, which allows 1) visualisation displays beyond the possibilities offered by seismic interpretation software, and 2) the application of spatial analysis tools developed for subaerial geomorphology, where studies within a GIS environment are more advanced.

- To characterise both the seabed and the buried deposits of three of the largest mass movement on the Norwegian Margin: the Tampen Slide, the Møre Slide and the Slide U, focussing especially on aspects such as the internal structure of these deposits, commonly described just as chaotic or structureless based on 2D seismic.

- To investigate the external morphology, internal structure, presence of kinematic indicators within these deposits and explore their relation with factors such as the underlying geometry, transport direction and degree of transport.

- To gain a greater understanding of the rheological behaviour and dynamics of mass movement processes by examining the seismic geomorphology of structures present on their deposits.

The outcomes of this work improves the understanding mass movement processes and their resulting morphology, internal structure and interaction, and contribute to the general knowledge of the role of mass movement processes into the development of glacier-influenced sea fans.

1.5 Outline of thesis

This thesis consists of seven chapters. The first three chapters provide an introduction to the research done during this project, chapters four and five present the main results. Finally, the discussion and conclusion of this work are exposed in chapter six and seven respectively.

Chapter Two

The second chapter addresses the geological setting of the study area. A general overview of the development of the Glaciated European Margin is given in section 2.2 and more detailed descriptions of the North Sea Fan and the Storegga Slide morphology and evolution are provided in sections 2.4 and 2.5. Additionally, the stratigraphic framework used in this thesis is presented in section 2.3.

Chapter Three

This chapter provides an overview of the used database and methodology. These datasets were integrated through a geographic information system and a seismic interpretation software package. Details of each dataset and of the integration process, together with the problems encountered, are presented. Special emphasis is given to the data visualisation of 3D seismic data and to the extraction of seismic attributes.

Chapter Four

This chapter presents the morphology description of the seabed and shallow subsurface of the study area, mainly based on 3D seismic interpretation. The seabed is sub-divided into five morphological zones named: Zone S, Zone Ch, Zone Cl, Zone B and Zone U. They are described individually with their interpretation.

Chapter Five

This chapter describes in detail the morphology of the three buried main Mid- to Upper-Pleistocene slides studied: Tampen Slide, Møre Slide and Slide U (sections 5.2, 5.3 and 5.4

respectively). The detail description and interpretation of each slide's deposits is preceded by an introduction to the key aspects of the corresponding slide event and the location of the study area within the slide scar.

Chapter Six

On this chapter, aspects related to the geometry and internal deformation observed on slide deposits are debated. This discussion couples the observation from the study area with other examples presented in the literature. Special emphasis is given to features along of sidewall (section 6.2) and along sliding surface (section 6.3), and to evidence of internal deformation (section 6.4). The implications related to the submarine mass movement deposits' geometry and internal structure are addressed in section 6.5.

Chapter Seven

The last chapter presents the main conclusions and key aspects of this thesis (section 7.1). Suggestions for further work are provided at the end (section 7.2).

Chapter 2

Geological Setting

2.1 Introduction

This chapter presents the geological setting of the area studied in this thesis, located on the Glaciated European Margin.

The Glaciated European Margin is considered as part of a *passive margin*. However, this region as experienced several episodes of tectonic activity during the Cenozoic and shows various differences from a classic model of post-rift evolution (Stoker et al., 2005a). Additionally, development of this margin was also controlled by an long history of glaciations and slope instability (e.g. Rise et al., 2005; Stoker et al., 2005a). Section 2.2 briefly outlines of the major events of this margin evolution. Sections 2.4 and 2.5 describes respectively the two main physiographic elements encountered on the southern Norwegian Margin/SE Nordic Seas, the North Sea Fan and the Storegga Slide depression. The detailed description of the morphology of the North Sea Fan northern flank is carried out in subsection 2.4.1 and subsection 2.4.2 describes the fan development and the its slope instability history. Finally, section 2.3 provide the reader with the stratigraphic framework used in this study. This aims to provide the reader with a broad overview of the surrounding area.

2.2 Glaciated european margin

The Glaciated European Margin extending from the Rockall Trough to the Svalbard Archipelago (Fig. 2.1) displays a complex bathymetry with a variety of cross-shelf troughs, prograding wedges as well as through-mouth fan systems, and failure depressions (e.g. Dahlgren et al., 2005). This complex physiography overlies crustal thickness variations resulting from Cenozoic rifting and magmatism during the opening of the North Atlantic Ocean (Knott et al., 1993; Stoker et al., 2005a). Based on its physiography and development, the margin can be divided into several regions (e.g. Rise et al., 2005; Stoker et al., 2005a): Rockall-Porcupine region, Farøe-Shetland region, the North Sea Fan/Storegga region, the Vøring Plateau region, Lofoten

margin region. The development of this margin was principally controlled by the tectonics, glaciations and slope instability (e.g. Ottesen et al., 2001; Rise et al., 2005; Stoker et al., 2005a).

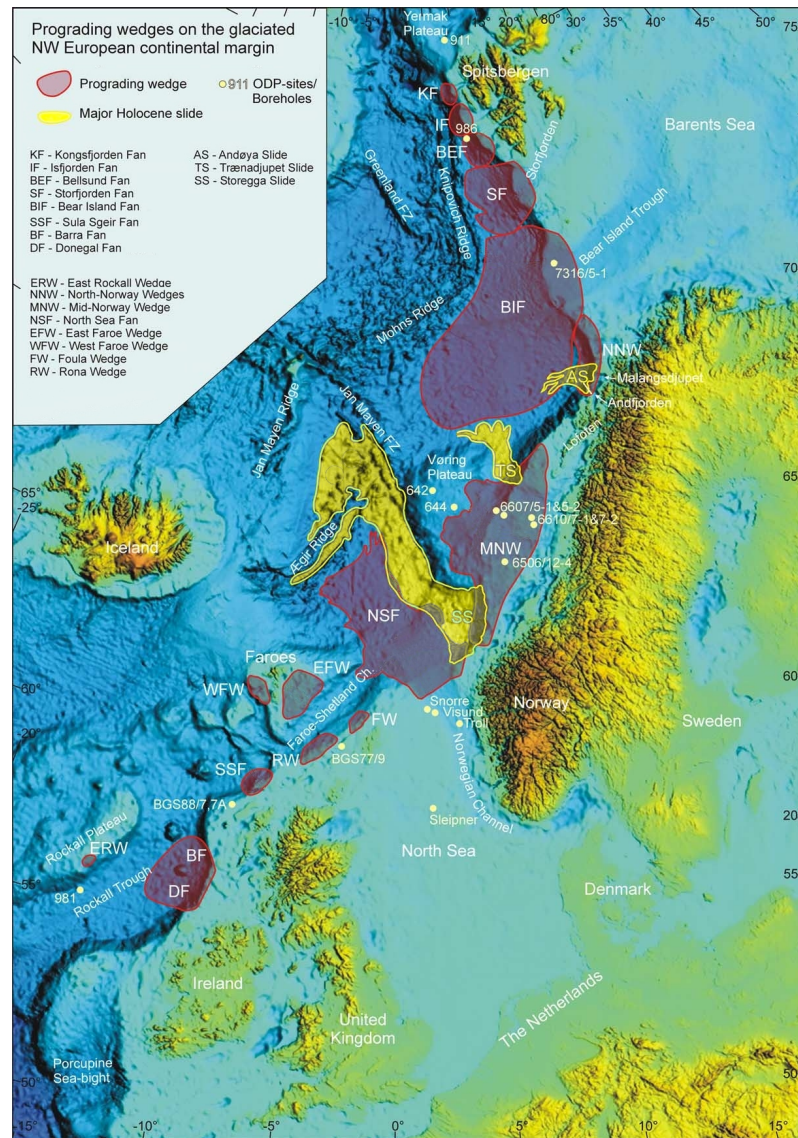


Figure 2.1: Distribution and extent of prograding wedges along the glaciated NW European margin. All prograding wedges except for the East Rockall Wedge are mainly of glacial nature. Modified from Dahlgren et al. (2005).

Tectonic evolution

The development of NW European margin is particularly associated to the opening of the NE Atlantic (Ziegler, 1988; Knott et al., 1993; Doré et al., 1999; Lundin and Doré, 2002). The extensional history of this margin spanned a c.350 Ma interval from the close of the Caledo-

nian orogeny to the Early Eocene break-up (Knott et al., 1993; Doré et al., 1999). Doré et al. (1999) explain the exceptionally long history of extension partially by changes in the extension direction, but mainly by lateral shifting of the successive rift axes. An extensional pulse from the latest Cretaceous to earliest Eocene age with extensive basaltic volcanism led to continental break-up separation of Europe and Greenland, at approximately 53 M (Doré et al., 1999; Skogseid et al., 2000). Four main extension episodes that can be distinguished from one another in time and space are presented on figure 2.2.

During the first stages of Mesozoic continental rifting and during the Late Mesozoic-Cenozoic continental separation and ocean spreading, pre-existing Precambrian and Palaeozoic accretionary structures resulting from the Caledonian collision that accreted of the Laurentia, Baltica and Eastern Avalonia blocks from the Silurian to Early Devonian (Woodcock and Strachan, 2000) were reactivated according to the prevalent stress pattern. A main period of syn-break-up volcanism associated occurred between 56-52 Ma (White and Lovell, 1997). The high degree of volcanism in this margin has been attributed to the presence of a mantle plume (White, 1988).

Doré et al. (1997) reviewed some of the Precambrian-Caledonian basement structures and their later tectonic development and connection with the three predominant fault trends present on the NW European margin (NE-SW, N-S and NW-SE). From this study, there are three essential points relevant to the study area: (1) The Cretaceous-Cenozoic basins are closely parallel to the major NE-SW shears of the Late Caledonian age, as the Møre-Trøndelag Fault Zone (MTFZ) which marks the south-eastern boundary of the Møre Basin (e.g. Blystad et al., 1995), (2) many of the N-S lineaments, associated to several rift basins as the Viking Graben (Badley et al., 1988), can be attributed to extension of Jurassic age, (3) the NW-SE transfer trend had a marked effect on the structural geometry and sedimentation patterns in the Cretaceous and Cenozoic depocentres. The Jan Mayen fracture zone (JMFZ) between the Møre and Vøring basins is one of the most prominent of these transfers zones, that intersect with the continent-ocean boundary and appears to control positioning and the extent of the Møre and Vøring marginal highs.

This margin is characterised by shallow platforms, shelves, ridges and banks separated by deeper-water basin developed during extensional periods and it is considered as a *passive continental margin*. However, its configuration may have become accentuated by compression, extension, and broad uplifts and subsidence that affected the continental margin during the mid- to late Cenozoic interval (Lundin and Doré, 2002), as shown by the structural inversion observed in the Vøring basin (Blystad et al., 1995; Lundin and Doré, 2002).

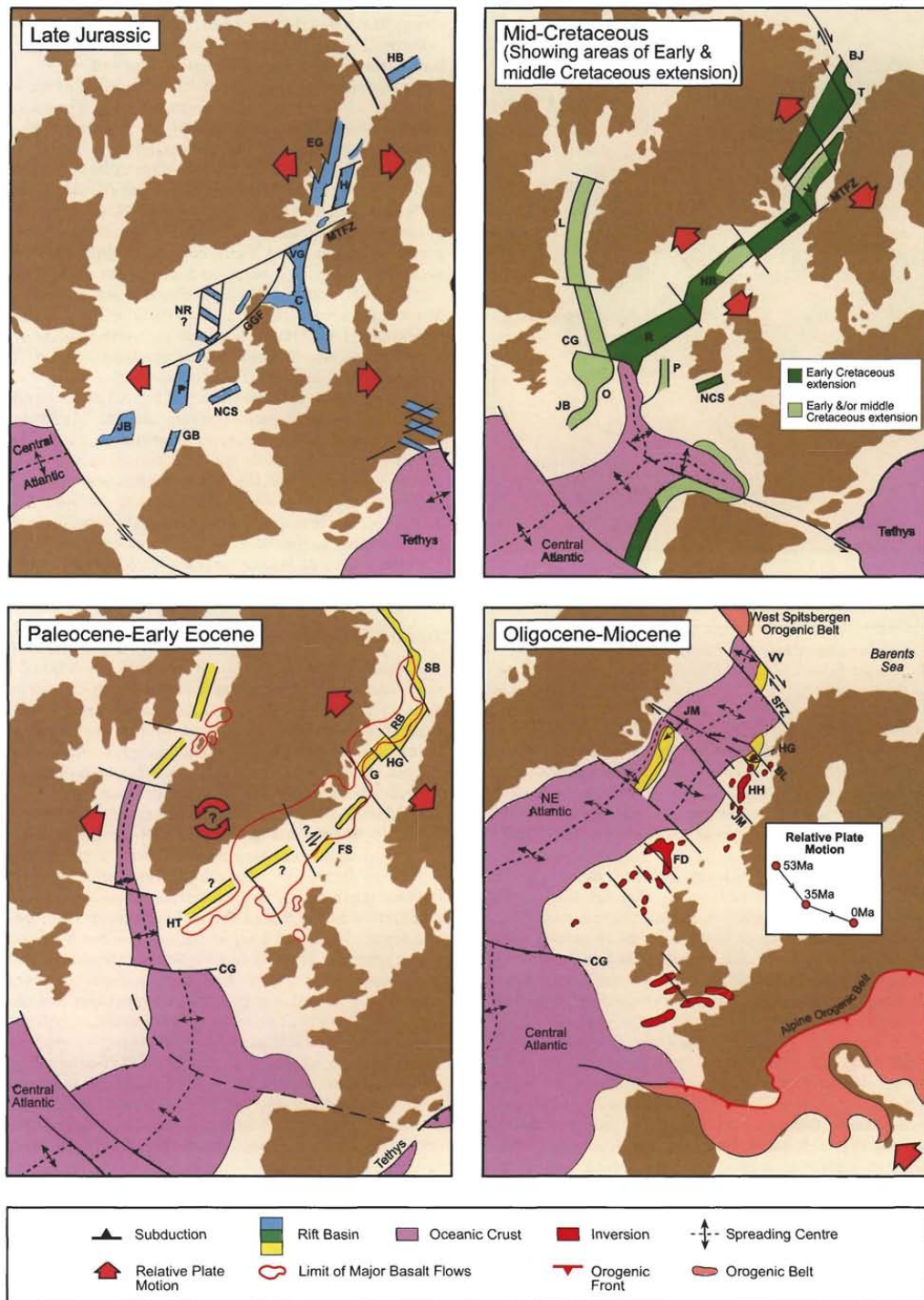


Figure 2.2: Late Jurassic, mid-Cretaceous, Paleocene-Early Eocene and Oligocene-Miocene plate reconstructions by Doré et al. (1999), showing relative plate motion, contemporaneous rifts and areas of inversion.

Glacigenic deposition

The *Mid-Pleistocene Revolution* (MPR), approximately 600-700 ka ago, marked the transition to stronger glacial-interglacial cycles with longer lasting glaciations causing development of more extensive northern hemisphere ice sheets (Berger and Jansen, 1994; Wright and Flower, 2002). Associated with these cycles, ice sheets have advanced and retreated across most of the glaciated NW European Margin. Research focused on regional morphology and sedimentary architecture of continental slopes (e.g Laberg and Vorren, 1995; Dowdeswell et al., 1996) has shown that during glacial maxima, the ice sheets expanded across continental shelves up to the shelf edge. However, the delivery of ice and sediments to the continental shelf edge was heterogeneous; patterns of flow-partition into low and fast-flowing ice (ice streams) have been described (e.g. Sejrup et al., 2000). Ice streams were responsible for discharging the majority of the ice and sediment within ice sheets. Thousands of cubic kilometres of sediment were transported to the Norwegian shelf edge (Hjelstuen et al., 2004) during the mid- and late-Pleistocene by ice streams. Ice streams' dynamic also played a critical role in driving abrupt changes in high-latitude climate and oceanography.

This high sediment flux supplied enough material for the development and the build-up of the large glacier-fed fan systems on the continental slope offshore of these fast-flowing ice streams. These fans have been termed Trough-Mouth Fans (TMFs) by Vorren and Laberg (1997) as they are located in front of depressions on the shelf. They were the main depocentres of glacigenic sediments on the Norwegian Margin during the Quaternary (King et al., 1996; Dowdeswell et al., 1998; Taylor et al., 2002). It has been estimated that 15-20% of the Late Weichselian sediment input to the deep-basins was by the North Sea Fan and the Bear Island Fan, contributing approximately 1000 km³ each (Taylor et al., 2002).

Slope Instability

The Glaciated European Margin presents long-term instability over the last 500 ka related to recurrent glacial-interglacial period cycles (Evans et al., 1996). Several examples of the large-scale sliding events occurred mainly during sea level rise from glacial to interglacial times. Through its evolution, the Glaciated European Margin has seen recurrent build up of failure preconditions induce by the combination of several factors. The main aspects are the high sedimentation rates that lead to an excess pore pressure due to the rapid loading by glacial sediments and the presence of weak layers deposits during interglacial periods. The isostatic rebound sub-

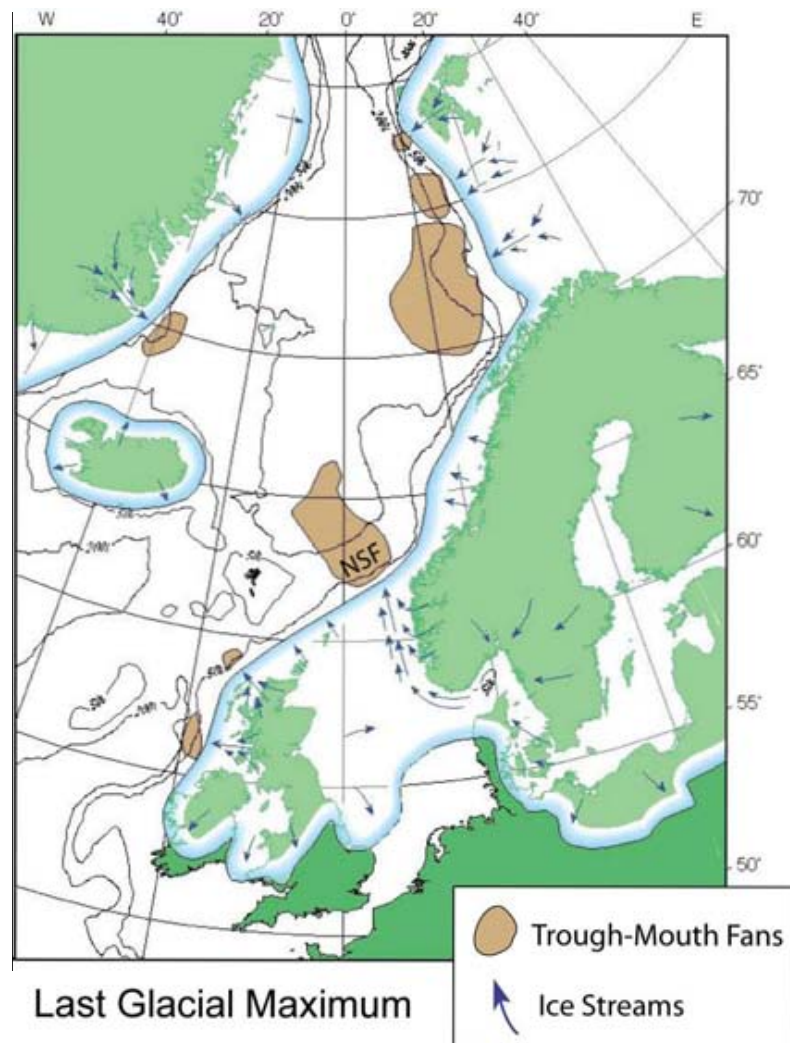


Figure 2.3: Last Glacial Maximum (28-22~ka) extent of the Fennoscandian, UK, and western Barents ice sheets, with distribution of glacial fed fans on the margins and possible location of former ice streams indicated (Sejrup et al., 2000). BIF - Bear Island Fan; NSF - North Sea Fan.

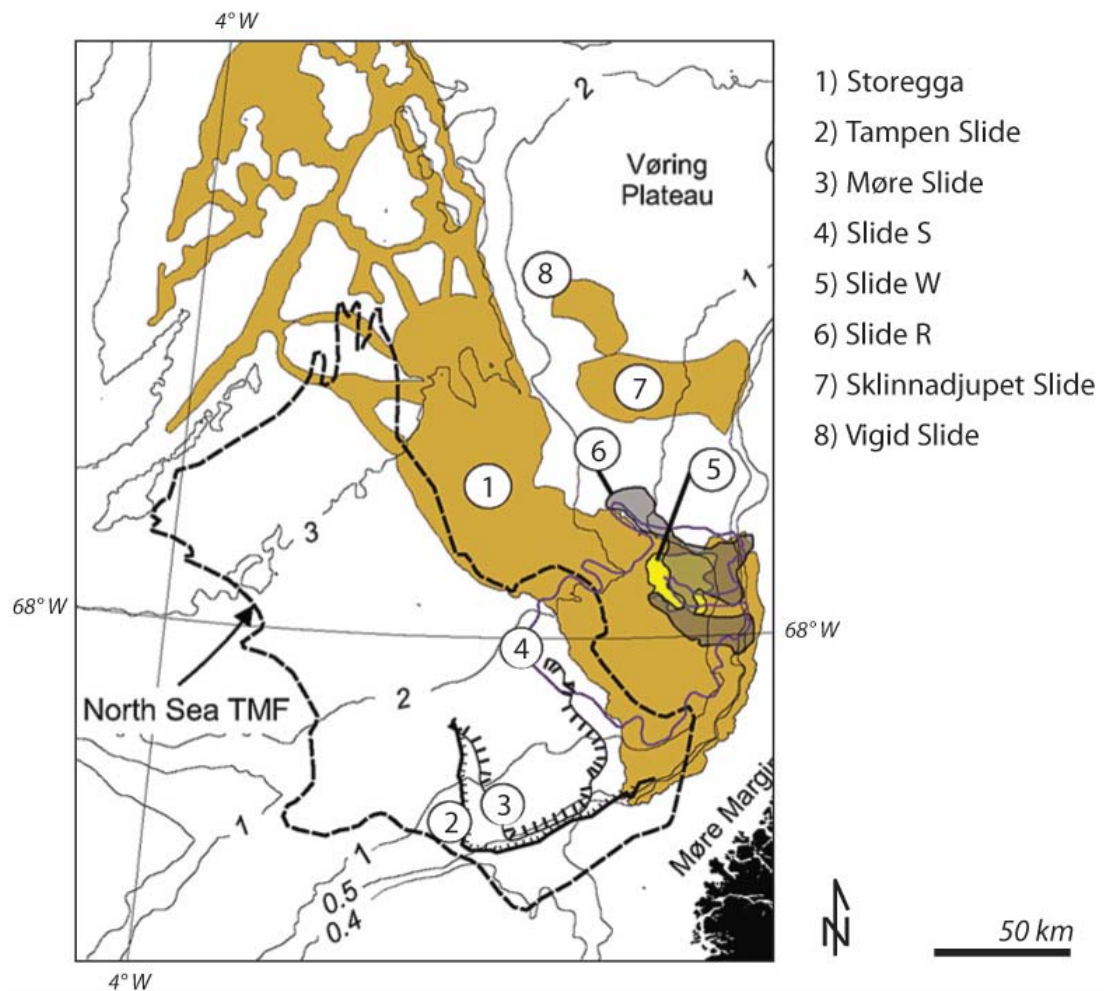


Figure 2.4: Location of the main mass movement deposits adjacent or within the North Sea Fan. Bathymetry provided in km. Modified from Hjelstuen et al. (2007).

sequent to major ice sheet retreats generated high-magnitude earthquake that could have act as final trigger mechanisms (Leynaud et al., 2009). As a result of its particular development, the glaciated European margin presents marked lateral changes in slope stability. These lateral changes are mainly associated with the lateral variation of material supply, resulting from the different sedimentation rate controlled by the location and dynamics of ice sheets and by the location of contourites on continental slopes. Figure 5.2 shows the location of the main mass movements deposits adjacent or within the North Sea Fan (Hjelstuen et al., 2007) and table 2.1 compiled by Leynaud et al. (2009) present the names, ages and volumes of submarine mass movements observed through the full glaciated European margin.

Name	Type	Age (ka)	Volume (km ³)	References
Northern Svalbard	Slide complex	> 20 and < 40	1350 ?	Cherkis et al. (1999), Vanneste et al. (2006), Winkelmann et al. (2006)
Bear Island Trough-Mouth Fan	Debris flows	15-20	800-1100	Laberg and Vorren (1995, 2003), Taylor et al. (2002)
Bear Island	Slide	> 200 ?, 18-20 ?	1100-1400	Laberg and Vorren (1996), Vogt and Jung (2002)
Fugly Bank	Slide complex	> 10 ?	NK	Dowdeswell et al. (2003)
Andya	Slide	Early Holocene (?)	900 ?	Vorren et al. (1998), Laberg et al. (2000), Taylor et al. (2002)
Trnadjupet	Slide	-4	900-1900	Laberg et al. (2002), Dowdeswell et al. (2003)
Nyk	Slide	> 16.3	NK	Lindberg et al. (2004)
Nyk	Debris flows	post LGM	NK	Laberg et al. (2002)
Finneidfjord	Slide	recent (1996)	0.001	Longva et al. (2003), Best et al. (2003)
Paleo-1	Slides	pre-Holocene	NK	Dahlgren et al. (2002), Bryn et al. (2003)
Storegga	Slide complex	8, 15	2400-3200	Bryn et al. (2003), Hafliðason et al. (2004)
Paleo-2	Slide	Pre-Holocene	NK	Bryn et al. (2003), Solheim et al. (2005)
North Faeroe	Slide complex	9, 85	135-1700	Van Weering et al., (1998), Taylor et al. (2002), Maslin et al. (2004)
Miller	Slide	Pleistocene	> 360	Long et al. (2003)
Afen	Slide	Holocene	0.2	Long et al. (2003), Wilson et al. (2003)
Sula Sgeir	Slides	Pleistocene	NK	Holmes et at. (2003)
Peach	Slide complex, debris flows	Pleistocene	135-675	Holmes et at. (1998), Holmes et al. (2003)
Donegal	Slides	Holocene	NK	Holmes et at. (2003)
Foreland	Slide complex	Pleistocene	NK	Holmes et at. (2003)
Porcupine and Rockall Banks	Slides, slumps, debris flows	15-16	NK	Van Weering et al. (2003)

Table 2.1: Glaciated European Margin slides. From Leynaud et al. (2009). The references present in this table are to be found in the original article

2.3 Stratigraphic framework

The middle to upper Cenozoic stratigraphic succession of the North Sea Fan area is divided into three main formations (Dalland et al., 1988): *Brygge*, *Kai* and *Naust* formations. In the area, the base of the Neogene is represented mainly by angular submarine erosion surfaces separating the Kai formation from older Palaeogene strata of the Brygge formation and the Intra-Pliocene unconformity separates the Kai and Naust formations.

According to the geomodel developed for the *Seabed Project*, these three main formations are products of very distinct environmental settings. During the Brygge formation times (Eocene to Earliest Miocene: 54 - 25.2 Ma) most of the deposition occurred in gently subsiding deep-water basins while sea-floor spreading was still occurring. During the Kai formation times (Earliest Miocene to Late Pliocene: 25.2 - 3.5 Ma), with well-established ocean currents, the sedimentation occurred mainly on deep waters environment and in tectonically generated irregular depositional surfaces. A series of big environmental changes occurred after deposition of the Kai Formation resulting on ice sheets cyclic advances and retreats during the Naust Formation times (Late Pliocene - 2.8 Ma - to Holocene). These formation divisions therefore reflect very marked contrasts in environmental conditions on the margin.

The seismic character of the Naust formation is noticeably different from the Kai and Brygge formations, mainly comprised of hemipelagic fine-grained clay and/or ooze deposits. The average deposition rate for Naust formation is more than an order of magnitude greater than the two preceding formations (Norwegian Deepwater Programme, unpublished, 2004). During interglacial periods, rates were probably broadly similar to those during Kai and Brygge times but during glacial periods deposition rates could be enormous, as shown by Rise et al. (2005); Stoker et al. (2005b) and the Norwegian Deepwater Programme (unpublished, 2004). The increase in sediment supply during the glacial periods resulted from the increase erosion due to the mainland uplift coupled with the onset of the glaciation in Scandinavia. The nomenclature proposed for the Naust Formation in the *Seabed Project* was adopted in this work according to which the Late Pliocene-Pleistocene formation is subdivided into five seismic regional sequences from oldest to youngest: N, A, U, S and T (Norwegian Deepwater Programme, unpublished, 2004). These sequences are linked to the main glaciations, but each sequence may contains more than one shelf glaciation (Fig. 2.5). Along the North Sea Fan the Naust forma-

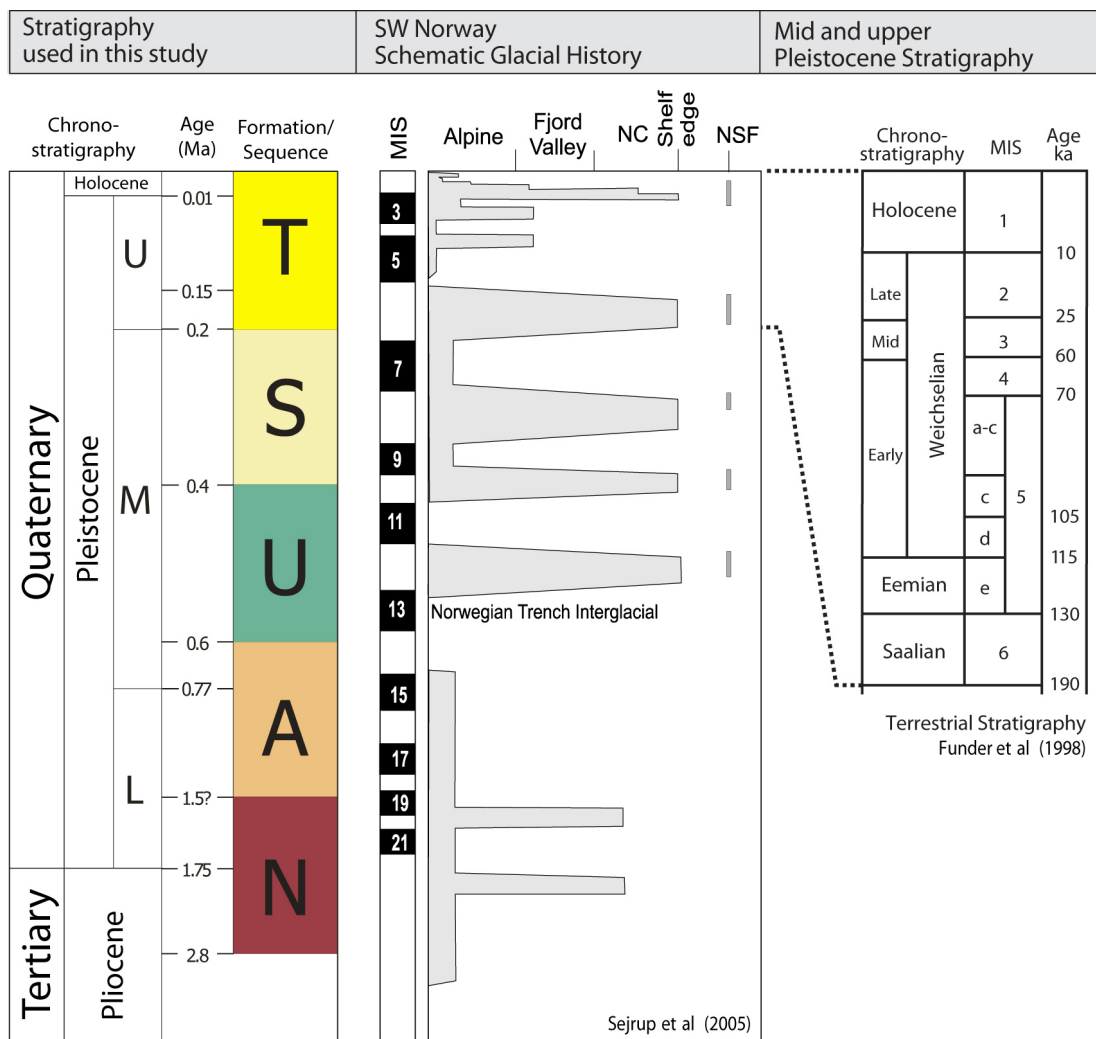


Figure 2.5: Diagram correlating the used stratigraphic scheme defined by the Norwegian Deep-water Programme (unpublished, 2004) with the SW Norwegian Schematic Glacial (Sejrup et al., 2005) and the Mid and Upper Pleistocene stratigraphy (Funder et al., 1998).

tion was dominated by the development of thick prograding sediment wedges (Dahlgren et al., 2005). Seismic sections from the shelf to slope of the Vøring Plateau show that the four oldest units of this formation tend to present dominating progradational wedgelike character, whereas Naust T, representing the last two glaciations, comprises mainly flatlying aggradational units (Fig. 2.6).

Five main seismostratigraphic units, Unit I (youngest) to Unit V (oldest), were identified in this study (Fig. 2.7). Building upon previous studies of the North Sea Fan area by King et al. (1996, 1998) and Nygård et al. (2005), the definition of the seismic units part of the Naust

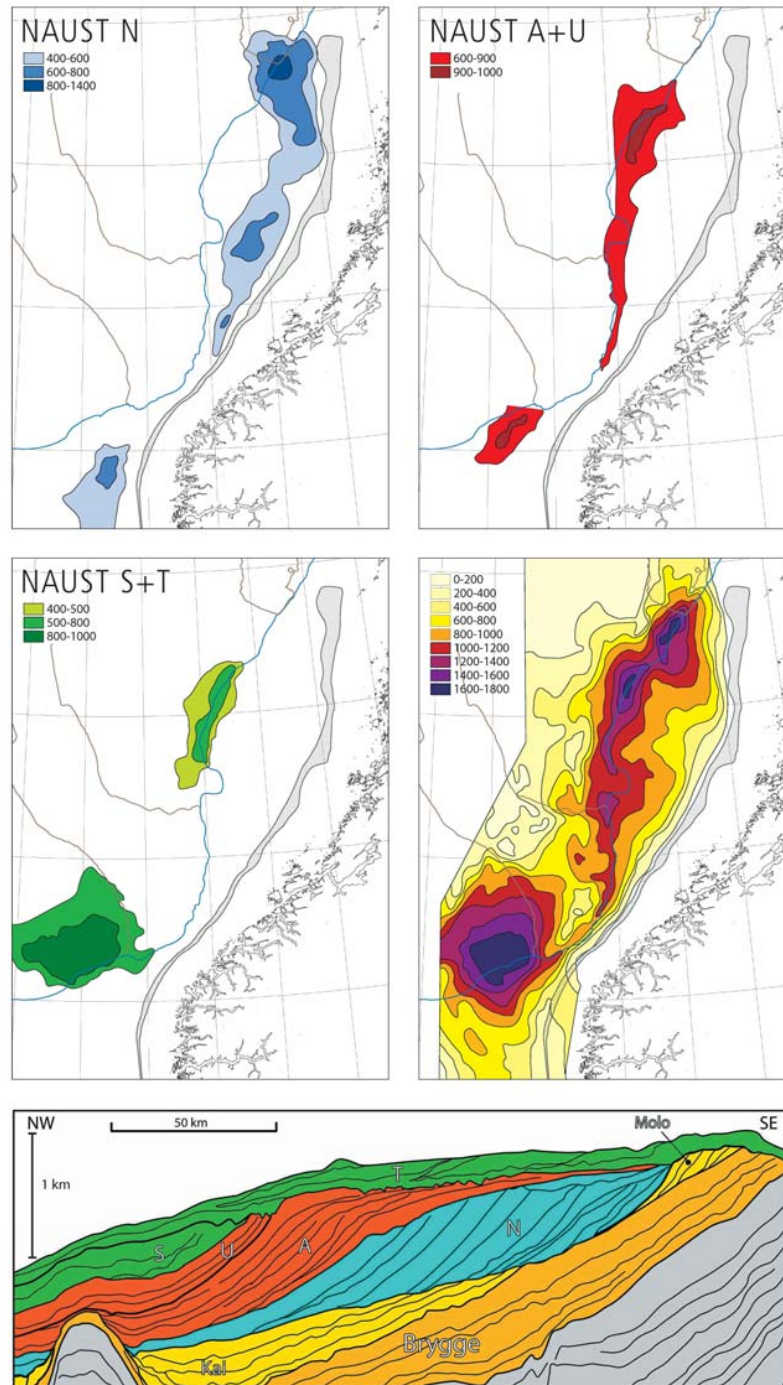


Figure 2.6: Time thickness maps in milliseconds of the Naust Formation and the Naust sequences. Top) Main depocentre for the Naust N sequence, the Naust A+U sequences, the Naust S+T sequences, and the total Naust Formation, respectively. Hachure shows the subcrop of the Molo and Kai Formations on the shelf. Bottom) Geoprofile of seismic line GMNR-94-310 across Haltenbanken (north of Storegga Slide). Extracted from Ottesen (2006).

formation was based on the identification of packages with distinctive seismic facies separated by strong and laterally-continuous key reflectors. Figure 2.7 presents the relation between the seismic units used in this study and sequences defined by the authors mentioned above. The nomenclature used in this study to name the key reflectors representing the boundaries between those seismic units area follows the nomenclature established by the Norwegian Deepwater Programme (unpublished, 2004). They were either named after their regional stratigraphic meaning (e.g. TNS - Top of Naust S) or the specific seismic unit boundary they represent (e.g. TTS - Top of Tampen Slide).

Stratigraphy and seismic units used in this study			Previous studies on the Proximal North Sea Fan		
			Seismostratigraphic units		Genetic Interpret.
			King et al. (1996)	Nygard et al. (2005)	
T (0-0.2)	I		Seq. 1-4	P 1a-d	GDFs
			Seq. 5	P 2	Glaci-marine ?
	II - TS	← TTS →	Seq. 6 TS	P 3 - TS	Debrite
			Seq. 6	P 4a-c	Mainly GDFs
S (0.2-0.4)	III		Seq. 7	P5	GDFs
		← INS →	Seq. 8	P6	Gravity flows/ gl. mar. ?
	V - MS	← TMS →	Seq. 9 MS	P7 - MS	Debrite
	VI	← TNU →	Seq. 9	P 8	Mainly GDFs
U (0.4-0.6)	VII - SU	← TSU →	Seq. 10	P9 - SC	Debrite

Figure 2.7: Correlation between stratigraphy and seismic units used in this study and the seismic units and genetic interpretation establish by previous studies. The used Naust sequences nomenclature is from the Seabed Project (Norwegian Deepwater Programme, unpublished, 2004). TS: Tampen Slide; MS: Møre Slide. Key reflectors: TTS (top of the Tampen Slide); TNS (top of Naust S); INS (Naust S internal reflection); TMS (top of the Møre Slide); TNU (top of Naust U).

2.4 North Sea Fan

The North Sea Fan is one of the largest trough-mouth fans on the Glaciated European Margin (Vorren and Laberg, 1997), covering an area of approximately 142000 km² (King et al., 1996). This trough-mouth fan is located on the SE Nordic Sea margin (Fig. 2.8), between the Storegga Slide depression and the Færøe-Shetland Channel (3°E-4°W). The fan stretches seaward from the mouth of the Norwegian Channel in the northern North Sea up to the extinct Ægir Ridge spreading axis (62°-66°N), starting at water depths around 400 m and reaching more than 3600 m depth. A large proportion of this fan is formed of glacial debris-flow deposits sourced directly from material deposited at the shelf break in front of the ice streams flowing along the Norwegian Channel during maximum glaciations (King et al., 1996; Sejrup

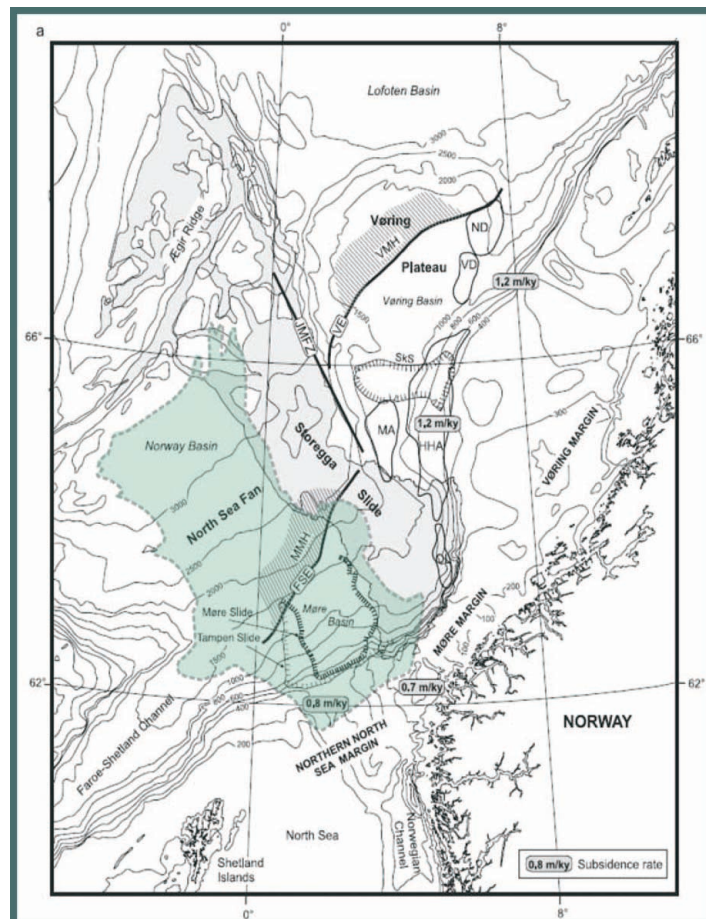


Figure 2.8: Bathymetry and main structural elements of the SE Nordic Seas margin. Outline of Storegga Slide from Haflidason et al. (2004), Tampen Slide, Møre Slide and North Sea Fan from Nygård et al. (2005), are shown. FSE: Færøe-Shetland Escarpment; HHA: Helland Hansen Arch; JMFZ: Jan Mayen Fracture Zone; MMH: Møre Marginal High; OL: Ormen Lange; VMH: Vøring Marginal High. Map is extracted from Sejrup et al. (2004)

et al., 2003; Nygård et al., 2005). In several occasions these deposits have failed in large-scale mass movements which wasted away from the fan large volumes of sedimentary material (King et al., 1996; Evans et al., 1996; Nygård et al., 2005). However the North Sea Fan can still be considered as a constructive area of the glaciated NW European, in part because there has been no major failure after the last major pulse of deposition, associated with the last glacial maximum.

2.4.1 Morphology

The North Sea Fan is 165 km wide at the shelf break and with 300 km maximum width at distal area (Vorren and Laberg, 1997). Figure 2.9 shows the main dimensions of the fan and its slope variations. Nygård et al. (2005) sub-divided the North Sea Fan into two main provinces separated by the volcanic Møre Marginal High (Fig. 2.10). The *proximal province*, with c. 50000 km², starts at the shelf break and extends through the continental slope up to approximately 2000 m water depth with slope gradients of 0.3°-0.7°. The *distal province* starts at water depths around 2500 m, and stretches to the Ægir Ridge in the Nordic Sea with slopes around 0.2°. The two North Sea Fan provinces are divided by a clear break of slope associated with the Møre Marginal Height, with gradients generally around 0.9° rising locally up to 10°, at the Møre Marginal High. The study area for this thesis is located within the *proximal province* defined by Nygård et al. (2005).

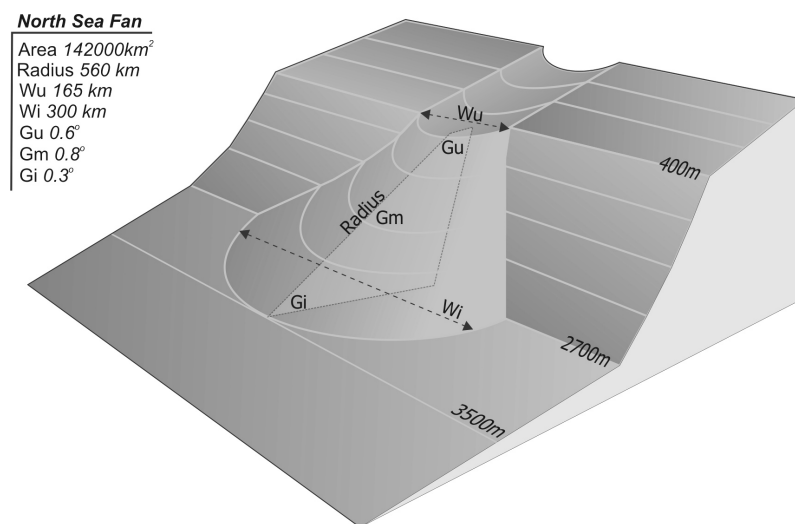
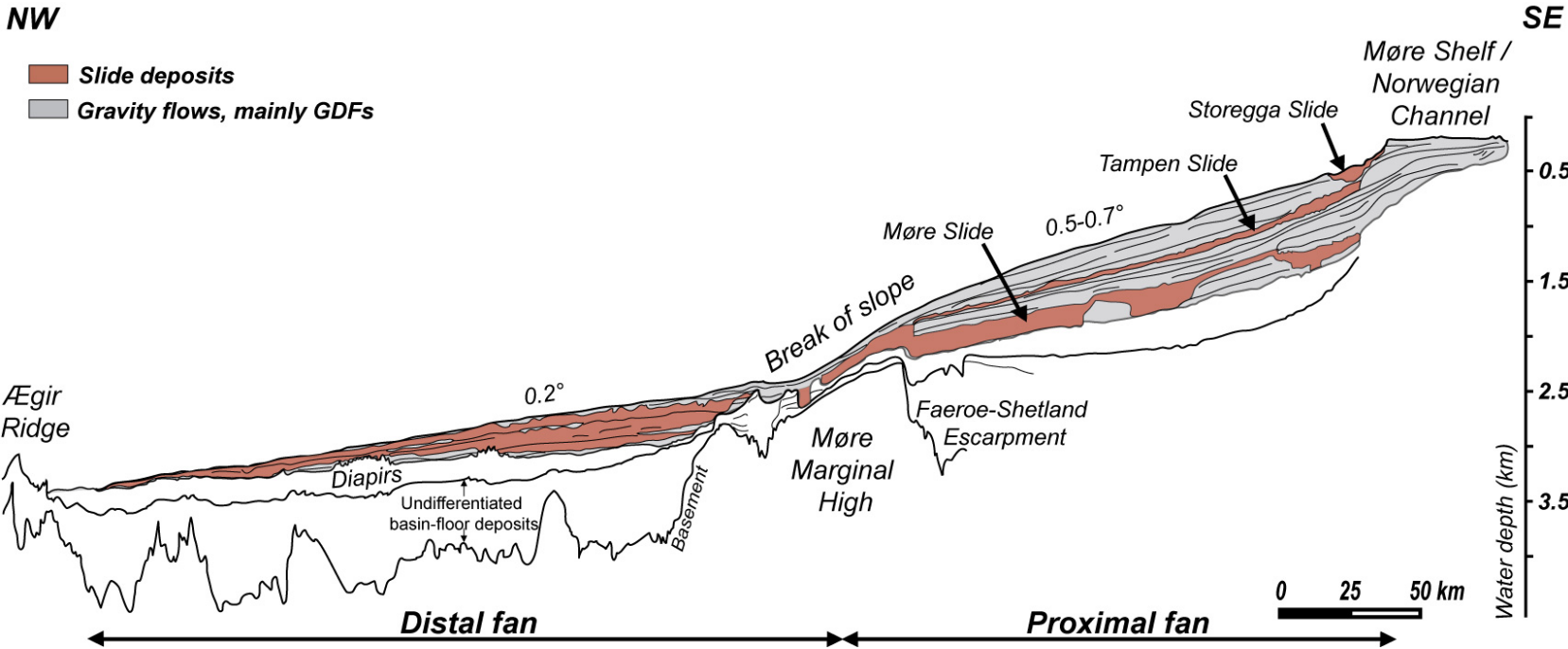


Figure 2.9: Sketch showing the main dimensions of the North Sea Fan. *R*, radius along the longest axis; *Wu*, width at shelf break; *Wi*, maximum width of the lower fan; *Gu*, *Gm* and *Gi*, gradients of the upper, middle and lower slope along the longest fan axis. After Vorren and Laberg (1997).



28

Figure 2.10: Composite geoseismic profile of the North Sea Fan close to its proximal to distal axis, reaching from the continental shelf to the Ægir Ridge in the Norway Basin. Note the break of slope separating the proximal and distal fan provinces, induced by the underlying volcanic Møre Marginal High. Simplified from Nygård et al. (2005).

A radial pattern of elongated sedimentary bodies can be observed at the present-day fan seabed (Fig. 2.11). This sedimentary structures are interpreted as individual debris flow deposits which stretch down-slope for several hundreds of kilometres. These type of deposits and glaci-marine sediments from the last glaciaton partly in-filled the major depression resulted from the large-scale Tampen Slide (Nygård et al., 2007). Yet, on the area of the North Sea Fan shown in figure 2.11, it can still be observed a NW-trending scarp that can reach up to 100 m high and that marks the present-day seabed expression of the Tampen Slide sidewall (Evans et al., 1996). Associated with this scar, a number of relatively narrow channels and gullies are observed extending over a few tens of kilometres upslope and a few tens of metres at most in depth. The channels and gullies were probably active after 14000 years BP, as they seem to cut the upper debris flow deposits (Masson et al., 2002a).

Although the fan central area and southern flank do not show evidence of large-scale mass movement, besides the superficial expression of the Tampen Slide sidewall (Fig. 2.11), the North Sea Fan northern flank was deeply affected by the recurrent instability on the Storegga Slide region (Fig. 2.1). The Holocene Storegga Slide event was the last of the large number of palaeoslides taking place in this area (Evans et al., 1996; King et al., 1996; Bryn et al., 2003; Nygård et al., 2005; Solheim et al., 2005a) that shaped the present-day Storegga depression.

2.4.2 Fan evolution and slope instability

The North Sea Fan was recognized by King et al. (1996) as a large progradational wedge of glacial sediments and major depocentre for continentally-derived quaternary sediments on the SE Nordic Sea continental slope. This fan was formed by an alternation between: (1) intense deposition of mainly glacial debris flow, (2) periods when hemipelagic sedimentation prevailed, and (3) erosion by large-scale mass movements. The measurements and estimates of volume by King et al. (1996) for the Quaternary North Sea Fan sequences are presented in figure 2.12. A minimum Quaternary sediment volume of 13,000 km³ was estimated yet King et al. (1996) acknowledge that the total volume should be closer to 20,000 km³ due to the extensive portion of the fan unsurveyed at the time of the study. Since King's study, the volume of sediment deposited in the North Sea Fan as been re-evaluated. Nygård et al. (2005) calculated that several thousand cubic kilometres of sediment was deposited on the North Sea Fan during each of the major glaciations and that in ~0.5 Ma, since ~MIS 12 until the present-day, the fan has received a minimum volume of 32,000 km³ of sediments.

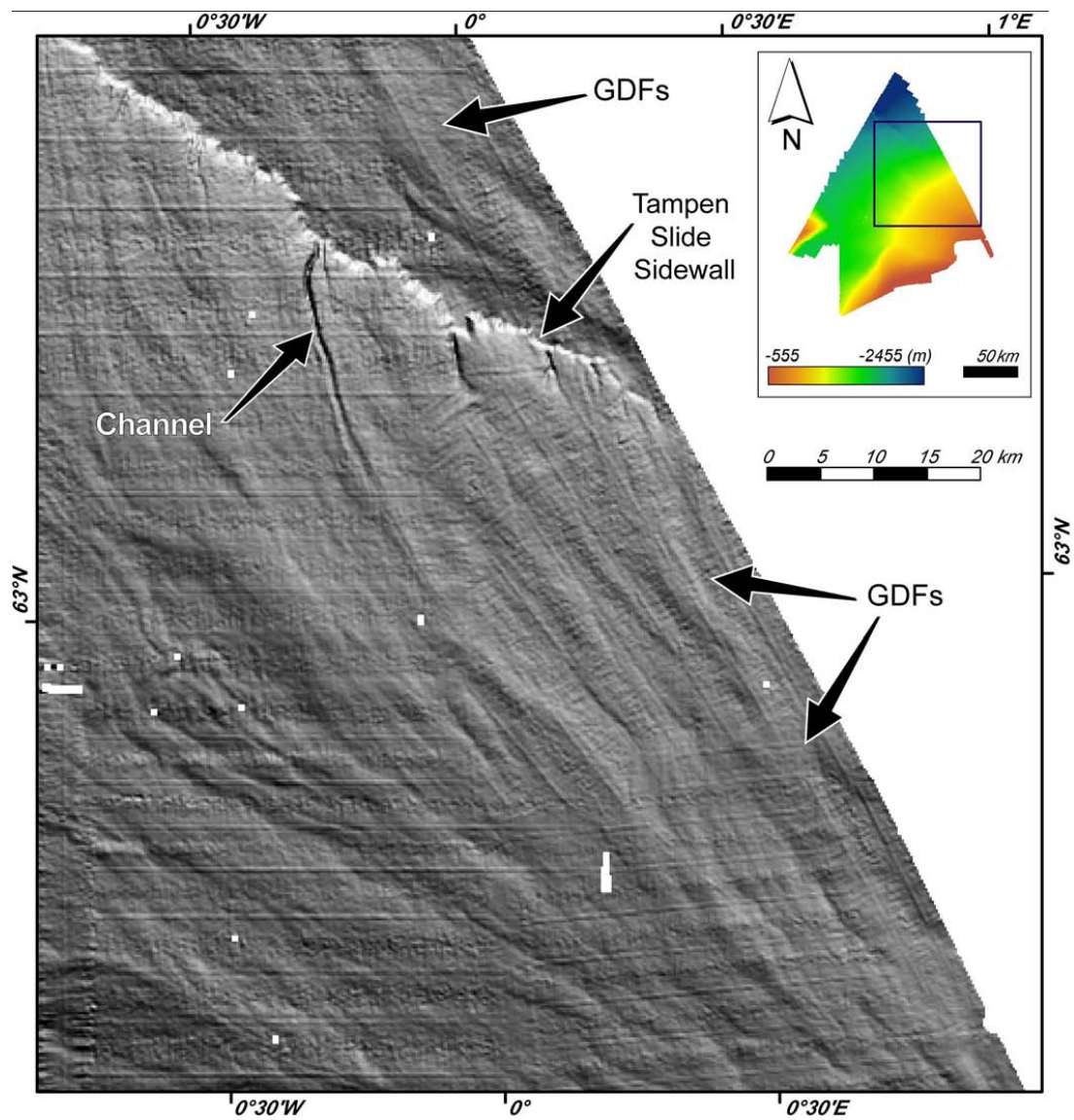


Figure 2.11: Shaded-relief map of the North Sea Fan present-day seabed, from the SEA4 swath bathymetric data. This image shows: a radial pattern of elongated reliefs interpreted to correspond to individual glacigenic debris flow deposits (GDFs), the seabed expression of the Tampen Slide sidewall, and the channel developed upwards from the sidewall.

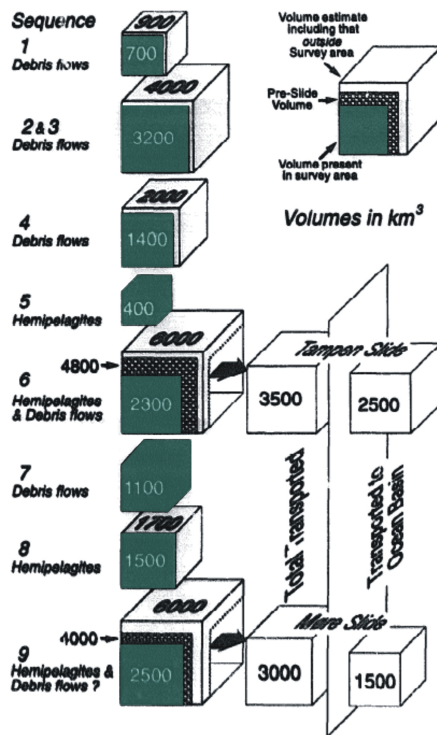


Figure 2.12: Volume measurements and estimates for the Quaternary (< 1.1Myr) North Sea Fan sequences. Volumes within the "survey area" include an area encircled by the outer limit of the seismic transects. Pre-slide volumes for sequences 9 and 6, which were largely removed by the Møre and Tampen slides respectively, are based on the reconstruction surfaces. The major glaciations, represented by Sequences 7, 6, and 4 through 1 generally deposited between 1000 and 2000 km³ on the Fan. Extracted from King et al. (1996)

As previously mentioned, the periods of intense deposition were punctuated by large-scale events of slope instability. These events have occurred on the fan since the start of the Plio-Pleistocene glacial-interglacial cycles (Bryn et al., 2003; Evans et al., 2005). Some of them, such as the Tampen and the Møre slide affected areas of at least >15000 km² and involved more than 3000 km³ of sediment (Evans et al., 1996). Yet these values should be regarded as a minimum estimate since the northern flanks of both slides extended further into the Storegga Slide Complex area and were subsequently eroded (Sejrup et al., 2004). That is especially evident in the case of the Tampen Slide, which deposits were partially eroded by the Holocene Storegga Slide and its headwall was truncated by this subsequent slide.

Although the timing of these erosional events on the North Sea Fan is still being debated partly due to the lack of sufficient penetrative cores (Nygård et al., 2005), based on their stratigraphical position it has been generally accepted that the Tampen and the Møre slides occurred most likely between MIS 10-MIS 8 and in the late MIS 6 respectively (Hjelstuen et al., 2005). Their ages are closely related to glaciations, when the ice sheets reached the continental shelf edge. What is also the case in other slides on the Norwegian Margin, as the Sklinnadjupet Slide (Sejrup et al., 2004).

Based on a vast database of seismic profiles and some additional core and boreholes from the North Sea Fan, Nygård et al. (2005) mapped the thickness of the main stratigraphic units (Fig. 2.14) and proposed a model for the fan development taking in account the presence of the Møre Marginal High (Fig. 2.13) that lead to the separation of the fan in the two provinces. According with this model, **(A)** it is considered that this marginal high constrained the dispersal of sediments from the Norwegian Channel towards the Ægir Ridge **(B)** leading to preferential deposition at the proximal province. **(C)** This province of the fan experienced major slope failures and the subsequently removal of material and formation of large slidescars, which then worked as main depocentres. After a period of slow marine/glaciarmarine followed by glaciogenic debris flow sedimentation, the preconditions required for a new cycle of depositional/erosional processes would be gathered. This model explains the marked dissimilarities between the two provinces of the North Sea Fan (see Fig. 2.10).

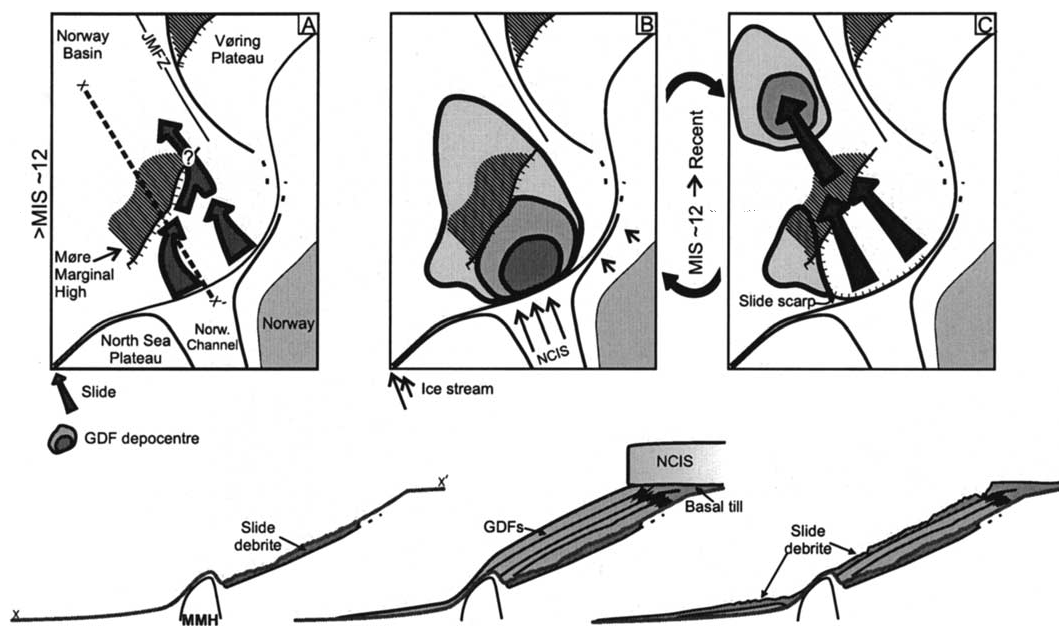


Figure 2.13: Conceptual model illustrating the development of the North Sea Fan and explaining the rule of the Møre Marginal High for the bipartite development of the fan (Nygård et al., 2005). NCIS, Norwegian Channel ice stream; JMFZ, Jan Mayen Fracture Zone.

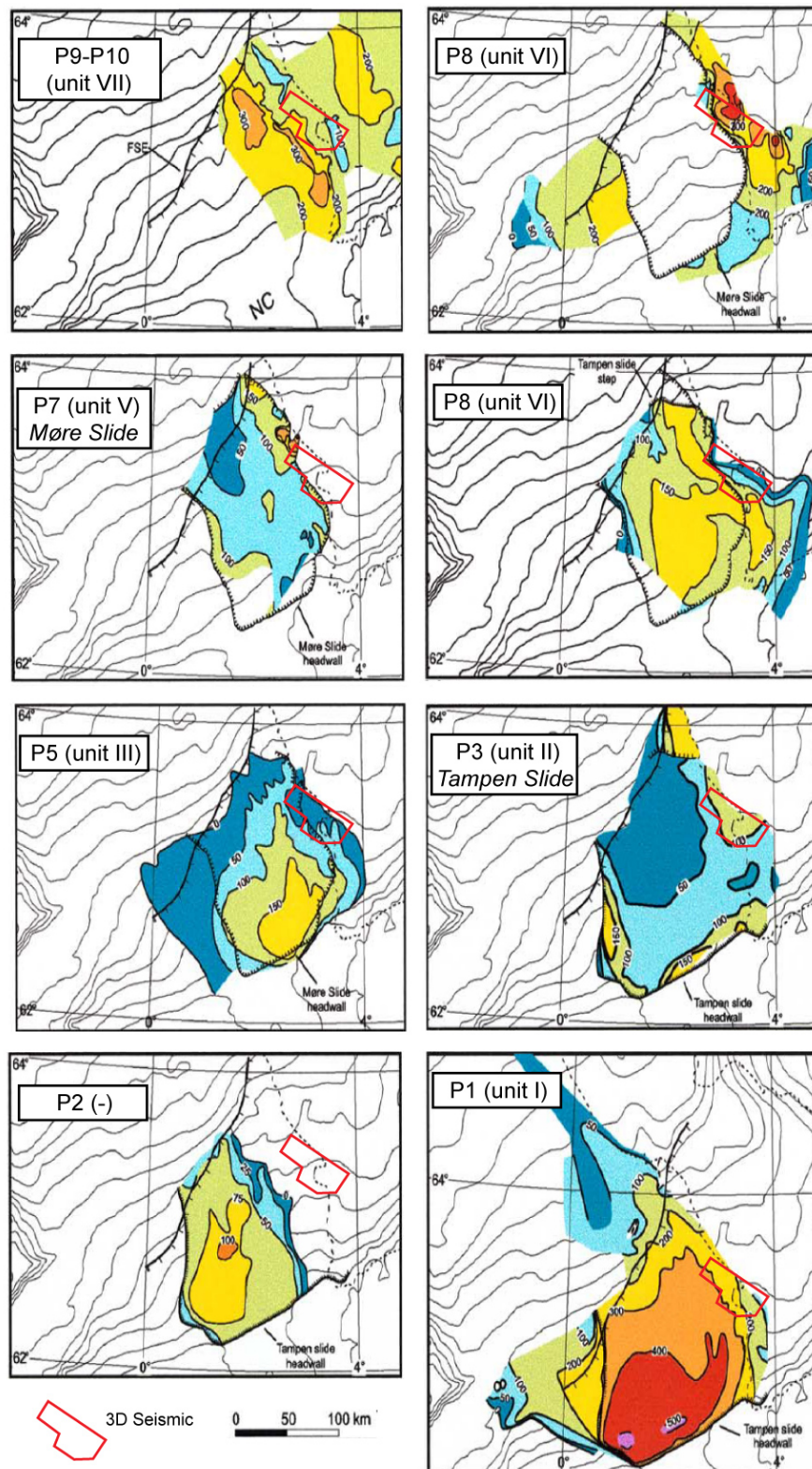


Figure 2.14: Isopach maps for the Nygård's units P10-1 (correspondent to the seismic unit I-VII used in this study). Note different contour intervals and the location of the 3D seismic volume used on this study. Modified from (Nygård et al., 2005).

2.5 Storegga Slide

Since it was first described by Bugge (1983), the Storegga Slide Complex have been object of continuous research. As a result a vast collection of papers has been published, Bugge et al. (1988); Evans et al. (1996); Bryn et al. (2003); Hafidason et al. (2004); Solheim et al. (2005a); Yang et al. (2006); Micallef et al. (2008) are just a few out of many. This continuous research is not only due to the fact that the Storegga Slide is one of the largest known submarine mass movements but also due to the geographic location of the Ormen Lange gas field. This gas field of nearly 400 billions m³ of estimated recoverable resources was found within the headscar area of the Holocene Storegga Slide.

The Storegga Slide Complex depression is located between the North Sea Fan, in the south, and the Vøring Plateau, in the north, and its shape was influenced by the deep structural features of the Jan Mayen Fracture Zone and the Farø-Shetland and Vøring Escarpments (Fig. 2.8). This depression is the result of a large number of slides that have occurred intermittently since the late Pliocene times (Evans et al., 1996). The most-recent large-scale slide has been the Holocene event, which took place about 8100 years ago (Hafidason et al., 2005). Due to extensive and repeated sediment removal, the volumes of the older slides are difficult to establish, but it seems likely that some were at least as large as the Holocene event (Evans et al., 2005).

The Holocene Storegga Slide event affected an area of c. 95000 km² of which 30% correspond to the slide scar (Bryn et al., 2005b). Hafidason et al. (2004) estimated that a minimum volume of 2400 km³ and a maximum volume of 3200 km³ material was displaced during this event. The area of erosion stretches from the shelf edge, situated at around 200 m water depth, to the lower slope, at 2500 m water depth. The zone of accumulation starts from that point and it stretches down to the abyssal plain in the Norway Basin. It contains debris-flow deposits and extensive, distal turbidite deposits (Hafidason et al., 2005). The Storegga headwall, situated along the present-day shelf edge, is 300 km in length (Fig. 2.16). The slide scar narrows downslope to only 60 km wide at water depths of 2000-2200 m, between the Møre and Vøring volcanic highs. The headwall, which is generally around 30 to 50 m height, can reach heights of up to 160 m at limited sections of the northern escarpment, where scarps with gradients of 10° to 45° are found (Micallef et al., 2008). The slope gradient along the failure planes is on average 1.1°-1.4°. Close to the slide scar it is commonly around 20° but is also found as high as 45°. The gradient in the area immediately below the main slide scar is commonly around 4° (Masson et al., 2002a).

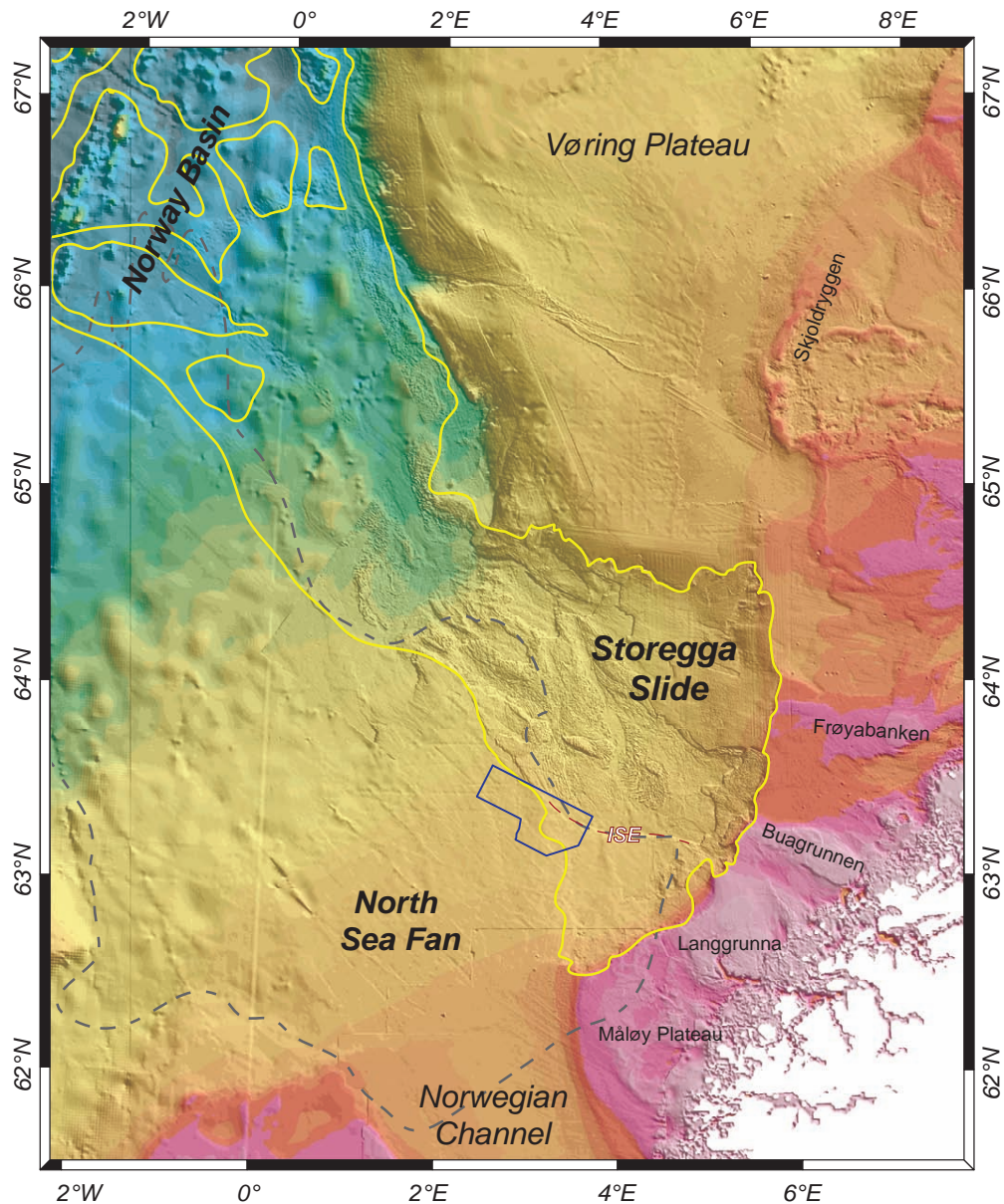


Figure 2.15: Shaded-relief map of the boundary between the North Sea Fan and the Storegga Slide. The yellow line represents the outline of the Holocene Storegga Slide, the red dashed line the Storegga Inner Slide Escarpment (ISE), the dashed line the outline of the North Sea Fan and blue line the limits of the 3D seismic volume.

The Holocene Storegga Slide scar contains morphological elements such as lateral spreads, debris slides and blocky debris-flow deposits on a variety of scales from a few metres to many kilometres (Fig. 2.16). According to Micallef et al. (2007), lateral spreading occurred over at least 25% of the Storegga Slide scar, and it can be identified by a recurrent extensional pattern of parallel ridges and troughs oriented perpendicularly to the direction of mass movement.

Lateral spread is the most common morphological feature on the northern and southern part of the Storegga Slide scar (Bryn et al., 2005a). Hafliðason et al. (2004) identified 58 smaller debris slide events within the Storegga slide complex. Blocky debris-flow deposits dominate the morphology in the central slide scar whereas the distal accumulation zone is dominated by disintegrated sediments deposited as debris flows and turbidites. Compression ridges of varying sizes occur over large areas of the central slide scar but the major compression zone is in the western part of the slide scar (Fig. 2.15), designated as the impact zone.

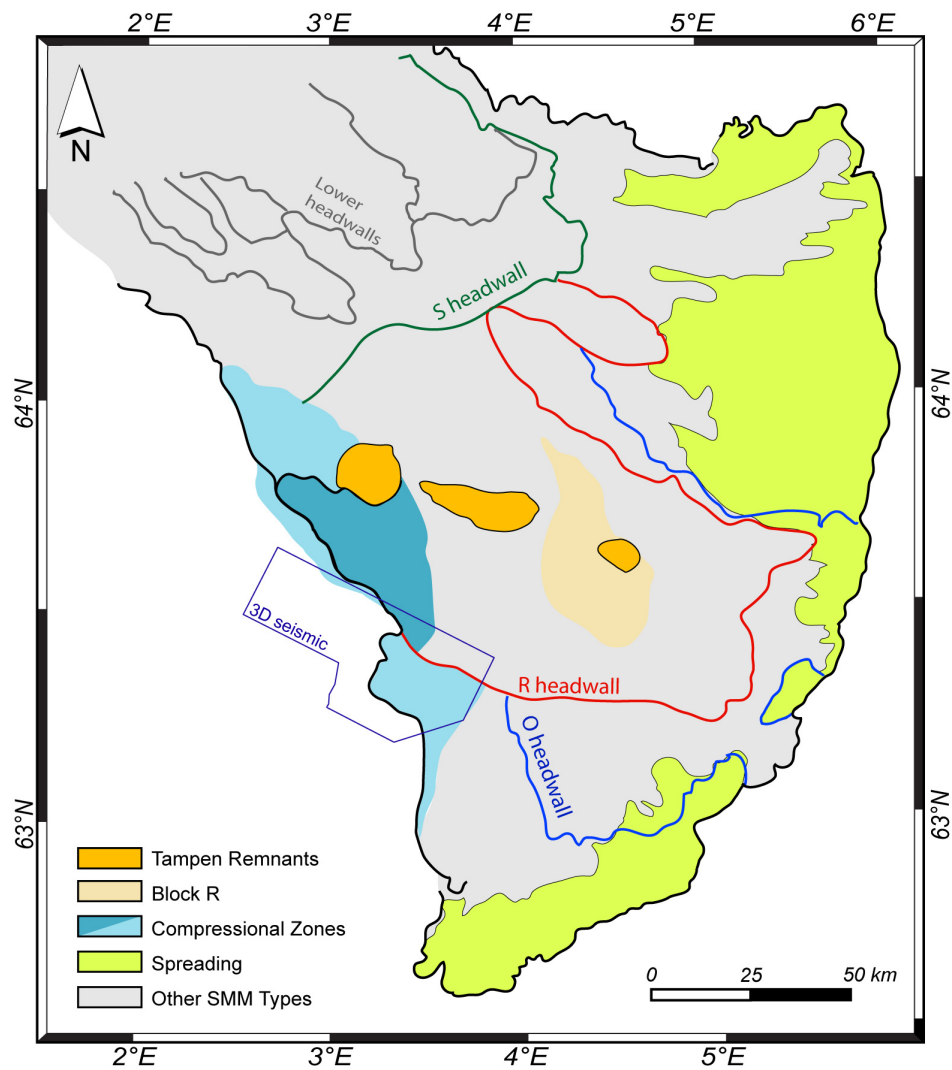


Figure 2.16: Map of the distribution of mass-movement types, headwalls, and other geomorphological features within the Holocene Storegga Slide. The names of the headwalls are derived from the sediment units in which failure took place (Bryn et al., 2005a). Modified from (Micallef et al., 2007)

Various regional models and scenarios have been proposed for the triggering of the Holocene Storegga Slide, many of which would also be applicable to older slides in the area. While some authors associate this failure event with excess pore pressures caused by gas-hydrate dissociation due to sea-level/water-temperature changes (e.g. Mienert et al., 2005), other authors consider that the Holocene Storegga Slide may have been triggered by offshore earthquakes (e.g. Atakan and Ojeda, 2005). Independent of the final trigger mechanism, the presence of hemipelagic and contouritic sediments appears to have been an important precondition (e.g. Solheim et al., 2005a). Normally, these sediments have a higher clay content, a lack of a coarser fraction and a higher sensitivity to variations of shear stress compared to the glacial deposits. Therefore the layers of hemipelagic and contouritic sediments deposited on the slope during ice-free will preferentially host the failure surfaces during slope instability events (Rise et al., 2005). Rise et al. (2005) presented a conceptual model for the development of the Møre margin during the last c. 0.5 My illustrating the cyclic deposition and the last three large slides in the Storegga area. Those probably occurred shortly after extensive glaciations fed glacial debris beyond the shelf edge (Fig. 2.17).

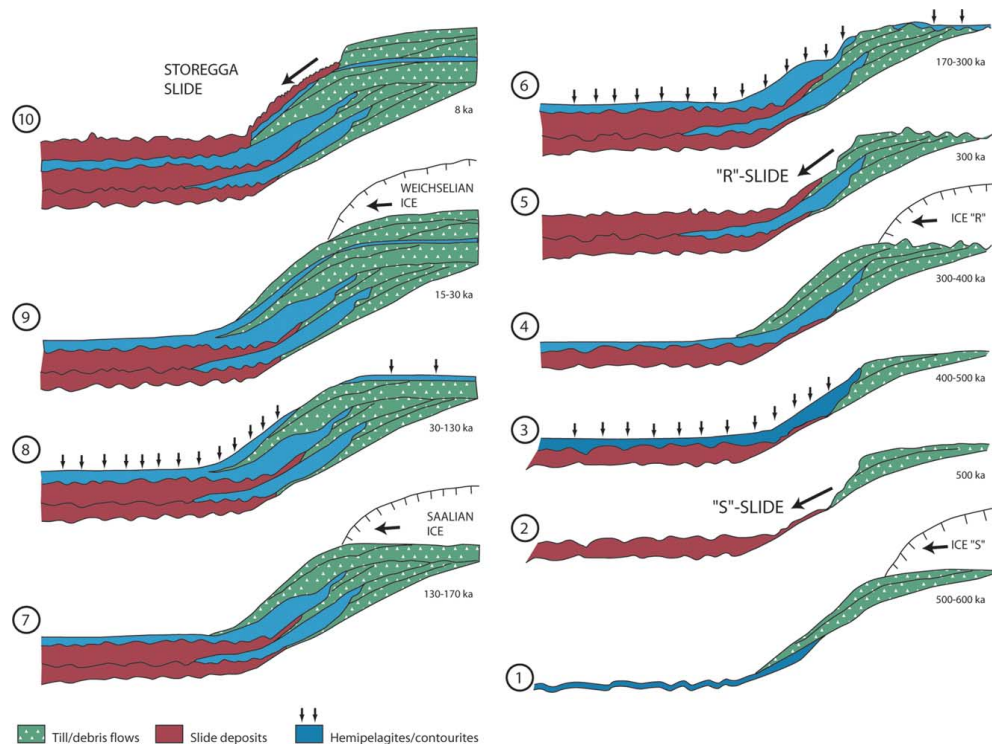


Figure 2.17: Conceptual model illustrating the development of the Møre margin during the last c. 0.5 My. The last three large scale slides seem to be cyclic events occurring after extensive glaciations. Showing that weak layers in the fine-grained sediments infilling the slide scars acted as sliding surface for subsequent slides. Extracted from Rise et al. (2005).

Chapter 3

Data and methodology

3.1 Introduction

This chapter provides an overview of the database and methodology used in this study. These data sets were integrated through the Geographic Information System (GIS) *ArcGISTM* and the seismic interpretation software *SeisWorksTM* from Landmark Graphics Corporation (LGC). Details of each dataset and of the integration process, together with the problems encountered, are here presented. Special emphasis is given to the data visualisation of 3D seismic data and to the extraction of seismic attributes.

3.2 Type and source of the data

The main data used in the study consist of industry 3D seismic data obtained through Statoil under a confidentiality agreement. A compilation of different types of data acquired by the *Seabed Project* (1996 - 1998) and the *Ormen Lange Project* (1998 - 2002) industry and academic consortia as part of the Norwegian Deepwater Program (NDP), and 2D seismic acquired by the British Geological Survey (BGS) from the North Sea Fan were also made available for the purpose of this thesis. These additional datasets provided a regional understanding of the area and a context to the study of the 3D data volume. All the data were provided in digital format, which allowed the full integration of the several datasets. Figure 3.1 shows the data made available for this study.

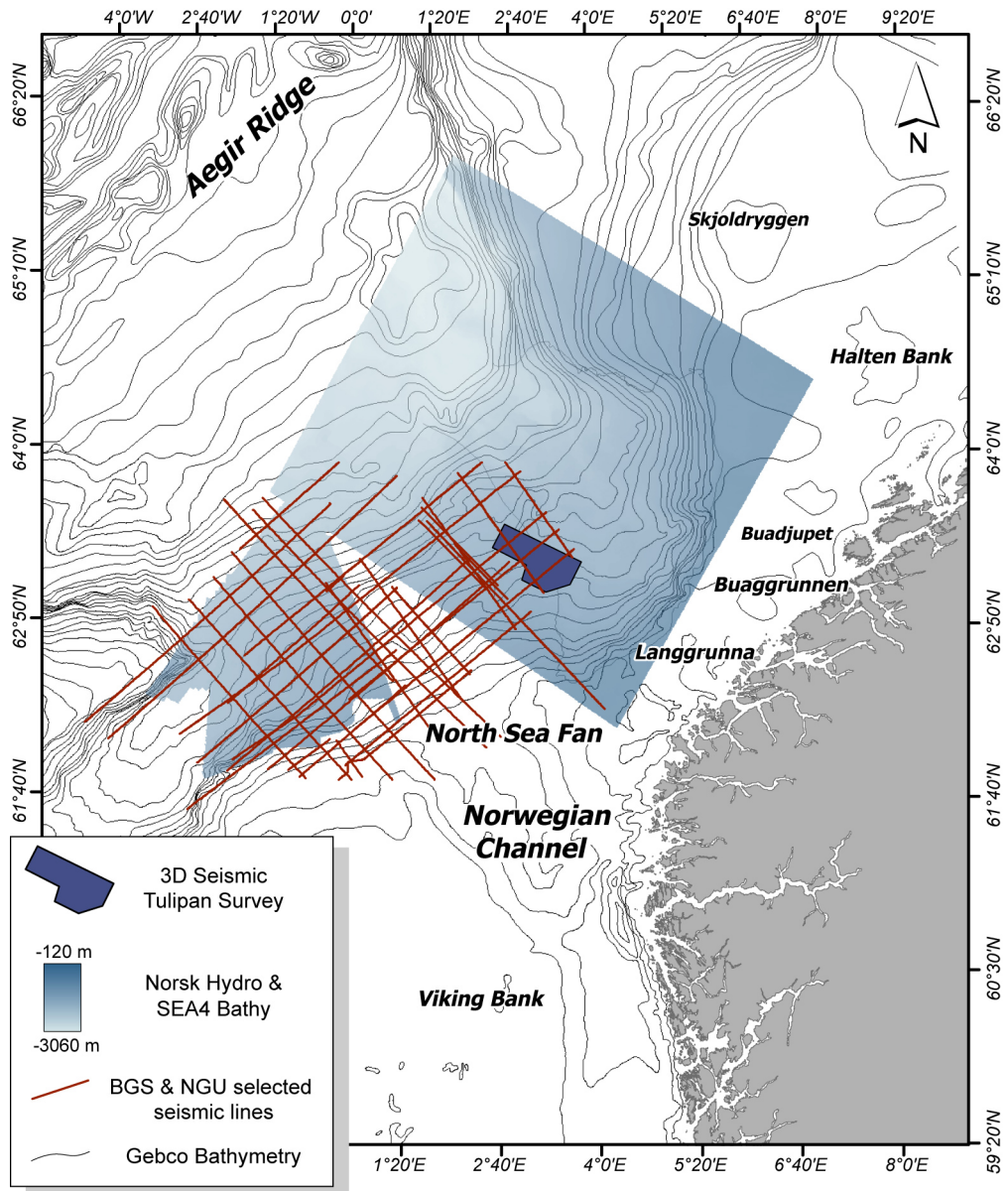


Figure 3.1: Tulipan 3D seismic survey coverage, SEA4 and Norsk Hydro multibeam datasets and trackline plot of the seismic data used in the study overlain on Gebco bathymetry (200 m isobaths).

Tulipan seismic volume

This study is based on the upper 3000 ms two-way travel time (TWT) of the commercial 3D seismic data volume Tulipan, recorded in 2001 by GECO, and provided by Statoil Exploration (now StatoilHydro). This 3D seismic dataset covers an area of 1618 km² with water depth ranging from 1310 to 1830 m. The Tulipan survey was acquired using a Bolt air gun array with total volume of 5058 cubic inches and was recorded with a sample interval of 4 ms and a last sample at 6996 ms. The lines and traces directions are N64°W and N26°E, respectively and its position was saved in UTM coordinates (zone 31N, datum ED50 and central meridian 3°E).

The 3D seismic data volume was initially provided by Statoil as a 16-bit scale and clipped volume within a working *LandmarkTM* project. After the analysis of the first obtained seabed amplitude map, it was observed that for the nature of this study, it would be necessary to work with an unclipped data volume, since the seabed's amplitude histogram was considerably reduced by the clipping process. Consequently, the 16-bit unclipped full-offset and the near-offset stacked migrated volumes were provided and loaded into the workstation. The option of working mainly with the full-offset data volume was based on the visual comparison between the seabed's amplitude map obtained with both seismic volumes, since there was stronger acoustic artefacts relate to the survey footprint.

The data volume that was used was processed by CGG (now CGGVeritas) in SEG-Y file format. A negative polarity was set for this seismic volume, meaning that negative sample corresponds to an increase in acoustic impedance and displays as a trough. The final bin spacing of the seismic grid is 12.5 m x 12.5 m, defining a grid with 6400 bin cells per sq km after processing. The header of the file is presented in Appendix A of this thesis, providing further information about the seismic volume and the processing applied. The dominant frequency of the seismic data varies with depth, being approximately 35 Hz at the levels of interest, yielding a vertical resolution of approximately 11 m ($\lambda/4$) assuming an average velocity of 1522 ms⁻¹ based on unpublished well data.

Other data

Two bathymetric datasets were used in this study, the *SEA4* dataset covering the big part of the NSF area and the Norsk Hydro dataset covering the Storegga Slide Complex area. The SEA4 swath bathymetry, with approximately 22500 km², covers the northernmost area of the UKCS known as the "northern triangle". It was acquired as part of the Strategic Environmental Assessment Project by the Challenger Division of the National Oceanography Centre (NOC),

using an EM 120 in water depths between 600 and 2400 m and EM 1002 multibeam in water depths < 600 m. The bathymetric dataset from the Storegga Slide area was compiled by Norsk Hydro during the *Ormen Lange Project* and comprises data from several sources and with different resolutions, from 50 m up to 5 m. Extending from the main slide headwall at the continental shelf edge (~200 m depth) down to a water depth of 2700 m, the coverage of this dataset add up to 94450 km² . This bathymetric dataset was compiled to assess the pre-Holocene slides in the greater Storegga area (Solheim et al., 2005b).

Additionally, an extensive coverage of 2D seismic profiles collected by the both BGS and the Geological Survey of Norway (NGU) was also made available for this study. These 2D seismic datasets consist of both single and multi-channel seismic and extend behind the study area. Only the most relevant seismic profiles were interpreted during this study, representing a small fraction of all the 2D seismic data available.

3.3 3D seismic data

The first 3D seismic surveys, in the early 1980s, consisted essentially in 2D surveys with small spacing between lines, which automatically enhances spatial resolution (Hart, 1999). The 3D picture of the structure was deduced by interpolating between the lines. Besides the improvement of the spatial resolution, later advances in data processing and the increase of computer capacities enhanced vertical resolution and imaging facilities. The volumetric seismic images produced provide more complete information about structural or sedimentological features such as faults, horizons and mounds than slice-by-slice 2D analysis. However and mainly because of the high cost of dense 3D surveys, academic institutions rarely acquired this type data and the vast majority of existing 3D seismic data have been acquired by the hydrocarbon industry (Davies et al., 2004). Nevertheless, in recent years, increasing collaborations between academia and industry has allowed a broader study of 3D seismic data and has initiated exciting technology-driven developments in a surprisingly wide range of earth science disciplines (Davies and Posamentier, 2005), which cross from structural geology to geomorphology to fluid migration (e.g. Cartwright and Dewhurst, 1998; Frey-Martinez et al., 2006; Ligtenberg, 2005).

3.3.1 From data visualisation to seismic attributes extraction

The collection of closely-spaced seismic lines allows three-dimensional processing of the seismic data volume that, additionally to a resolution of a few metres over thousands of square metres, allows the use of a broad range of new visualisation tools. The viewing of arbitrary lines, time-slices and seismic slices obtained along or parallel to a tracked horizon becomes as easy as the viewing of standard vertical seismic sections. Although these different displays of the seismic volume represent by themselves a significant improvement, they are still two-dimensional displays of the seismic data. Truly three-dimensional displays of the seismic data are nowadays offered by several specialised software packages, allowing the integration of the geometry and seismic characteristic of several locations and additional information. An extensive description of the tools available to a 3D seismic interpreter is provided by Brown (1996).

3.3.1.1 Tracking horizons

Multiple horizon-tracking methods are generally provided by the several seismic interpretation software packages available, allowing the choice between automated methods and manual picking. The automated methods, normally called autopickers or autotracker, offer a rapid horizon picking across the survey from a given seed-point (Fig. 3.2). The autopicking software searches in the seed-point adjacent traces for picks with similar or equal seismic attributes. If these picks obey the user-defined tracking criteria, they will be tracked and become new seed-points themselves, allowing the propagation of the horizon until no additional picks are found (Corporation, 2004). While using an autopicking method, it is important to know what type of autopicker is being used and the path it follows through the data (Dorn, 1998) since serious interpretation pitfalls can result from incorrect application. Herron (2000) discusses the source of some of autopicking interpretation pitfalls, the selection of the input control grid for autopicking, the "directional" behaviour of autopickers, and autopicking in areas with low signal/noise ratio.

From the three picking criteria offered by Landmark's Z-MAP™: amplitude data, instantaneous phase data and, "value" data, only the amplitude data criterion was used to pick the horizons in this study. Depending on the complexity of the picked reflector different controls were specified, such as *picking onset* (Fig. 3.3), *window size* and *maximum jump allowed*. All the picked reflectors were picked with the control *Nearest Peak* rather than the *Largest Peak*.

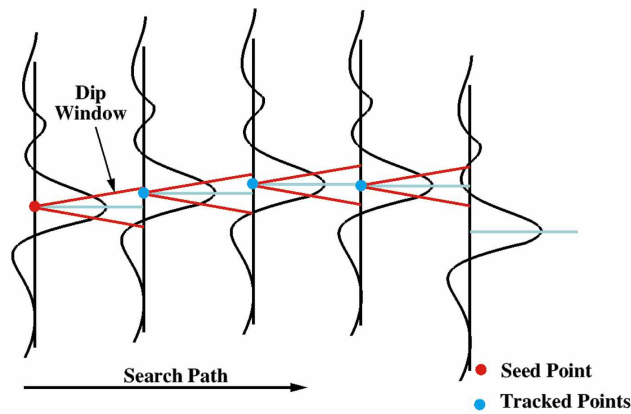


Figure 3.2: Sketch of a simple autopicking algorithm. The seed-point is used as initial control for the autopicking operation, from which the algorithm will look for a similar feature on a neighbouring trace, within specified constraints. If it finds it, it will pick that trace and move on to the next trace (Dorn, 1998).

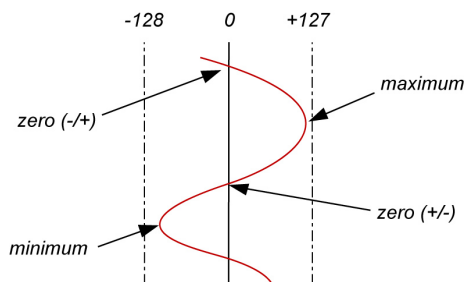


Figure 3.3: Sketch of a seismic trace showing the onsets (-/+ zero, maximum +/- zero and minimum) that can be used for autopicking.

Confidence map

Confidence maps are a visual display of the reliability of the picks tracked during horizon generation. These maps can be used to identify areas of questionable integrity of autopicking. This assessment is made based on the resemblance between the picks and the seed points from which they were generated, taking in consideration differences in time (or depth), amplitude value and wavelet width (Corporation, 2004). The interpreter, using Landmark's Z-MAP™ can specify what percentage of each confidence value will be derived from the comparison of these three criteria. The software calculates the confidence values (Cv) as follows:

$$\begin{aligned}
 Cv = & (\text{shiftpercentage} \cdot \text{shiftfactor}) \\
 & + (\text{amplitudepercentage} \cdot \text{amplitudefactor}) \\
 & + (\text{widthpercentage} \cdot \text{widthfactor})
 \end{aligned}
 \tag{3.1}$$

3.3.1.2 Seismic attributes

Chopra and Marfurt (2005) described seismic attributes as any quantitative measure of seismic characteristic that helps the seismic interpreter to better visualise or quantify relevant features on the seismic data. Some seismic attributes can be extracted over a time interval or a defined window within the seismic volume. This window can be 1) flat, defined by a start and end time, 2) of a constant interval defined relative to a horizon, or 3) of an irregular interval defined relative to two horizons. The horizon-based attributes are generally more precise and detailed than the windowed maps. However, they depend significantly on the accuracy of the tracking, whereas the windowed attribute extraction is, to some degree, less sensitive to tracking errors (Brown, 1996). The development of seismic attributes has been related to advances in computer technology, and there are now more than 50 distinct seismic attributes calculated from seismic data and applied to the interpretation of geologic structure, stratigraphy, and rock/pore fluid properties (Chopra and Marfurt, 2005). However, with this proliferation of different types of seismic attributes that can be used, concern has been raised over the appropriateness of the use of some seismic attributes (e.g. Barnes, 2007; Brown, 2005; Lindseth, 2005). Barnes (2006) emphasise that: 1) seismic attributes should be unique, i.e. only one seismic attribute should be used to measure a given seismic property, 2) seismic attributes should only be used if their meaning are understood, 3) seismic attributes that differ only in resolution should be treated as being the same attribute and that 4) seismic attributes that vary greatly in response to small changes in the data should be avoided. Thus, only the following seismic attributes were used in this study: dip-azimuth, amplitude, RMS amplitude, and shaded relief. A description of each of those is provided below.

Dip-azimuth

This geometrical attribute measures the direction and magnitude of the maximum dip and is calculated by comparing each sample of the horizon with two adjacent samples in orthogonal directions. A dip-azimuth map normally combines reflection dip and reflection azimuth through a circular two dimensional colour-bar for which azimuth controls the hue and dip controls the intensity. This horizon-based attribute is particularly useful for fault mapping, since it can allow the identification of small scale faults by displaying organised dip and azimuth variations (Dalley et al., 1989). Within the scope of this study, the dip-azimuth maps were principally

useful for identify and characterise ridges and more subtle slope changes at the seabed surface.

Amplitude

The peak-to-peak amplitude is the direct measure of the distance between the peak and trough of the reflected wave, which depends on the energy of the incidence wave and the acoustic impedance contrast between the material above and below the interface that generated the reflection. Therefore abrupt changes in amplitude can be the result of alterations in the material's physical properties. The reflection amplitude of a horizon can, under the correct circumstances, be related to porosity or net pay in a reservoir interval (Dorn, 1998). However, changes in amplitude can also indicate layer thickness, since amplitude variations can also arise from tuning effects associated with thin beds (Widess, 1973).

During this study numerous amplitude maps were extracted from the seismic volume from key horizons. To avoid the overlap of information related to variations of acoustic impedance within the material above and below the reflector, several horizons were generated at a constant interval from the tracked reflector. The amplitude map of a horizon, for instance 8 ms above a key reflector, only shows acoustic-impedance changes within the overlying material, allowing a clearer display and a better understanding of its internal structures (Fig. 3.4). The vertical offset applied to generate these horizons varied from ± 5 to 15 ms and was defined by the individual and detail observation of the waveform response near the key reflector. This innovative approach is particularly interesting and revealing when applied to the study and characterisation of mass movement deposits since it can show the internal structure of the deposits rather than the features at the basal surface. However it requires a careful interpretation of the data extract from these *shifted* horizon as variations on the resulting seismic attribute maps can also be resulting from changes on the waveform of the key reflector.

RMS amplitude

The root-mean-square (RMS) amplitude is one of the most used types of amplitude-statistics windowed attributes. The amplitude value of individual samples is disregarded and a single value is calculated per point, representing the entire seismic data for the time interval considered. This single value is calculated as the root mean square over time of the square of the vertical distance. The squaring of the amplitude values within the window gives the high amplitudes maximum opportunity to stand out above the background contamination. This seismic

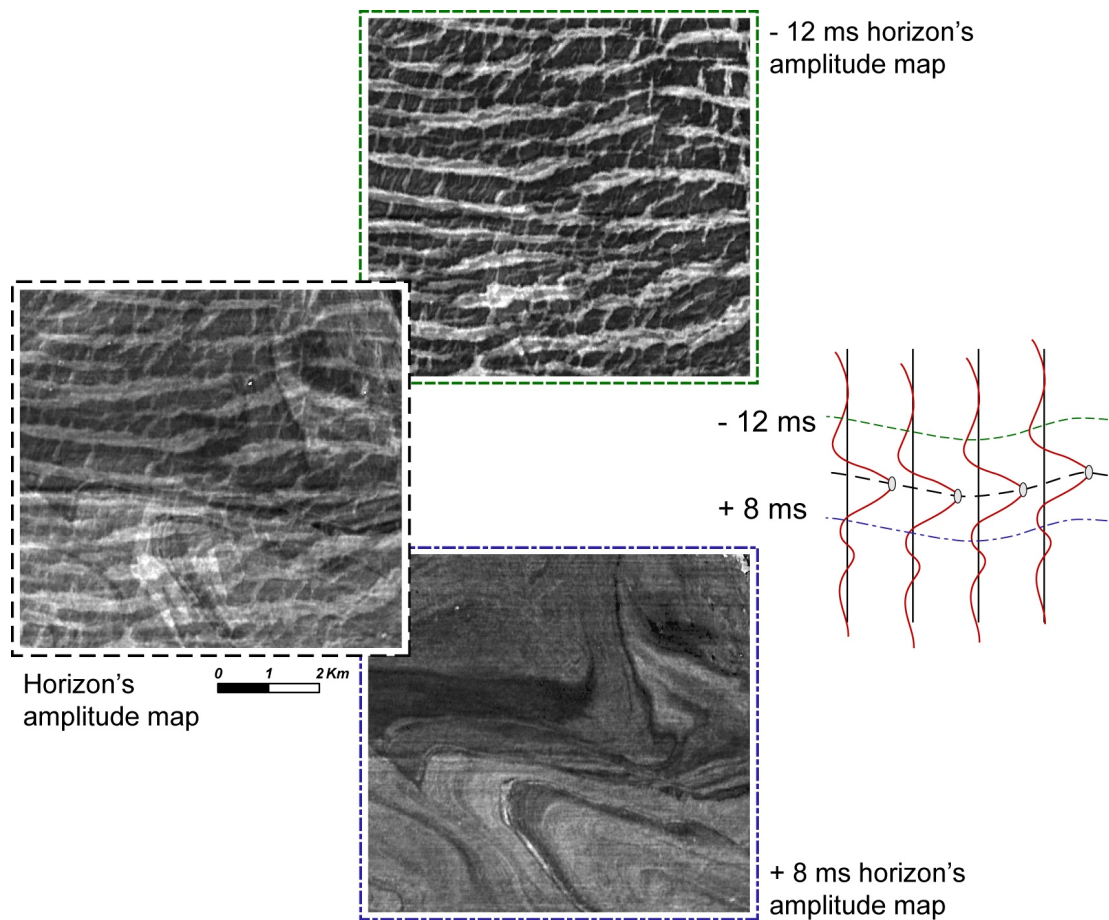


Figure 3.4: Example of the extraction of multiple amplitude map from a key horizon. Left: The amplitude maps from above and beneath show distinct patterns whereas the amplitude map from the horizon itself shows the overlaying of the combination information from both below and above. The sketch on the right shows the position of the sub-horizons.

attribute can be used over a large flat or structured time window to identify various small bright spots at different levels within a formation (Brown, 2005). The majority of the RMS amplitude maps obtained for the purpose of this study were extracted from irregular seismic data intervals defined relative to two horizons, and were used to identify and characterise the internal structure of slide deposits.

Shaded-relief

Rather than displaying the magnitude of an attribute, shaded-relief maps display how the attribute's surface would reflect a given light source (Lynch et al., 2005). Batson et al. (1975) introduced the concept of the *shaded-relief* image to display digital elevation data, by simulating 3D surfaces using 2D textures. The patterns of light and shade in the resultant image look "real" to the visual cortex, tricked by the fact that the apparent brightness of a surface point depends on its orientation with respect to the viewer and the artificial light source. Shaded-relief maps obtained from horizons' DEM allow 3D visualisation of features such as faults and channels. Whereas shaded-relief maps obtained from horizons' seismic attribute, such as amplitude, allow the 3D visualisation of the seismic discontinuities and highlight small variations.

The attributes described above were, in some cases, coupled to produce combined maps. This is achieved by overlaying the coloured image of an attribute and the grey-scaled image of the second attribute (Fig. 3.5). For the purpose of this study, the most useful combinations used were: 1) depth overlaying the surface's shaded-relief 2) unit's thickness overlaying the shaded-relief its basal surface 3) amplitude overlaying the surface's shaded-relief, 5) amplitude overlaying the amplitude's shaded-relief, and 6) amplitude overlaying confidence.

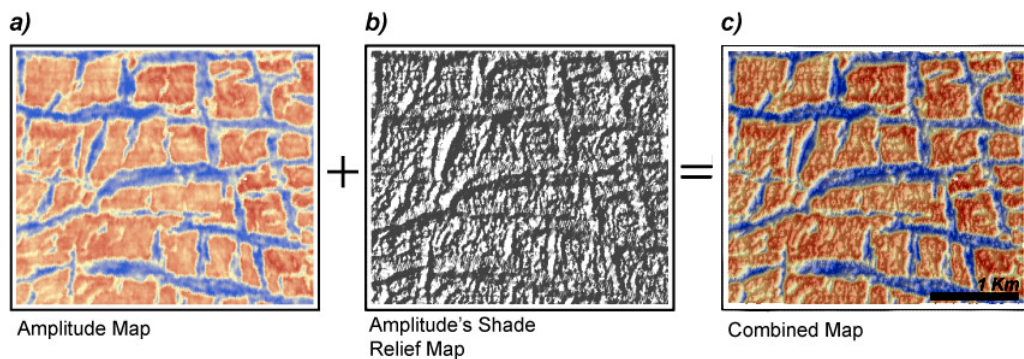


Figure 3.5: Example of a combined map obtained by coupling the seismic amplitude map with the shade relief map using the superposition of a semi-transparent, coloured amplitude map and a the grey-scale shade relief map.

3.3.1.3 Image artefacts

The identification of data processing artefacts within the 3D seismic data was mainly based on the visual inspection of the images obtained from the data used in the study. The areas presenting features with unlikely geological origin or appearing to be affected by artefacts were

then examine in profiles. Some of these artefacts are "intrinsic" to 3D seismic data, related to the process of acquisition of the data itself while others are created at a later stage. On the studied 3D seismic volume, two main types of artefacts were recognised: terracing effect and survey footprint. Other type of false structures such as migration artefacts due to data gaps or to the survey boundaries can also be observed, however they affect small areas and are easily differentiated from potential "real data".

The terracing effect results from the common practice, when loading of the seismic volume into the workstation, of scaling and clipping the largest amplitudes to conserve disc space. Rather than with initial 32-bit real numbers, the seismic data is loaded into the workstation as 8-bit integer numbers, which reduces the dynamic numerical range of the data. To compensate for, the largest amplitudes are clipped in order to enhance the appearance of the majority of seismic reflectors (Bulat and Long, 2007). However that may cause the seismic horizon auto-picker to generate surfaces with marked step-like geometry, especially while tracking the seabed reflector, since it tends to present much higher amplitudes than the remaining reflections and therefore was the most clipped event. On Figure 3.6, **a** and **b** show how the automatic tracking software snaps to the nearest sample once the data is clipped and **c** shows the resulting terracing artefact on the auto-tracked seabed surface.

Terracing Artefact

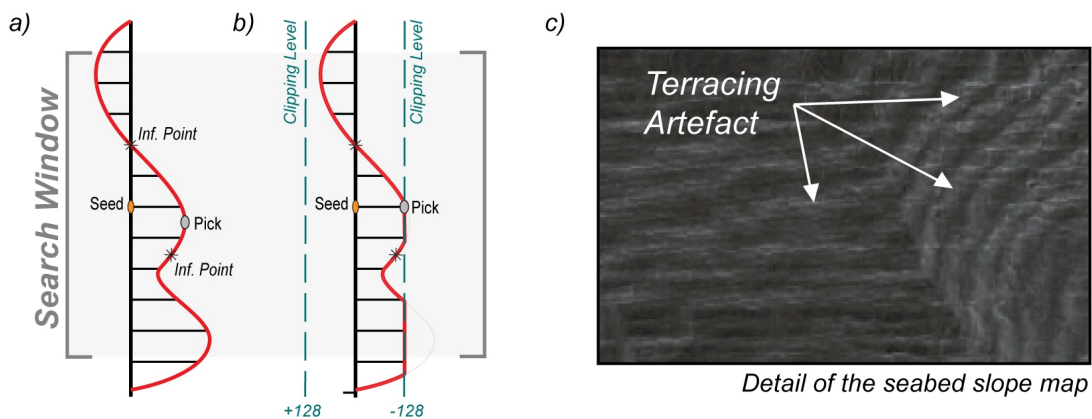


Figure 3.6: The effect of amplitude clipping on the automatic picking. a) Amplitude picking of unclipped data: the autopicker looks for the closer inflection point above and below the seed. The position of the point of maximum amplitude is then evaluated between these two points by using a quadratic interpolation. Note that the picked position may not correspond the highest sample due to the interpolation b) Amplitude picking of clipped data: The same method is followed as above, except that the quadratic interpolation cannot be made. The horizon is simply "snapped" to the nearest sample. a) and b) were adapted from Bulat and Long (2007). c) Detailed image from the seabed slope map showing the terraces-like geometry resulting from the clipped data.

The survey footprint is quite strong on the studied 3D seismic volume, resulting in marked lineations parallel to the survey acquisition direction. Marfurt et al. (1998) define this artefact as systematic noise related with the acquisition geometry, due to small vertical datum time shifts between the acquired lines. The visual impact of a survey footprint on shaded-relief images can be attenuated by choosing artificial illumination direction sub-parallel to the seismic acquisition direction (Bulat and Long, 2001; Long et al., 2004), since this direction of artificial illumination reduces the footprint shadows.

3.3.2 Data handling and integration

Integration of the various data types was crucial to provide a context to the detail study of the 3D seismic data. To accomplish this, a variety of the computer programs were used to handle the data. The methodology applied in this study is briefly described below:

- The seismic data, both 2D and 3D, were loaded into a Landmark's SeisWorks' 2D3D project. This allowed the combined visualisation and interpretation of the several seismic datasets.
- Key reflectors, which best describe the study area and that could be related to the established regional seismic stratigraphy, were recognised on the 2D seismic lines and identified on the 3D seismic data.
- These key reflectors were picked manually on reference vertical sections and then propagated throughout the rest of the volume using autopicking software. Based on the visual analysis of the generated surface and its confidence map, problematic areas were identified. These areas were then manually re-picked and more accurate autopicking obtained. Iterative manual re-picking was required in some cases to obtain satisfactory results.
- Amplitude maps were calculated from the final horizon surface generated for each key reflector. Additionally, multiple "sub-horizons" were generated by the addition or subtraction of a constant value to the TWT depth of the key horizon surfaces. These "sub-horizons" played a crucial role in the generation of RMS amplitude maps and to the

extraction of added amplitude maps (see above *Amplitude map* description).

- Each of the generated horizon surfaces, and respective seismic attributes, were exported to the Geographic Information Systems (GIS) package *ArcGISTM* along with several extracted time-slices. Due to software incompatibilities, the data had to go through a multi-stage conversion from Seisworks to Z-map Plus, then to ERDAS ER Mapper and finally to *ArcGISTM*.
- Once within the GIS environment, spatial analysis tools were used to produce slope and shaded-relief maps of various surfaces. Thickness maps were also calculated from top and base horizons of each seismic unit.
- The display options offered by *ArcGISTM* software packages, such as overlaying of several maps and the 3-D visualisation of seismic attributes draped on top of the respective horizon DEM surface, allowed integrated display of the data (Fig. 3.7) and were particularly useful for detailed geomorphologic characterisation.

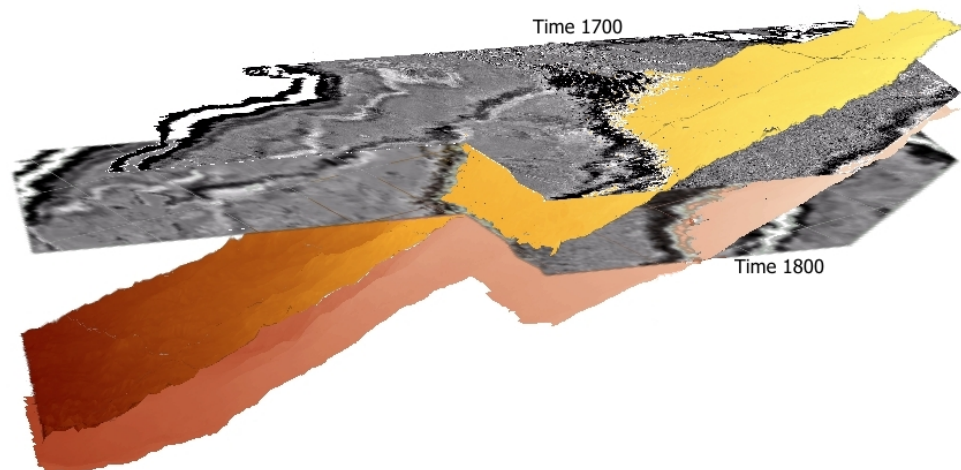


Figure 3.7: 3D image of the DEM of the Tampen Slide deposits' top and base, cutting through two time-slices 100 ms apart.

- Finally, in areas where distinct geometry and texture were identified, the seismic data were re-examine to evaluate the deeper control on the surface morphology. The re-

interpretation of the seismic data within the workstation provided the geological context to the morphological interpretation of these distinct areas.

As result of this methodology a vast number of maps was generated. Figure 3.8 gives an example of the basic work-flow followed to characterise each studied seismic-unit. In this example, the generation of RMS amplitude maps is not represented since these windowed attribute maps were only obtain from the slide deposits.

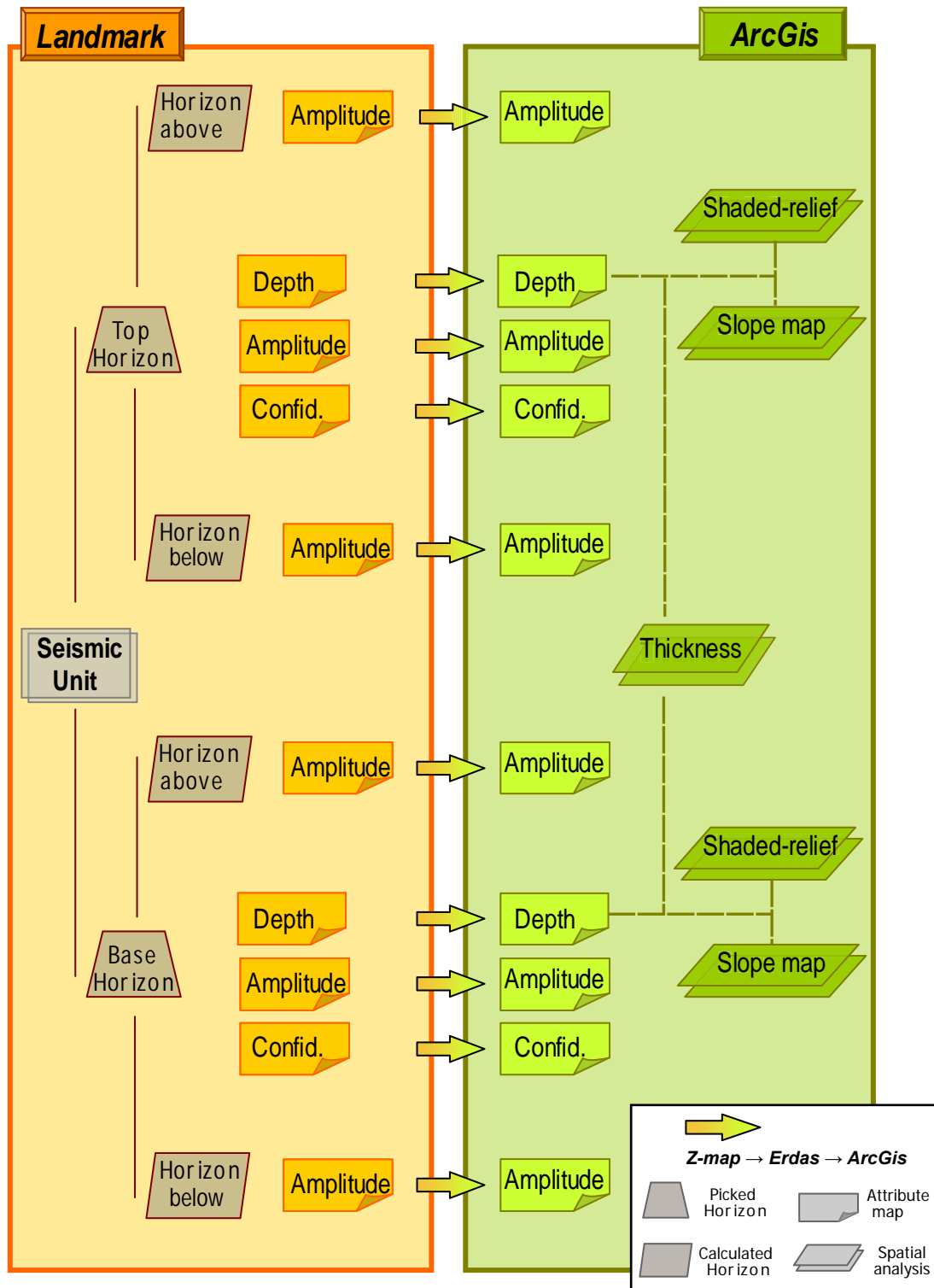


Figure 3.8: Flow-chart summarising multi-stage generation of the surface maps gathered within the GIS environment from a given seismic unit.

3.3.3 Recognition and characterisation of submarine mass movement deposits on 3D seismic data

The key criteria established by numerous previous authors such as Woodcock (1976); Varnes (1978); Bugge (1983); Coleman and Prior (1988); Nemeč (1990); Lee et al. (1991); Hampton et al. (1996); Mulder and Cochonat (1996); Moscardelli and Wood (2008) were used in this thesis to recognise submarine mass movement deposits in this study. However, due to the limited coverage of the data in comparison to the total dimensions of the studied deposits, in some occasions it was impossible to follow some of these criteria. For instance, on the absence of the data covering the headwall of the mass movement, criteria linked to the deposits' character become critical to its identification. Frey-Martinez (2005) faced similar challenges and presents several considerations about the most important criterion for the recognition of submarine mass movement deposits, which are characterised as internally chaotic or highly disrupted seismic facies that cover an area large enough to be identifiable as a discrete stratigraphic unit.

The effect of vertical exaggeration and the resolution of the 3D seismic datasets are an important aspect that needs to be taken in consideration when interpreting submarine mass movement deposits and when making comparisons between modern and ancient submarine mass movement deposits. For instance, the profiles in this thesis are generally presented with a vertical exaggeration equal to 10 times or even higher, which produces a reasonable amount of vertical distortion. In compensation, the vertical exaggeration can also enhance some of the submarine mass movement features. Considering that most industry 3D seismic surveys are acquired with peak frequencies of approximately 30 Hz, that gives a vertical resolution of 12.5 m, and that the horizontal resolution is defined by the original 'bin' size of the survey; typically 12.5 m, many of the outcrop-scale features are far too small to be imaged or are even below seismic resolution. Features, such as the axial-planar cleavages described by Woodcock (1976), would not be recognised on the 3D seismic.

The vertical scale used is itself another aspect that must be taken in consideration when studying submarine mass movement deposits on 3D seismic data since it is normally presented in seconds or milliseconds on two-way-time (TWT), which can be approximately converted into metres. Nevertheless, the depth of a specific reflector can be determined using boreholes or a seismic velocity function and applying the following equation:

$$D = \frac{TWT}{2} \cdot \frac{V}{1000} \quad (3.2)$$

where D, TWT and V are respectively the *Depth* in m, *Two-Way-Travel time* in ms and the *Velocity* in m/s. Based on unpublished well data, velocities varying from 1510 to 1610 m/s were used to calculate conversion values of 0.756, 0.761, 0.784 and 0.803 ms for the Seabed, Tampen, Møre and Slide U deposits, respectively. The conversion values were used to convert the horizon's DEM from depths in time to depths in metres, using the ArcMap's math tool that multiplies the values of the raster by a constant given value on a cell-by-cell basis. This conversion is required for a more accurate reconstruction of the palaeo-morphology and specially important for the creation of slope and thickness maps.

Chapter 4

Seabed and shallow subsurface geomorphology

4.1 Introduction

This chapter presents the description of the morphology of the North Sea Fan northern flank. The detailed seabed and shallow subsurface morphology is described mainly based on the interpretation of the studied 3D seismic volume. The seabed of the study area was first described in detail by Gafeira et al. (2007) who sub-divided it into five morphological zones named: Zone S, Zone Ch, Zone Cl, Zone B and Zone U. This classification is kept in this thesis and each morphological zone is described individually in section 4.2 with interpretations, in some cases, complemented by its comparison with published data from other continental margins.

4.2 Detailed geomorphological characterisation

The approach used to sub-divide the seabed, in which a multitude of interacting factors are simultaneously analysed and determined, could be called a "morphogenetic" approach as described in Chapter 3. The five geomorphological zones presented here reflect more than just a classification based on topographical criteria (e.g. relief, roughness), seismic attributes (e.g. amplitude, instantaneous phase) or seismic character (e.g. degree of disintegration). These geomorphological zones reflect distinct settings of erosional, compressional and depositional processes acting at the seabed. The informal names given to these zones are reflective of their main characteristics: Zone S (Storegga main failure); Zone Ch (higher compression zone) sub-divided in two lobes: Ch¹ and Ch²; Zone Cl (lower compression zone); Zone B (blocky debris) and Zone U (undisturbed North Sea Fan) (Fig. 4.1).

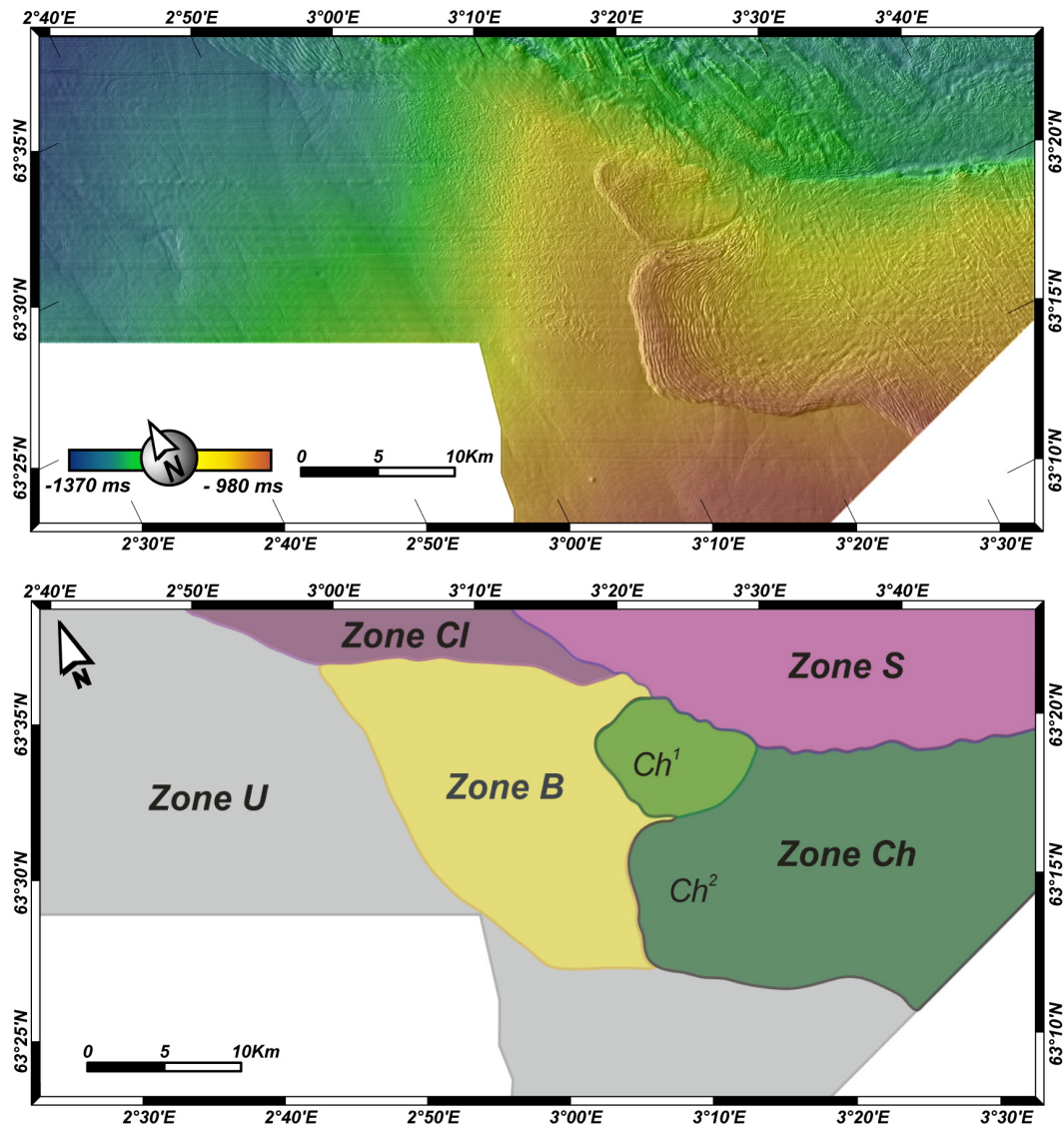


Figure 4.1: (Upper) Shaded-relief map of the seabed with a northwest illumination source at 45°. (Lower) Distribution map of the five morphological zones: Zone S (dark pink), Zone Ch subdivided into to Ch¹ (light green) and Ch² (dark green), Zone Cl (purple), Zone B (yellow) and Zone U (grey).

4.2.1 Zone S

Zone S corresponds to the area of the seabed depression where the sediments were largely remoulded by the Holocene Storegga deep failure (Fig. 4.2). The southern limit of this zone is defined by an escarpment designated as Storegga Inner Slide Escarpment (ISE, see figure 2.15) that extends up-slope from the study area (Hafliðason et al., 2004, 2005). Across the ISE the seabed drops more than 80 metres and the slope along this escarpment can vary from ~5° to ~15°. The northern limit of this zone is defined by the Tampen Slide remnants, situated ~80 km

northeast of the Inner Slide Escarpment (Fig. 2.16). The downslope limit is quite diffuse; there is a gradual passage from the Zone S to a deep compression zone with positive-relief (Fig. 4.2). In both zones, sub-parallel troughs and ridges trending north-northwest can be observed.

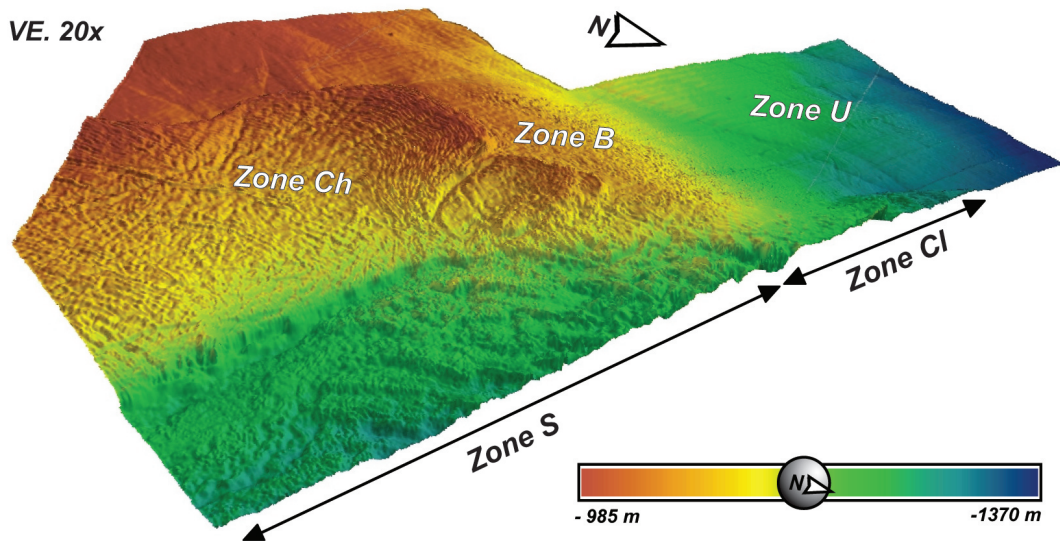


Figure 4.2: Three-dimensional perspective view from East showing Zone S, the area largely remoulded by the Storegga deep failure at the foreground.

The disruption observed at the seabed extends through the subsurface approximately up to c. 500 mbsf, down to the top of the Slide U. This surface worked as the detachment surface for the Storegga deep failure. A progressive loss of coherence is observed heading upslope, from a seismic reflection character where the original stratification is still recognisable to chaotic and transparent facies. The displaced Tampen Slide deposits provide a good marker horizon within the remoulded material (Fig. 4.3). It shows that Zone S comprises a succession of pop-up blocks in the 10 km nearest to the western edge, a succession of graben-and-horst blocks through the next ~8 km and, father away there is a succession of completely disrupted material.

The presence of the Tampen Slide deposits also enables measurement of the loss of material in overlying sediments within Zone S. On the seismic profiles an abrupt reduction of the thickness of material overlying the Tampen Slide deposit is observed from the adjacent zones into Zone S (Fig. 4.3). Within the study area, the sediment sequence above the Tampen Slide deposit, outside of Zone S, varies from 80 to 170 mbsf, whereas within Zone S this sequence is typically ~75m and can be virtually absent, even above the grabens (Fig. 4.3). The tops of the pop-up blocks are the areas where this sequence is thinner.

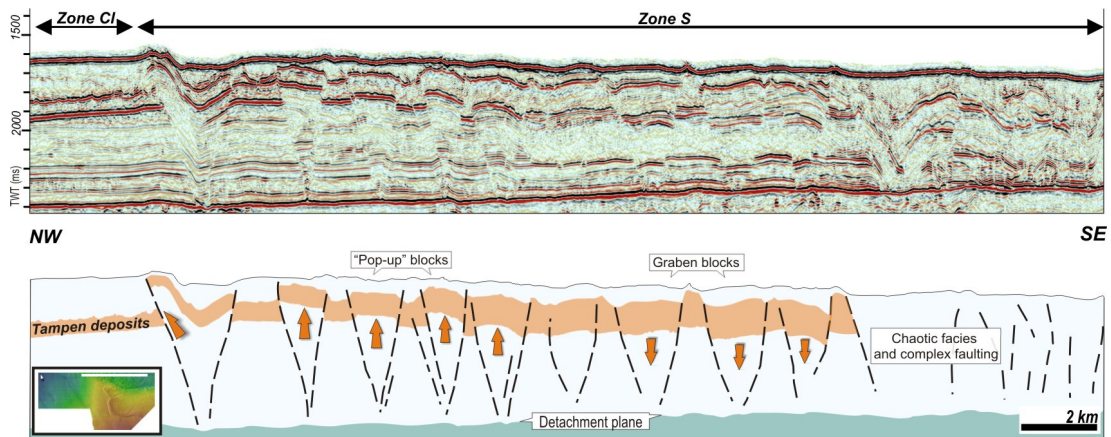


Figure 4.3: Seismic line through Zone S showing upslope progressive loss of coherence and succession of graben-and-horst blocks followed by a succession of pop-up blocks closer to the edge of Zone S.

4.2.1.1 Interpretation

Both pop-up blocks and graben-and-horst blocks are defined by conjugate faults, but they result from different stress histories. The succession of pop-up blocks in Zone S is interpreted as compression structures resulting from volume and energy released by a deep failure in the Ormen Lange area (Fig. 4.4a). These structures accommodate shortening by vertical displacement through thrust faults. The adjacent succession of graben-and-horst presents the same fault dip angle geometry as the pop-up succession. It is interpreted as the result of the reactivation of some of the faults from the pop-up succession which probably extended further upslope than its present limit. The reactivation of the thrust faults as normal faults resulted in the subsidence of the pop-up blocks. Besides the fault geometry, this interpretation is supported by the fact that several graben blocks preserve dragging folds consistent with reverse faulting rather than with subsidence. The reactivation of the pop-up faults can be explained by subsequent tension due to the escape of material to the north-west, through the gateway between the Tampen Slide remnants. The escape of material created space and allowed regressive extension of part of the previously compressed section (Fig. 4.4b).

The abrupt thickness reduction of material above the Tampen Slide deposit, observed on the profiles sub-parallel to the axis of the fan, cannot be justified solely by lateral variations in sedimentation rate associated with gradual thinning on the North Sea Fan flank. This reduction of thickness is considered to be associated with the Storegga main deep failure. The energy release and large ground acceleration caused by the failure may have caused liquefaction - a

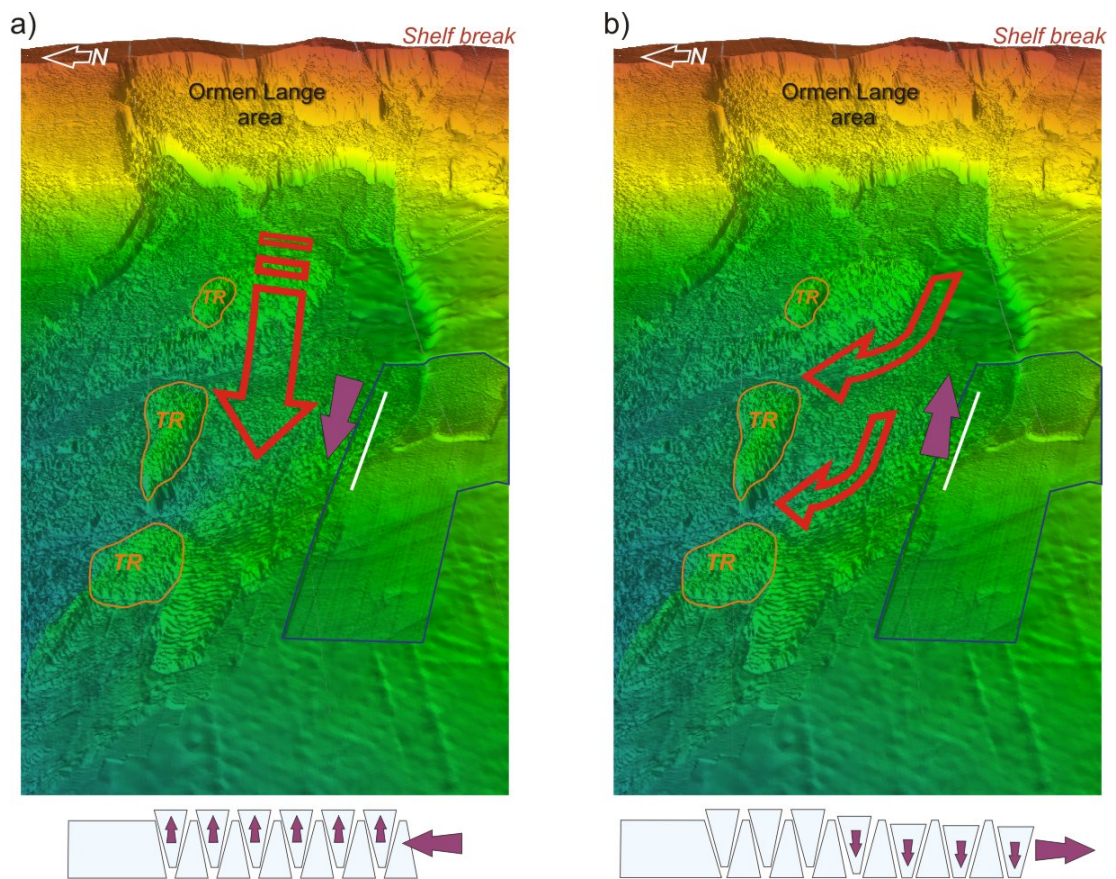


Figure 4.4: a) Failure in the Ormen Lange area generated deep impact and initiated compression on the area south of the Tampen remnants (TR) and the formation of a succession of pop-up blocks. b) Escape of material through the Tampen remnants changed the stress regime and induced the reactivation of the pop-up reverse faults, resulting in the formation of graben-and-horst blocks. The white lines represents the location of the profile schematically represented under each image and blue line the outline of the limits of the 3D seismic survey. Red arrows represent the main direction of transport and the purple arrows the direction of local motion within Zone S.

time-dependent loss of strength and stiffness - of the unlithified sediments in the upper part of the sedimentary column. Although a massive loss of material volume is not likely to occur as consequence of sediment liquefaction, this process could explain the thickness decrease of the upper part of the sedimentary column by fluid dissipation as well as the repacking of the sediments into a more favourable orientation.

4.2.2 Zone Ch

The compression Zone Ch has the most prominent positive relief in this area. It is situated at water depths varying from less than 985 m to 1370 m and covers an area of approximately

390 km² (Fig. 4.5a). It appears well preserved in the present-day seabed, with sub-parallel ridges and well-defined boundaries. The ridges are generally ~150 m wide and several kilometres long, but become gradually less pronounced towards the centre of the compression zone. The ridges are mainly parallel to the frontal section of the escarpment and oblique to the lateral boundary.

This compression zone comprises two lobes (Ch¹ and Ch²) separated by an elongated area of partially undisturbed, horizontally stratified, sediments (Fig. 4.5c). With an area of more than 340 km² and a frontal escarpment 9.5 km long, the lobe Ch² is the larger of the two lobes. Lobe Ch¹ is considerably smaller with an area of 50 km². Additionally, Ch¹ frontal escarpment also presents a smaller relief; the Ch² frontal escarpment can reach up to 30 m height, whereas the Ch¹ generally presents 20 m relief (Fig. 4.5b).

On seismic profiles, the compression Zone Ch is characterised by crenulation and/or disruption of most of the seismic reflectors as a result of its internal deformation. The structural configuration of this compression is of an imbricated sequence of closely spaced thrust faults which can be traced down to a well-defined detachment surface on the top of the Tampen Slide deposits (Fig. 4.6). In plan view, individual thrust faults can be traced over ~5 km, generally parallel to the frontal escarpment, and regularly spaced. Near the seabed surface the thrust faults are expressed as concentric fold traces, which result in the ridges observed on the seabed bathymetry.

These structures are re-folded close to the southern lateral boundary of Zone Ch, and a second family of thrust faults can be observed close to the separation of Ch¹ and Ch². A marked pattern of high and low amplitude also resulting from refolding can be observed in the central area of the compression Zone Ch, especially on the amplitude map of the seabed (Fig. 4.7) and time-slices.

Despite the disruption of most of the seismic reflectors within the compression Zone Ch, a stratigraphic character comparable with the surrounding sediments can locally be identified on the 3D seismic volume. Additionally, on the seabed amplitude map and shallow time-slices, pre-existing sedimentary features are also recognisable inside the compression zone. Different glacial debris-flow deposits, identifiable on the seabed amplitude map by their contrasting amplitude signatures, can be followed within the deformed seabed and used as deformation markers (Fig. 4.7).

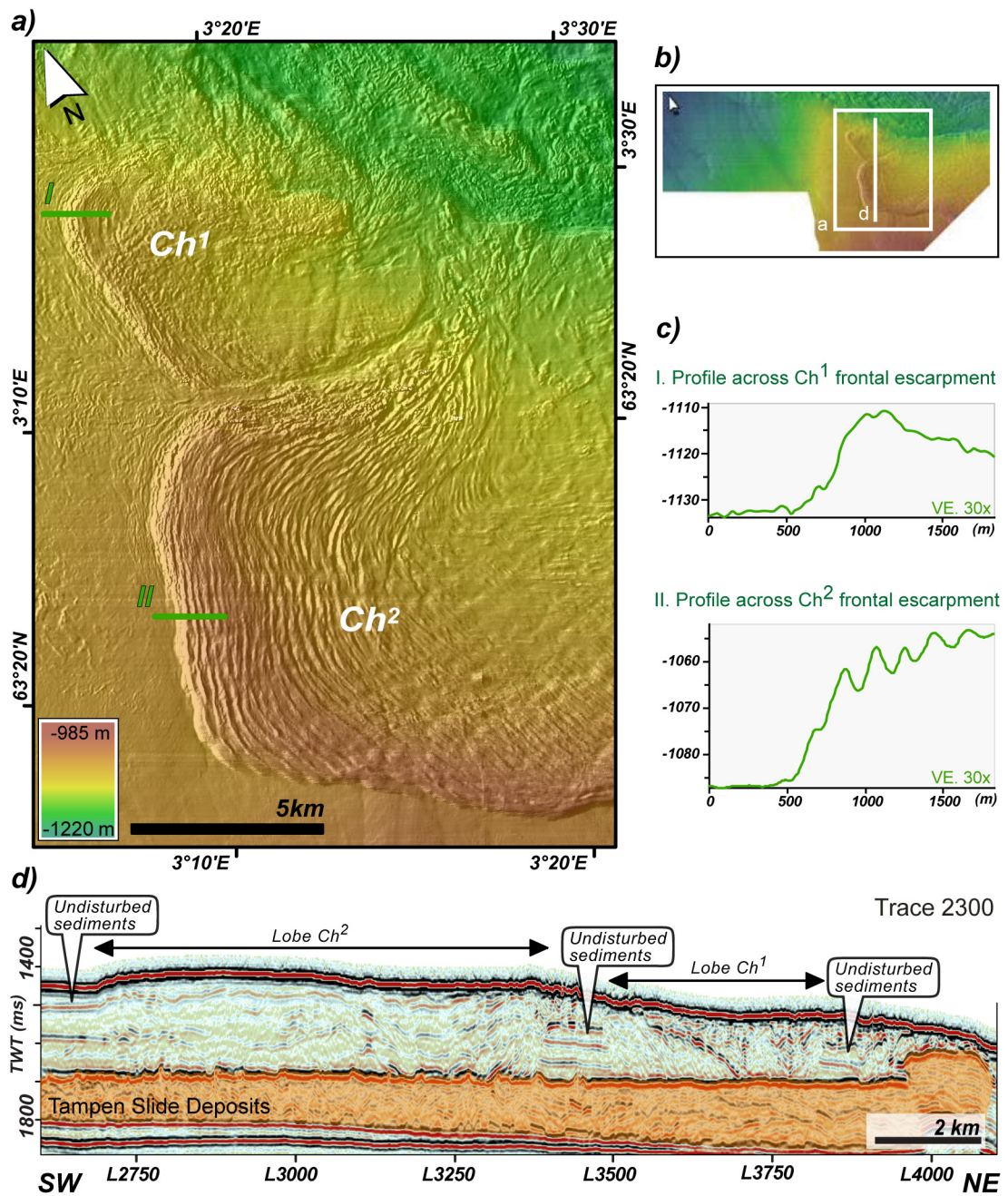


Figure 4.5: a) Shaded-relief map of the seabed showing the compression Zone Ch, which is comprised of two lobes (Ch^1 and Ch^2). b) Location map. c) Bathymetric profiles of Zone Ch^1 and Ch^2 , showing the height difference between the Ch^1 and Ch^2 frontal escarpments. Note the high vertical exaggeration (30x). d) Seismic profile across the compression Zone Ch (Trace 2300) shows the horizontally stratified and undisturbed sediment package outside Zone Ch and between lobes Ch^1 and Ch^2 . Bathymetric profile locations are marked in green on the shaded-relief map.

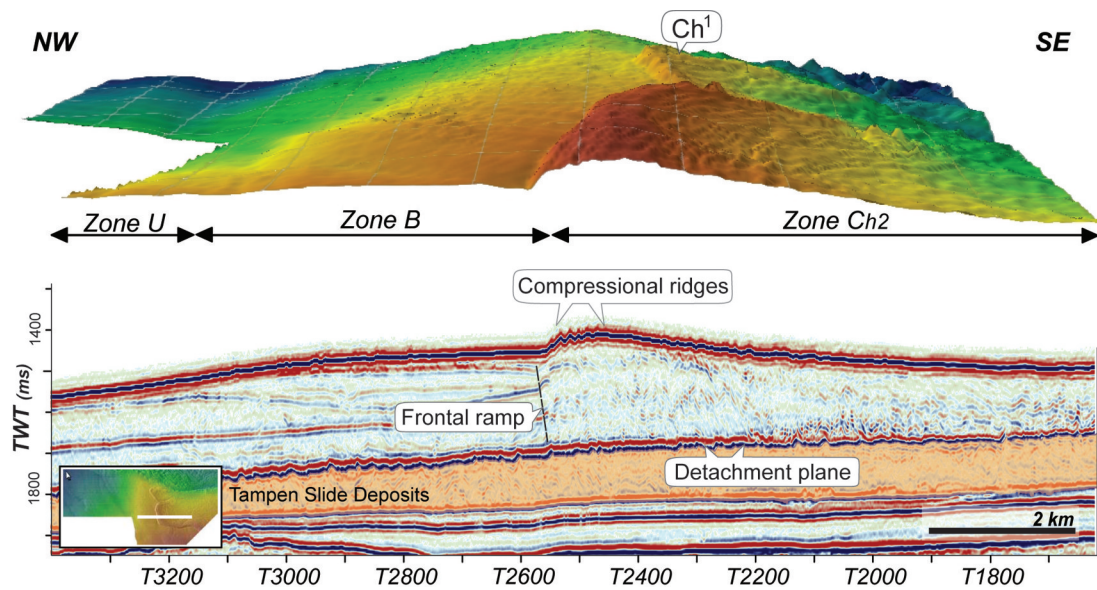


Figure 4.6: a) 3D perspective view of the present-day seabed cutting through Ch^2 looking towards northeast. Note the difference in size between the compression zones Ch^1 and Ch^2 . b) Seismic profile across the toe region of the zone Ch^2 , showing compressional ridges, frontal ramp and well-defined detachment plane following the top of Tampen Slide deposits.

The seabed seismic reflection amplitude map also reveals a distinctive area of 30 km² in the central part of the lobe Ch^1 (Fig. 4.7), where the seabed has a bright chaotic seismic signature, very different from the seismic signature of the front of the lobe Ch^1 . As in the case of lobe Ch^2 , the front edge of lobe Ch^1 presents a seismic signature that is continuous with the surrounding seabed, although disrupted by the compressional ridges. The boundary between the frontal compression part and the central part - where the material has no internal structure - can be identified and followed on seismic profiles across lobe Ch^1 (Fig. 4.5d). This marked boundary presents a 3D curved amphitheatre-shape, with steep sidewalls and a flat base at the top of Tampen deposits.

4.2.2.1 Interpretation

Imbricated thrust faults, originating at the flow base and extending through to the top of the flow deposit, are common features near the termini of mass movement deposits (e.g. Frey-Martinez et al., 2006). Such thrust faults are thought to be oriented transversely to the flow direction and are valuable kinematic indicators of translation associated with the mass movement (e.g. Strachan, 2002). Based on the observed orientation of the thrusts and fold systems, a dominant WNW transport direction is assumed within the Ch^2 lobe (Fig. 4.8). This transport direction

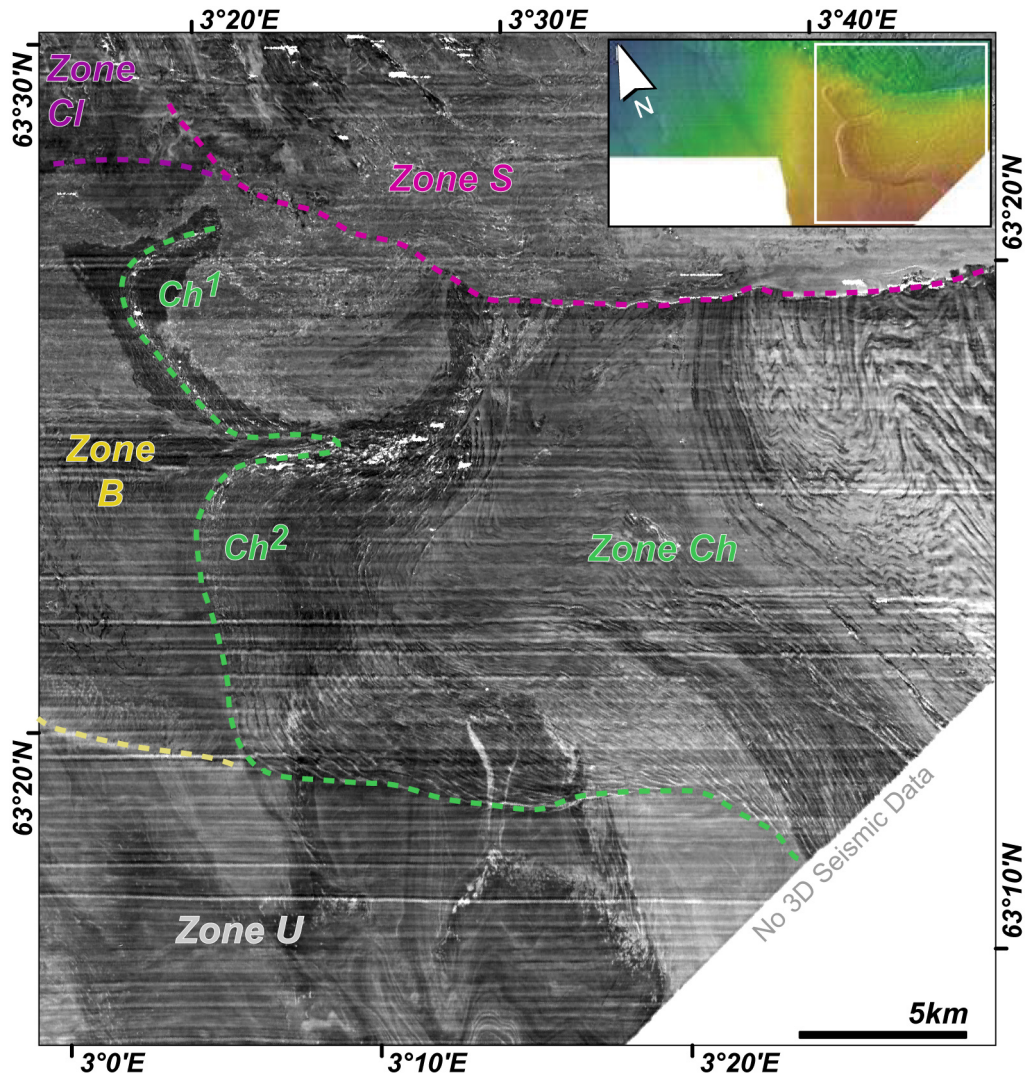


Figure 4.7: Seismic reflection amplitude map of the seabed showing Zone Ch. Note the bright chaotic seismic signature of the Ch¹ central area and the contrasting amplitude signal correspondent to different glacial debris flow deposits which can be recognisable through the compression zone

diverges from the main trend inferred from the glacial debris flows deposits, and links it with the an event that was part of the Holocene Storegga Slide. The headwall scarp has not been identified, as the area upslope of the compression zone was affected by later events of instability, but it is consider to have been east of the study area (Fig. 4.9).

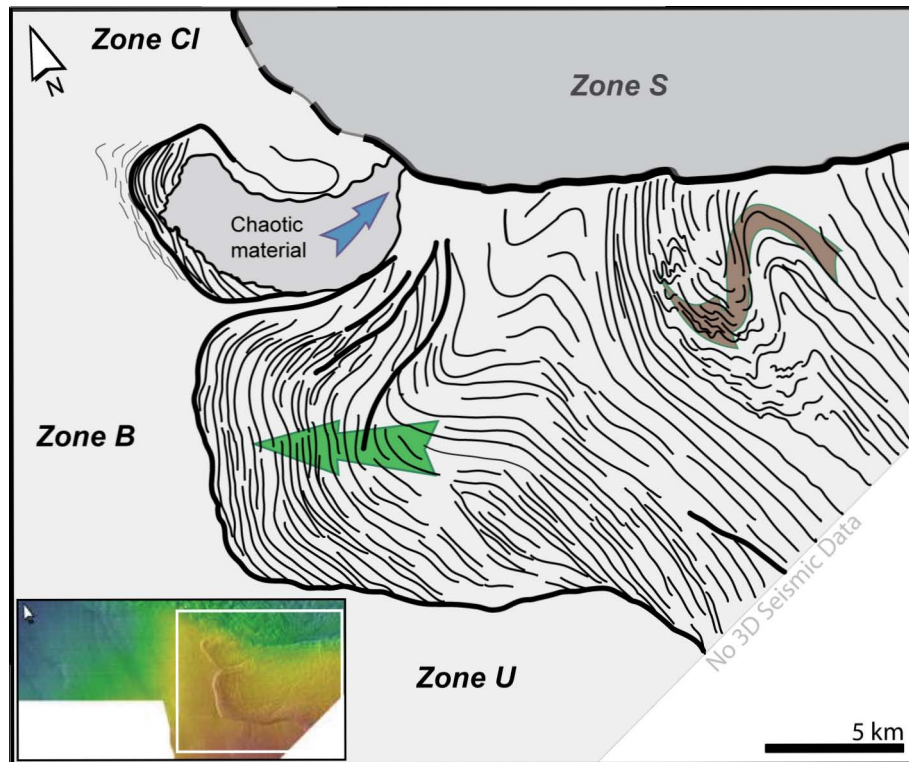


Figure 4.8: The deformation pattern expressed on the compression zone Ch derived from the combined interpretation of several seabed maps obtained from the 3D seismic data: shaded-relief map, gradient map, amplitude map and aspect map. Green arrow shows the general direction of transport with in this compression zone, blue arrow shows the direction of transport of Ch¹ sidewall collapse and the brown arrow shows the second order deformation affecting zone Ch. White box on location map shows position of Zone Ch map.

Considering its internal deformation structure, Zone Ch is interpreted as the toe of a mass movement deposit. However it does not exhibit all the characteristics of a completely developed slope failure (as defined by Varnes, 1978) as this failure did not over-thrust the down-slope sediments. Presenting the main characteristics of what Frey-Martinez et al. (2006) define as *frontally confined* submarine landslides; compressional toe region buttressed by a frontal ramp, small bathymetric expression compared to the total thickness and a relatively modest down-slope movement (Fig. 4.9). Not many studies describe mass movement deposits associated with failures in which the displacement ceased before the over-thrusting of the sliding material over the down-slope sediments. However, some authors recognised failures that could also be

classified as frontal confined landslide (e.g. Trincardi and Argnani, 1990; Huvenne et al., 2002; Lastras et al., 2004a).

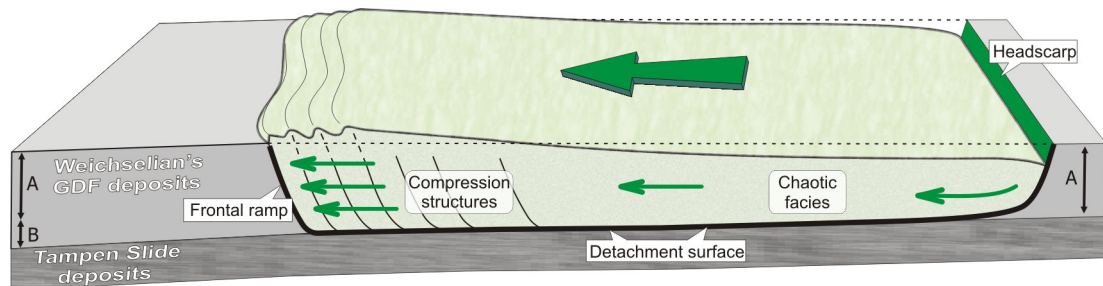


Figure 4.9: Schematic representation of the internal structure of Zone Ch. The mass translation stops against frontal ramp without abandoning the detachment surface that lies on top of Tampen Slide deposits; development of compression structures at the toe region and gradual loss of internal structure upslope. Note: The thickness of Unit I, sediments above the Tampen Slide, increases significantly down-slope. Not to scale.

Down-slope displacement stops or over-thrusts the seabed when the acting down-slope driving stress becomes lower than the sediment package internal shear strength. That can happen by loss of mass potential energy and/or by the increase of the down-slope sediments internal shear strength. Considering the down-slope increase of sediments thickness above the detachment surface - the top of the Tampen Slide (Fig. 4.9) - it is reasonable to believe that a thicker sediment column could present higher internal shear strength, due to compaction, preventing the propagation of the displacement.

The increase in thickness of the sediments above the detachment surface could also be responsible for constraining the lateral extension of this movement. The lateral boundary of the compression zone Ch is sub-parallel to the North Sea Fan thickness contour lines, which are essentially defined by the sedimentary accumulation subsequent to the Tampen Slide and reflecting the thickness variations of the upper part of the sedimentary column. This sediment package consists of hemipelagites of the Eemian/Ipswichian interglacial periods and glaciogenic debris flow deposits from the Weichselian period.

In unconsolidated sediment, both ductile and brittle deformation can occur. The compression zone Ch presents a gradual vertical transition from a ductile behaviour on the upper section (characterised by folding), to a brittle behaviour at the base (characterised by faulting). This gradual change reflects rheological changes through the sediment column as a consequence of the increase in shear strength and reduction in pore water with depth. This vertical transition of ductile to brittle is also observed in the shear-stress features, predominantly close to the

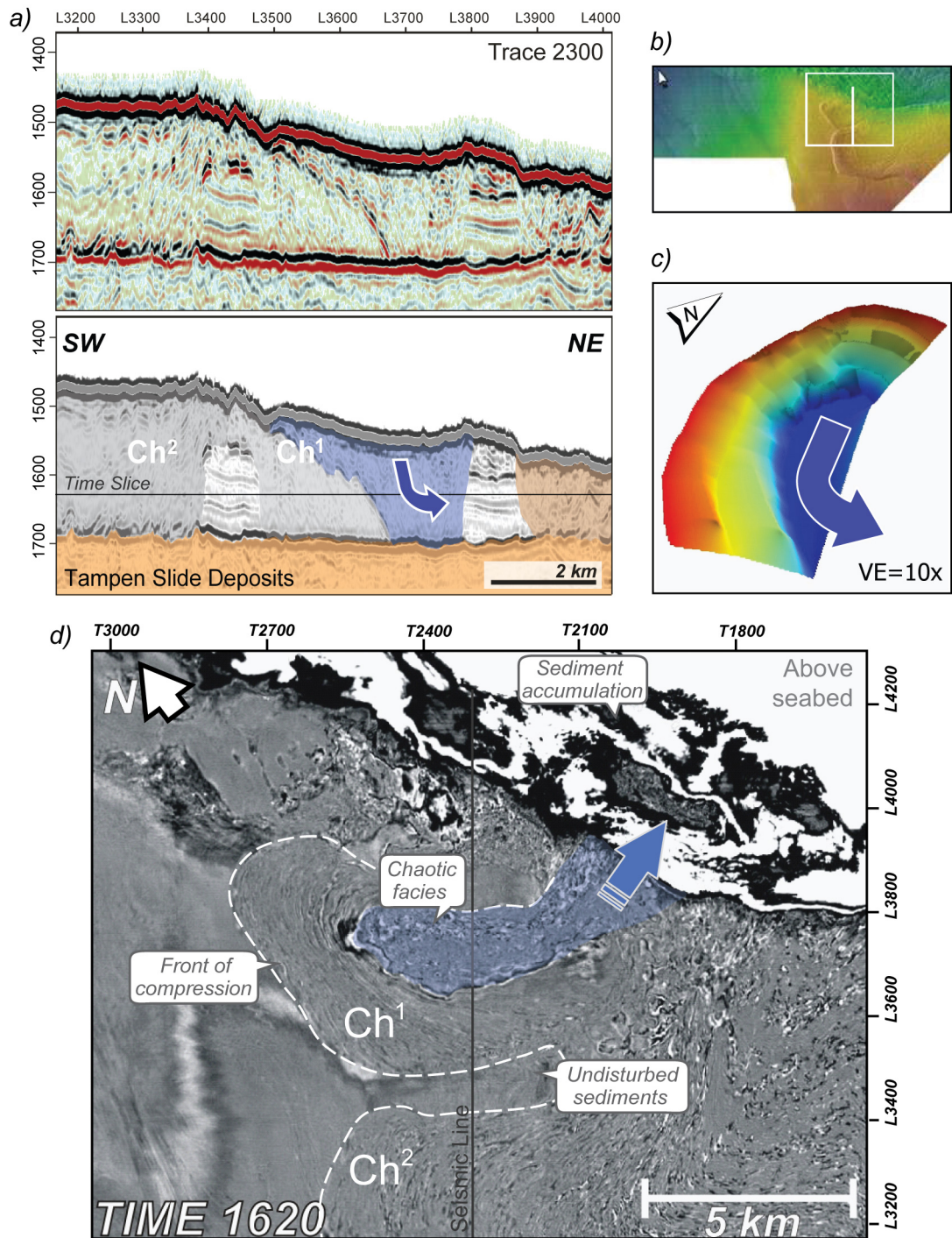


Figure 4.10: a) Seismic profile transverse to lobe Ch¹, crossing through the central area, and its interpretation. b) Seismic line and time-slice location map c) Perspective view of the Ch¹ internal boundary surface. Vertical exaggeration: 10x. d) Detail of the time-slice (at 1620 ms TWT) from the lobe Ch¹. It shows the undisturbed area between the two lobes Ch¹ and Ch², the Ch¹ internal boundary between the frontal area with the compressional facies and the chaotic facies, and the deposits accumulated in Zone S.

southern lateral boundary of the compression Zone Ch. Within the compression zone Ch, the upper glacial debris flow deposits are continuous, indicating that they were deformed under ductile conditions.

The absence of internal structure in the central area of lobe Ch¹ can be explained as being the result of small-scale slope failure event. The collapse and disintegration of sediments that had been previously deformed by compression would explain the existence, and geometry, of the marked boundary between the chaotic material at the central part and the front of the lobe Ch¹ (Fig. 4.10). The occurrence of such material transport is corroborated by the accumulation of sediments at the mouth of the amphitheatre structure, filling part of Zone S (Fig. 4.10). This slope collapse is interpreted as a retrogressive failure, probably resulting from the removal of lateral support and increased shear strain during the Holocene Storegga deep failure event.

Although the timing for the formation of the compression zone Ch is uncertain, some consideration can be given to its relative chronology. The sediment package above the Tampen Slide top, and deformed by the compression zone Ch, consists of Eemian to Holocene deposits, most of which are Weichselian glacial deposits. As far as the 3D seismic resolution allows, there was no significant deposition subsequent to the formation of the compression zone, placing it later than the last glacial event. On the other hand, both lobes of the compression zone are cut by the Holocene Storegga deep failure, which provides a minimum age of 8200 years ago (Bryn et al., 2005a) for this compression since it has to be penecontemporaneous with, or older than, the main Holocene Storegga deep failure.

4.2.3 Zone Cl

Zone Cl corresponds to the zone of the study area where another succession of compressional ridges is well preserved at the present-day seabed (Figs. 4.1 and 4.11). The southern boundary of Zone Cl is characterized at seabed by the limit of a sequence of sub-parallel escarpments oblique to the Zone Cl boundary. These ramps of $\sim 7^\circ$ slope normally reach 15 m relief, and have a distinctive bathymetric profile from the ridges within Zone Cl. The sub-parallel ridges within Zone Cl are ~ 120 m wide and approximately 6 m high, flanked by roughly symmetric slopes of $5^\circ \pm 2^\circ$. They are the seabed expression of a complex arrangement of folds and thrust faults, with its detachment surface on top of the Tampen Slide deposits. On seismic profiles the internal structure of this zone resembles the pop-up blocks found on the down-slope edge of zone S. However, these structures are significantly smaller than the ones in Zone S; with

vertical displacements of c. 10-40 m, through thrust faults with dip angle as low as c. 28° and affecting a sedimentary package of c. 150-350 m thick (Fig. 4.12).

The extent of the Zone C1 on the 3D seismic data, observed only on the northern limit of the seismic cube, corresponds to just a small part of its total distribution. The bathymetry compiled from the region shows that this compression zone extends towards northwest for tens of kilometres (Fig. 4.11) in front of a deeper compression zone developed in continuation with Zone S.

4.2.3.1 Interpretation

Zone C1 is interpreted as the result of the propagation of compression down-slope from the Holocene Storegga deep main failure and deep compression zone, at a shallower stratigraphic level. On the 3D seismic data, as well as in 2D seismic profiles outside the detailed study area (Færseth and Sætersmoen, 2008), it can be observed that the frontal limit of the deep compression zone overthrusts part of the sediment column to the west, forming fault-bend-fold in some areas (Figs. 4.12a and 4.13). The associated impact was propagated through the sediment column above the Tampen Slide deposits, generating compressional pop-up structures. The Tampen Slide deposits are also disrupted by this compression but only in areas very proximal to the deep compression zone.

The majority of the ridges in Zone C1 are situated along the contacts between different pop-up blocks. These ridges are coincident with the intersection of two opposite thrust faults at the surface. During the rising of adjacent pop-up blocks lateral compression developed on their edges by convergent lateral movement, thus building up the ridges (Fig. 4.13c). The seismic resolution available does not allow definition of the internal structure of these ridges. However based on what was observed on the compression zone Ch, which presents similar rheological conditions and comparable type of deformation, it is assumed that the shallowest sediments are predominantly affected by ductile deformation.

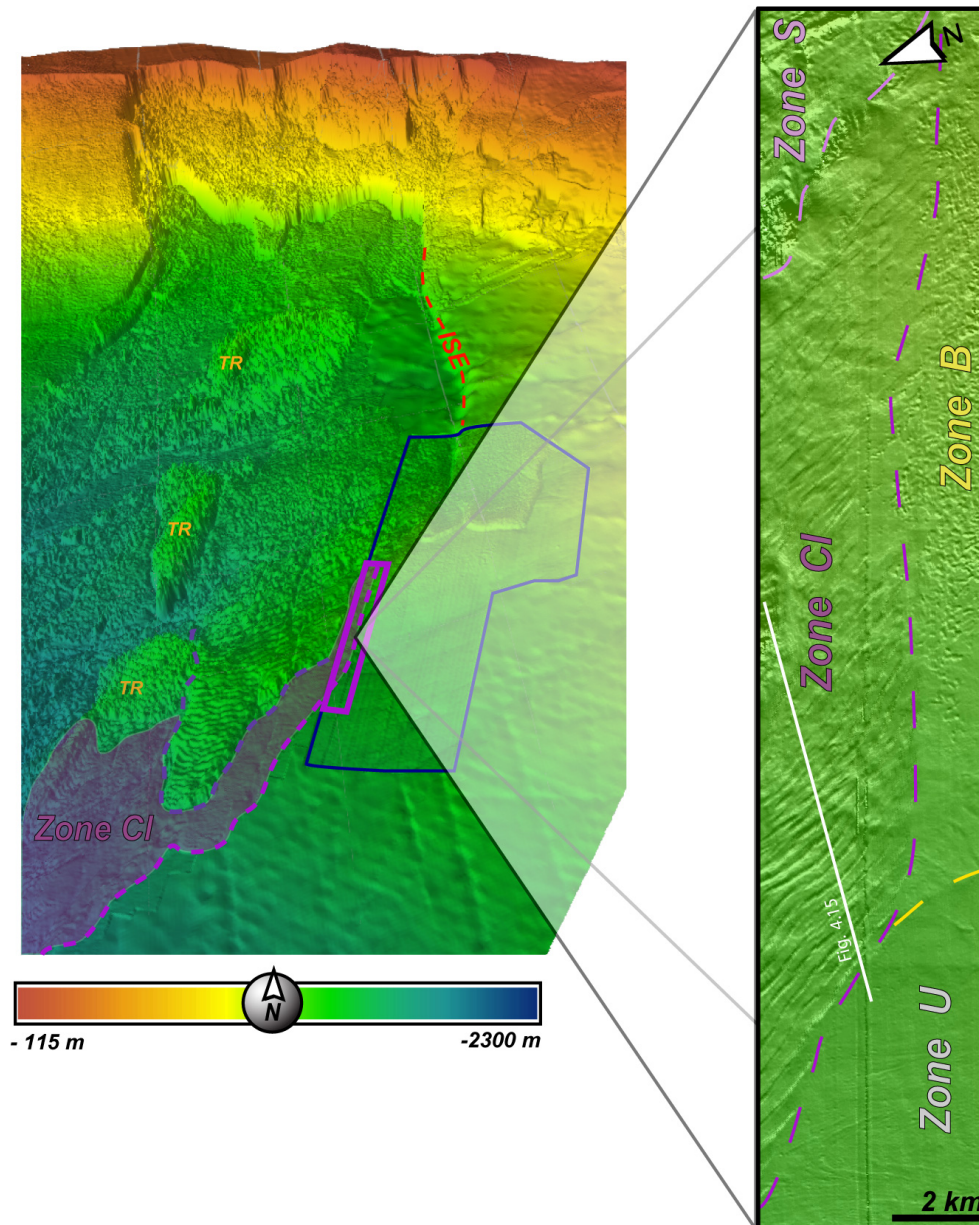


Figure 4.11: Left: Shaded-relief map of the boundary between the North Sea Fan and the Storegga. TR - Tampen Slide deposits remnants; ISE - Storegga Inner Slide Escarpment; Blue line represents the outline of the limits of the 3D survey. Right: Detail of the seabed image obtained from the 3D seismic data showing Zone Cl. White line shows the location of Fig. 4.12

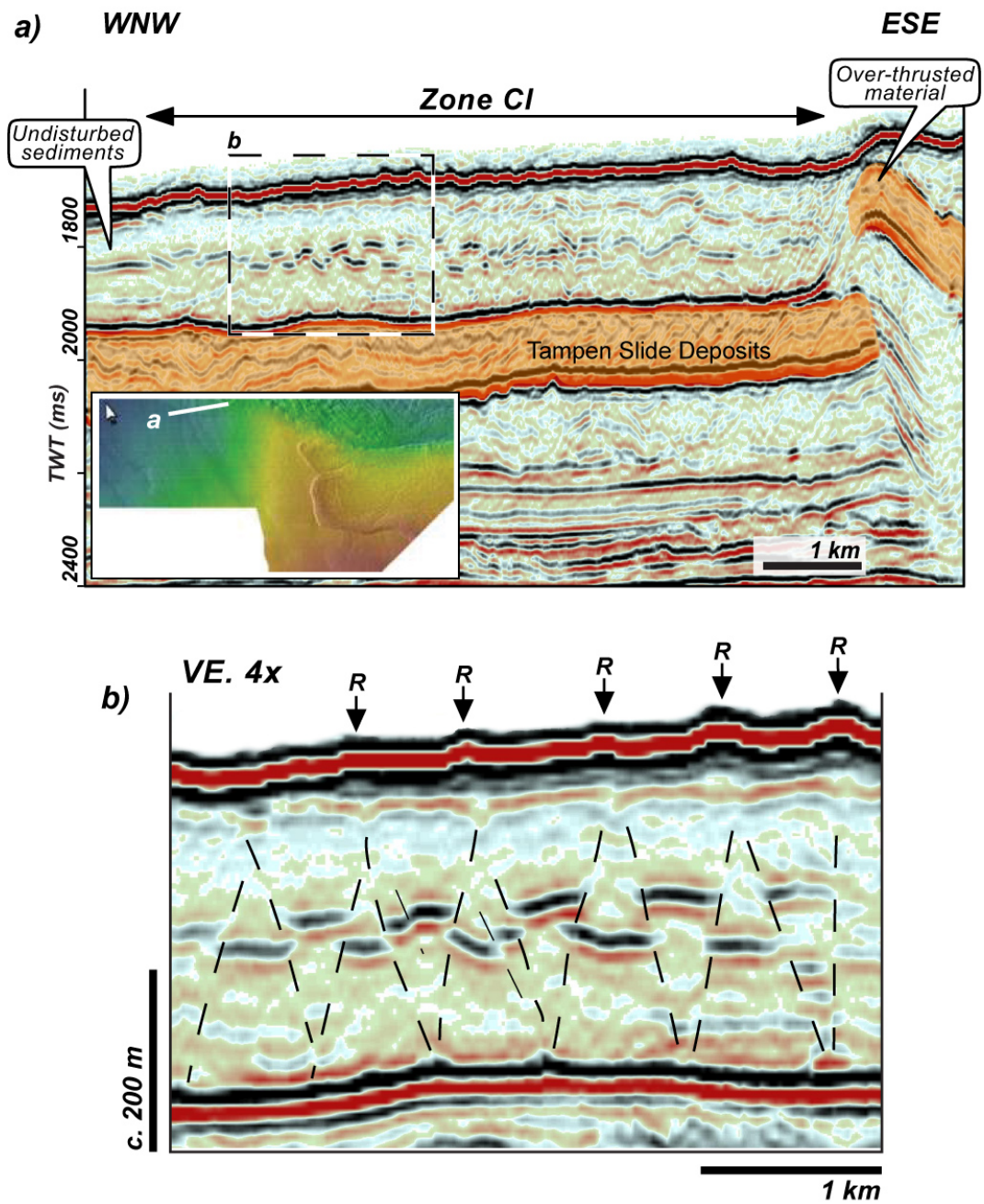


Figure 4.12: a) Seismic profile through Zone C1 showing the succession of pop-up blocks b) and enlarged view of a part of this succession. The pop-up blocks are defined by thrust faults of dip angles around c. 28° (note the seismic profile vertical exaggeration) and with vertical displacement on the c. 10-40 m range. R arrows point to ridges observed at seabed.

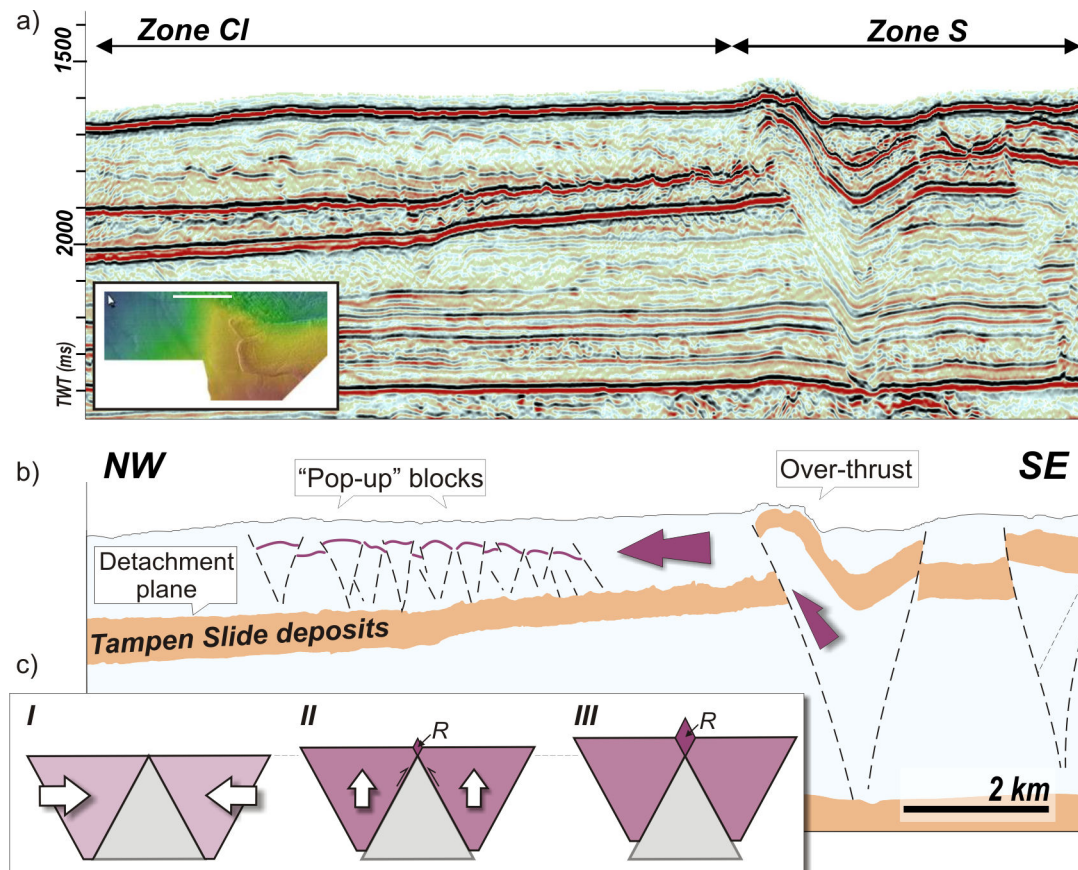


Figure 4.13: Seismic profile cutting through Zone CI (a) and its interpretation (b). It shows the over-thrust at the frontal limit of Zone S and the disturbed material above the Tampen deposits through Zone CI. Note the pop-up structures above the Tampen Slide deposits in Zone CI. c) Schematic illustration of the development of the CI ridges. I - Lateral compression and delineation of the pop-up blocks. II - Rise of the pop-up blocks and build up of the ridge (R) at the edges of the pop-up blocks. III - Full developed ridge (R).

4.2.4 Zone B

Zone B, in the central part of the study area and covering an area of 93 km², corresponds to an area of disturbed seabed. Tabular blocks of ~100 to 250 m in length and ~5 m high can be identified (Fig. 4.14). On seismic profiles, a well-developed detachment plane can be observed ~600 m down-slope from the frontal escarpment of the compression zone lobe Ch¹ (Fig. 4.15). It is there that this deposit is thickest, reaching c. 70 m, getting gradually thinner, both down-slope and southward. The southern limit of this deposit coincides with the limit of the frontal escarpment of the compression zone lobe Ch². The western limit of Zone B is defined by a local change in slope direction, located 15 km down-slope of the Ch¹ frontal escarpment. Zone B northern limit overlaps with the southern limit of the compression zone CI. On the amplitude

map (Fig. 4.14b) and time-slice, a connection between Zone B and Zone S can be observed. It consists of an elongated section of disrupted material immediately north of lobe Ch¹.

4.2.4.1 Interpretation

The Zone B blocky deposit is thought to result from sediment overbanking from the Storegga deep main failure, followed by localized slope instability in front of the compression zone Ch. Lateral transport of upper material may also have occurred from Zone S, especially of sediments liquefied by ground acceleration. The sediments would have then overbanked the limits of Zone S and spread through the area that becomes Zone B. Once the seabed was suddenly loaded by the overbanking material, slope failure could then have been triggered originating Zone B. However the erosion taking place at the basal layer of the spreading material could also have been sufficient to trigger the slope failure of the underlying material. It is not possible to establish the exact triggering mechanism with the available data.

The resolution of the 3D is also insufficient to distinguish the internal structure of the Zone B, making it impossible to determine whether the tabular blocks correspond to intact detached blocks rafting on a mobile matrix of chaotic material, as described for example by Gee et al. (2005), or if the blocks correspond to any type of fault arrangement, as described for example by Huvenne et al. (2002). Independent of the process of disintegration and formation of detached blocks, the tabular blocks moved for a certain distance before the displacement ceased. They are probably composed of relatively consolidated sediments, internally undisturbed, and result from stratigraphic inhomogeneous sediments, i.e. sediments containing bedding planes separating the stacked glaciogenic debris-flow deposits.

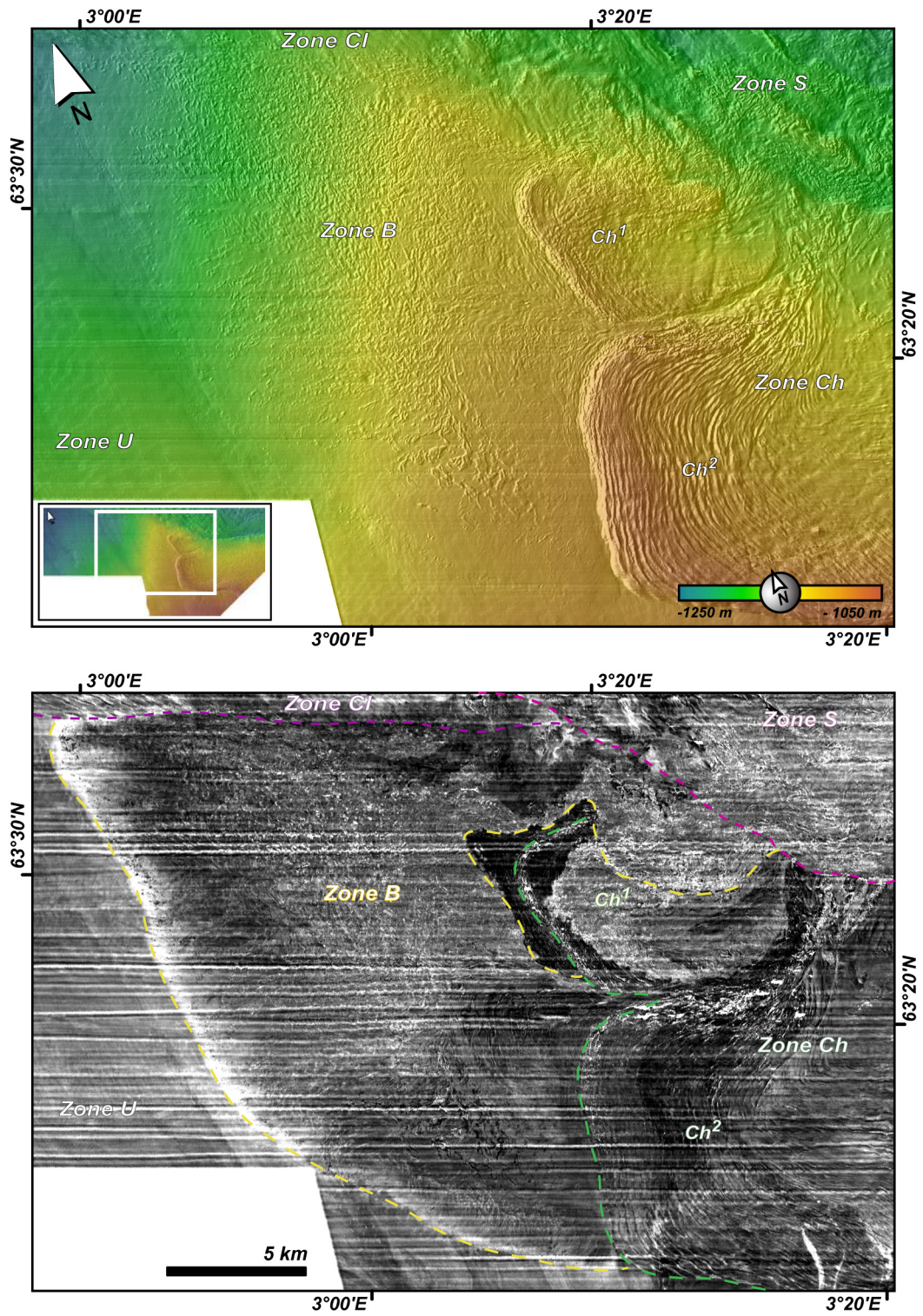


Figure 4.14: Shaded-relief (top) and amplitude maps (bottom) showing Zone B. The tabular blocks are well defined on the shaded-relief map; the matrix external limits are well defined on the amplitude map. Note the relatively undisturbed swath of seabed, in front of the Ch¹.

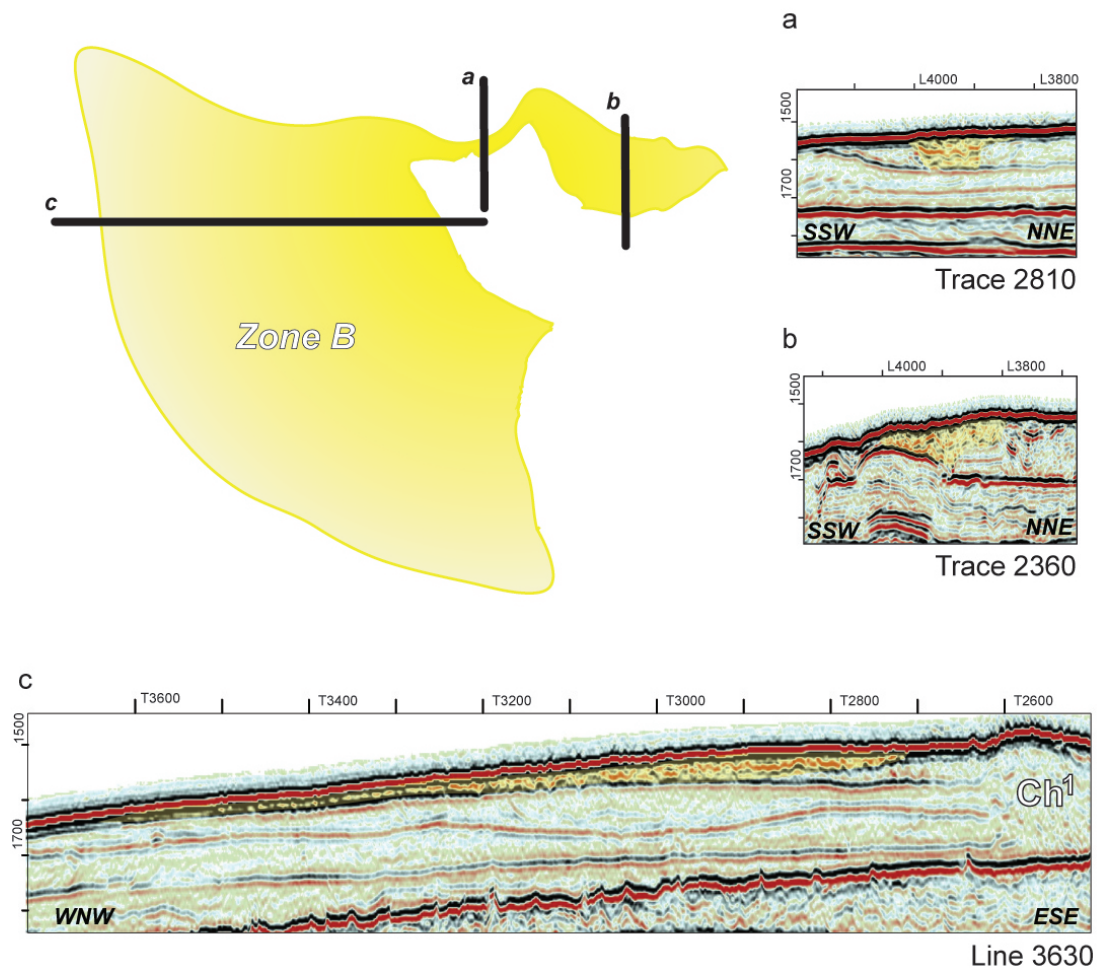


Figure 4.15: Schematic illustration of the spatial extent of Zone B, and the localisation of the seismic sections displayed (a),(b) and (c). The disturbed material considered as part of Zone B is highlighted in yellow.

4.2.5 Zone U

Zone U corresponds to the North Sea Fan seabed deposits that were undisturbed by the Storegga Slide Complex, in the study area. In this zone, it is possible to identify several glacial debris-flow deposits. These deposits comprise several stacked bodies showing long run-out transport towards the north, with minor changes of flow direction responding to local slope variations due to the geometry of previous glacial debris flow deposits. In some of these deposits, it is possible to recognise a well developed central core with strong chute-flank separation, suggesting a laminar movement within the glacial debris-flow core (Fig. 4.16).

4.2.5.1 Interpretation

The uppermost glacial debris flow deposits observed in Zone U correspond to the last sequence of glacial debris flow deposited during the Late Weichselian maximum (King et al., 1998). The overall northwards transport direction shown on this zone is consistent with the regional radial distribution observed on the North Sea Fan. It results from a common material source area situated at the mouth of the Norwegian Channel.

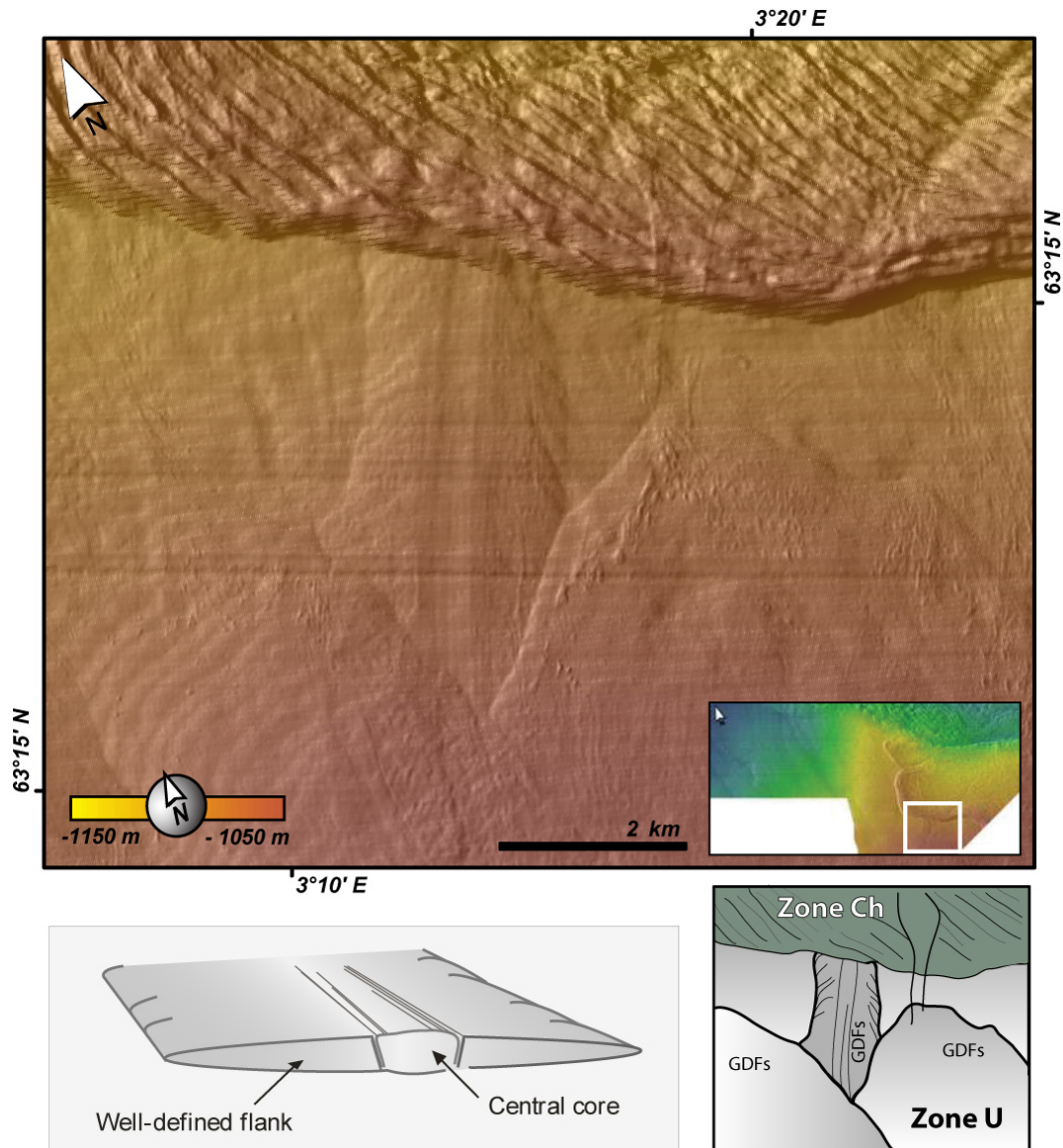


Figure 4.16: Shaded-relief map of the seabed showing GDF's deposits on the area adjacent to the Ch^2 zone. The central GDF deposit, 2 km wide, with strong chute-flank separation displays marked flow lines concentrated along the core suggesting a laminar movement within the GDF core as on the left bottom diagram. This GDF deposit is partially covered by more recent GDF's deposits, as illustrated in the diagram on the right bottom.

4.3 Summary of Events that shaped the present day seabed

3D seismic interpretation followed by geomorphologic analyses on the northern edge of the North Sea Fan has shown the existence of five distinctive morphological zones in the study area. These zones have been given the names of: Zone S - where the slope sediments were remoulded; Zones Cl and Ch - where the seabed has marked ridges resulting from compression of the sediments; Zone B - dominated by blocky deposits; and Zone U - where the North Sea Fan sediments are undisturbed.

The proposed sequence of main events that led to the development of these distinctive morphological zones is described below and illustrated in figures 4.17 and 4.18. However, this relative chronology is only one of the possible sequences of events. A major uncertainty resides on the exact timing and nature of the instability slope process that shaped Zone B since this area of blocky deposits could alternatively be related to the development of compression zone Ch.

- Deposition of Weichselian glacial debris flows above the Tampen Slide deposit during the North Sea Fan build up.
- Development of compression zones Ch¹ and Ch² by a frontally confined slide induced slope instability located East of the study area (Figs. 4.17 and 4.18a).
- Major slope failure during the Holocene Storegga Slide event generated Zone S, truncated Zone Ch and led to the formation of compression zone Cl (Figs. 4.17 and 4.18b).
- Also associated with this major event, sediment overbanking may have occurred from the Storegga main failure causing slope instability on Zone B (Figs. 4.17 and 4.18c and d).
- Due to lack of lateral support the northern lobe of the compression zone Ch, sub-zone Ch² collapsed into Zone S during or shortly after the major slope failure (Fig. 4.18e).

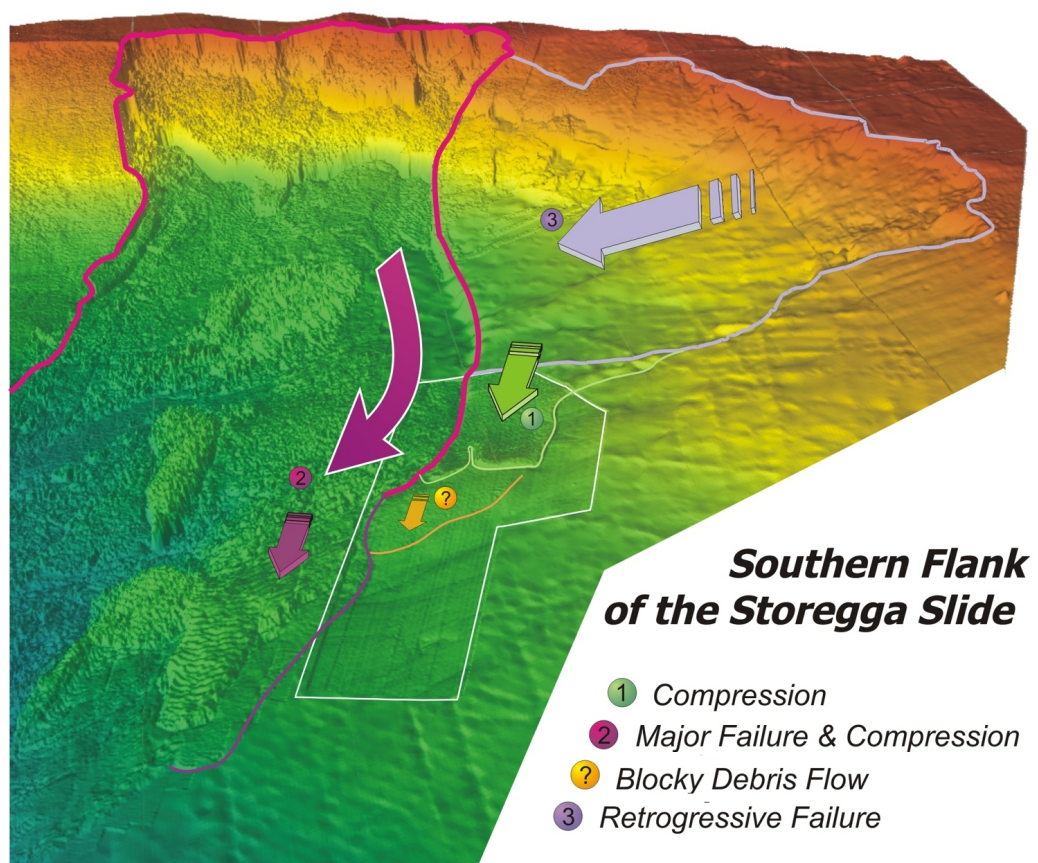


Figure 4.17: 3D perspective view of the southern flank of the Storegga Slide (Norsk Hydro bathymetry) looking eastward, with the suggested chronology for the major events leading to the formation of the present-day morphology.

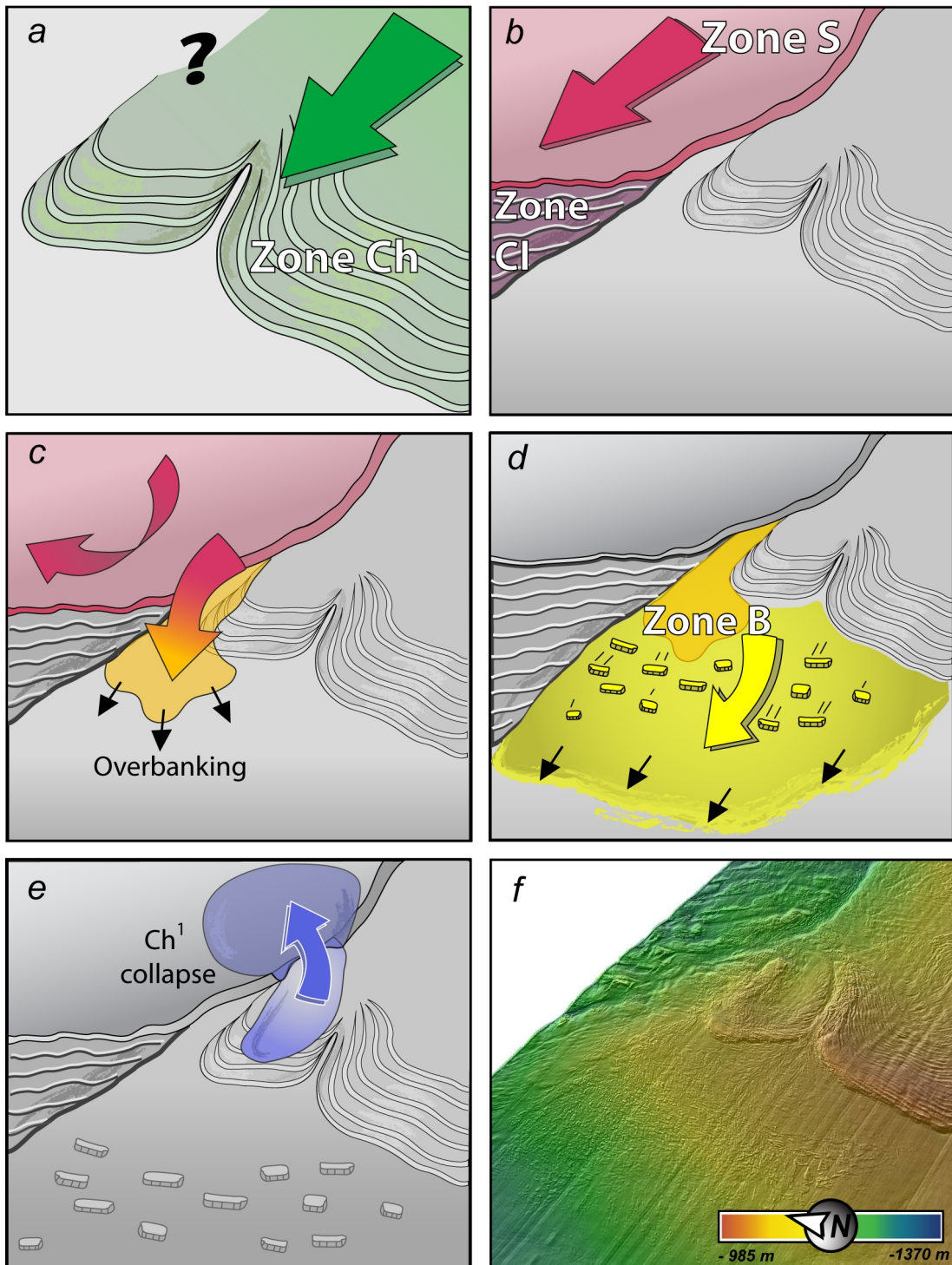


Figure 4.18: Sketch representation of the main events shaping the seabed in the proximities of Zone Ch¹. (a) Formation of compression zone Ch. (b) Holocene Storegga Slide, cuts of zone Ch and leads to the formation of zones S and Cl. (c) Overbanking of material from Zone S during the major slide. (d) Spreading of the material through the area in front of Ch compression zone and development of slope instability. (e) Collapse of the sub-zone Ch². (f) Present-day seabed 3D perspective view of Zone Ch¹ and surrounding areas.

Chapter 5

Geomorphology of the middle and upper pleistocene slide deposits

5.1 Introduction

Several palaeoslide deposits were identified at different stratigraphic levels of the North Sea Fan. In the present work, the three upper slide deposits respectively named Slide U, the Møre Slide and the Tampen Slide were studied. The stratigraphic positions of these slides are presented in figure 5.1. The age of each of these Mid- to Upper-Pleistocene slides is given by its top reflector while the bottom of the slide representation gives their depth of incision. More precise information related to their age and geographic position will precede each slide description in this chapter. This chapter describe in detail the geometry, seismic facies and sliding surface of the three buried slides followed by the interpretation of their features and characteristics observed. Sections 5.2, 5.3 and 5.4 present respectively the Tampen Slide, the Møre Slide and Slide U deposits.

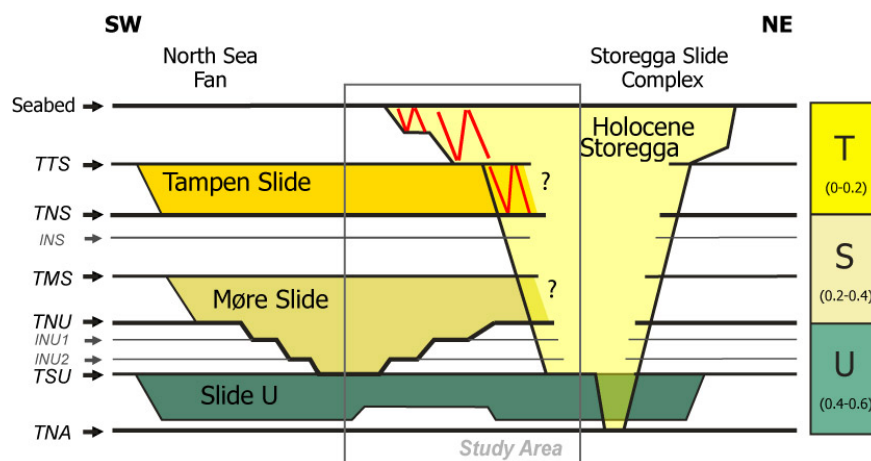


Figure 5.1: Schematic representation of the relative stratigraphic position of the mega-slides. The top surfaces of the slides mark their age in terms of the seismic stratigraphy of the Naust Formation. Vertical extent gives indication of erosion by the slides, whereas the horizontal extent gives a sense of their lateral extension.

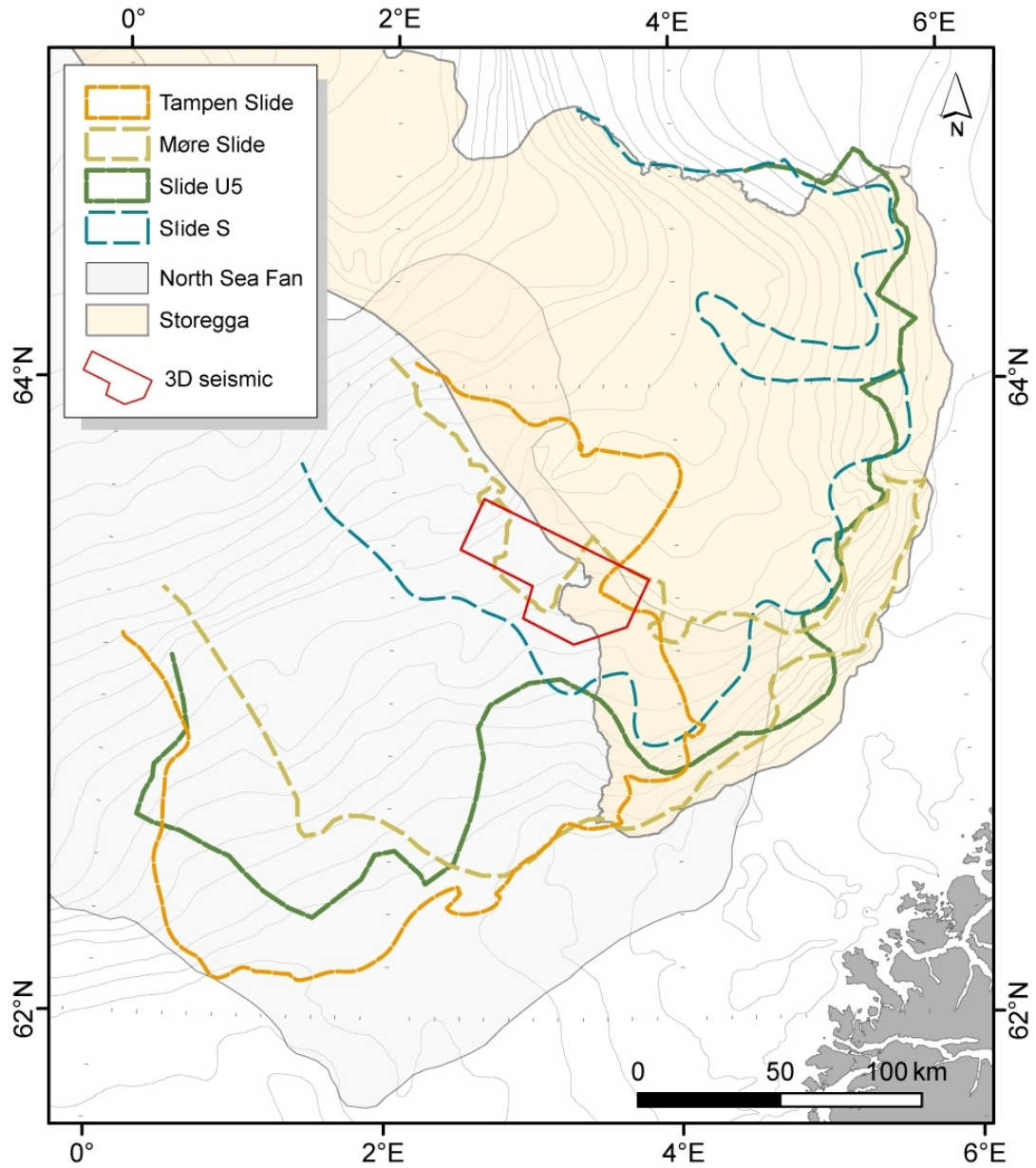


Figure 5.2: Map of the region surrounding the study area, showing the spatial extent of the slide discussed in the present study. The outline of the Tampen Slide and Slide S deposit was taken from Solheim et al. (2005a), whereas the outline of the Møre Slide and Slide U5 was obtained from the phase II of the Seabed Project (Norwegian Deepwater Programme, unpublished, 2004). Note that it was not defined if slide deposits from the slide named Slide U in this thesis are part of the previously mentioned Slide S and U5.

5.2 Tampen Slide

The Tampen Slide has affected an area of at least 15000 km² and involved more than 3000 km³ of sediment (Evans et al., 1996). This slide removed from the North Sea Fan a large part of GDF deposits that accumulated on during the Saalian glacial period (MIS 6), which can be up to 400 m thick on the western section of this fan (Nygård et al., 2005). The smooth upper surface of an older GDF sequence, possibly draped with MIS 7 interglacial sediments, may have acted as a sliding surface for the Tampen Slide (Sejrup et al., 2004). Additionally, Nygård et al. (2005) suggested that the resistance to erosion by the Tampen Slide of the MIS 8 GDF deposits might be attributed to consolidation before the Tampen Slide event.

The 200 km-long headwall of the Tampen Slide was totally buried by glacimarine sedimentation and later GDF deposits, despite being locally in excess of 220 m high (Evans et al., 1996). The eastern sidewall of the Tampen Slide, as well as part of the headwall, was truncated by the Holocene Storegga Slide. Therefore, the known dimensions of the Tampen Slide correspond most likely to minimum numbers. The study area is located within the area of sediment removal by the Tampen Slide, approximately 65 km downslope from its headwall and immediately before the contact with the Holocene Storegga Slide main failure that remoulded the northern margin of the Tampen slide deposits.

5.2.1 Description

The Tampen Slide deposits are easily recognised in seismic profiles as a seismic unit of chaotic to discontinuous seismic reflections - here designated as Unit II (Fig. 5.3). This unit is the most recognisable unit in the study area, and is well defined by high-amplitude reflections, that show smooth base and an irregular top. These reflections mark the contrasting contact between the Tampen Slide deposits and the underlying and overlying seismic units, which display more continuous internal seismic reflections.

The strong, bright signal of the top of the Tampen Slide deposit, the *TTS* reflector, may represent the contrast between (1) the slide deposits and the material which settled out of suspension immediately after the slide, (2) the slide deposits and hemipelagic sediments that settled later, or perhaps (3) between the slide deposits and late-phase sliding generated in response to the radical new topography that has just been created. Whatever the nature of the overlying material, the irregular topography of the top of the deposit was preserved (Fig. 5.3).

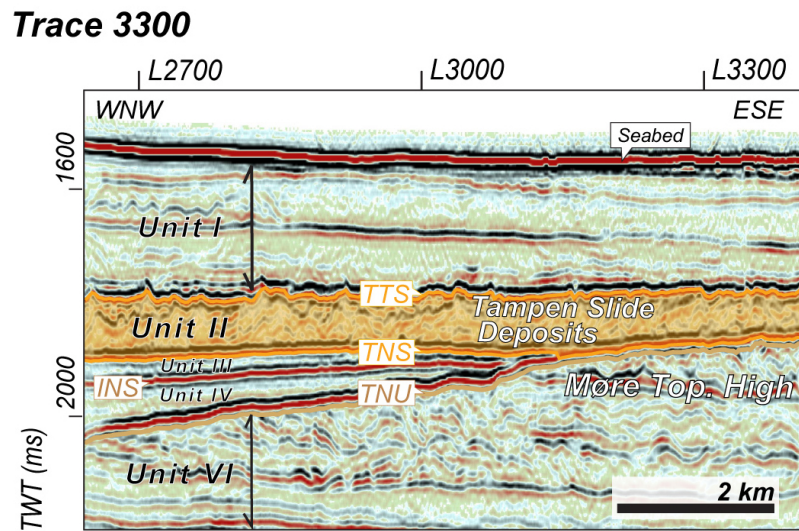


Figure 5.3: 3D seismic profile through the MTH showing the Tampen Slide deposits at the contact between the top of Unit III and the top of the MTH. The Tampen Slide deposits are highlighted in orange and are delineated by the reflectors TTS and TNS. Note the seismic signature contrast between these reflectors.

The strong signal of the base of the Tampen Slide deposits, *TNS* (Top of Naust S), is likely to represent the contact between the slide deposits with the subjacent debris-flow deposits of both Unit III and Unit VI (Fig. 5.3). No erosional truncation is evident between the Tampen Slide deposits and Unit III, as the internal reflectors below the Tampen Slide deposits are sub-parallel to the unconformity marked by the *TNS*. In contrast a visible, irregular and uneven erosional surface marks the contact between the Tampen Slide deposits and Unit VI. In fact, the area of contact between the Tampen Slide deposits and Unit VI corresponds to the top of an erosional high, named in this study as the Møre Topographic High (MTH; see Fig. 5.3 and 5.5).

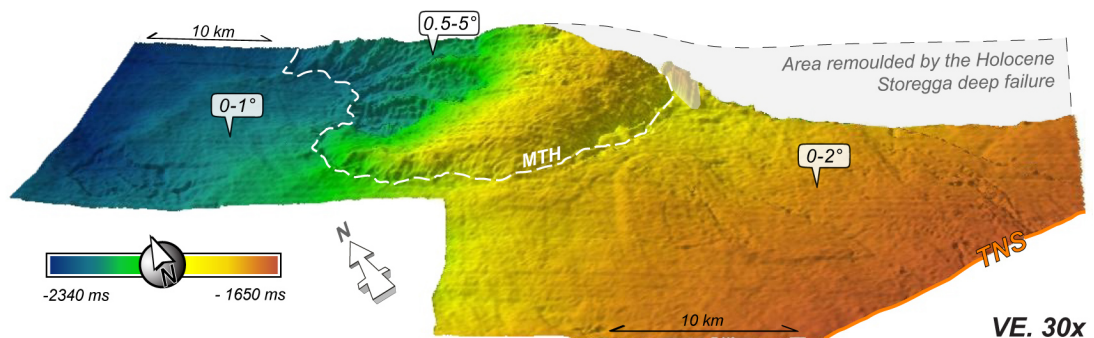


Figure 5.4: Three-dimensional perspective view of the *TNS* reflector's DEM from south-southeast. The dashed white line marks the contact between the top of Unit III and the MTH. Note the gradient change from the surroundings areas to the MTH. The area in grey correspond to the area where is impossible to track the *TNS* reflector.

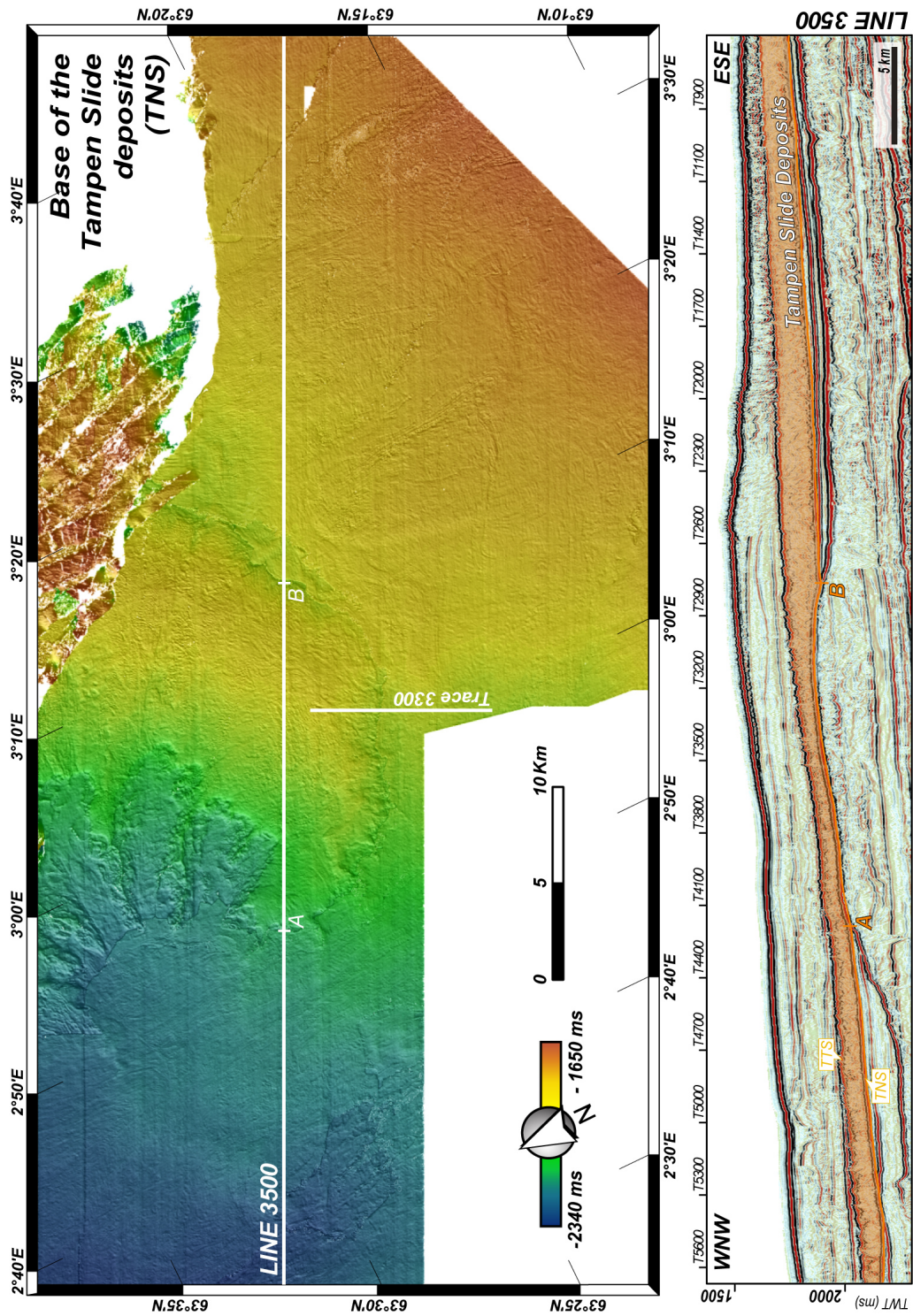


Figure 5.5: (Left) Shaded-relief map of the TNS reflector with artificial illumination from northwest at 45°. The white lines show the location of Line 3500 and section of the trace 3300 on Fig. 5.3. (Right) Seismic line 3500 across the MTH with the Tampen Slide deposits highlighted in orange. The A and B mark, both in map and in the seismic line, show where the base of the Tampen Slide deposits become directly above the MTH.

The Tampen Slide DEM together with the seismic profiles (Fig. 5.5) show that the basal surface of the Tampen Slide follows the top of Unit III for over 75% of the study area. Where Unit III is not present the slide overlies the MTH. The Tampen Slide sliding surface passage from the top of Unit III to the top of the MTH is marked by evident changes of surface morphology. On the MTH area this surface presents higher slope values ($0.5-5^{\circ}$) compared to the typical values on surrounding areas ($0-2^{\circ}$). On seismic profiles, parallel to the acquisition direction ($N26^{\circ}W$) and passing through the MTH, the *TNS* reflector has a characteristic convex-shape in this area (Fig. 5.5).

The Tampen Slide deposits show significant variations of two-way travel time (TWT) thickness in the study area ranging from 40 to 180 ms thick (Fig. 5.6), which corresponds to metric thicknesses ranging from c. 30 to c. 136 m. Over an area of more than 40 km^2 immediately southeast of MTH, the Tampen Slide deposits are more than 160 ms (c. 122 m) thick. In contrast, above the MTH the Tampen Slide deposits can be as thin as 50 ms (c. 38 m). Nevertheless, it is on the western edge of the seismic volume that the thinnest deposits of Tampen Slide are found (40 ms; c. 30 m). The spatial variation in thickness within the deposits (Fig. 5.6) suggest that the relief of the MTH have influenced the distribution and geometry of Tampen Slide deposits in the study area.

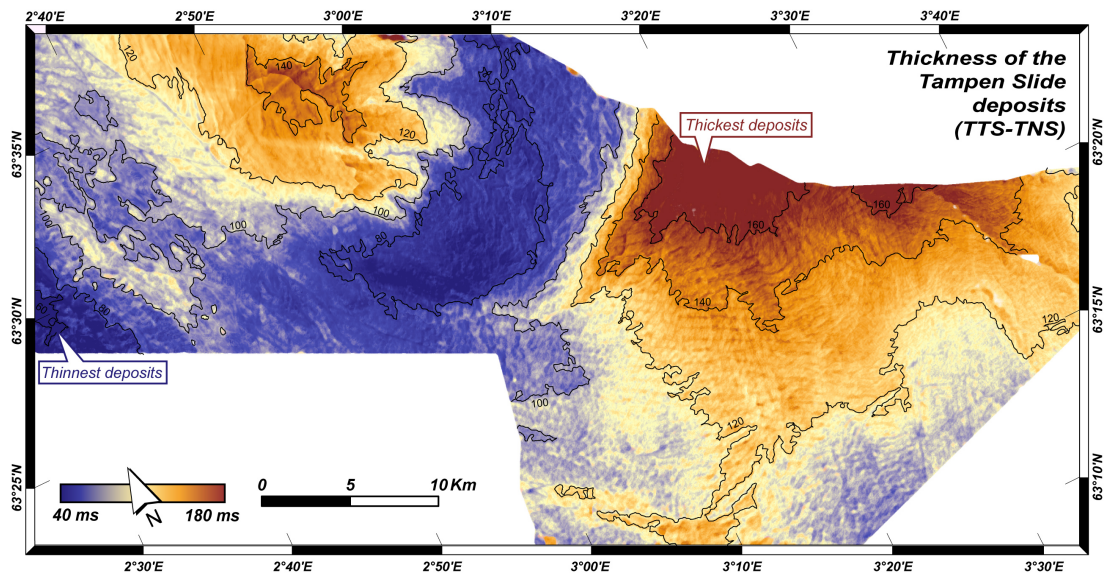


Figure 5.6: Tampen Slide deposits time-thickness map calculated from *TNS* and *TTS* reflectors depth values. Warmer colours represent thicker deposits (up to 180 ms TWT) and cooler colours represent thinner deposits (up to 40 ms TWT). Contour lines every 20 ms.

The amplitude map for the reflector at the base of the Tampen Slide, the *TNS* reflector, shows marked patterns of lower (darker) and higher (lighter) amplitude values. However, its interpretation is challenging and confusing since it reflects changes of seismic response from the material both above and beneath the seismic event (Fig. 5.7). These patterns are clearer on the amplitude map of horizon *TNS-12ms* (Fig. 5.8) generated by vertically raising the reflector *TNS* by 12 ms (TWT), as explain on figure 3.4. This horizon allows the observation of lateral changes in the seismic response above, and only above, the reflector *TNS*, reflecting the seismic properties at the base of the Tampen Slide deposit. The patterns of higher and lower amplitude values observed vary from area to area and, using this technique, it is possible to identify four main fabrics: a) Anastomosing fabric, b) Curvilinear fabric, c) Rectilinear fabric, and d) Wispy fabric (Fig. 5.8).

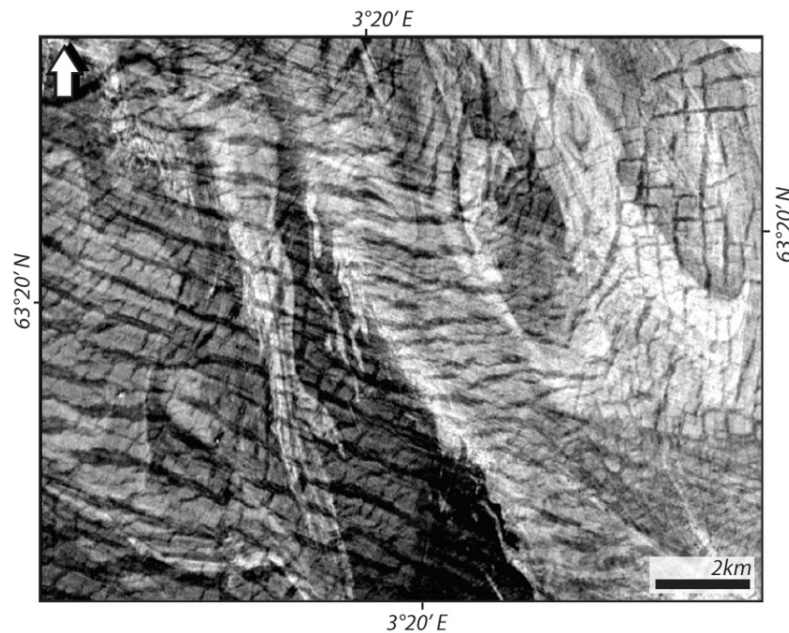


Figure 5.7: Detail of the amplitude map from the horizon *TNS* showing the complex amplitude pattern observed at the interphase between the Tampen Slide deposits and the underlying material deposits reflecting the acoustic changes in both seismic units.

The Anastomosing fabric is characterised by lighter, lenticular blocks delineated by darker stripes that reconnect after initial branching out. The Curvilinear fabric is characterised by broken curvilinear lighter stripes separated by narrower dark stripes. These sinuous stripes can be predominately concave or convex dependently of the areas. The Rectilinear fabric is characterised by rectilinear lighter blocks delimited by straight, parallel dark cracks and less pronounced perpendicular cracks. The Wispy fabric is characterised by thin, bifurcated, dark stripes that become thinner and weaker at the edge.

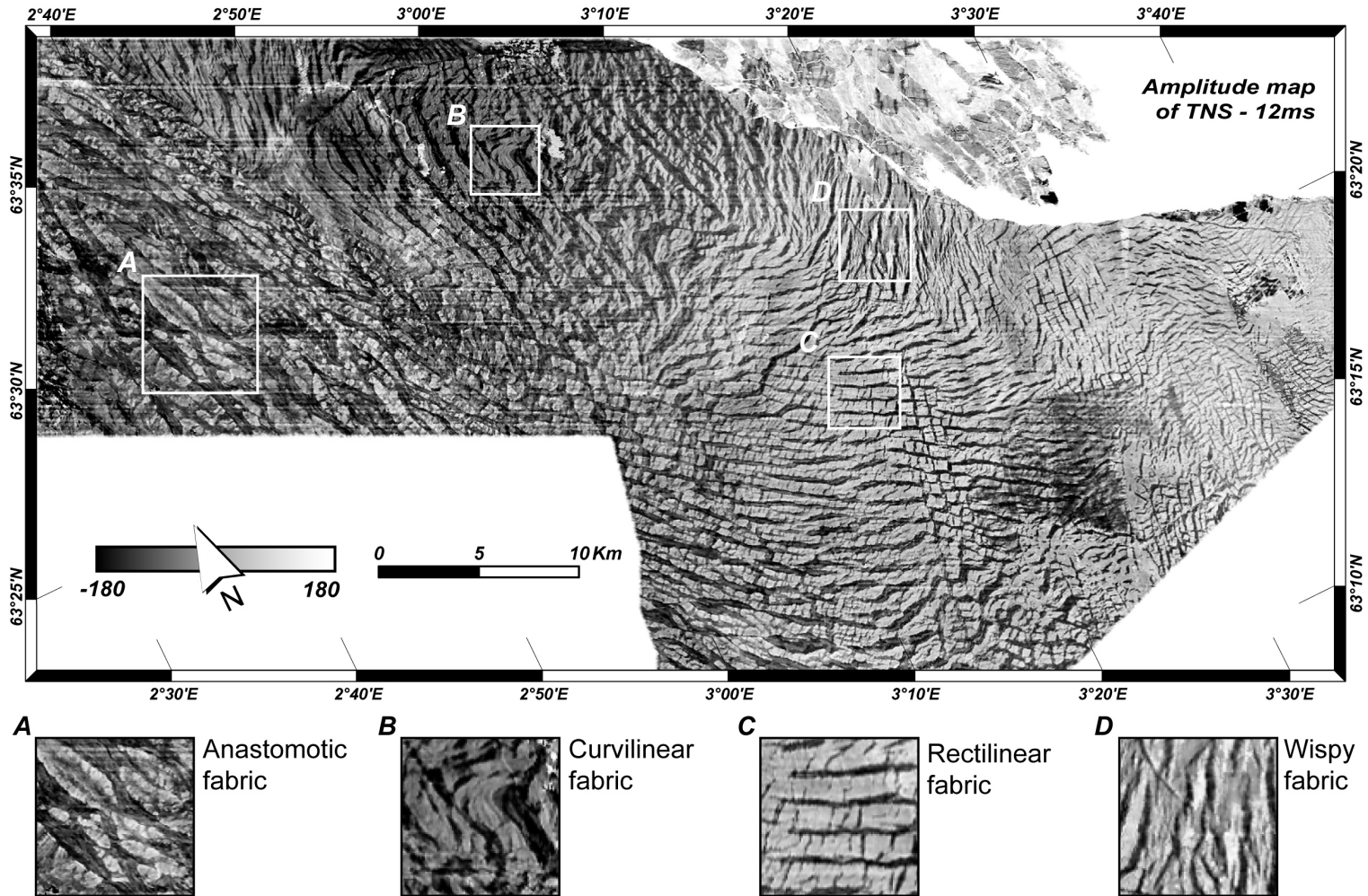


Figure 5.8: (Top) Amplitude map of the horizon TNS-12ms showing the overall distribution of the amplitude pattern observed at the base of the Tampen Slide deposits. (Bottom) Detail views of the main recognised fabric: (A) Anastomosing fabric, (B) Curvilinear fabric, (C) Rectilinear fabric, and (D) Wispy fabric.

The spatial analysis maps from the DEM of the *TTS* reflector shaded-relief map (Fig. 5.9) and slope map (Fig. 5.10), reveal that the irregular topography of the top of the Tampen Slide presents a variety of textures. Based on the configuration of these textures it is possible to identify four fabrics that can be correlated directly with the fabrics observed at the *TNS-12ms* amplitude map of the base of the Tampen Slide deposits. The Anastomosing fabric is at the top of the deposits characterised by lenticular blocks defined by relative steep edges surrounded by gaps, with gentler surface, which branch out and reconnect. The curvilinear fabric is characterised by arcuate terraces with relative steep edges changing to discontinuous sinuous ridges downslope. The Rectilinear fabric is characterised by straight, discontinuous, parallel ridges with small, perpendicular, ramifications. The Wispy fabric is characterised by bifurcated thin ridges that become diffused at the edge. Each of these fabrics is illustrated and described in Figure 5.11.

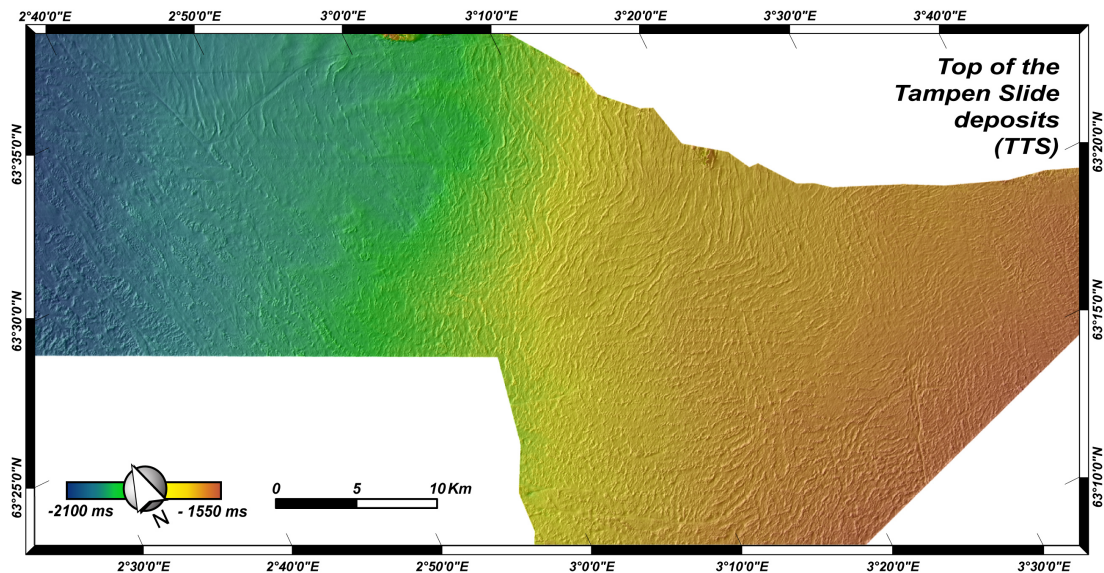


Figure 5.9: Shaded-relief map of the top of the Tampen Slide deposits obtain from the DEM of the *TTS* reflector, with artificial illumination from northwest at 45°. The texture of the top surface of the Tampen Slide deposits varies from zone to zone.

Together, the amplitude map of the *TNS-12ms* horizon and the maps generated from the *TTS* reflector's DEM were used to divide the Tampen Slide deposits into seven fabric regions (A1, A2, B, C1, C2, D1 and D2) dominated by one of the four main identified fabrics, surrounded by areas of complex or undefined fabric (Fig. 5.12). Contrary to the seven fabric regions, in surrounding areas the pattern observed tends to change gradually without definable transition boundaries, combining features from two or more of the main identified fabrics.

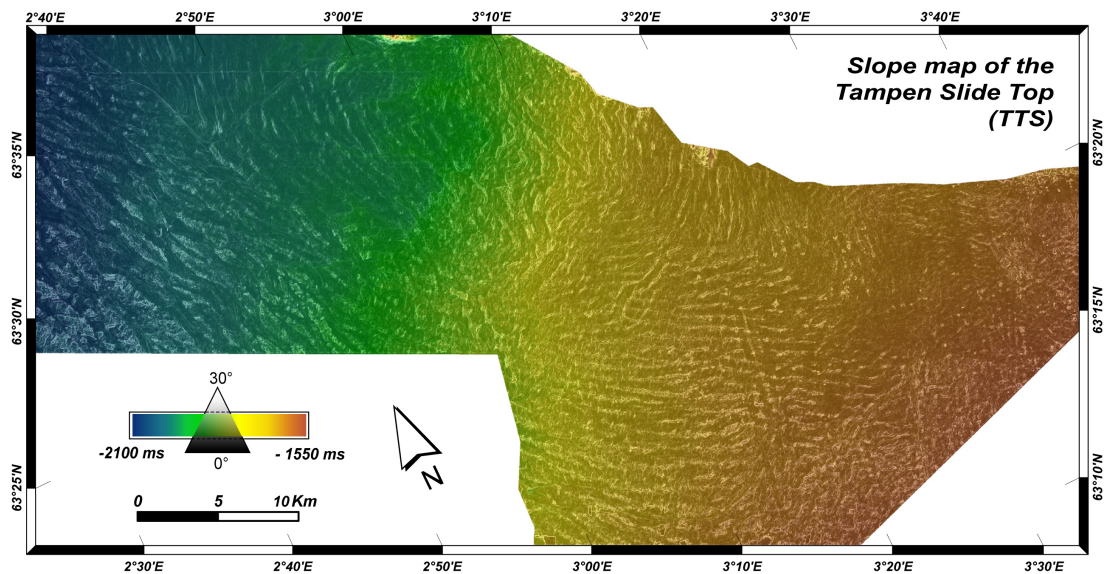


Figure 5.10: Gradient and depth map of the top of Tampen Slide deposits (TTS). The brightness shows the gradient with low slope values in black and higher slope values in white (note that white correspond to slope higher than 30°). The colour-scale shows the depth in ms (TWT).

The Anastomosing fabric covers approximately one third of the study area and can be identified in two separated areas, A1 and A2, nevertheless this division is probably artificial and results from the geometry of the 3D seismic volume. The deposit's thickness varies between 50 and 110 ms (c. 38 to 84 m) where this fabric occurs. The Curvilinear fabric is found essentially on the area where the base of the Tampen Slide deposits contact directly with the top of the MTH, area B. Rapid changes in thickness are observed within this area, from 60 ms (c. 46 m) to more than 140 ms (c. 107 m), closely controlled by the topography of the MTH. The Rectilinear fabric, spatially the least significant fabric, occurs in two limited areas, C1 and C2, both south of the MTH. No major thickness variations are observed within the areas. The Wispy fabric can be found immediately southeast of the MTH in area D1, and up slope in D2, where the deposits are thicker than 150 ms (c. 114 m).

The RMS amplitude maps from a sub-volume of 30 ms and 40 ms thickness at 25 ms 35 ms and 45 ms above the *TNS* reflector show that the distinctive fabrics at the top and base of the Tampen Slide deposits are the surface expressions of the internal structures, which penetrate throughout the deposits. For illustration, a detail of the RMS amplitude map of the 30 ms window centred 40 ms above the base of the Tampen Slide deposits, *TNS*, is presented on Figure 5.13. The internal structures can also be observed on the seismic lines featuring as discontinuities that go through the deposits, marked by strong amplitude variations at the base of the deposits and by


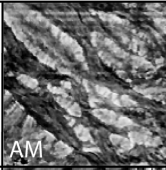
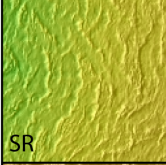
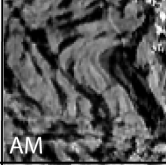
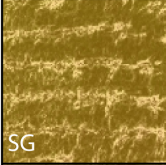
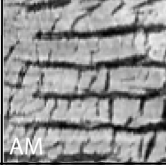
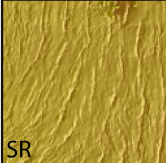
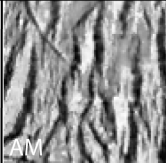
<i>Fabric at the top</i>		<i>Fabric at the base</i>	
	SG - slope map SR - shaded-relief map		AM - amplitude map
	Anastomosing Top: Lenticular blocks defined by relative steep edges surrounded by gaps, with gentler surface, which branch out and reconnect. Base: Lighter blocks delineated by darker stripes that reconnect after initial branching out.		
	Curvilinear Top: Arcuate terraces with relative steep edges changing to discontinuous sinuous ridges downslope. Base: Broken curvilinear lighter stripes separated by narrower dark stripes.		
	Rectilinear Top: Straight, discontinuous, parallel ridges with small, perpendicular, ramifications. Base: Rectilinear lighter blocks delimited by straight, parallel dark cracks and less pronounced perpendicular cracks.		
	Wispy Top: Bifurcated thin ridges that become diffused at the edge. Base: Thin, bifurcated, dark stripes that become thinner and weaker at the edge.		

Figure 5.11: Fabric classification used in this study to describe the patterns observed on the Tampen Slide deposits. Data are classed according to appearance on a combination of spatial analysis generated maps from the top of the Tampen Slide deposits (SR - detail of the shaded-relief map, SG - slope gradient map) and the amplitude map (AM) of the reflector TNS at the base of this deposits.

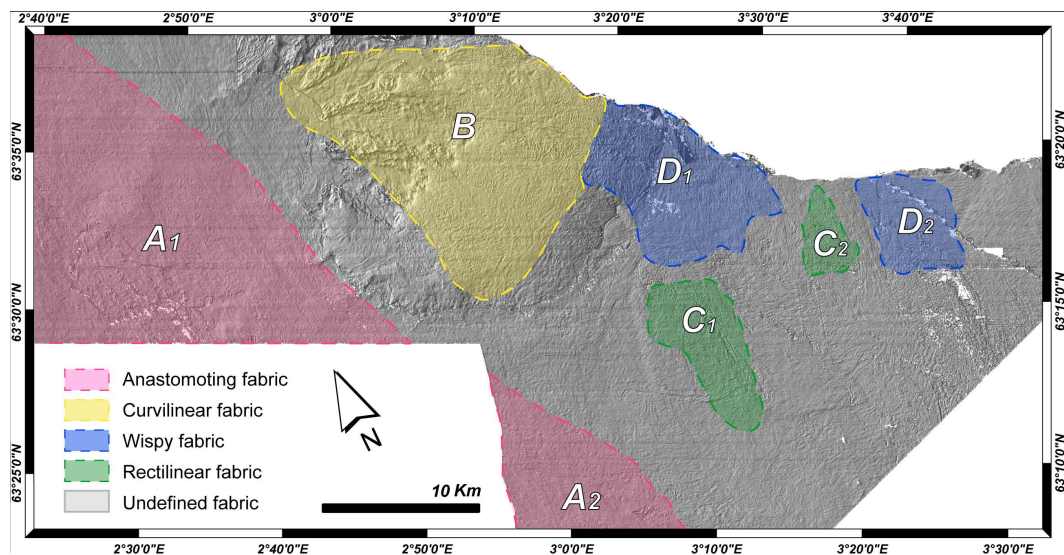


Figure 5.12: Distribution map of the types of fabric recognised on the Tampen Slide deposits overlying the shaded-relief map of the base of the Tampen Slide deposits (TNS reflector). It was identified seven fabric regions (A1, A2, B, C1, C2, D1 and D2) dominated by one of the four main types of fabric, surrounded by areas of complex or undefined fabric.

less-marked variations at the top. These discontinuities tend to be coincident with irregularities on the top of the Tampen Slide deposits (Fig. 5.13c).

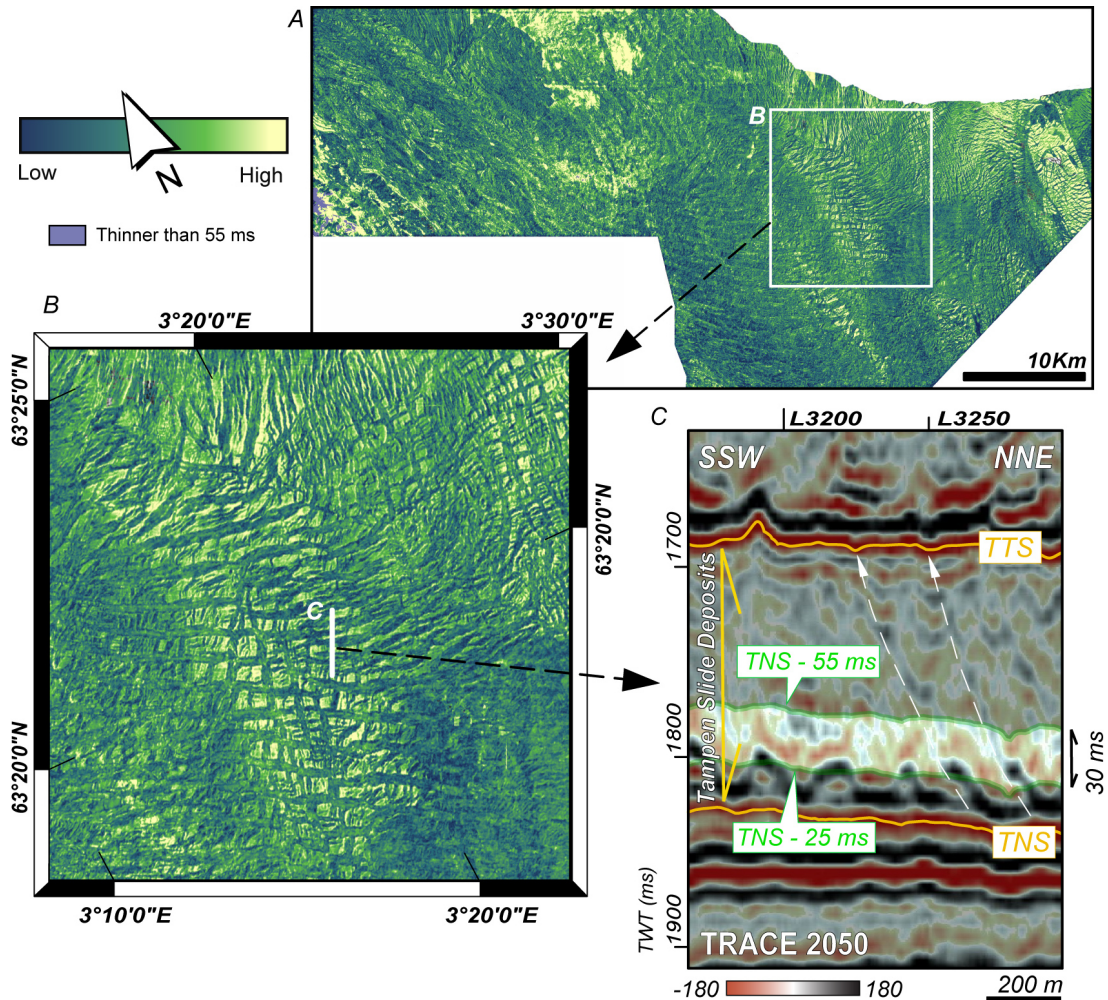


Figure 5.13: This display combines overall internal structure of the Tampen Slide deposits obtained by A) the RMS amplitude for a 30 ms window centred 40 ms above the Top of the Naust S - reflector (TNS) B) detailed view of the area C1 (see Fig. 5.12) and C) seismic section cutting through part of C1 area.

On Figure 5.14 where the *TNS-12ms* amplitude map, with a red-white-blue colour scale, is overlaid on top of the *TNS* slope map it is possible to relate the amplitude signal patterns changes to the slope changes at the sliding surface. Although the major changes on the patterns observed on the Tampen Slide seem to be controlled by the presence of the MTH, small slope variation appears to be also sufficient to induce a pattern into the slide deposits. For example, the area of rectilinear fabric named C1 (see Fig. 5.12) seems to be related to a minor slope variation due to the morphology of the glacial debris flow deposits on top of Unit III (Fig. 5.14d).

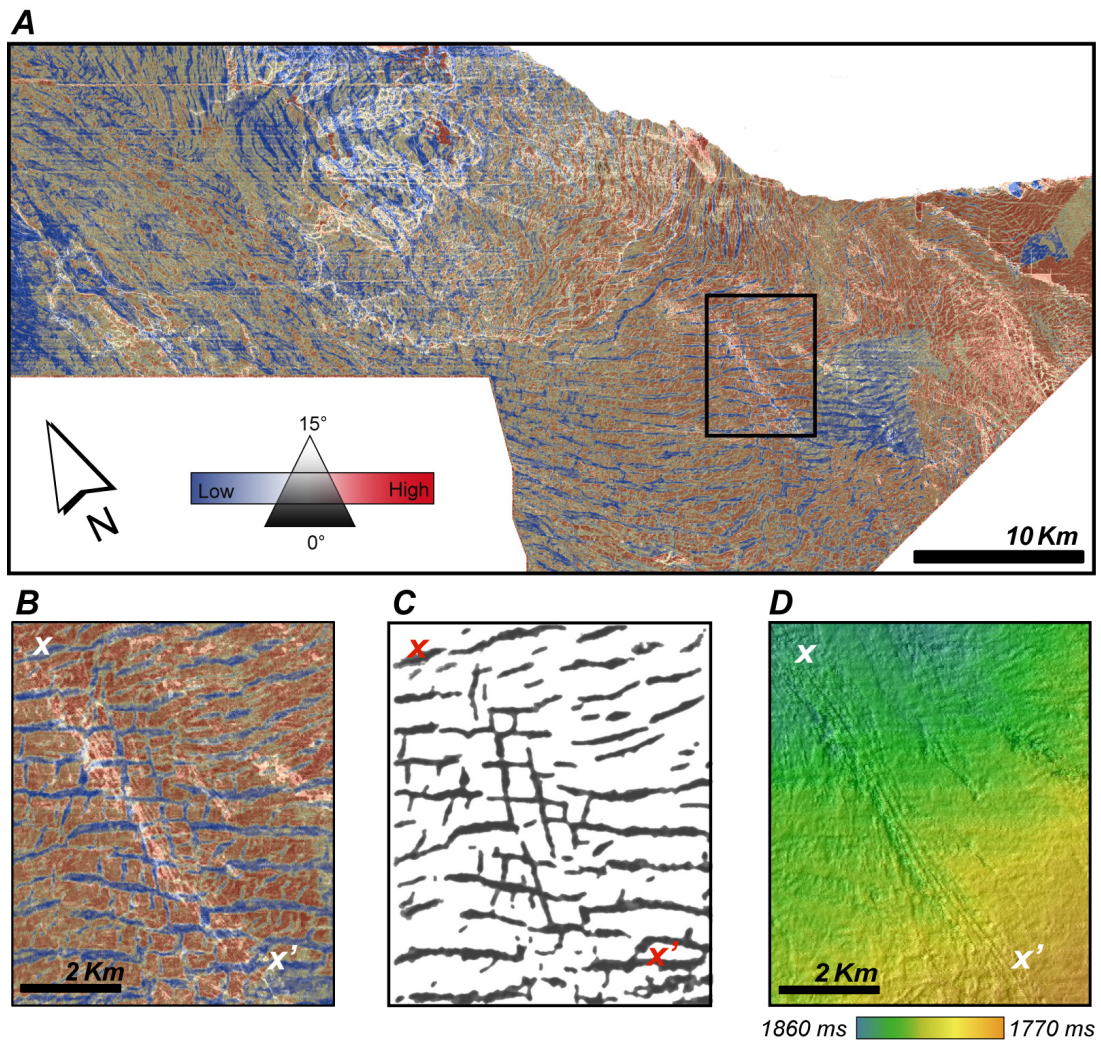


Figure 5.14: The display shows how the fabric at the base of the Tampen Slide deposits can be controlled by small variations in the topography of the sliding surface. a) Amplitude map of the TNS reflector, the base of this deposits, overlaid onto the TNS's slope gradient map. The black rectangle shows the location of b) detailed view of the above map, c) the acoustic fabric highlighted and d) detail of the shaded-relief map of the TNS reflector's DEM.

5.2.2 Interpretation

Although the surface between the Tampen Slide deposits and the underlying Unit III does not present recognisable erosion features, the base of the Tampen Slide deposits is thought to be an erosive surface developed during this mass movement event. The smooth surface of the top of Unit III, comprised mainly of GDF's deposits, acted where present as the sliding surface for the Tampen Slide. In the central part of the study area, the sliding surface of the Tampen Slide followed the top of MTH (Fig. 5.4 and 5.5). Probably due to the higher degree of consolidation and/or to the presence of interglacial deposits draped on top of the MTH, this topographic feature was not reshaped during the Tampen Slide event, preserving erosional features related to a previous episodes of slope instability (see subsection 5.3.2).

The spatial variations of thickness within the Tampen Slide deposits (Fig. 5.6) indicate that the relief of the MTH influenced the distribution and thickness of material remoulded during the Tampen Slide event in the study area. The increase in thickness of these deposits immediately south-east of the MTH and subsequent reduction above this topographic high is consistent with a mainly north-westward direction of transport. The thinning of these deposits westward of the MTH can be interpreted as the response of an efficient transport of remoulded material away from the influence of the flow obstacle that the MTH must have represented. Therefore, morphological changes on the Tampen's sliding surface may have also induced changes on the mass-flow behaviour, by diversion of the transport direction, and influencing the transport velocity.

The Tampen Slide deposits show several fabrics linked to the spatial configuration of penetrative acoustic discontinuities. These acoustic discontinuities create patterns of high- and low-amplitude (Fig. 5.8 and 5.13) that appear to be expressed in the morphology of the upper surface of the slide deposits (Fig. 5.9, 5.10 and 5.13c). Bull et al. (2009) examining the same 3D seismic data consider that these discontinuities correspond to the edges of disaggregated remnant blocks of material within the slide deposits and compare their seismic signature to the acoustic patterns identified by Huvenne et al. (2002) within the Porcupine/Magellan Slide deposits. However, that comparison may be questionable considering that the acoustic patterns found on the Tampen Slide are quite distinct from the ones shown by Huvenne et al. (2002). In the case of the Porcupine/Magellan Slide, the blocks do not present any apparent size, shape or orientation trend except on the toe area of the slide (Huvenne et al., 2002) whereas in our studied area the discontinuities define distinct organized fabrics showing evidence of continuity

and gradual transition between the different fabrics. Additionally, these two deposits occur in very different settings. The Porcupine/Magellan Slide stopped at an early stage of development (Huvenne et al., 2002) and can be classified as a frontally confined slide in the sense of Frey-Martinez et al. (2006) due to characteristics such as limited displacement, whereas in the case of Tampen Slide the acoustic patterns described are found in the slide's translational section with marked sediment removal (Nygård et al., 2005).

Although the source of these acoustic discontinuities is not certain, it is thought that they result from deformation structures developed during downslope translation of the remoulded material. Considering the scale and characteristics of these penetrative discontinuities, they result probably from fractures developed throughout the remoulded material. After the fragmentation of the remobilized material and during the last stages of transport, the development of a degree of coherency probably occurred with the deceleration of the flow motion and dewatering of the material. At that stage, some amount of displacement could have been accommodated in a brittle manner, generating fractures that would induce the acoustic discontinuities observed on the seismic data.

According to this model of fabric generation, the developing fabric responds to both changes in the material rheological properties and changes on the local stress regime. Since the fabrics observed on the top of the slide deposits mimic the fabrics observed at the base (Fig. 5.11), it is interpreted that the remoulded material presented the similar brittle behaviour and rheological properties, from top to bottom. That interpretation is reinforced by the fact that the discontinuities defining these fabrics propagate throughout the thickness of the slide deposits (Fig. 5.13). The change from one type of fabric to the other tends to be gradual and continuous, as if the *imprinting* of the fabric took place as an ongoing process where the fractures within the slow-moving material were adjusted and readjusted in response to the different stress regimes. Therefore, the Tampen Slide deposits should not have presented major changes of rheological properties, either laterally or vertically, and the major factor controlling the spatial configuration of the fractures seems to be the local stress regimes.

This proposed mechanism for the formation of the discontinuities within the Tampen Slide deposits can be compared to the development of crevasses in glacier, despite the rheological differences and without the lateral constraint from the valley glacier walls. In general, every crevasse undergoes modification by glacier flow, either due to flow differences between the centre and the margin of the glacier or changes on the stress regime resultant along the glacier flow,

and this makes possible to deduce the flow direction from the crevasse distribution (Nye, 1952). The study of crevasse also revealed that they respond effectively to changes on the underlying morphology (Paterson, 1994). Slope changes are known to have superficial expression, and induce the development of extensional flow and/or compressional flow (Fig. 5.15).

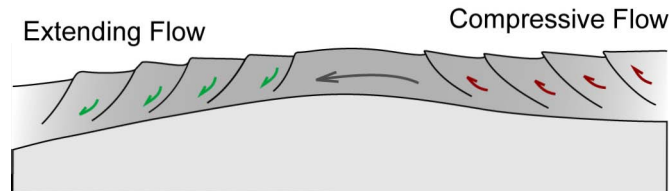


Figure 5.15: Model of compressive and extending flow in a glacier. Compressive flow takes place where the bed flattens, and extending flow takes place where the bed steepens. After Nye (1952).

Taking this comparison further and assuming that the fractures on the remoulded material were essentially controlled by local stress regime, the fabrics of the Tampen Slide deposits can be used as indicators of flow type and transport direction at the last stages of slide deposits motion. Therefore, the observation that the morphology of the sliding surface is controlling the fabrics distribution (Fig. 5.12 and 5.14) appears to validate the hypothesis that the morphology of the sliding surface induced changes on the transport direction and mass flow behaviour.

Figure 5.16 presents the relationship between the fabrics observed in the Tampen Slide deposits and the transport of remoulded material across the MTH. Knowing that MTH represented an obstacle to the transport direction of the remoulded material, the distribution of wispy fabric region D1 (Fig. 5.12) suggests the development of compression flow on the south-eastern edge of the MTH edge (see T1 and B1 on Fig. 5.16). Once the remoulded material overcame the MTH, arcuate terraces and sinuous ridges were developed suggesting a semi-cohesive extending flow resulting from motion acceleration (see T2 on Fig. 5.16). As the flow reached the erosive features, ridges and depressions, on the western edge of the MTH the discontinuities pattern were reshaped in response to the even morphology. The principle stress possibly laid almost parallel to the flow direction near the centre of the MTH depressions, rotating the discontinuities to right angles of the flow direction. However, the stress pattern and consequently the resulting fabric were probably also influenced by the drag of the material above the ridges of the MTH what developed a marked curvilinear fabric (see T3 and B3 on Fig. 5.16). Channelized by the erosive features on the sliding surface, the flow direction of the material above the MTH appears to have been shifted westwards, forcing this material to join the flow that followed around

the MTH. The thinner deposits and the anastomosing fabric observed on the regions A1 and A2 (Fig. 5.12) suggest a relatively fast flow of remoulded material around the MTH. Due to the difference on flow velocity, it is assumed that shear zones developed along the eastern margin of region A1 (see B4 on Fig. 5.16).

From all the information extracted from the seismic data and by inferring the mass-flow behaviours from the distinctive fabric patterns recognised on the Tampen Slide deposits, an interpretative map of the material transport during the last stages of remobilisation was compiled (Fig. 5.17). This map highlights changes of transport main directions and type of flow. The Tampen Slide's inferred transport direction changes throughout the study area, generally range from NNW to NNE but immediately downslope of the MTH, the flow seems to have diverted from NNW to W. The fastest mass flow material took place west of the MTH along the A1 region, whereas the slowest mass flow took place immediately downslope of the MTH. Compressive and extending flows developed in response to velocities changes across the MTH and shear zones developed near the MTH in response to differences on transport velocity between flows. The morphological changes on the Tampen's sliding surface, especially the presence of the MTH, played a major role in the deposits distribution, fabric development and mass flow behaviour (Fig. 5.17).

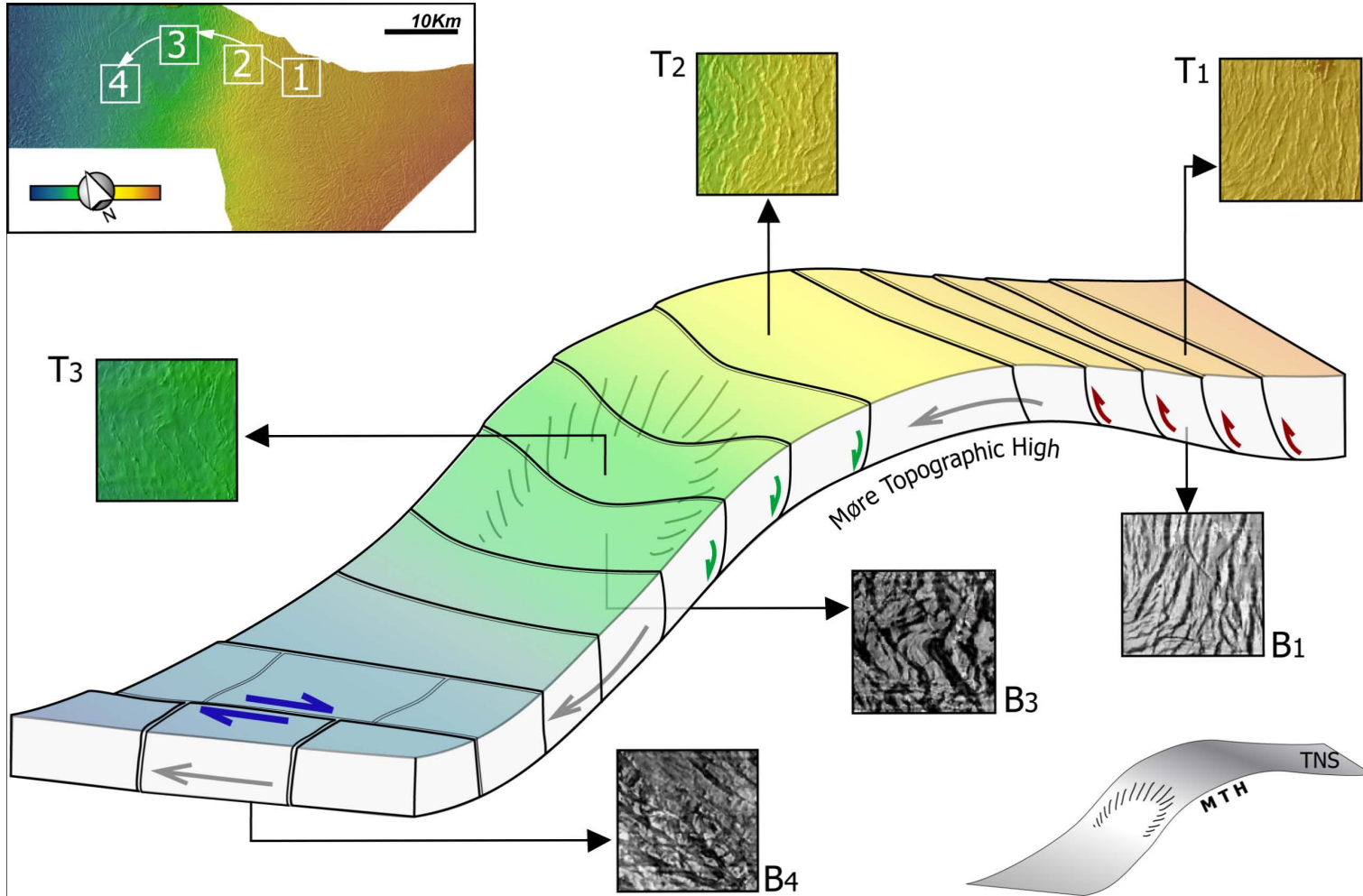


Figure 5.16: Graphic representation of the relation between the fabrics observed on the Tampen Slide deposits and the inferred mass flow behaviour across the MTH. Arrows show the direction of transport and relative movement within the flow. Note the curve trajectory of the remoulded material controlled by the morphology of the MTH. Both the representations of the TNS's morphology (on the lower right corner) and the remoulded material patterns are vertically over-exaggerated.

L6

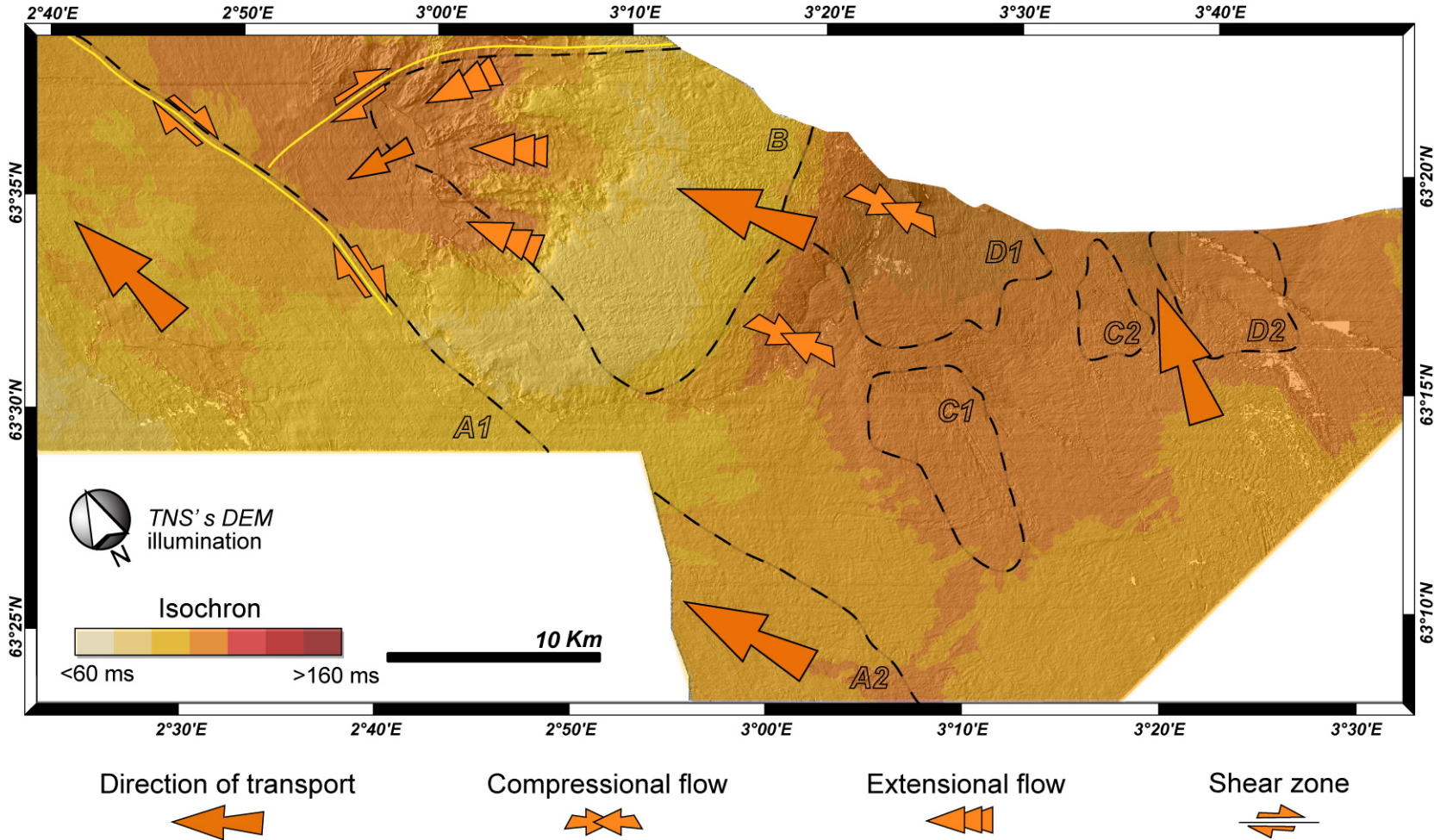


Figure 5.17: Interpretative map of the Tampen Slide deposits showing the main direction transport inferred from the recognised fabrics. The background of the map shows the thickness and main fabric distributions overlaying the TNSreflector's shaded-relief map. Note that the size of the arrows showing the direction reflects its relative velocity.

5.3 Møre slide

The Møre Slide deposits has long been identified on the NSF covering an area of over 15000 km² (Evans et al., 1996; King et al., 1996). This slide carried away a significant proportion of mid-Pleistocene deposits from the fan and left a distinct 160 km long and 50-90 ms height headwall (Solheim et al., 2005a). Although the sliding surface presents stepwise shifts near the headwall (Solheim et al., 2005a), this sliding event occurred along the same stratigraphic horizons across long distances (King et al., 1996). The slide scar was filled with up to 90 m of slide deposits and overlain by Naust S deposits (Solheim et al., 2005a) indicating a pre-TNS age, probably between MIS 10 - MIS 8 (Hjelstuen et al., 2005). According to the slide extension presented by Nygård et al. (2005), the study area is located near the eastern sidewall of the Møre Slide.

5.3.1 Description

The Møre Slide deposits observed in the study area are irregularly distributed and locally absent in the central region dominated by the Møre Topographic High (MTH). Where present, these deposits show marked thickness variations, sliding surfaces at different stratigraphic levels, different degrees of disintegration and distinctive seismic attributes (Fig. 5.18b). However, and regardless of the complex geometry of the Møre Slide deposits, the surface of the palaeo-seabed generated by the Møre Slide event is easily recognised. In this thesis, this surface is referred to as post-Møre surface (Fig. 5.18). It is marked by a distinguishable high-amplitude reflection event (Fig. 5.18b) related to the contact of the overlying seismic units with 1) the Møre Slide deposits, where present, or with 2) the Unit VI deposits, where the slide deposits are absent. Depending of the underlying material, this seismic reflection event corresponds to the *TMS* reflector or to the *TNU* reflector respectively. Similar to the *TTS* reflector, this strong reflection event may represent the contrast of the Møre Slide deposits or the glacial debris flow of MTH with (1) the material which settled out of suspension immediately after the slide, (2) hemipelagic sediments that settled later, (3) infilling contourites or perhaps (4) late-phase sliding generated in response to the radical new topography that had just been created.

In contrast to the easy identification and tracking of the post-Møre seabed surface, the interpretation of its amplitude map (Fig. 5.19) is rather challenging, especially due to the multiplicity of contacts between both underlying and overlying material (e.g. Unit IV overlying Møre Slide

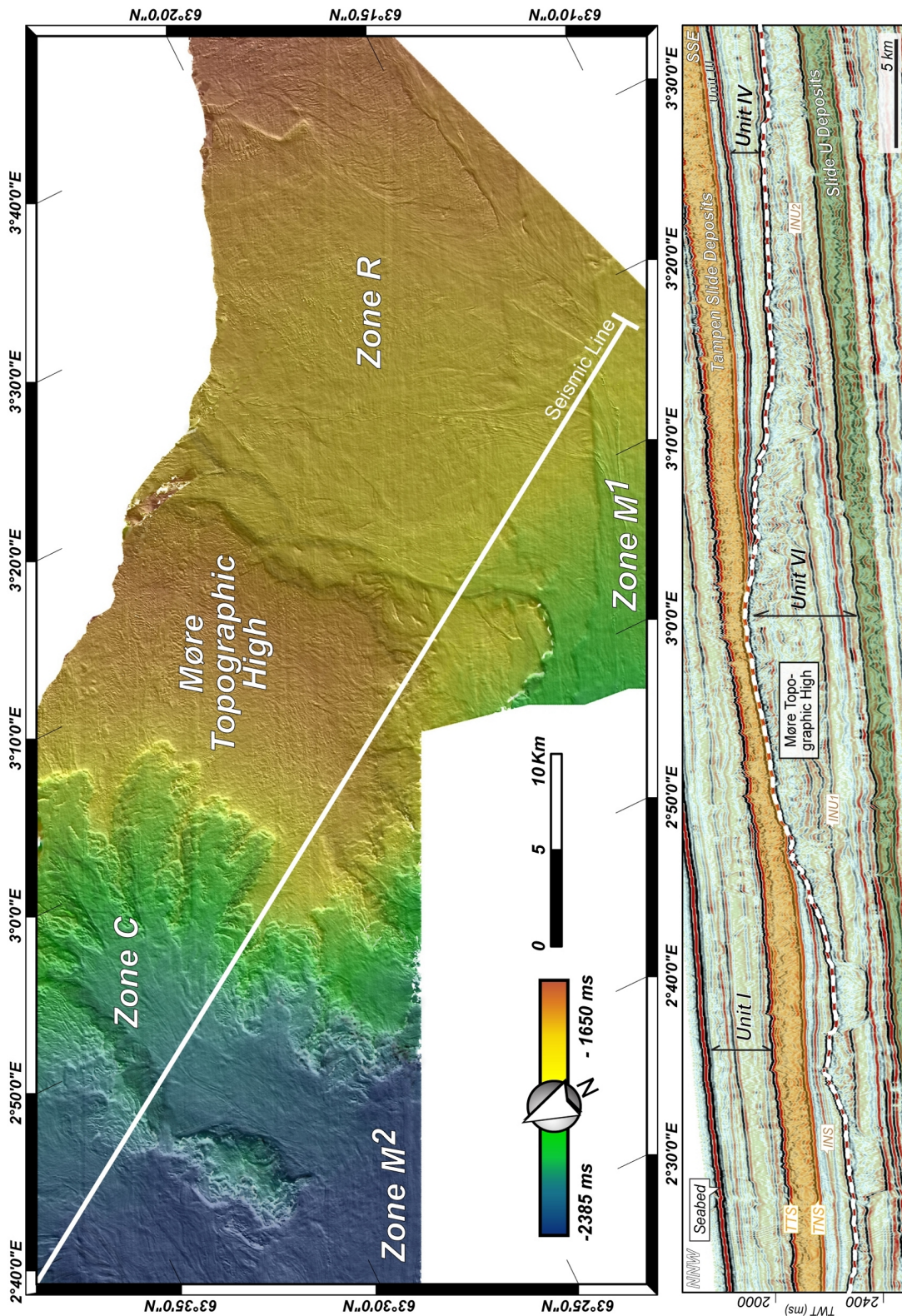


Figure 5.18: a) Shaded-relief map of the post-Møre surface DEM in ms (TWT), with artificial illumination from northwest at 45°. This surface was sub-divided in four main zones: MTH, Zone M (1 and 2), Zone C and Zone R, as described later in this sub-section. b) 2D seismic profile across the study area. The dashed white line marks the post-Møre surface.

deposits, Unit III overlying Unit VI and Tampen Slide deposits overlying Unit VI). For instance, on the south-eastern edge of the MTH the passage from underlying remoulded material to Unit VI deposits (see boundary **b** on Fig. 5.19) is less marked than the passage from overlying Unit III deposits to Tampen Slide deposits (see boundary **a** on Fig. 5.19), whereas on the north-western edge of the MTH it is the change of underlying material that stands out on the seismic amplitude map (Fig. 5.19). In fact, the bright "trace" that delineates the contact between the Tampen Slide deposits and the Unit VI deposits on the south-eastern edge of the MTH (Fig. 5.19) can be partially considered as a seismic artefact. This bright "trace" is likely to result from destructive interference between the *TNU* and *TNS* reflectors close to their actual junction. As for the bright trace on the north-western edge of the MTH (Fig. 5.19 a), it delineates the passage from thinner to thicker slide deposits rather than the actual passage from Unit III to Møre Slide deposits (Fig. 5.19 b).

The RMS maps from beneath the post-Møre Slide palaeo-seabed surface avoid the complexity on multiple overlying deposits. Nevertheless when interpreting these maps it is necessary to be conscious that depending of the size of the time window considered, it is possible to have the superposition of information related to distinct deposits. For example, in some RMS amplitude maps of windows centred beneath the post-Møre surface the area north of the upper part of MTH presents a bright seismic signature (high amplitude) characteristic of the MTH deposits (Fig. 5.20). However pathways defined by the superficial material above the MTH are also observed (Fig. 5.20).

Based on topographical criteria, seismic attributes and seismic character, the Møre Slide deposits were sub-divided into three zones (Fig. 5.18). These geomorphological zones reflect distinct settings of erosional and depositional processes associated to the Møre Slide event. The names given to these zones are related to their main characteristic:

Zone M : Corresponds to the area of the main Møre Slide deposits and it is sub-divided into M¹ and M² situated respectively south-westwards and westwards of the MTH. This division is probably artificial, resulting from the spatial coverage of the 3D seismic survey.

Zone C (or collapse zone) : Corresponds to the area dominated by the slide scar of a retrogressive sliding event on the north-western edge of the MTH.

Zone R : Situated south-eastward the MTH, corresponds to the area covered by deposits of a major retrogressive sliding event associated with the Møre Slide event.

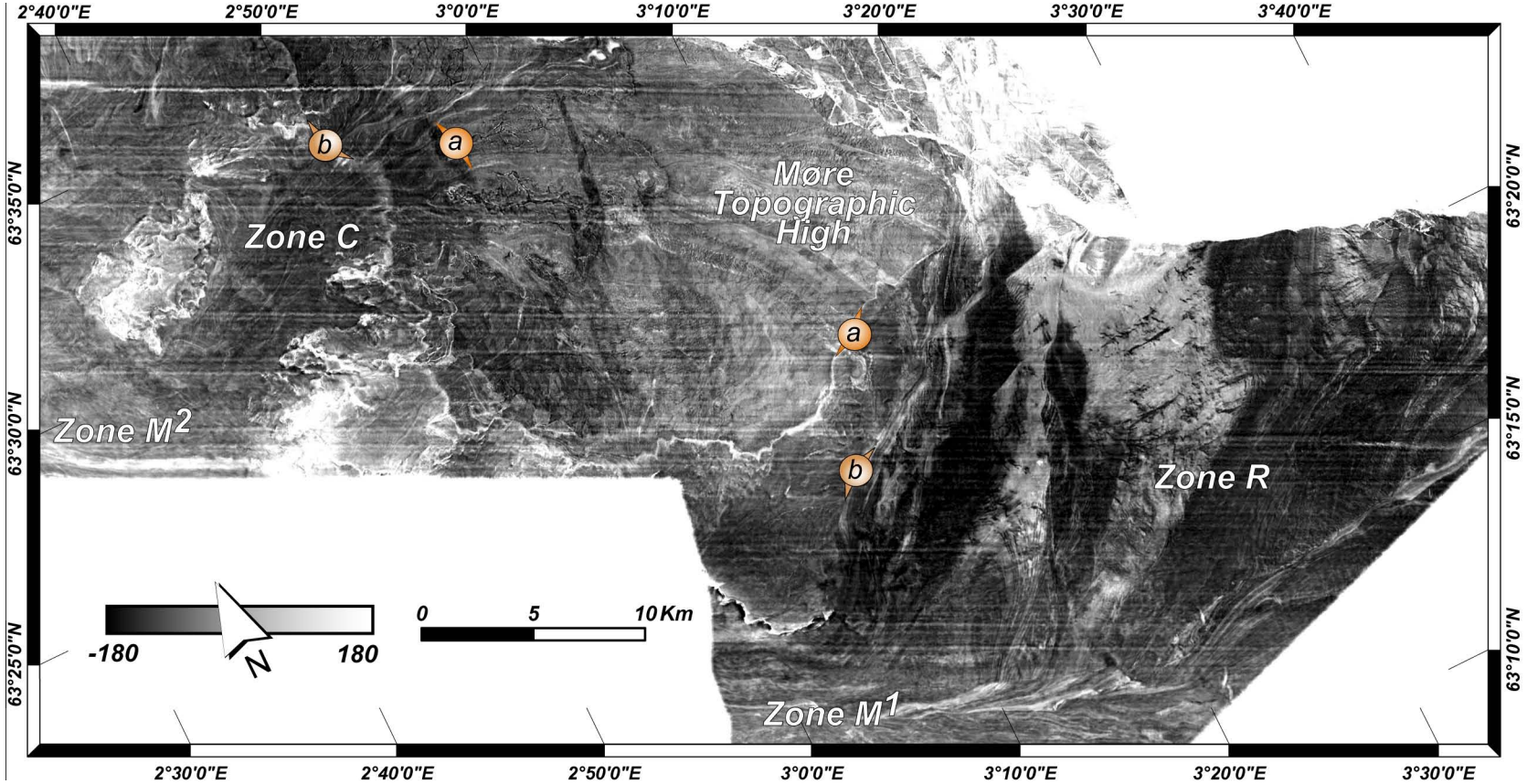


Figure 5.19: Amplitude map of the post-Møre slide surface. *a* - intersection between the upper part of the MTH and the base of the Tampen Slide deposits. *b* - intersection between the MTH and underlying Møre Slide deposits. Note that on the south-eastern edge of the MTH trace *a* is more visible than trace *b* and that in contrast on the north-western edge trace *a* is less marked than trace *b*.

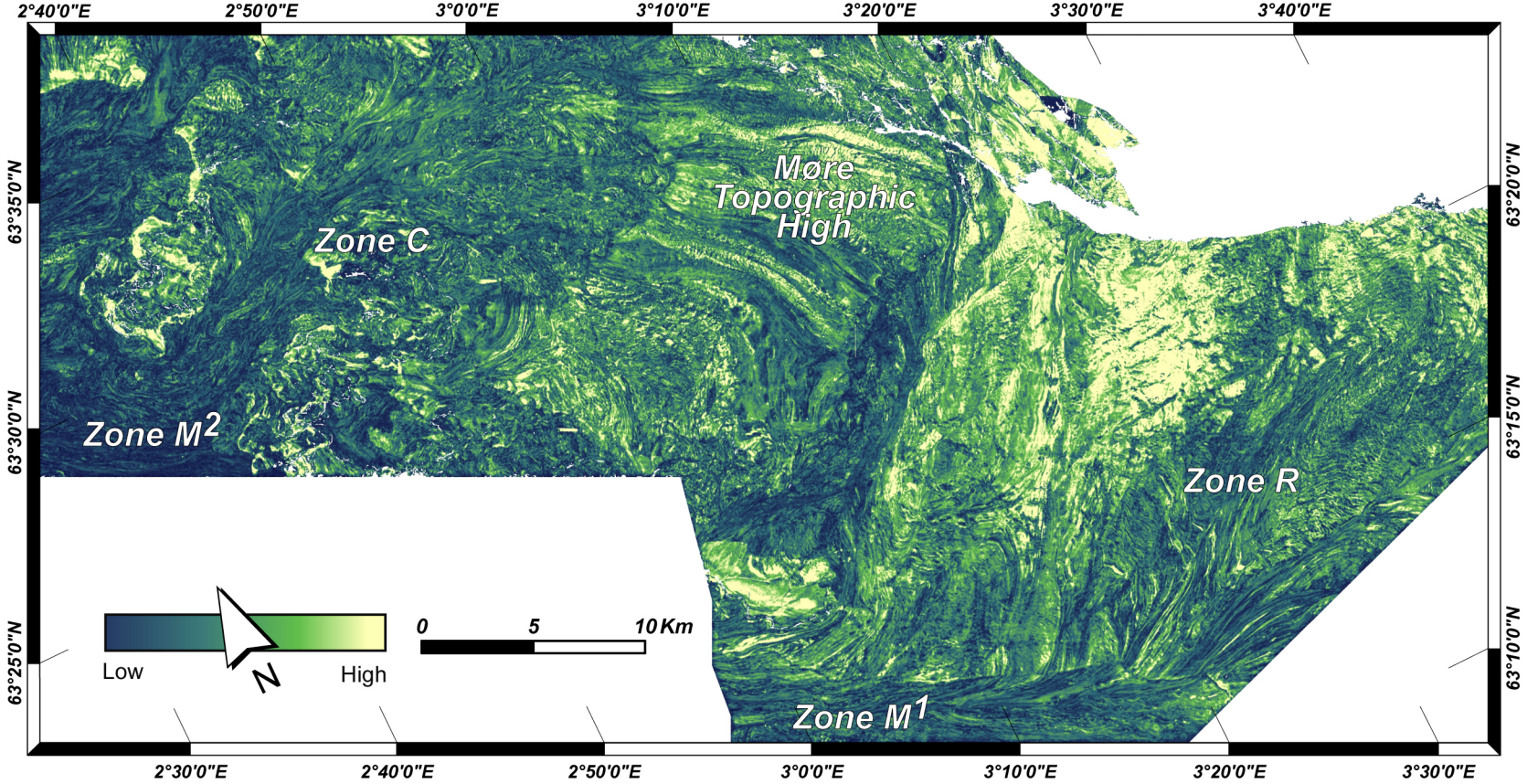


Figure 5.20: RMS amplitude map for the 20 ms window centred 30 ms below the post-Møre surface. This map shows the flow patterns on the remoulded material.

The slide scar that characterises Zone C is the most striking morphological feature of the post-Møre surface within the study area. This cauliflower-shaped depression displays a wide, roughly semi-circular, uppermost scar area 15 km wide westwards from a narrower corridor of ~4 km wide bounded by relatively steep flanks (Figs. 5.18 and 5.21). An area of 285 km² extending approximately from 63°27' to 63°36'N and from 2°46' to 3°07'E was affected by this slide event. However the total area affected by this slide must exceed that measured on the study area since the 3D seismic data does not cover entirely this morphological feature. By extrapolating this feature geometry beyond the study area, it is believed that it could reach up to 310 km². Over 15 km the post-Møre surface shows a vertical drop of c. 275 m, from 1900 ms at the MTH to 2250 ms at the internal depositional area.

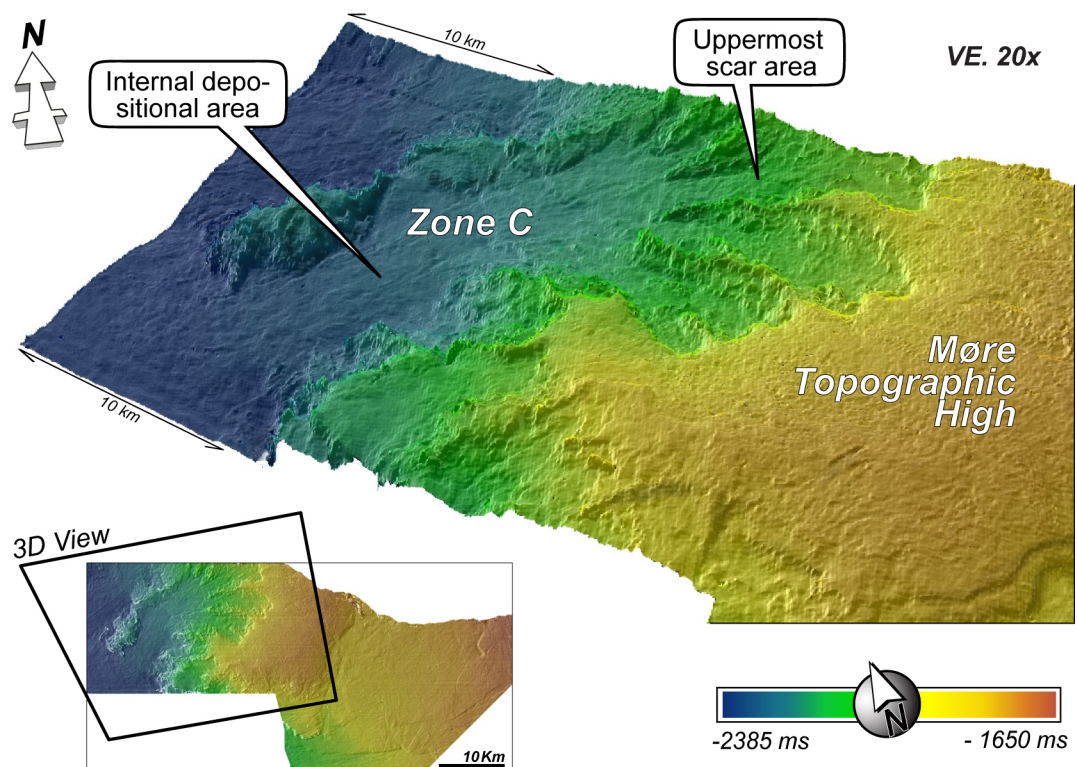


Figure 5.21: 3D view of the Post-Møre surface looking north-northeast. This view provides a good perspective towards the side scar that characterise Zone C. Note the relative smooth surface of the depositional areas (in blue) in contrast with the irregular relief of shallower areas. The vertical scale is approximately 20x exaggerated and horizontal scale varies with distance in the perspective.

The uppermost scar surrounds most of the slide scar and consists of numerous headwalls of ~10 m high and secondary scarps. Radial ridges are abundant within the headwall area separating it into several lobes and presenting geometric similarity at different scales (i.e. contains

scaled copies of itself). Due to its complex geometry the headwall area presents a rough surface marked by breaks and changes of slope, from gradients as low as 0.1° to up to 22° . In this area of the slide scar it is impossible to define with precision the thickness of the remoulded deposits. This probably results from the combination of two aspects: 1) the thickness of the deposits may be thinner than the maximum vertical resolution of the seismic data, as only a relatively thin layer of remoulded sediments should be left on that area of the slide scar, and 2) the contrast between the remoulded material and the underlying material may not be acoustically significant. In fact, the underlying material down to *INU1* reflector tends to appear partially disturbed, showing a seismic character similar to the one observed on the internal depositional area, but with sporadic and scattered acoustical reflections (Fig. 5.22).

In contrast to the uppermost scar area, the internal depositional area, comprising about 30% of the total area affected by this slide, presents a smoother surface with slope gradients of less than $\sim 1.5^\circ$. On seismic profiles these deposits display semi-transparent seismic acoustic facies without strong internal reflectors or structures, and can reach up to 150 ms (c. 118 m) in thickness (Fig. 5.22). The internal depositional area is marked by an offset in the sliding surface defined by a step of approximately 80 ms (c. 63 m) to the *INU2* stratigraphic level (see boundary **2** on Fig. 5.22b). Although most of the sliding surface within the depositional area sits at the same stratigraphic level as the *INU2* reflector, near the mouth of the slide scar the sliding surface jumps to a deeper stratigraphic level and the remoulded material directly overlies the Slide U deposits (see boundary **3** on Fig. 5.22b).

The RMS imagery (Fig. 5.22a) shows lineations thought to represent the sediment pathways, where remoulded material flowed towards Zone M². The geometry of the sediment pathways closer to the headwall is similar in form to stream catchments in mountainous regions with multiple tributaries. Based on the lineations observed, a main WSW flow direction within the slide scar area can be derived, which is consistent with the general geometry of the slide scar. Although deflected at the mouth of the slide scar, the flow lineations can be followed beyond the slide scar area into Zone M². The orientation of the lineations in Zone M² show a NW flow direction which suggest the incorporation of the material within the Møre main slide. Therefore the total run-out distance of this slide cannot be determined.

The slide scar described above is the main geomorphologic feature of Zone C but other features are present (Fig. 5.18). On the northern edge of the 3D seismic data, an internal depositional area of similar characteristic and scale can be recognised (Fig. 5.23). The source area of the

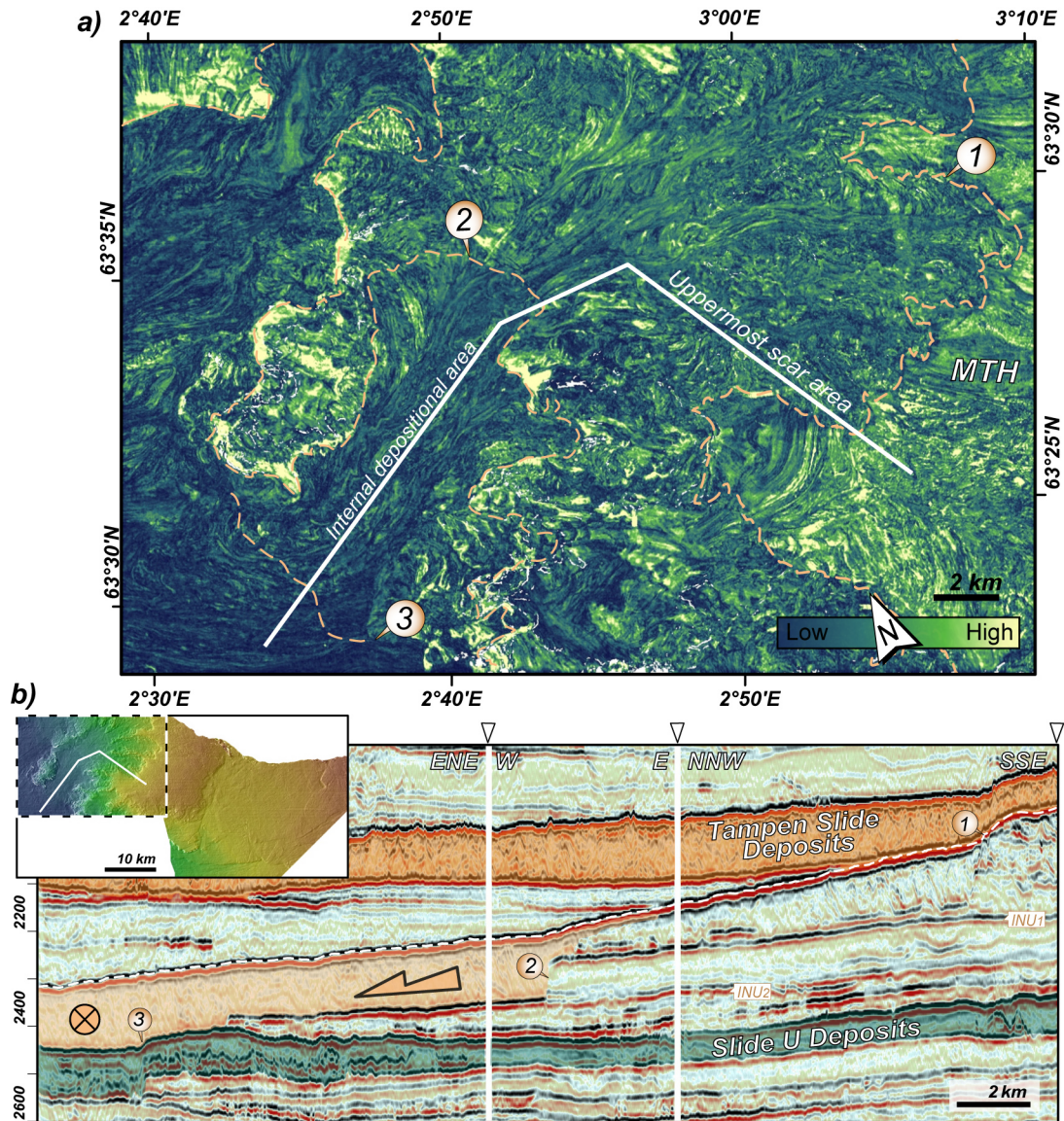


Figure 5.22: a) Detail of the RMS amplitude map (see Fig. 5.20) showing Zone C area. Brown dashed lines map the main boundaries that characterise slide depression: (1) headscarp upper limit, (2) upper limit of the internal depositional area and (3) boundary between the internal depositional area and Zone M². b) Seismic profile across slide scarp cutting through the southern part of the headwall, the internal depositional area and Zone M². Location marked by white line on the above RMS amplitude map and location map. Arrows show the interpreted transport direction.

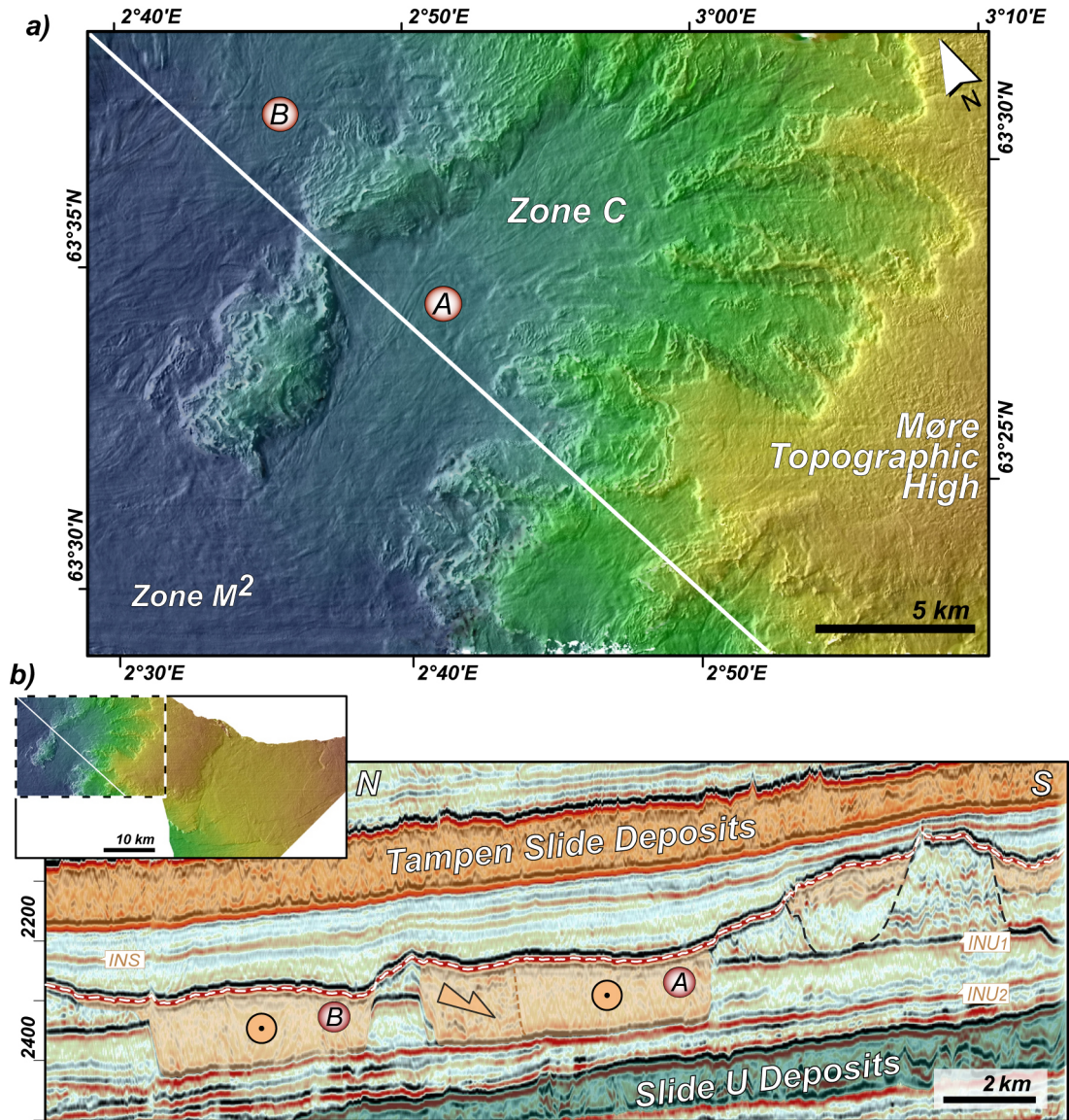


Figure 5.23: a) Detail of the shaded-relief map (see Fig. 5.18) focused on Zone C area, showing both internal depositional areas (A and B) and the main slide scar headwall area. Note the smooth surface of the depositional area A contrasting with its headwall area. b) Seismic profile across the two internal depositional areas and location map. Note the segment of undisturbed material between the depositional areas. Arrows show the interpreted transport direction and dashed white line the post-Møre surface.

remoulded material was probably situated NE of this depositional area and is not shown on the present data set. The two depositional areas of Zone C are separated by a promontory of undisturbed material (Figs. 5.23 and 5.24 c). This 15 km long promontory varies in width, from 1 km to 4 km wide (Fig. 5.24 c). On its narrowest central section the promontory is also less prominent, being c. 70 m lower than the internal and external edges (Fig. 5.21) and being partially buried by material released from it.

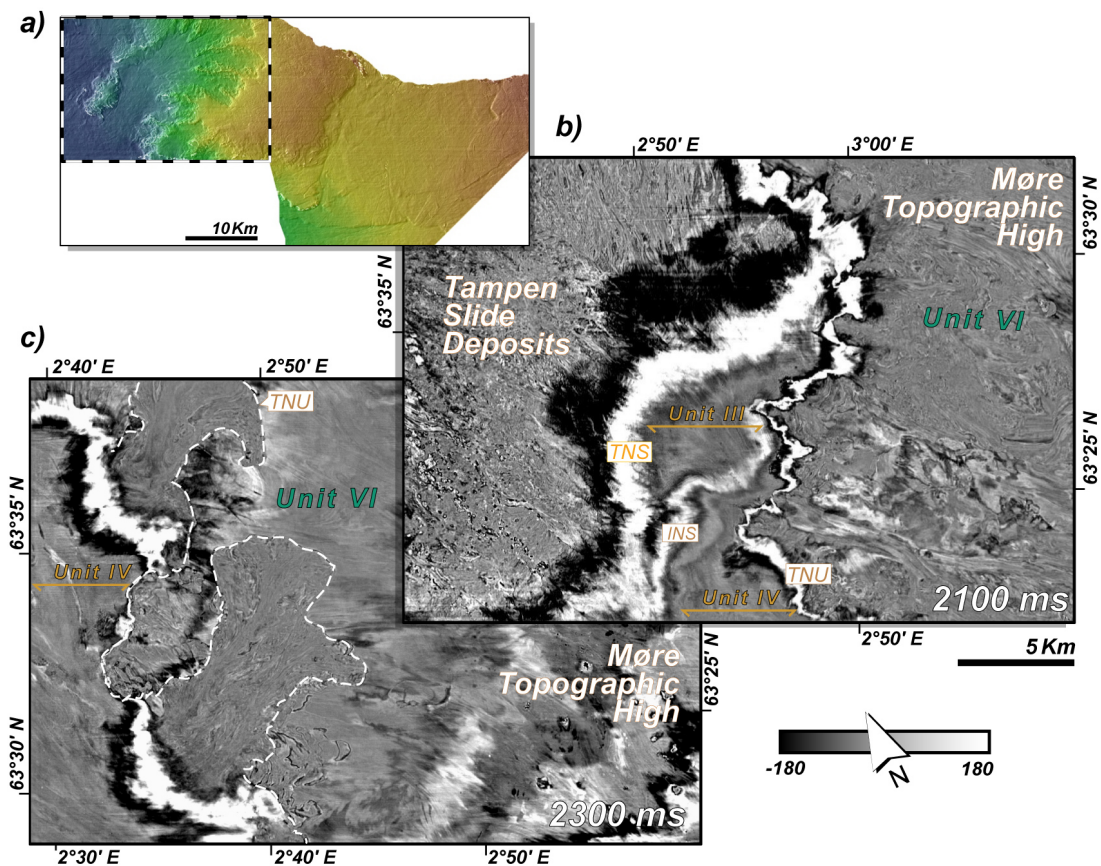


Figure 5.24: a) Location map of b) and c). b) Time-slice at 2100 ms TWT showing the contact of Unit VI with: Tampen Slide deposits (upper part), Unit III (central part) and Unit IV (bottom part). c) Time-slice at 2300 ms TWT showing the deeper area remoulded within the slide scars A and B (marked by white dash line). Note the promontory of undisturbed material that separates the two internal depositional area.

The Zone R of the Post-Møre surface is characterised by a smooth topography gently dipping westwards that corresponds to the top of the remoulded material (*TMS* reflector). The thickness of these deposits varies from no more than 50 ms (c. 39 m) up to 250 ms (c. 196 m). The total area occupied by these deposits extends beyond the 3D seismic data to east-northeast. However, even with a broader data set it would be rather difficult, if not impossible, to define the total area of these deposits as a significant part of it was severely disrupted by the Storegga

main deep failure. Within the study area, the north-western limit of Zone R is set by the MTH and the south-western limit is defined by its boundary with Zone M¹.

Compared to the irregular boundary between MTH and Zone C, the boundary between MTH and Zone R is rather sharp. This probably results from the fact that the sediment movement occurred mainly parallel to this boundary. Nevertheless, several morphologic features are displayed along this sidewall: **1**) a single regular slope in the easternmost segment, relatively steep with evidence of minor slope instability on its upper part (Fig. 5.25b), **2**) a slope sheltered by a block of the undisturbed material (Fig. 5.25c) and **3**) a complex slope in the westernmost segment (Fig. 5.25d), where the sidewall height decreases and it is intersected by Zone M¹. Locally the sidewall is partially buried by material released from the MTH.

On the eastern edge of Zone R a buried block (1.8 km wide and 2.5 km long) is observed and it can be considered as an "island" of undisturbed sediments. Although it lies within the remoulded material this block kept its primary stratification and is over c. 78 m high (Fig. 5.26d). Its abrupt edges show a clear contrast between the undisturbed material and the surrounding chaotic matrix, both on time-slices (Fig. 5.26b) and seismic profiles (Fig. 5.26d). A thickening of the deposits immediately ENE the block is observed, whereas immediately WSW marked thinning is observed (Fig. 5.26c). On acoustic map views, i.e. time-slice and amplitude maps, it is possible to recognise a set of WSW-trending flow lineations that propagate from the undisturbed block (Fig. 5.26b). These semi-parallel lineations extend for more than 18 km without crosscutting each other. It is also possible, especially on the upper part of these deposits, to recognise a group of distinct curved lineations developed from the block's north-western edge (Fig. 5.26c).

The south-western edge on the Zone R, defined by its boundary with Zone M¹, is marked by changes of deposit thickness, sliding surface and direction of transport (Fig. 5.27). There is a general and marked reduction of the Zone R deposits thickness close to this boundary. The Zone R deposits tend to be only 50 ms (c. 39 m) thick on its south-western edge, when just 10 km north-eastward within Zone R the typical thickness values are 100 ms (c. 78 m), if not 150 ms (c. 117 m) or greater. In spite of the marked changes in thickness, it is the sliding surface's stratigraphic step that defines the boundary between zones R and M¹. The sliding surface can drop abruptly by 120 ms (c. 94 m) from Zone R to Zone M¹ (Fig. 5.27c). Another characteristic aspect of the boundary is the deflection of the flow lineations. The directions of transport, inferred from the flow lineations, range from SW to W in Zone R, whereas in Zone

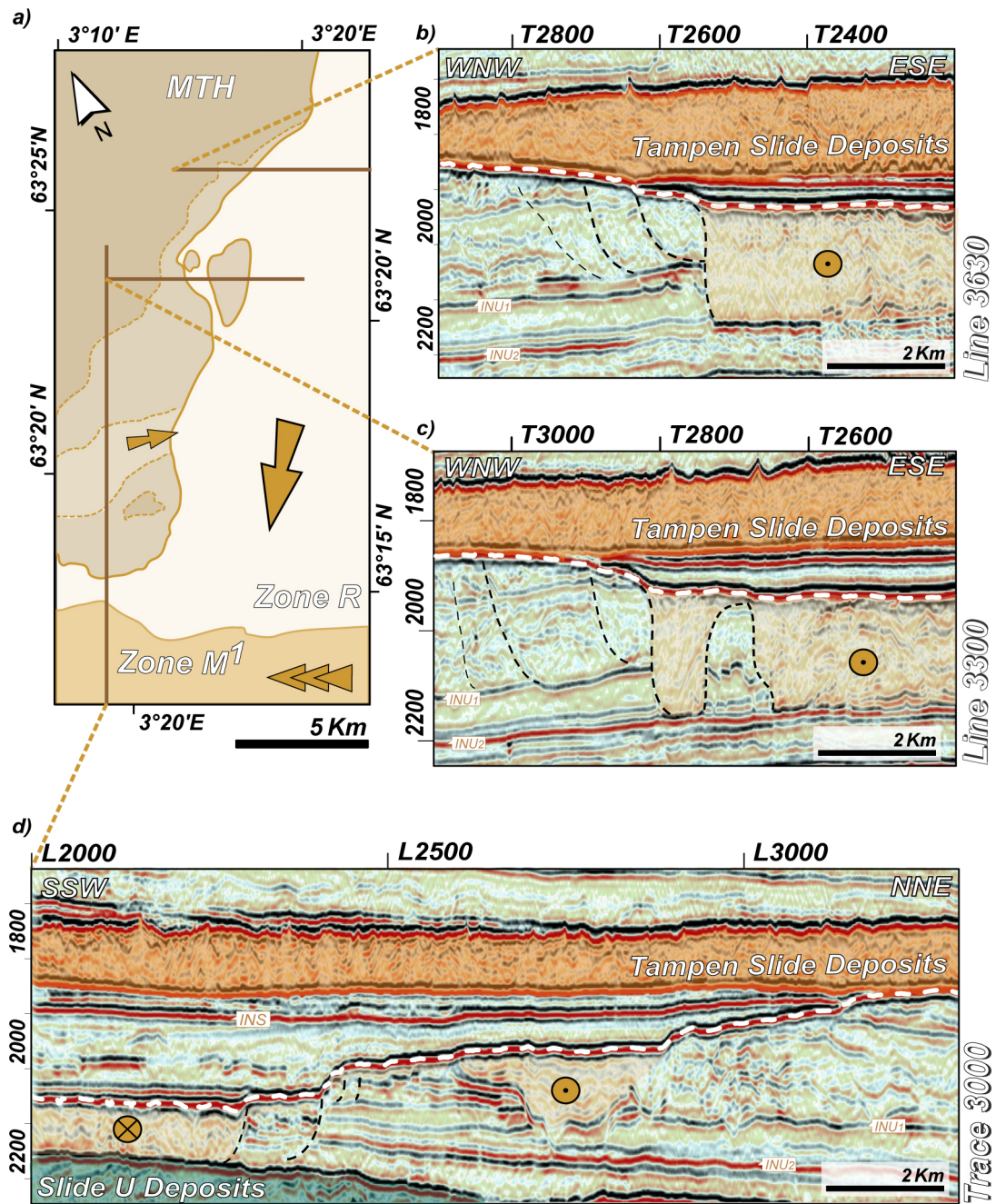


Figure 5.25: Schematic representation of the south-eastern edge of the MTH (a) and segments of seismic profiles across it (b, c and d). b) Seismic profile across the upper part of the boundary between MTH and Zone R. It shows a steep slope marked by evidence of instability. c) Seismic profile across the central part of the MTH-Zone R boundary, it shows a steep slope preceded by a block of the undisturbed material. d) SSW-NNE seismic profile across the westernmost part of MTH edge. It shows a complex slope marked by gradual thinning of the MTH and by major evidence of instability. Vertical exaggeration of 12x. Arrows show the interpreted transport direction.

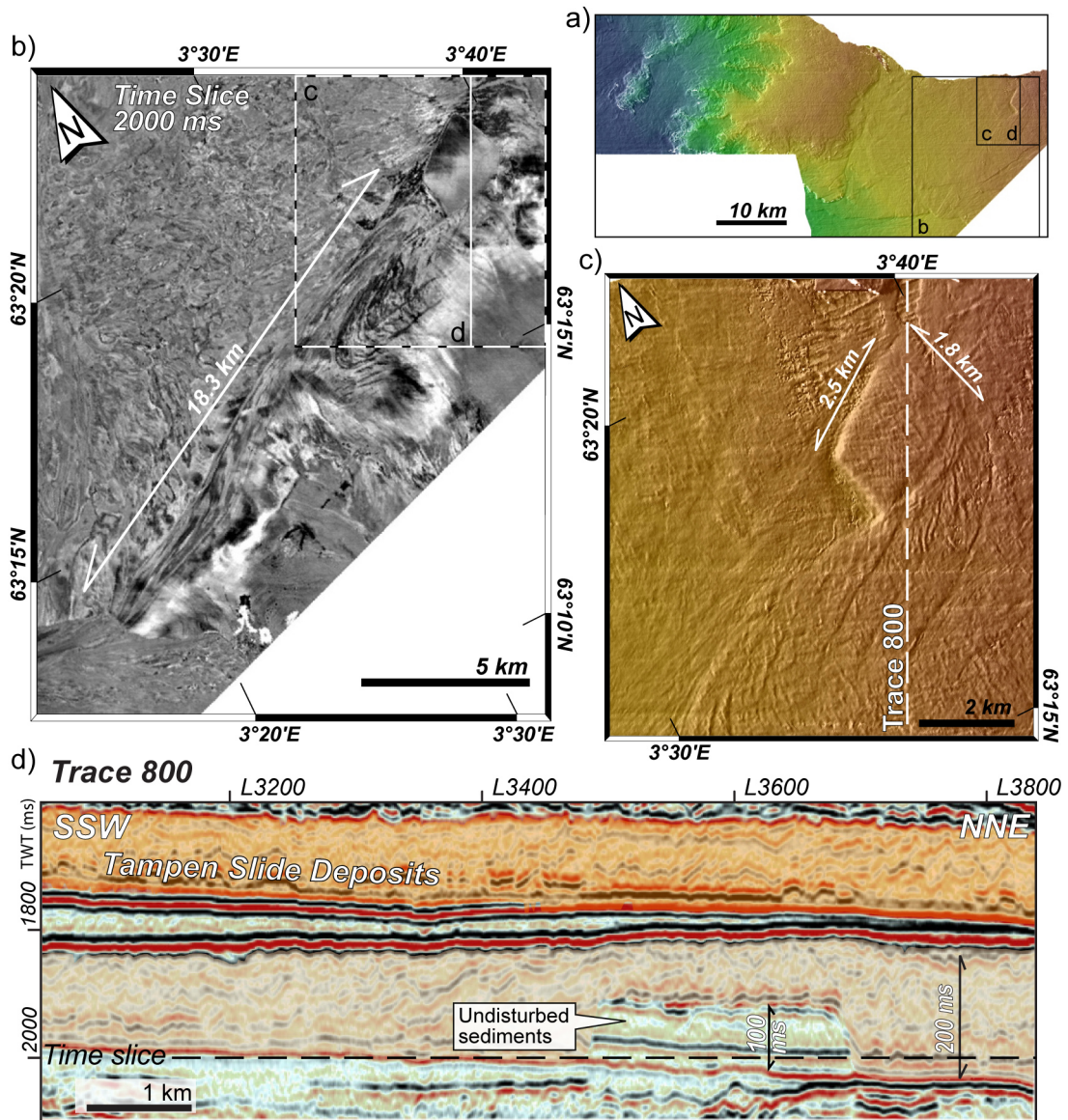


Figure 5.26: Block of undisturbed material within Zone R. a) Location map. b) Detail of the 2000 ms TWT time-slice showing the block of undisturbed material on the upper-right corner of the image. From this block and through for more than 18 km there are recognisable WSW-trending flow lineations. c) Detail of the shaded-relief image (see Fig. 5.18) showing the top of the remoulded material that buried the block of undisturbed material. The topography of the post-Møre surface reveals the location and contours of the underlying 1.8 km wide and 2.5 km long block. d) Segment of the seismic trace 800 cutting through the block of undisturbed material. Note the block height (100 ms) and thickness of the surrounding deposits (200 ms) were measured on this seismic profile.

M¹ the flow lineations show a mainly NW direction of transport (Fig. 5.27b).

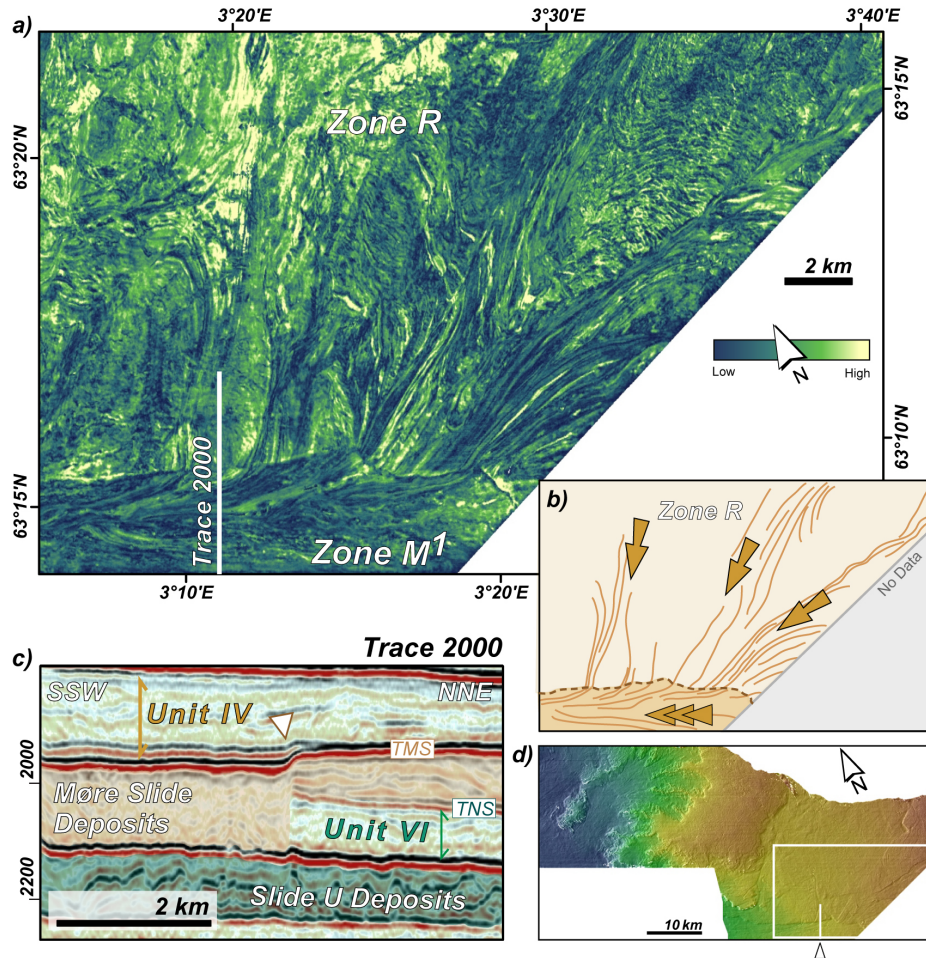


Figure 5.27: a) Detail of the RMS amplitude map (see Fig. 5.20) through part of Zone R - Zone M¹ boundary, showing mass movement flow lineations. b) Schematic representation of the main flow lineations observed on the RMS amplitude map (a) and the direction of transport inferred from these lineations. Note how the flow lineations are deflected on the boundary between Zone R and Zone M¹ (brown dashed line). c) Segment of seismic trace 2000 centred on the boundary between Zone R and Zone M¹, where a stratigraphic step in the sliding surface is observed. d) Location map.

5.3.2 Interpretation

Sliding surfaces can step between various stratigraphic levels even if they were developed during a single slide event (e.g. Frey-Martinez et al., 2005; Solheim et al., 2005a). However, the complex geometry of the Møre deposits in the study area suggests that the main stratigraphic steps observed at the base of the Møre Slide deposits result from multi-stage collapse. Evidence like different transport directions and diverse sliding styles suggest that stratigraphic steps mark the boundary between the main Møre Slide and areas affected by retrogressive sliding.

Along its eastern sidewall the Møre Slide remoulded and carried away a major proportion of the Naust U deposits, thus opening up free space within the slide scar and decreasing the lateral confining pressure on the sidewall, destabilising the adjacent material and triggering retrogressive failure in some sections of the sidewall. As a result, the principal tension direction of the retrogressive failure would be perpendicular to the sidewall and consequently not collinear to the Møre Slide's direction of transport along the sidewall. Although there are marked differences between the Zone R and Zone C, both zones are believed to correspond to the retrogressive failures initiated at the sidewall. These retrogressive instability events occur probably simultaneously with the Møre Slide, since the flow lineations observed in zones R and C can be followed beyond their slide scar areas into the Zone M¹ and M² respectively (Figs. 5.22 and 5.27). This suggests that the material from this two zones was fully incorporated within the main Møre Slide.

The main slide scar in Zone C shows an apparent fractal distribution of the mass movement that has produced the cauliflower-shaped geometry (Figs. 5.21 and 5.23). The distribution of the sediment pathways shown on Figure 5.28, which was inferred from the post-Møre surface amplitude map and RMS amplitude map (Figs. 5.19 and 5.22), suggests that the uppermost headwall of Zone C slide scar was formed by a succession of debris-flows. This interpretation is corroborated with comparison between its morphology and the headwall morphologies presented by Micallef et al. (2008). In this study Micallef et al. (2008) evaluate the use of the headwalls shape as morphological proxies for the identification of submarine mass movements. These authors show that the shape of the composite headwalls is dependent on the mass movement processes and that headwalls formed by debris-flows present a higher curvature comparatively to that formed by spread, since plastic deformation is required to evacuate a curvilinear headwall.

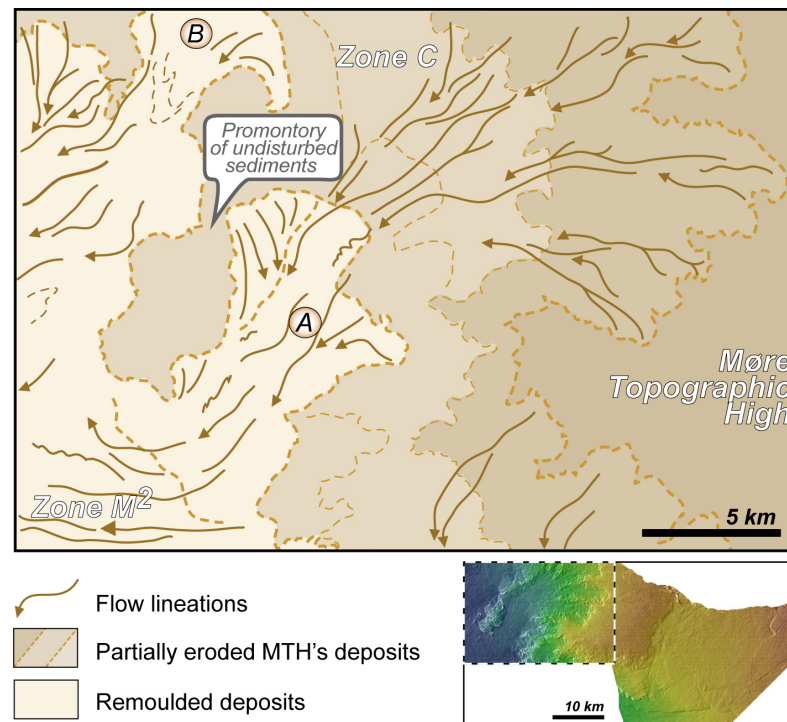


Figure 5.28: Interpretative map of the Zone C, showing the distribution of sediment pathways inferred from the post-Møre surface amplitude maps (see Figs. 5.19 and 5.22). Note the abrupt change of the transport direction between the internal depositional area A and the Zone M² and the similarities in form between the pathways distribution within the uppermost scar area and mountain tributaries.

Therefore, the development of the main slide scar in Zone C did not occur across the entire affected area simultaneously, but started as one or a few mass movements located close to the sidewall of the main Møre Slide, not necessarily as a debris-flow at that stage (Fig. 5.29 II). This failure destabilised the surrounding areas and the instability propagated upslope through the progressive collapse of the headwall. As the slope failure propagated upslope, each collapse triggered an increasing number of smaller mass movements that gradually presented failure surfaces at shallower stratigraphic levels (Fig. 5.29 III) preserving more of the Unit VI and shaping the northern edge of the MTH (Fig. 5.29 IV). The lack of a defined reflector on the uppermost scar area marking the base of the remoulded material is consistent with debris-flow development. This mass movement process tends to present a 1) high rate of material removal, leaving thin deposits at the scar area, and 2) gradual fragmentation of the remoulded material, with the remoulded material close to the head scar still having properties similar to the underlying material. Additionally, the deposits formed by successive debris-flows may present a multiplicity of sliding surfaces, as the top of the initial collapse deposits could have been used as a sliding surface and was buried by the material remoulded by subsequent collapses.

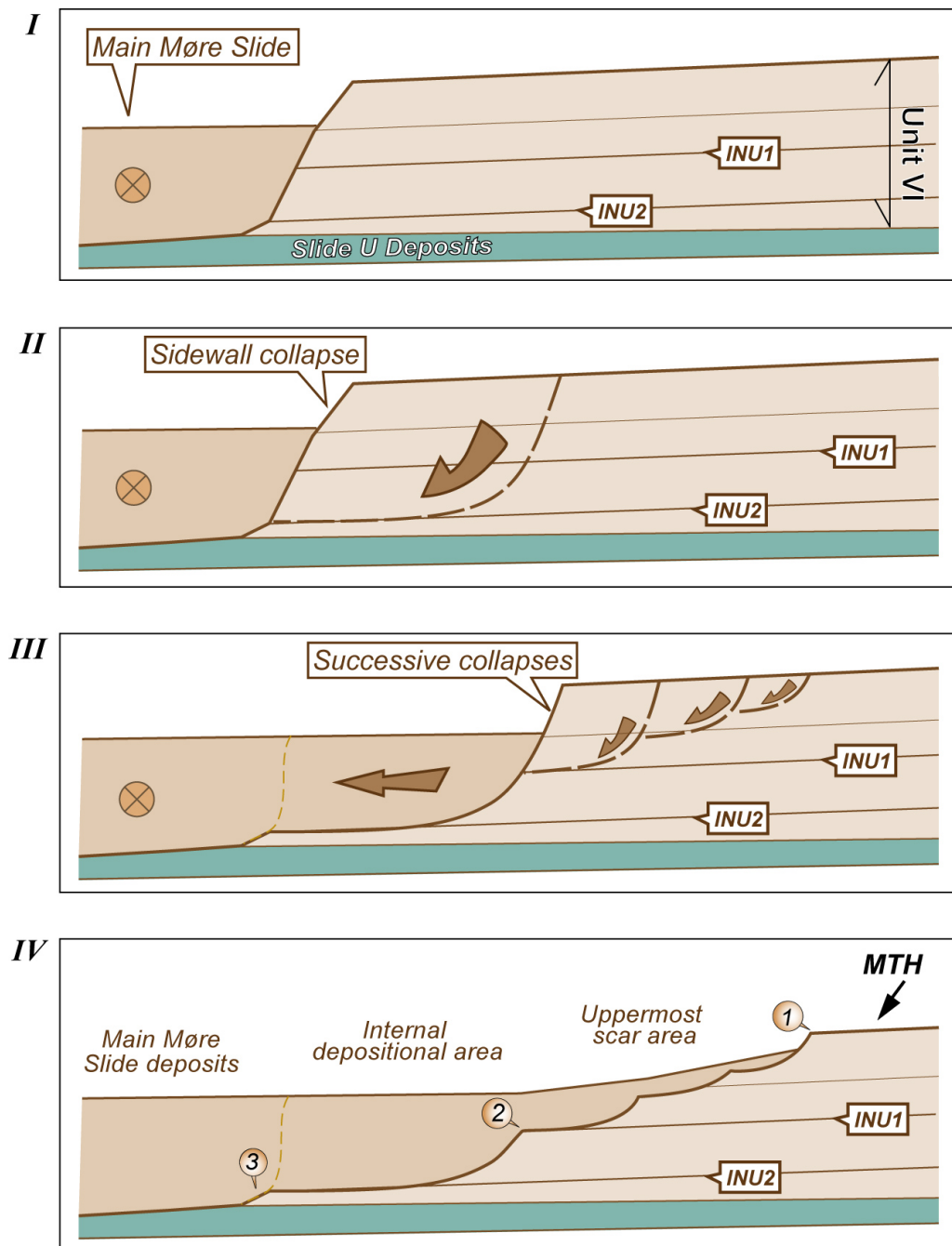


Figure 5.29: Conceptual model of the Zone C main slide scar development. I - Unit VI deposits are truncated by the main Møre Slide event. II - Collapse of the Møre Slide sidewall, with a failure surface reaching INU2. III - Instability propagates upslope through progressive collapse of the headwall, at upper stratigraphic levels. IV - Final stage of development of the Post-Møre surface. (1), (2) and (3) point the main boundaries that characterise this slide scar (see Fig. 5.22).

Contrary to what is observed in the uppermost scar area, the base of the remoulded material in the internal depositional area **A** (see Fig. 5.28) is very well defined and coincident with the *INU2* reflector (Fig. 5.22). Taking into consideration its geometry and the marked stratigraphical step, this suggests a different mass movement process than debris-flow. The debris-flow deposits that partially fill this depositional area could have been carried from the uppermost scar area, without being indicative of the type of mass movement that initiated the retrogressive failure. Independent of the initial type of failure, the similarities between the internal depositional area **A** and the smaller internal depositional area **B** (Fig. 5.28) indicate comparable development and suggest the existence of an upper scar upslope of the depositional area **B**, out of the study area. Regardless of the type of mass movement, the failure development and final geometries may also have been controlled by the strength variability within the Unit VI deposits, comprised mainly by GDF's deposits.

Covering an area at least 10 times larger than the internal depositional area **A**, Zone R is thought to correspond to the internal depositional area of a major sidewall collapse. The specific type of mass movement that took place in Zone R is unknown, and the headwall of this depression was probably eroded by the Holocene Storegga Slide event making it impossible to determine its exact location and characteristics. However, the similar sliding surface, the seismic characteristics of the deposits and the constant stratigraphic level suggest that the failure process that took place in Zone R resembled the initial retrogressive failure process that created the internal depositional areas **A** and **B** downslope.

Rigid blocks of undisturbed material within slide scars can be interpreted as detached blocks transported downslope for some distance (e.g. McAdoo et al., 2000; Keating et al., 2000; Gee et al., 2005; Lastras et al., 2005; Solheim et al., 2005a; Vanneste et al., 2006). However, the buried block of undisturbed material recognised within Zone R is believed to be *in situ*, as 1) it exhibits seismic lateral concordance, 2) it is clearly continuous to the underlying sedimentary unit and 3) there is no visible detachment surface present at its base 5.26. Similar "islands" of undisturbed material were also observed in other slides (e.g. Masson et al., 1998; Frey-Martinez et al., 2005; Garziglia et al., 2008). Nevertheless, how or why portions of *in situ* material can be retained within a large scale slide is still unclear (see section 6.3.2).

The block of undisturbed material observed within Zone R represented an obstacle to the material remoulded by the retrogressive failure, affecting the local thickness distribution of deposits. The observed thickening (Fig. 5.26 d) and thinning (Fig. 5.26 c) of the remoulded deposits, re-

spectively ENE and WSW of the block, indicate a main WSW transport direction on this area of Zone R. This transport direction is consistent with the WSW-trending lineations that extend from the block of undisturbed material. These lineations are thought to result from the confluence of remoulded material that followed different paths around this obstacle, corresponding to the sub-vertical planar flow boundaries (Fig. 5.30). Although shortly after being deflected the remoulded material appears to have followed semi-parallel trajectories, these flow boundaries were preserved for more than 18 km suggesting semi-linear flow behaviour.

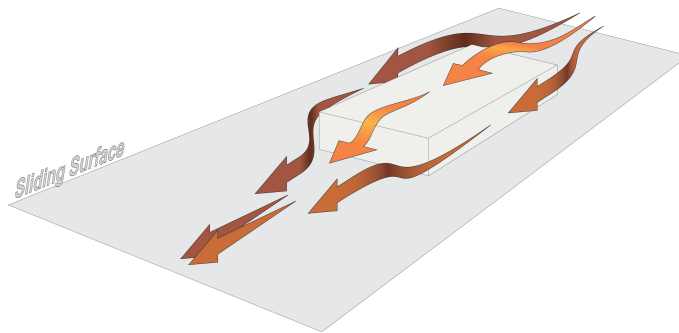


Figure 5.30: 3D diagram of the deflection effect on the flow of remoulded material caused by the presence of a block standing out of the sliding surface.

On the north-western edge of Zone R it is possible to infer the transport direction and behaviour of the remoulded material from the interpretation of the amplitude map and RMS amplitude maps (Fig. 5.31). The offsets of the acoustic patterns shown on the amplitude maps (Fig. 5.31) suggest brittle behaviour within the remoulded material. As the offsets are observed in amplitude maps from both the top and base of the remoulded material (Fig. 5.31 b, c and d), it is reasonable to consider that the displacement took place along penetrative, sub-vertical surfaces. The two main offsets, oriented NE-SW, were named **A** and **B** and are thought to represent the boundary that define the limits of the brittle shear zone. The offsets orientated approximately W-E are interpreted to result from dextral Riedel faults across the brittle shear zone. The sense of motion of the Riedel faults was inferred from the acoustic patterns offset whereas the general shear sense was essentially deduced from its location, i.e. knowing that the MTH must have acted as a fixed wall and that the remoulded material within Zone R was mainly transported towards Zone M¹.

A conceptual model of the development process of this shear zone is presented on Figure 5.32. According to this model, the south-eastern edge of the MTH acted as a detachment surface while the material was remobilised by the retrogressive slide. With the increase of shear strain, an internal brittle zone developed between the more plastic zones due to distinct rheological

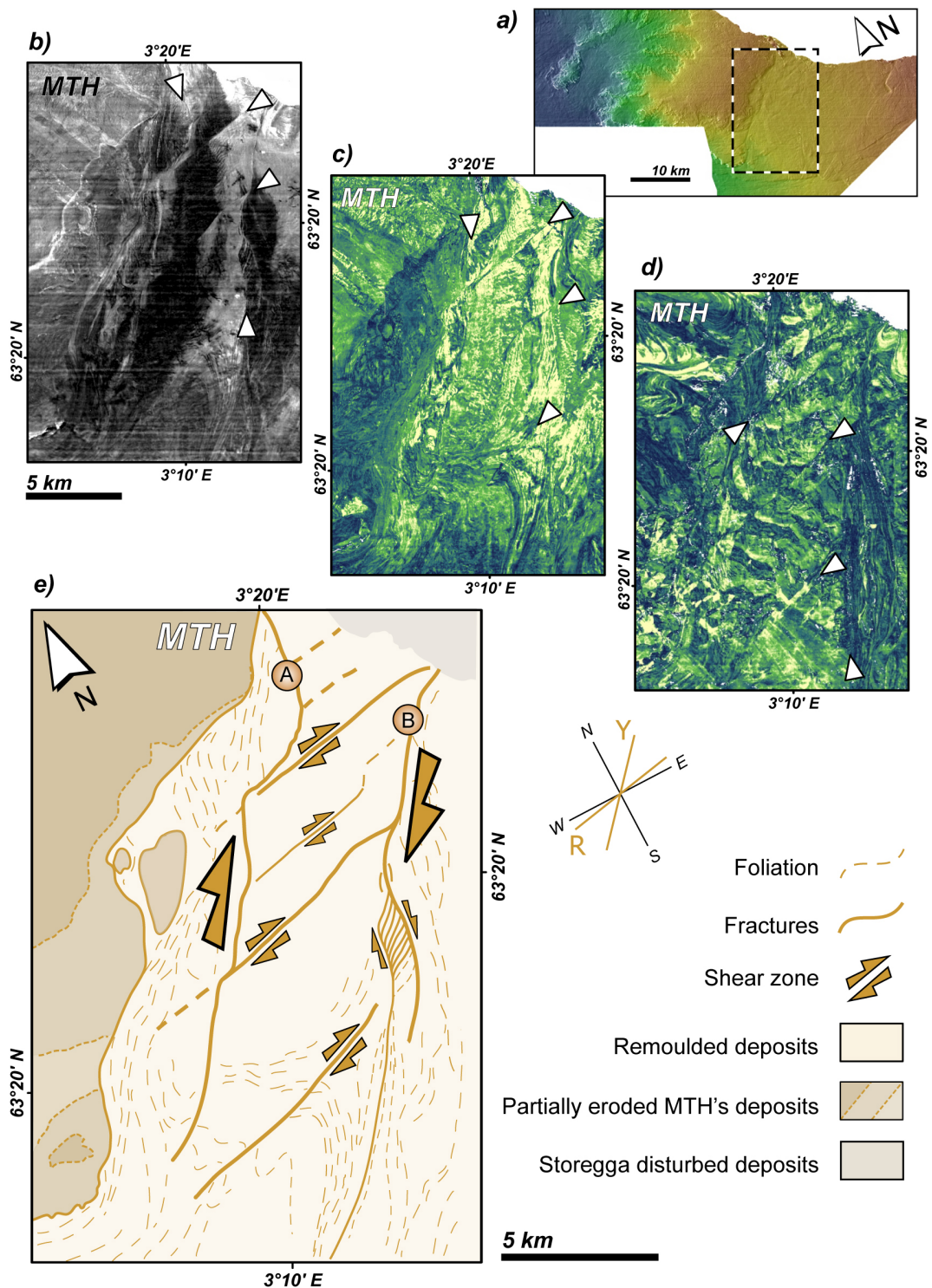


Figure 5.31: Shear zone on the north-western edge of Zone R. a) Location map. The dashed rectangle shows the location of b, c, d and e. b) Detail of the Fig. 5.19 amplitude map c) Detail of the Fig. 5.20 RMS amplitude map. d) Detail of the RMS amplitude map for the 10 ms window centred 20 ms above the INU2 reflector. Note that the arrows point towards the displacements of the acoustic pattern shown on the amplitude maps. e) Interpretation map. Y shows the main orientation of the boundary fault A and B, whereas R shows the main orientation of the Riedel faults.

properties within the remoulded material and/or from deformation partition. The **A** and **B** faults formed and acted as boundary faults for this brittle shear zone (Fig. 5.32 *I*). At an early stage, part of the movement was transferred to faults that formed between the shear zone boundaries with the same displacement sense as the primary shear fractures (Fig. 5.32 *II*). As the shear zone evolved, its boundaries expanded, the **A** fault, closer to the static MTH, "froze" and was cut by the internal faults whereas the **B** fault continued accommodating deformation and was deflected (Fig. 5.32 *III*). Although not evident in the conceptual model, sub-parallel lineations can be recognised outside of the brittle zone showing ductile deformation (Fig. 5.31). Nevertheless, these lineations are consistent with the proposed development of this shear zone.

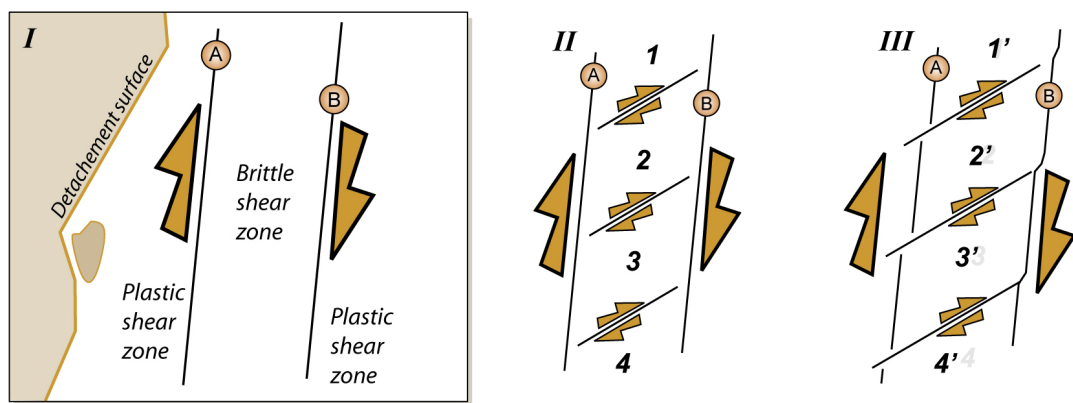
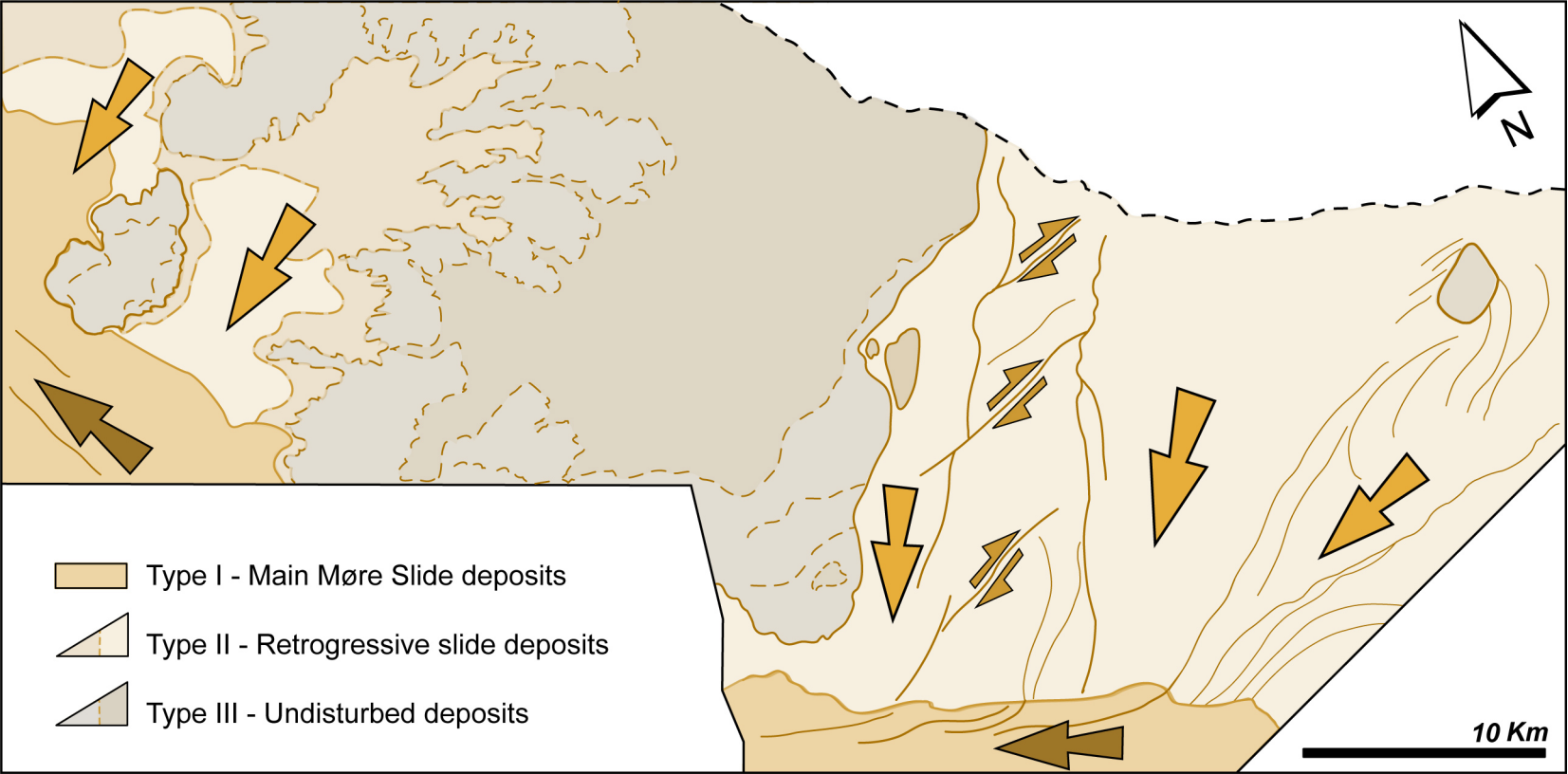


Figure 5.32: Model of development of the shear zone on the north-western edge of Zone R. **I** - Schematic diagram showing the geometry, characteristics and main shear sense of the shear zone. A and B act as boundary faults for the brittle shear zone. **II** - Early development of dextral Riedel faults across the brittle shear zone. **III** - Further development led to the propagation of the Riedel faults behind the shear zone, offsetting A boundary and deflecting B boundary. Note that block 4 shows the biggest displacement.

Throughout the post-Møre surface, it is possible to identify different types of underlying deposits. These deposits are classified into three main types according to their characteristics and instability history:

- Type I** : the deposits remoulded by the main Møre slide itself, which show transport mainly towards NW,
- Type II** : deposits at a upper stratigraphic level that show transport south-westwards and that are associated to the collapse of the Møre Slide sidewall and successive retrogressive failures, and
- Type III** : Unit IV deposits that predate the Møre Slide and were only partially eroded by this slide event

An interpretative map of the post-Møre surface was compiled (Fig. 5.33) from all the information extracted from the seismic data. This map shows the distribution of the different types of underlying deposits and highlights the changes of main transport direction inferred from the Møre Slide deposits and adjacent remoulded material. Although the limits between each type of the deposits tend to be well marked by changes of deposit thickness and stratigraphic steps, the passage from deposits Type II to Type III within Zone C cannot be precisely defined with the given seismic resolution (Fig. 5.22). Considering that the post-Møre surface geometry in the uppermost scar of Zone C is mainly controlled by the morphology of the eroded material, areas that probably already presented a thin cover of material Type II are still mapped as Type III deposits. The directions of transport were inferred essentially from the lineations observed on amplitude maps. On the main Møre Slide deposits the directions of transport range from WNW to NNW, whereas for the retrogressive slide deposits the main inferred directions of transport range from WSW to SSW. Locally the retrogressive slide deposits present a higher variability of transport directions, reflecting changes in style of mass movement, irregularities on the sliding surface or interaction with sidewalls. These deposits also present evidence of higher variability of the rheologic behaviour compared to the deposits of the main Møre Slide and this probably results from a lower degree of remobilisation and a lesser transport distance.



← Møre Slide main direction of transport ← Retrogressive slides main direction of transport ⚡ Shear zones

Figure 5.33: Interpretative map of the Slide U deposits showing main direction transport inferred from the material remoulded and the location of the ramps that characterise the sliding surface.

5.4 Slide U

Since the slide deposits that underlay the Møre Slide deposits were first recognised in this area by King et al. (1996), referred at the time as NSFSlide-1, several designations have been used. In the studies for the Norwegian Deepwater Programme (unpublished, 2004), these deposits were considered as part of a mega North Sea Fan slide complex named U5 Slide whereas Solheim et al. (2005a) in their study of the Storegga Slide Complex referred to them as part of the Slide S deposits. Additionally, Nygård et al. (2005) introduce the P9 Slide Complex designation including the NSF Slide 1 and Vigra slide deposits. Without a consistent nomenclature, these deposits are named in this thesis as Slide U deposits after its seismostratigraphic level.

According to the extension of Slide S and Slide U5 presented by Solheim et al. (2005a) and the Norwegian Deepwater Programme (unpublished, 2004) respectively, the study area is located near Slide S southern sidewall and very close to an undisturbed area within the U5 slide. The Slide S affected an area of 23700 km² and its headwall 40 to 120 m high centred on the Storegga Complex area extends through more than 200 km (Solheim et al., 2005a), whereas the mega-scale palaeoslide U5 extends from the Storegga area into the North Sea Fan, even to the SW of souther limit of the Tampen Slide (Norwegian Deepwater Programme, unpublished, 2004).

5.4.1 Description

The Slide U deposits correspond to Unit VII and can be observed throughout the study area. The top of this seismic unit is well defined by a strong reflection event, the *TSU* reflector (Fig. 5.34). The *BSU* reflector that marks the base of this seismic unit is less well defined and its strength varies greatly, from as strong as *TSU* reflector to as weak as the internal reflections of the underlying material. The variations in strength of the seismic event at the base of Slide U deposits appear to be associated with variations in seismic signature throughout this unit. Where the unit presents bright chaotic seismic facies, the *BSU* reflector tends to be stronger and where the seismic unit is dominated by transparent seismic facies, the *BSU* reflector presents very weak reflectivity and is defined essentially by the change of reflector geometry associated with the seismic signature between the slide deposits and the underlying material. As well as changes in seismic signature, the Slide U deposits show variations both in thickness and in sliding surface stratigraphic level.

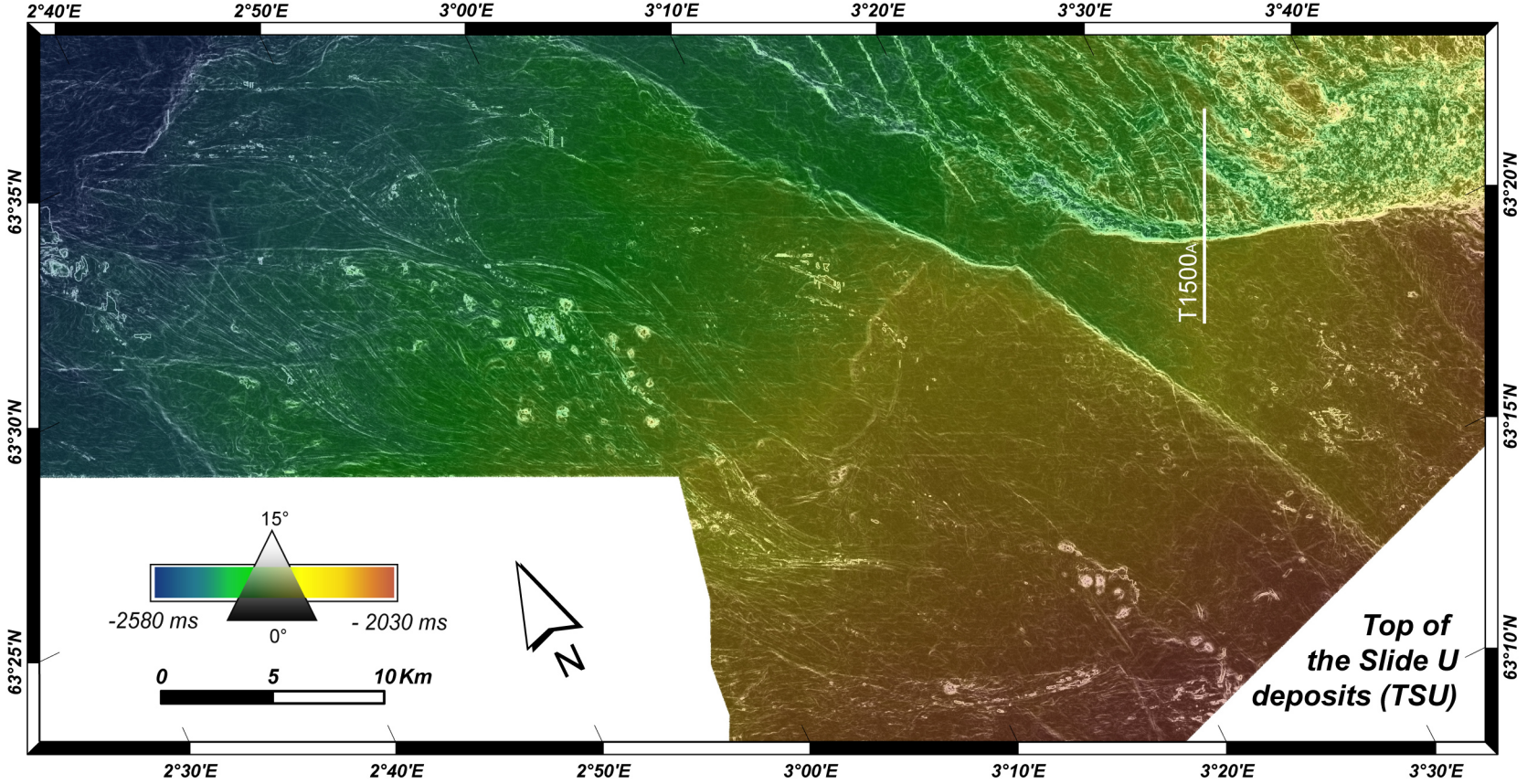


Figure 5.34: Gradient and depth map of the top of Slide U deposits (TSU). The brightness shows the slope gradient (back - flat and white slope higher than 15°) and the colour-scale shows the depth in ms (TWT). Location of trace 1500 segment displayed on figure 5.35.

In the study area, the Slide U deposits are the uppermost deposits that were not remoulded by the Holocene Storegga Slide. Nonetheless, beneath the Storegga deep failure area, the seismic reflections of Slide U deposits are partially disturbed and shifted down by as much as 100 ms. However, the observed vertical displacement is considered to be a seismic artefact. This push-down effect can be explained by relatively low sound velocity through the remoulded material of the deep failure area that creates an apparent depression of the underlying reflectors. This artefact is stronger on the eastern corner of the study area and its intensity decreases north-westward, which is consistent with the decreased degree of disruption of the remoulded material within the Storegga deep failure area (Fig. 4.3). Where the Storegga's remoulded material presents lateral alternation between chaotic-transparent facies and relatively coherent facies, the push-down effect is stronger under the chaotic-transparent facies sections (Fig. 5.35). Elongated apparent depressions trending north-northwest seen on the *TSU* (Fig. 5.34) are spatially associated with the push-down effect (Fig. 5.35). In this thesis, the disruption and push-down effect of Slide U deposits seismic record will be referred to as the *footprint* of the Storegga Slide deep failure.

Besides the disruption caused by the Storegga footprint, the relatively smooth surface of the top of the Slide U deposits also presents two areas with several sharp protuberances (Fig. 5.34 and marked on 5.36). One of these areas is centred at 63°22'N, 2°58'E and is characterised by circular protuberances of 200 to 500 m diameter and up to 50 ms (c. 40 m) high. They result from irregularities on the Slide U deposits, possibly due to the existence of rigid blocks within the remoulded material. The other area, centred at 63°15'N, 3°22'E, is characterised by elongated and circular protuberances that can be more than 1.5 km long and more than 60 ms high (c. 48 m). In most cases, these protuberances resulted from the push-up effect induced by fluid migration, i.e. the *TSU* reflector shows steep antiforms generated by fluid migration. Besides push-up generated protuberances this area also presents some protuberances resulting from Slide U deposit irregularities. Figure 5.36 provides a good perspective view of features described above.

Although the top of Slide U deposits normally dips gently towards NNW, it presents three relatively steep slope changes, dipping towards SW, NNW and ENE respectively (Fig. 5.34 and 5.36). The changes of slopes observed on the top of the Slide U are the superficial expression of stratigraphic steps on the sliding surface. These stratigraphic steps define ramps at the base of the Slide U deposits that are named in this thesis Ramp W, Ramp N and Ramp E, respectively

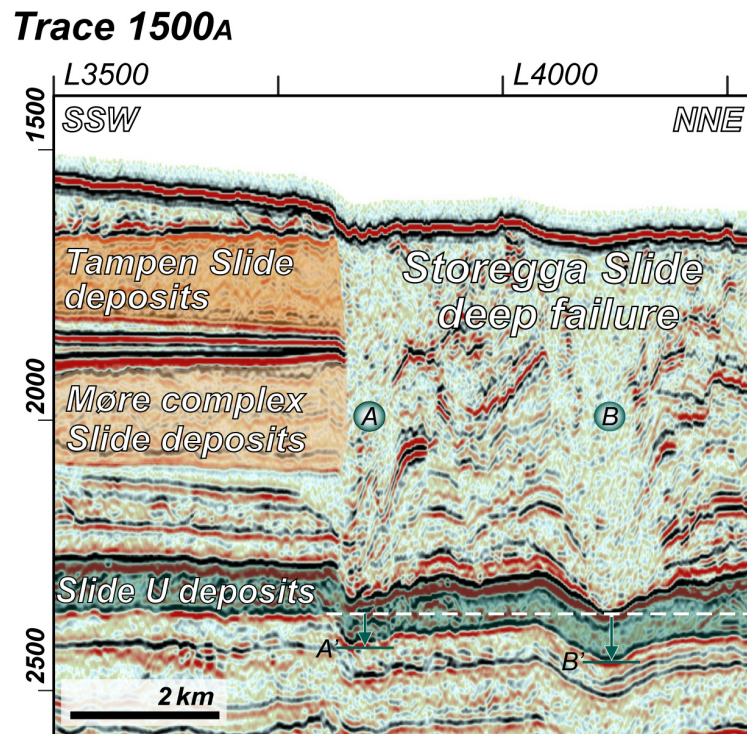


Figure 5.35: Segment of seismic trace 1500 showing the boundary between undisturbed sequence of the North Sea Fan (on the left) and the Storegga Slide deep failure (on the right). Push-down effect can be recognised on the Slide U deposits beneath the Storegga Slide deep failure. White dashed line marks the projected continuation of BSU, ignoring the push-down effect. Beneath the chaotic-transparent sections **A** and **B** the base of Slide U seismic record is respectively 84 and 120 ms deeper than the expected. Location is shown on Fig. 5.34.

(Figs. 5.36 and 5.37). Due to the inconsistent strength of the *BSU* reflector, it was not possible to track the base of Slide U deposits with the same degree of accuracy as the other studied seismic events. However it was still possible to characterise the ramps at the base of Slide U through the observation of both seismic profiles and the *BSU* reflector's DEM (Fig. 5.37). Table 5.1 shows these observations and presents the ramps' main orientation, marked changes of orientation, dip direction, vertical drop and changes of deposits' thickness across and above the ramp. Figure 5.38 presents the different combinations possible from changes of deposits' thickness across and above the ramp.

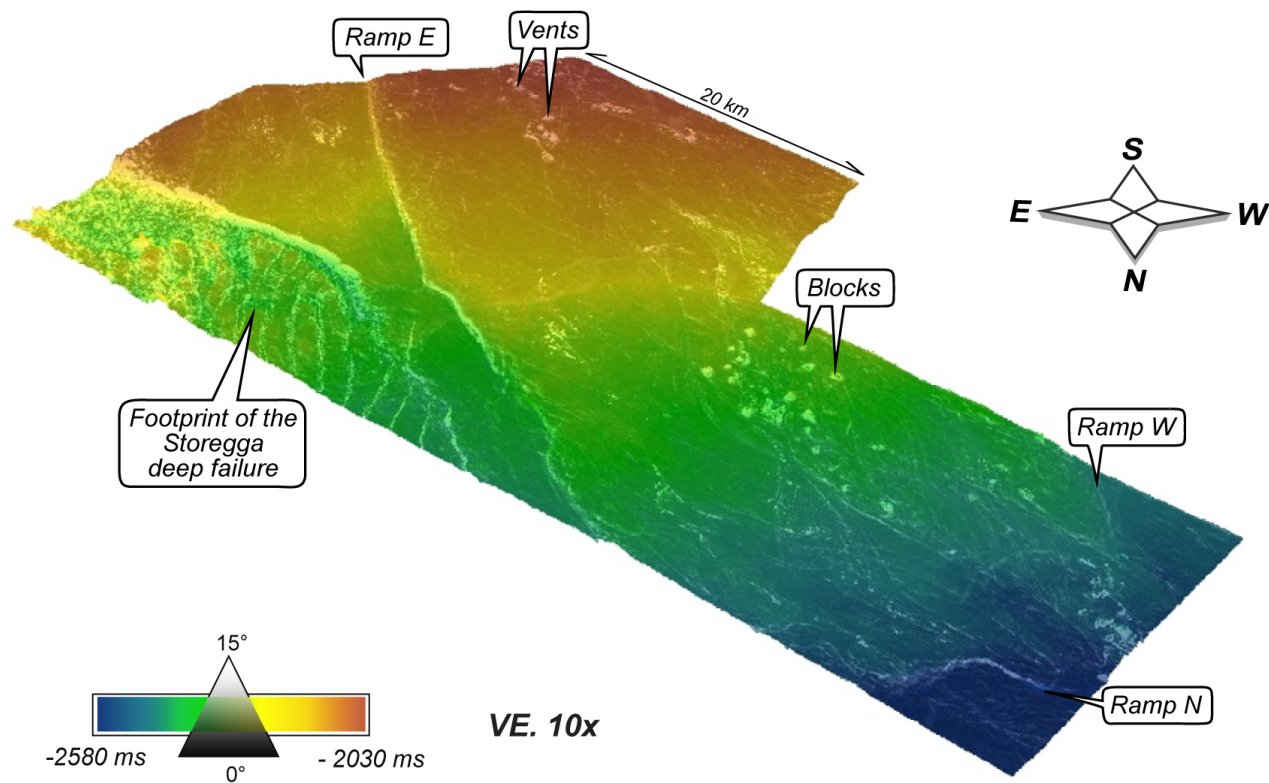


Figure 5.36: 3D view of the top of Slide U looking southward. The brightness is given by the local steepness and the colour scale indicates the deepness in ms (TWT). The vertical scale is exaggerated 10× and horizontal scale varies with distance in the perspective. Note that the designation used for the steep slopes of the TSU surface corresponds to the names of the sliding surface ramps from which they result.

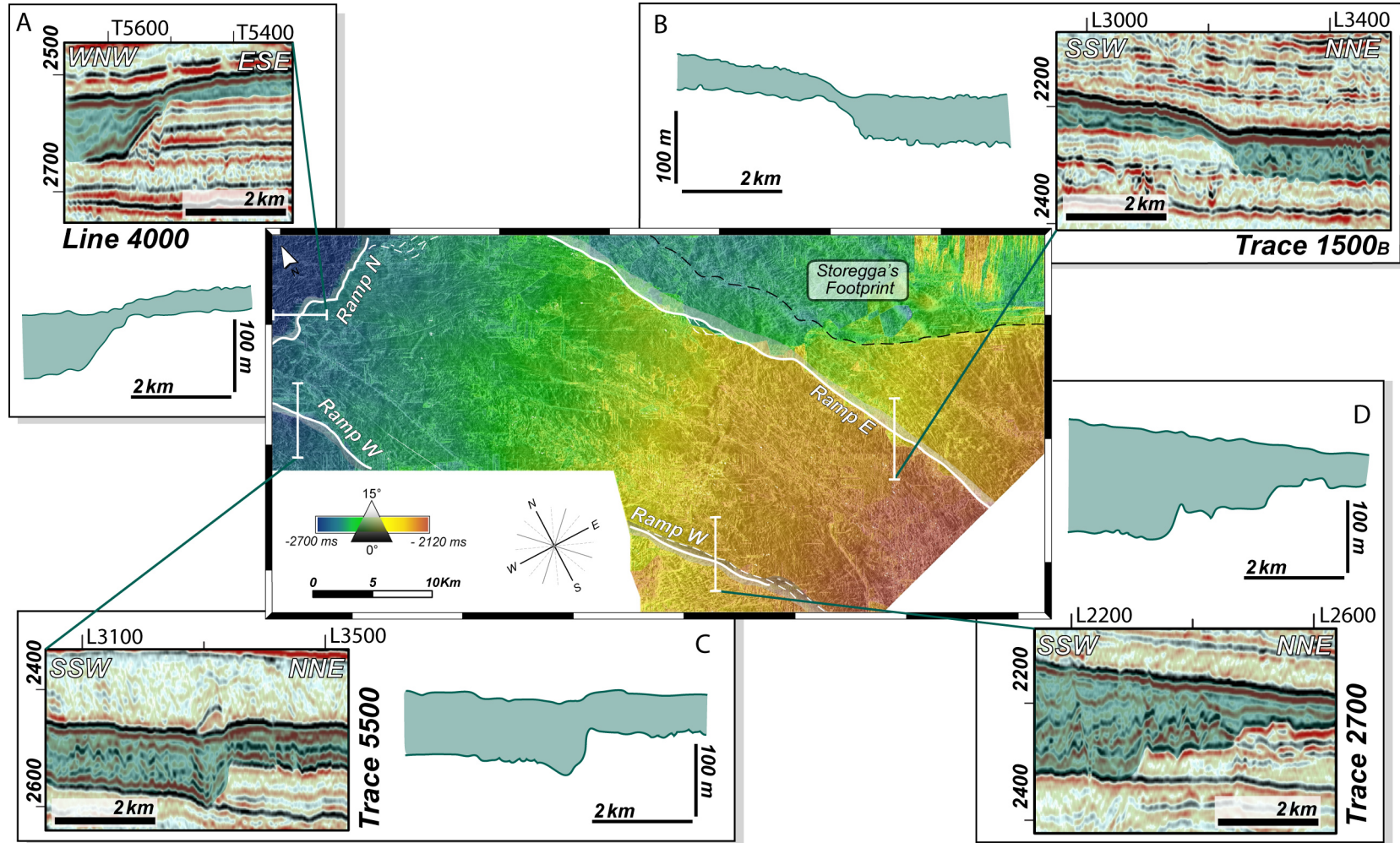


Figure 5.37: Geometry and orientation of the ramps identified at the base of Slide U. The slope and depth map of the BSU reflector, on the centre of the figure, display the ramps orientation. Cross-sections A and B illustrate the geometry of Ramp N and Ramp E, respectively, and the cross-sections C and D illustrate respectively the geometry of the northern and southern segment of Ramp W. Slide U deposits are highlighted.

	Ramp W	Ramp N	Ramp E
Main orientation	NW-SE	WSW-ENE	NNW-SSE
Marked deviation of ramp orientation	×	✓	×
Dipping	SW	NNW	ENE
Vertical drop	30 - 80 ms	~ 100 ms	70 - 100 ms
Changes of deposits thickness across the ramp	✓	✓	✓
Deposits thinning above the ramp	×	✓	✓

Table 5.1: Description of the main characteristic of the three ramps observed at the sliding surface of Slide U. It presents aspect of both the geometry of Ramp W, Ramp N and Ramp E and the overlying deposits thickness.

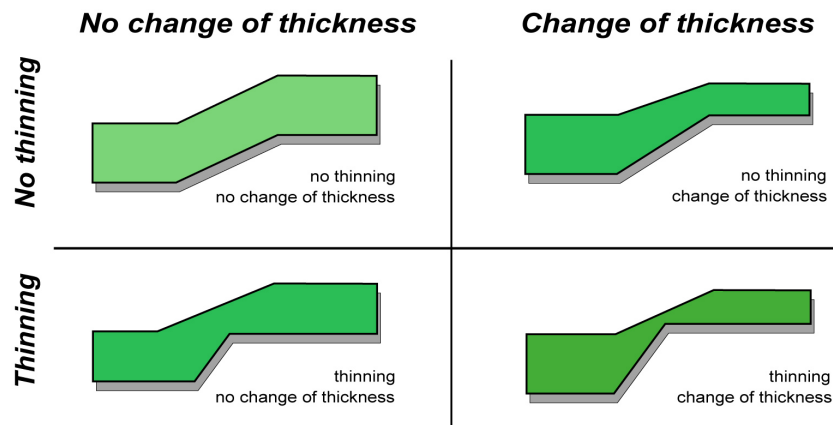


Figure 5.38: Schematic diagram illustrating possible slide deposits profiles across a sliding surface ramp, combining the presence or absence of deposits thinning immediately above the ramp with the preservation or change of its thickness across the ramp. Note that all the profiles shown on fig. 5.37 present changes in thickness and that profiles **A** and **B** present thinning above the ramp whereas profiles **C** and **D** do not.

Both Ramp W and Ramp E present similar orientation, NW-SE and NNW-SSE respectively, almost perpendicular to the orientation of Ramp N, that lies roughly WSW-ENE (Fig. 5.37). Ramp N is the only of the three ramps that presents marked changes of orientation, varying every few hundred metres from sections trending WNW to sections trending ENE. The changes of orientation consequently affect the dipping direction of this ramp but it is possible to say that the predominant dipping direction is NNW, while Ramp W dips towards SW and Ramp E towards ENE. Vertical drops of up to 100 ms (c. 80 m) are observed on the sliding surface along Ramp N. Such vertical drops are only sporadically observed along Ramp E that normally presents vertical drops of around 70 ms (c. 56 m). Ramp W presents the biggest range of vertical drop values, ranging from 30 to 80 ms (c. 24 to 64 m) height. It reflects the fact that the geometry of Ramp W varies quite dramatically from a well-defined ramp on its northern section to a diffuse ramp on its southern section, without superficial expression.

It is partially due to its geometry that the southern section of, Ramp W does not have superficial expression at the top of Slide U deposits (Fig. 5.37 D). Another factor that determines the ramps' superficial expression is the thickness variations across the ramps. All the ramps show a thickness increase from upslope to downslope (Fig. 5.37), especially across Ramp N where the deposits' thickness abruptly increases by more than 60 ms (c. 48 m) in just a few hundred metres (Fig. 5.37 A), from no more than 40 ms (c. 32 m) to more than 100 ms (c. 80 m). Marked changes of deposits' thickness occur across all the three ramps, however thinning immediately above the ramp only occurs above ramps N and E, which are covered by less than 40 ms (c. 32 m) of deposits (Fig. 5.37 A and B).

Although the biggest thickness changes tend to occur adjacent to the sliding surface ramps, gradual changes are observed throughout the study area. The thickness of Slide U deposits varies from 40 ms to more than 160 ms thick, which corresponds to deposits' thicknesses ranging from approximately 32 m to 128 m (Fig. 5.39). The thickest Slide U deposits are observed on the NE and SW corners of the study area and the thinnest deposits are observed on the upper edge of ramps N and E. As the contour lines of the thickness map tend to be sub-parallel to the sliding surface ramps (Fig. 5.39), even the gradual changes of thickness appear to be primarily controlled by the morphology of the sliding surface.

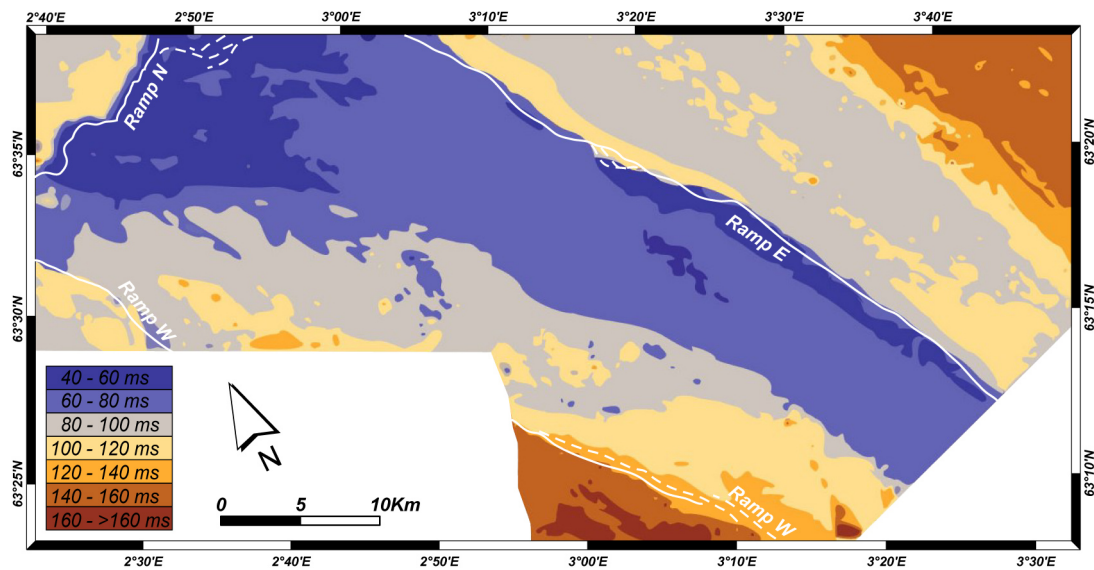


Figure 5.39: Thickness map of the Slide U deposits, with contour interval of 20 ms. Note that was necessary to reduce the resolution and use a simple class colour scale to avoid noise resulting from the irregular strength of BSU reflector. The white lines mark the location of the sliding surface ramps.

Besides changes in thickness, the Slide U deposits' seismic characteristics also vary over short distances. Three distinctive types of seismic signature can be found throughout the deposits, and were named I, II and III. This seismic record classification takes into account both the seismic facies presented on seismic profiles and the patterns shown on amplitude-based attribute maps. The main characteristics of these types of seismic signature are summarised below and their appearances are displayed on Figure 5.41.

Type I - On seismic profiles: irregular, discontinuous, high-amplitude internal reflections.

On the amplitude-based attribute maps: areas of high amplitudes delimited by narrow stripes of lower amplitude with irregular anastomosing distribution.

Type II - On seismic profiles: acoustically structureless, low-amplitude internal reflections.

On the amplitude-based attribute maps: curved lineations of lower and higher amplitude stand out from a generally low-amplitude background.

Type III - On seismic profiles: irregular, high-amplitude internal reflections.

On the amplitude-based attribute maps: few lineations of slightly lower amplitude on a generally amorphous high-amplitude background.

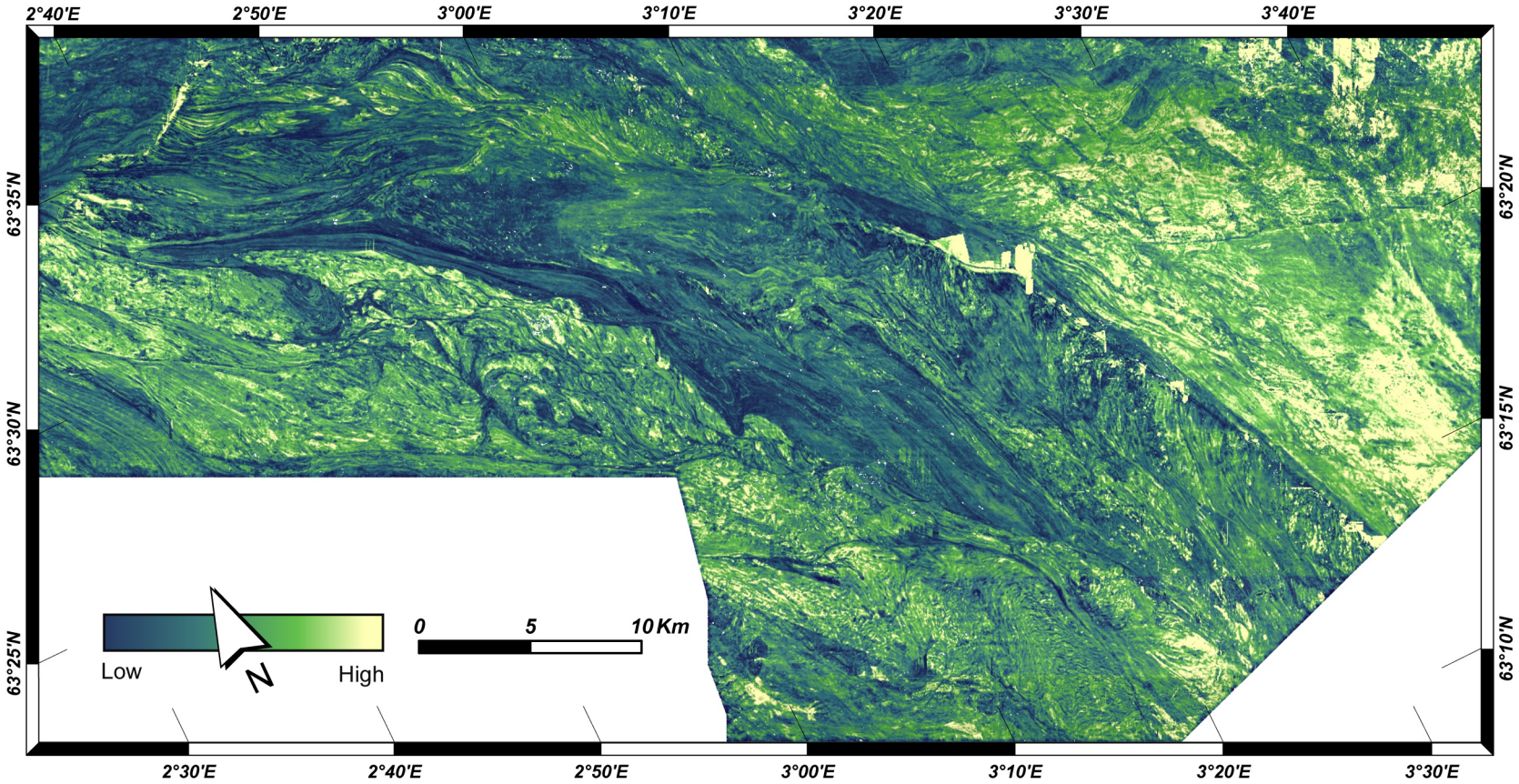


Figure 5.40: RMS amplitude map for the time window between the horizon TSU+20ms and the horizon BSU-15ms. Note that the thickness of the window varies through the study area, according to thickness variation within the deposits. This map shows the flow patterns by highlighting different seismic responses from the remoulded material.

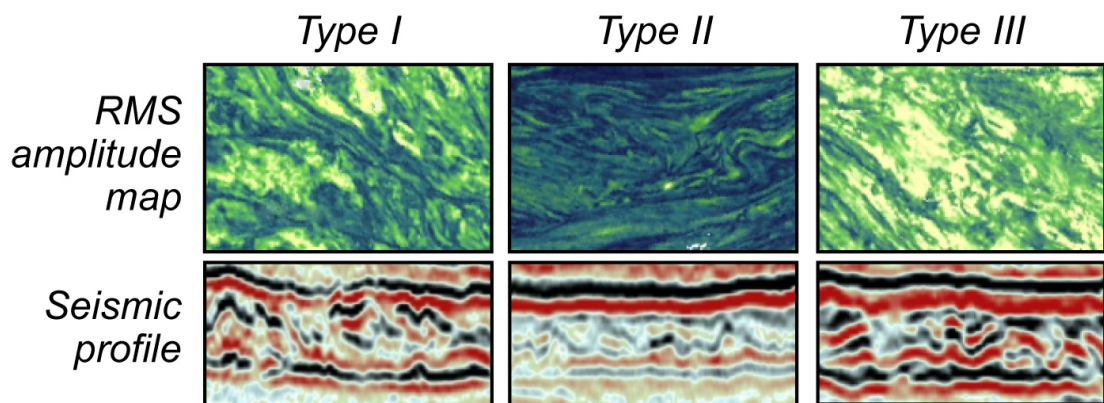


Figure 5.41: Diagram illustrating the main characteristics of the three types of seismic signature of Slide U deposits in the study area, defined from RMS amplitude map (above) and from seismic profiles (below). On the RMS maps blue shows low-amplitudes and yellow high-amplitudes.

On RMS amplitude maps the boundaries between areas of different seismic signatures are fairly evident (Figure 5.40). In combination with other seismic displays it was possible to map the limits of each type of Slide U seismic record and to produce the map shown in Figure 5.42.

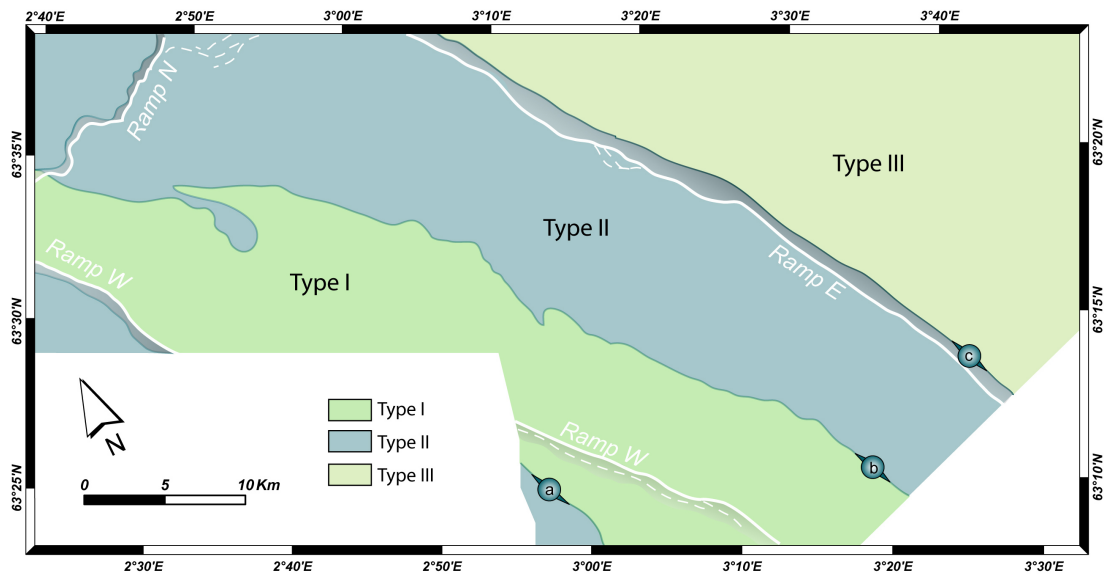


Figure 5.42: Distribution map of the three main types of seismic record observed on the Slide U deposits: Type I, Type II and Type III. The white lines mark the location of the main edge of the sliding surface ramps and the boundaries between types of seismic signature and named a, b, c.

Figures 5.43 and 5.44 show the direct relationship between changes of Slide U seismic signature on seismic profiles and the patterns of low and high amplitude observed on the RMS amplitude map (Fig. 5.40). On both figures, a detailed view of a RMS amplitude map is displayed together with a seismic profile extracted from that area. The boundary **b** between Type I and II of Slide U deposits can be observed on seismic trace 3500, at its intersection with line 3500 (Fig. 5.43 b and c). The boundary **c** between Type II and III of Slide U deposits can be observed on trace 1800, a few hundred metres downslope from Ramp E and close to the intersection of this trace with line 3500 (Fig. 5.44).

Besides Slide U deposits' signature differences, on Figure 5.43 the seismic profile shows that boundary **b** between deposits Type I and Type II is also marked by change of deposits' thickness. As the Type I deposits tend to be 40 ms thicker than the eastward deposits Type II, the change of thickness can be observed across the full extension of this boundary (Fig. 5.45). Changes of thickness are also observed across the others seismic signature boundaries, however they are mainly control by the morphology of the sliding surface. The boundary **b** is the only seismic signature boundary in the study area that is not related to the presence of a sliding surface ramp and it is also the only one that presents a relatively irregular border. Instead of the smooth border trending NW-SE that can be observed on boundaries **a** and **c**, boundary **b** presents changes of orientation and irregular border, with local recesses of Type I deposits (Fig. 5.46b) and enclaves of deposits Type II (Fig. 5.46c).

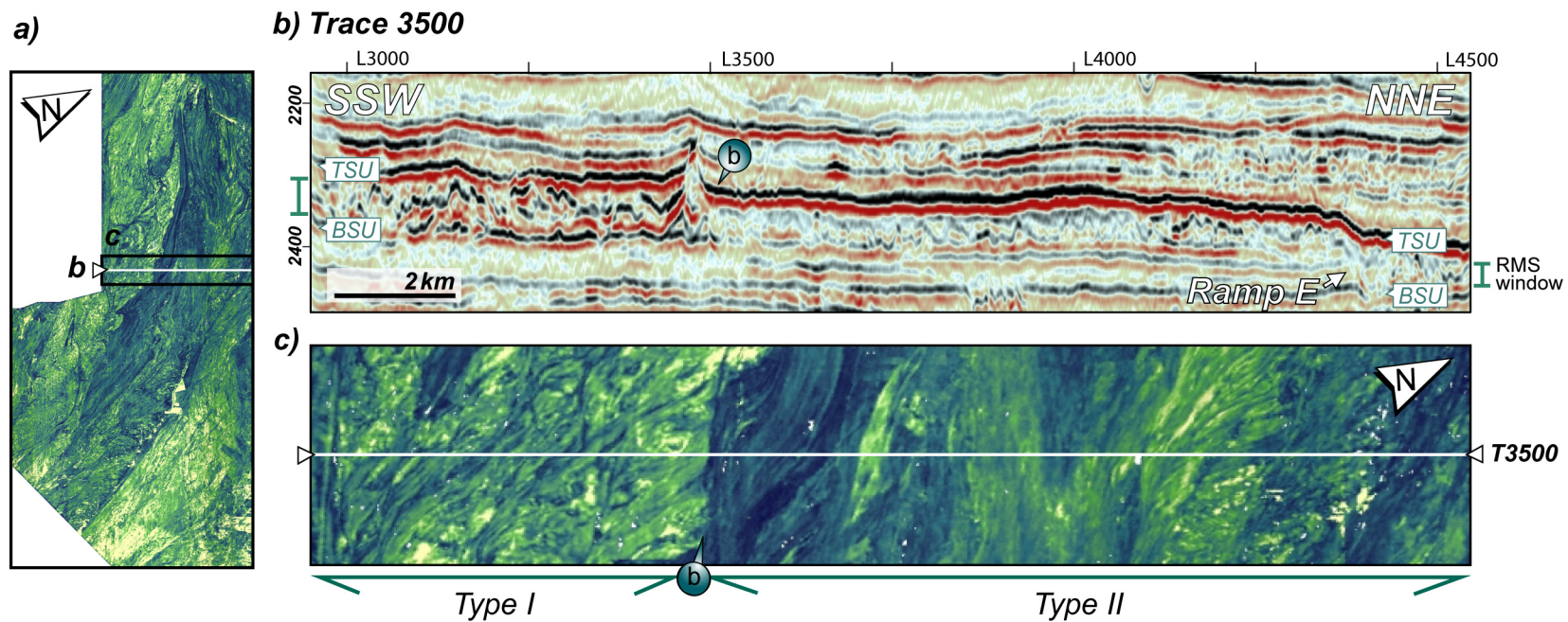


Figure 5.43: Transition from seismic signature Type I to Type II. *a)* RMS location map (Fig. 5.40). *b)* Segment of the seismic trace 3500, showing Slide U deposits between TSU and BSU reflectors. *c)* Swath from the RMS map centred at trace 3500. *b* marks the boundary between Type I and Type II. Note the differences of seismic facies, internal reflectivity and amplitude patterns between the two types of seismic signature of Slide U deposits.

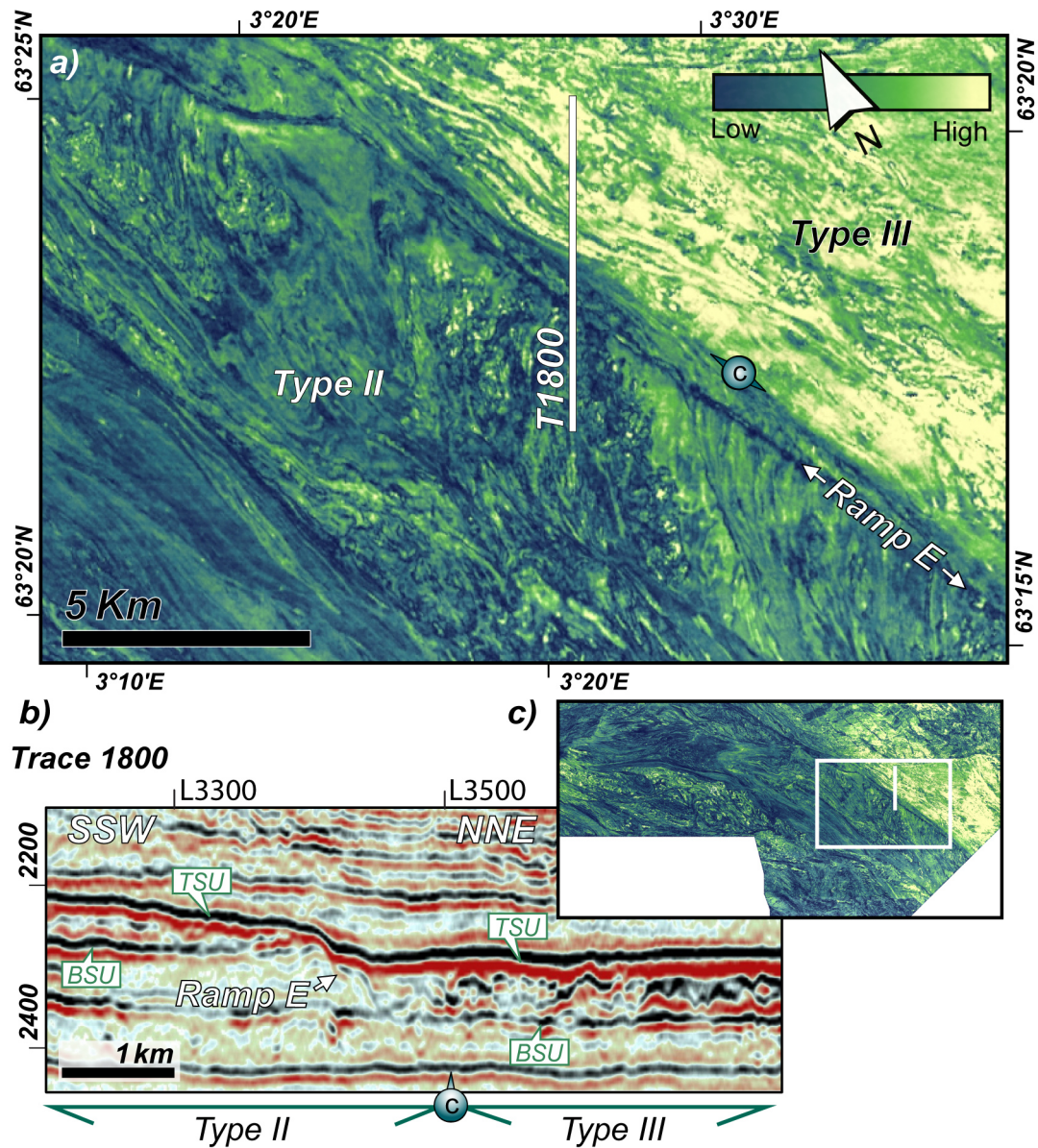


Figure 5.44: Transition from seismic signature Type II to Type III across Ramp E. a) Detailed view of the RMS map obtained from the 20 ms window centred 30 ms below the top of the Slide U deposits - TSU reflector. b) Segment of the seismic trace 1800 across Ramp E. c) RMS location map. Note that transition from Type II to Type III, marked by the boundary **b**, occur few metres downslope Ramp E.

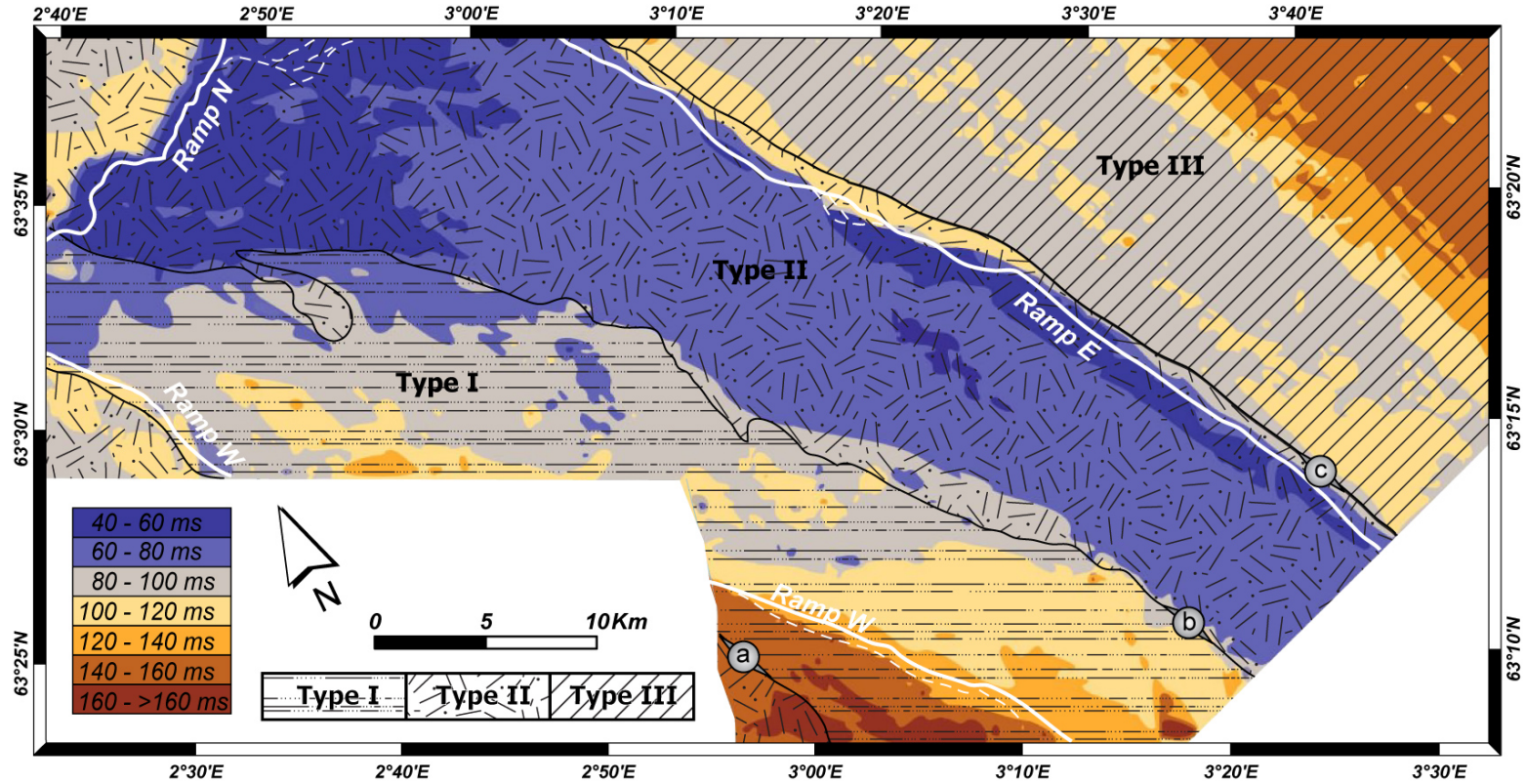


Figure 5.45: Spatial distribution of the three types of Slide U deposits' seismic signature (Types I, II and III) overlying the deposits' thickness map (with 20 ms interval class). The white lines mark the location of the sliding surface ramps.

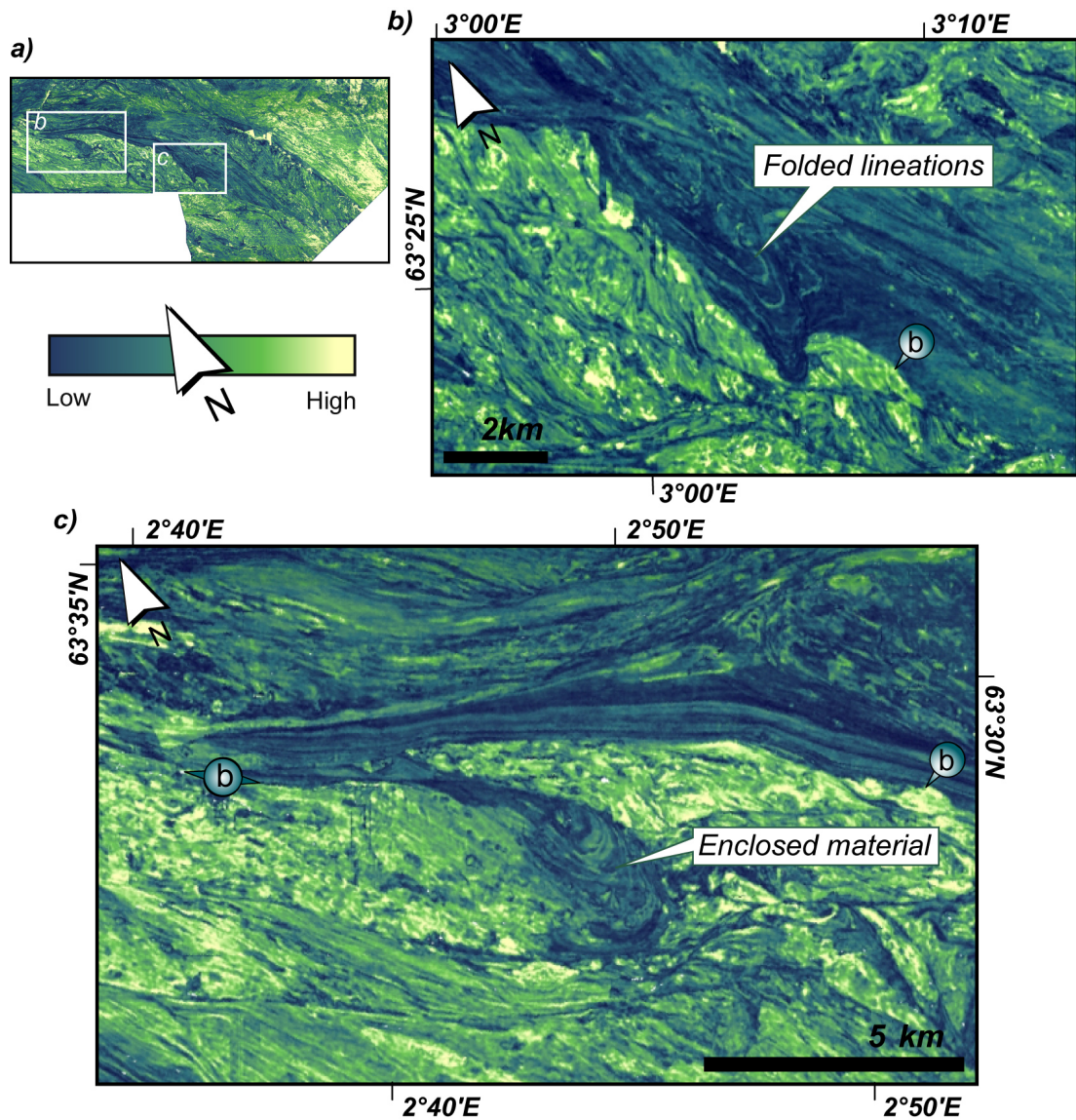


Figure 5.46: Details of the morphology of the boundary **b**, between Type I and Type II Slide U seismic signature. a) Fig. 5.40 RMS amplitude map with the location of the enlarged views (b) and (c). b) Detail of RMS amplitude map showing a bay-shaped segment of boundary **b**. c) Detail of RMS amplitude map showing Type II deposits enclosed within deposits Type I. Note the folding and deformation patterns of high-amplitude lineations on the Type II deposits close to the boundary.

5.4.2 Interpretation

Many submarine slides present stratigraphic steps between different sections of their sliding surfaces (e.g. Laberg and Vorren, 2000b; Bryn et al., 2003; Frey-Martinez et al., 2005; Solheim et al., 2005a; Vanneste et al., 2006). These stratigraphic steps can be due to several factors, such as multiple phases of sliding, changes of mass movement processes, lateral variation of material's strength and changes in the main weak-layer morphology. With the dataset available, it is impossible to be certain which was the key factor that controlled the development of the three ramps in the sliding surface of Slide U earlier described (Fig. 5.37 and Tab. 5.37).

However the orientations of Ramps W and E, sub-parallel to the main direction of transport, suggest that their geometry was controlled by lateral erosion even if they originally result from intrinsic changes of the material's shear strength. Considering that no major changes were observed on the internal properties of the material confined by the sliding surface ramps, the fact that the Ramp N is the only ramp showing marked changes of orientation corroborates that interpretation. By being roughly perpendicular to the main direction of transport (Fig. 5.37) this ramp was not exposed to the lateral erosion and suffered different processes of sediment removal. Therefore the final geometry of these ramps is considered to reflect the local changes in the mass movement mechanics.

Although the geometry of the sliding surface's ramps was probably shaped by the transport of the remoulded material, there is evidence that the material's transport was also controlled by the presence and geometry of these ramps. For instance, the lineations recognised on amplitude maps from the Slide U deposits (e.g. Fig. 5.40) are thought to indicate the flow direction and deflect from NNW to NNE upslope from Ramp E (Fig. 5.47). It is thought that the flow of remoulded material would accelerate on the edge of the stratigraphic step, thus affecting the flow patterns and causing the deflection of the transport direction.

The impact of these stratigraphic steps might have gone beyond the local effect on the direction of transport. The boundary **c** (between deposits Type II and III) and the northern section of the boundary **a** (between deposits Type II and I) are sub-parallel to existing stratigraphic steps, respectively Ramp E and Ramp W (Fig. 5.42). This suggests that the distribution of the different types of Slide U deposits were, at least partially, controlled by the sliding surface geometry, either by affecting the flow dynamic or by defining areas with a different sources of remoulded material. An analysis of the upslope continuation of this area would be required to properly

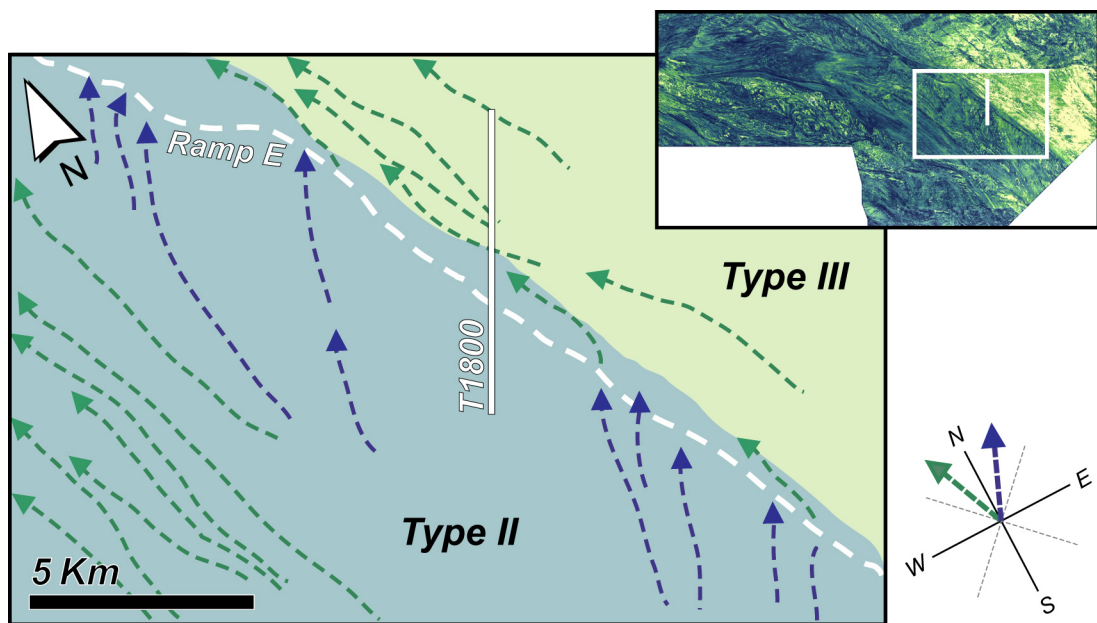


Figure 5.47: Interpretation map of detailed view of the RMS amplitude map displayed on Fig. 5.44, showing the changes on the direction of transport upslope Ramp E. Arrows show the inferred transport direction (green - NNW, blue - NNE) and white dashed line marks the upper part of ramp.

assess the exact effect of these stratigraphic steps on the material removal.

In contrast to the other boundaries in the study area, the boundary **b** between deposits Type I and Type II does not coincide with any significant irregularities on the morphology of the sliding surface. Nevertheless, the two types of deposits present significantly different thicknesses (Figs. 5.43 and 5.45). As it is not morphologically confined, the abrupt passage from deposits Type I to deposits Type II appears to have been defined by the dynamic interaction between two distinct flows of remoulded material.

Features, like lineations sub-parallel to the **b** boundary and Type I material apparently dragged into deposits Type II (Fig. 5.46), suggest that the deposits Type II experienced a faster transport than the deposits Type I. Figure 5.46 shows deposits Type II partially enclosed within the deposits Type I, that also corroborate the hypothesis that deposits Type II experienced a faster transport. Assuming a faster transport for the remoulded material Type II, two models (A and B) were considered to explain the development of this "enclave" (Fig. 5.48). In model A, a ductile behaviour is assumed and the "enclave" develops by progressive folding of the boundary between the two flows of remoulded material. In model B, a semi-rigid behaviour is assumed and the "enclave" results from the motion of blocks of remoulded material along this flow

boundary. However, neither of the two models explains totally the features observed in these areas and it is thought that aspects of both models played a role. For instance, the internal geometry of the deposits Type I is consistent with the accumulation of semi-rigid blocks, whereas the geometry of the boundary itself is more consistent with a ductile behaviour. Irrespective of which model better describe the development of this "enclave", the initial geometry of the flow boundary appears to have key role on the generation of the "enclave".

The weak reflectivity generally observed at the base of the Type II deposits (Figs. 5.41 and 5.43) may result from physical similarities between the slide deposits and the underlying material. However, it is known from both outcrops and drill cores that sliding surfaces generally consist of more than just one planar contact, ranging from a few centimetres to a few metres thick (Dykstra, 2005). Therefore, the low impedance contrast at the base of these deposits could also be interpreted as the result of a poorly-defined contact between the slide deposits and the underlying material, as a diffused sliding surface with increasing deformation toward the top would lead to gradual changes on the deposits' acoustic proprieties and low impedance contrast.

Along with the information extracted from the seismic data, the geometry of the boundaries between the different types of deposits Slide U coupled with their thickness distribution and the geometry of the sliding surface (Fig. 5.45) was used to unravel the characteristics and mechanisms involved during the last stages of the Slide U event. The compiled interpretative map of the Slide U deposits (Fig. 5.49) shows the distribution of the different types of deposits and highlights both the internal features and the main transport direction inferred from the deposits. The main directions of transport inferred from lineations within the Slide U deposits varies only from NW to NNW, although locally a broader range of direction of transport can be observed. Relative transport velocities were inferred from the geometry of the boundary between different types of deposits, such as the boundary **b** between the Type I and Type II. However, it is necessary to acknowledge that deflected flow lineations that apparently suggest an area with a faster flow can indicate an area where the transport of remoulded material ceased at a later stage. , Several shear zones developed within the Slide U deposits, as a result from either transport velocity contrasts or different durations of transport. Deformation patterns within the remoulded material indicated the location, length and sense movement of the shear zones presented on the interpretative map (Fig. 5.49).

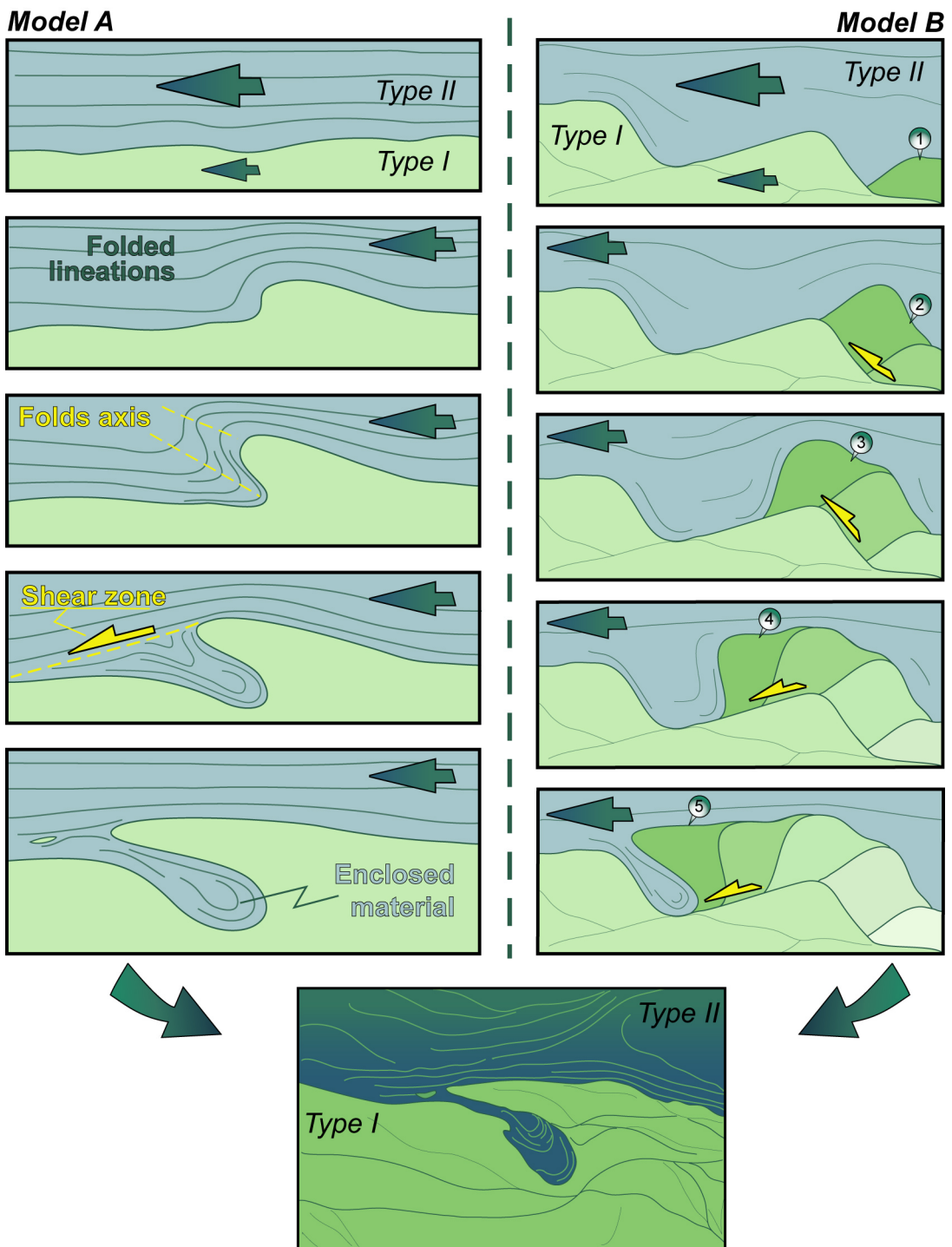


Figure 5.48: Development of Type II deposits' enclosure within the Type I deposits in plan view. Left - Model A: (1) Small irregularities along the boundary between two sediment flows with different transport velocities. (2) Initial folding of the flow boundary and flow lineations. (3) Progressive folding and development of fold axis. (4) Development of a shear zone. (5) Material enclosure and drag of part of the Type I remoulded material. Right - Model B: Successive transport of semi-rigid blocks of remoulded material Type I along the flow boundary, from position (1) to position (5). This transport is associated to shear deformation. Bottom: Graphic representation of the "enclave" shown on Figure 5.46 c. Note that the two models are at different scales and that the initial contact shape assumed for each model is different.

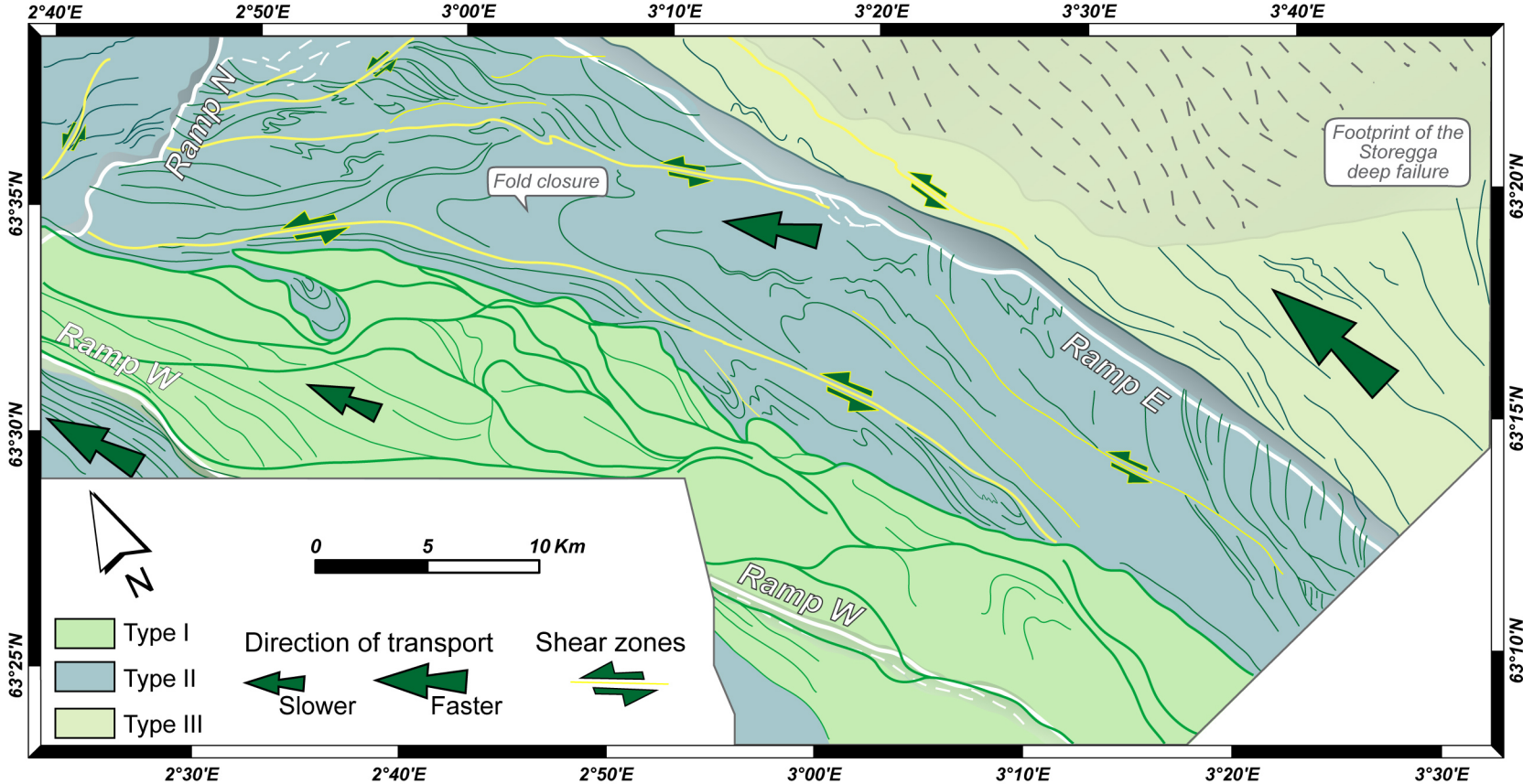


Figure 5.49: Interpretative map of the Slide U deposits showing the distribution of the different types of seismic signatures, the location of the sliding surface ramps and both the inferred directions of transport and the material deformation features. The sizes of the arrows that show direction of transport reflect its relative velocity.

Chapter 6

Deposit geometry and internal deformation

6.1 Introduction

The study of the geometry and internal structure of mass movement deposits offer an crucial insight into the processes involved and the behaviour of the remoulded material during its transport and deposition. On this chapter, aspects related to the geometry and internal deformation observed on slide deposits are debated. This discussion couples the observation from the study area with other examples presented in the literature. Special emphasis is given to sidewall collapse (section 6.2), to features along sliding surface (section 6.3), and to evidence of internal deformation (section 6.4). Some of potential implications related to the submarine mass movement deposits' geometry and internal structure are addressed in section 6.5.

6.2 Collapse of the sidewall

The sidewalls of a slope failure, also referred to as failure *lateral margins*, normally lie parallel to the main direction of transport and represent a lateral, confining boundary to the mass movement from the headwall up to the beginning of slide frontally emergent section, where material move downslope freely over the seabed. Depending of the overall structure and type of collapse, the sidewalls may only have minor superficial expression on the slide upper section or can represent marked morphological features generating a steep relief. For example, both Hinlopen and Gebra slides present sidewalls exceeding 165 m (Imbo et al., 2003; Vanneste et al., 2006, respectively) that, in the Gebra Slide case, have a mean gradient of 17° . However, these are expectational examples and most of the slope failures will generate lower relief and more gentle morphology. Regardless of whether a topographic relief is generated, the sidewalls tend to be easily recognisable on seismic profiles normally showing a discrete passage from the undistributed material to the material with acoustic signature characteristic of remoulded material (e.g. see fig. 13 in Wilson et al., 2004).

Within the slide development, the sediment thickness on its upper section tends to get thinner and the sediment package on the slide sidewalls becomes unsupported above the contemporaneous top of the failed material on that section, which may finally lead to the failure of those sediment packages as a direct result of the main failure (Ayers, 2007). This process of sidewall collapse can explain the slope failure features described in the Ch^1 compression zone at the present day seabed (see Fig. 4.10) and both on Zone R and C of the Møre Slide Complex (see Fig. 5.18). Ayers (2007) also adds that lateral collapse will occur at a shallower stratigraphic level than the main failure, dictated by the depth of support removal. However, on all cases observed on the 3D seismic volume and mentioned above, the detachment surface of the lateral collapses developed at the same or slightly higher stratigraphic level than the main failure, but deeper than the top of the failed material. This may reflect the importance of weaker layers controlling the slope instability in the study area, consistent with what has been already reported from other submarine mass movement on the Norwegian continental margin (e.g. Bugge et al., 1987; Laberg and Vorren, 2000b).

The collapse of the sidewall can be contemporaneous with the main failure, in which case it can even be considered as a particular example of retrogressive failure and part of the main event, or it can occur at a later state (e.g. Greene et al., 2006). In the case of the collapse that affected the central part of Ch^1 , it must have occurred with the emplacement of the Storegga Inner Slide Escarpment (ISE) even if the timing of the sidewall collapse is not yet well constrained in relation to the overbanking of the material from the compression zone formed by the Holocene Storegga Slide and the development of seabed Zone B (see section 4.3). By contrast, in the cases of the lateral collapse along the Møre Slide sidewall, the evidence suggests the collapses occurred during the Møre Slide main slide itself (see section 5.3). Depending on the stage of development and transport mechanism of the main failure, the laterally sourced material may be incorporated into the main flow of material. The flow lineations of the Møre Slide deposits, especially visible on seismic attribute maps like RMS amplitude (see Figs. 5.22 and 5.27), are strong evidence of the integration of the failed material from the sidewall into the main flow.

As mentioned above, in some cases the collapse of a sidewall could be considered as a particular example of retrogressive failure. Retrogressive failure is a common mechanism for submarine mass movement and can be link to different types of mass movement (from spreading, e.g. Kvalstad et al. (2005), to translational slide, e.g. Vanneste et al. (2006)). During the incipient stage the opening of free space under the headwall of the initial failure will decrease the con-

fining pressure and cause extensional fractures to form parallel to the headwall (Martel, 2004; Dykstra, 2005). Following that initial state, the headwall will propagate upslope, perpendicularly to the direction of the minimum compressive stress (σ_3) that tends to be parallel to the slope and to the main direction of transport. In the case of the sidewall collapses, failure will also respond to the decrease of confining pressure and develop perpendicular to σ_3 , however that direction will not be parallel to either the main direction of transport or to the slope direction. In fact, σ_3 can even be almost perpendicular to these directions. Therefore, the use of the orientation, geometry and internal transport of a sidewall collapse to define paleo-slopes has to be cautious especially for outcrop studies of ancient deposits. Additionally, the style of mass movement observed on a sidewall should not be used directly as an indicator of the initial style of the main slope failure.

6.3 Sliding surface

As remarked in Chapter 1 - section 1.2.1, the terminology used in the literature for submarine mass movement elements and processes is not always consistent from author to author, therefore there is a need to define some of the terms used below. *Sliding Surface* is used here to refer to all surfaces above which mass movement transport took place. These surfaces tend to correspond to the lower boundary of the remoulded material, marked by the contact between the undeformed underlying material and the mass movement deposits. However, the presence of overlying material is not a requirement to define a sliding surface since it is possible to have total removal of the material above this surface, especially on the headscar region. The *Sliding Surface* defined this way differs from the Varnes' *Rupture Surface* (1978) by also including the surface of transport beyond the frontal ramp. Figure 6.1 illustrates the four main sections of the sliding surface, from the headwall to the toe of the mass movement: 1) failure surface, 2) detachment surface, 3) frontal ramp and 4) runout surface.

The characterisation and mapping of sliding surfaces have been previously achieved using 2D seismic and echo sounder methods and, in the case of partially barren sections of this surface, using sidescan sonar and multibeam (e.g. McGregor, 1977; Laberg and Vorren, 2000b; Lastras et al., 2004b). However, these methods do not provide the 3D geometry of this basal subsurface that is only uncovered by the use of 3D seismic data. Especially in the last 5 years, studies like the ones presented by Gee et al. (2005); Frey-Martinez et al. (2006); Gee et al. (2006); Laberg and Andreassen (2007); Moscardelli and Wood (2008); Tripsanas et al. (2008) have been reveal-

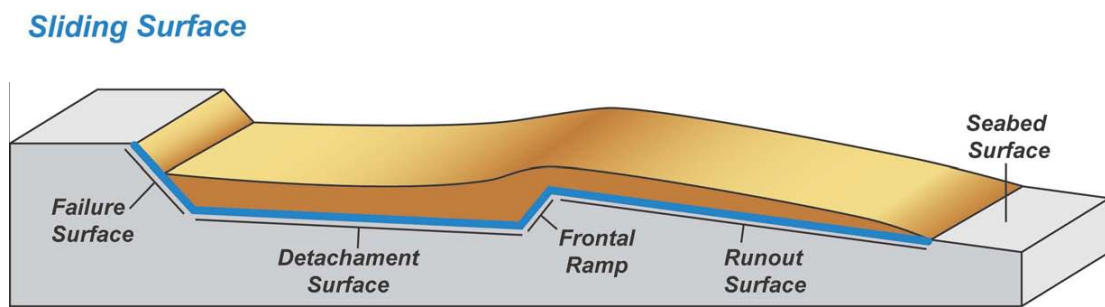


Figure 6.1: Schematic diagram of the decomposing the sliding surface into its basic four components, failure surface, detachment surface, frontal ramp and runout surface, from the headwall to the toe of the mass movement.

ing a more complex image of the submarine mass movement sliding surfaces. Both erosional and 'resistance' features have been described, varying from giant striations (Gee et al., 2005) to the presence of *in situ* blocks that resisted the surrounding erosion (Frey-Martinez et al., 2006). Special attention will be given in the following subsections to the existence of internal ramps within the detachment surface between different stratigraphic levels (subsection 6.3.1), and the presence of areas or *islands* of undisturbed material above the detachment surface (subsection 6.3.2).

6.3.1 Sliding surface ramps

Along sliding surfaces, in both ancient and modern slide deposits, abrupt changes have been recognised from one stratigraphic level to another, either up-cutting or down-cutting the sedimentary record relative to the local direction of transport of the remoulded material (e.g. Gawthorpe and Clemmey, 1985; Trincardi and Argnani, 1990; Laberg and Vorren, 2000b; Frey-Martinez et al., 2005; Solheim et al., 2005a; Garziglia et al., 2008). While more frequent in large-scale slide complex, stratigraphic *jumps* along sliding surfaces can be observed even in smaller and 'simpler' slides like the Afen Slide, offshore the Shetland Islands (Wilson et al., 2004). These stratigraphic jumps can be recognised in seismic profiles as conspicuous erosional features against which underlying seismic reflections are truncated, and in 3D view as remarkably steep ramps that connect the varying segments set at different stratigraphic levels. Although most of the up-cutting or down-cutting ramps described in the literature are mainly perpendicular to the main direction of transport, it is also possible to find detachment ramps with other orientations, including parallel to the main motion direction as was observed on the Slide U deposits and described in Chapter 5, section 5.4.

According to Gawthorpe and Clemmey (1985), if a sliding surface ramp is up-cutting or down-cutting it can be named respectively *contractional ramp* or *extensional ramp*, this relates to the compressional or extensional geometry displayed by the remoulded material. This local deformation occurs in order to accommodate for the topographic gradient of the detachment surface at the top of internal ramps (Trincardi and Argnani, 1990). This section mainly focuses on the diversity of processes and factors involved in the development of these stratigraphic jumps, and section 6.4 of this chapter gives further discussion of the deformation structures that can be found associated to the sliding surface ramps.

Sliding surface ramps can result from the failure process itself, as certain types of slidescar development generate stratigraphic jumps by a multi-phase collapse, either upwards due to retrogressive slope failure or downwards through progressive collapses. Almost all of the down-cutting, internal ramps described in the literature are interpreted as the result of retrogressive failure (e.g. Trincardi and Argnani, 1990; Wilson et al., 2004; Solheim et al., 2005a; Garziglia et al., 2008). This back-stepping failure model is widely accepted for headscarp development, and it is characterised, on sections perpendicular to the main direction of transport, by a staircase-like geometry where each of these ramps can be regarded as one of the initially developed headscarps and later truncated. This would explain the similarities between some down-cutting ramps and headwall and how deep these stratigraphic jumps can be. In the study area, the Møre Slide Complex presents several ramps sloping parallel to the direction of transport of the main Møre Slide (see Figs. 5.22 and 5.27) interpreted as the result of sidewall collapse (see Fig.5.29) and therefore, regardless of their orientations relative to the main Møre Slide, have a development similar to what is described in case of back-stepping failures.

It should be highlighted that along the main Møre Slide northern sidewall, the ramps that mark the boundary between the main Møre Slide and respectively Zone C and Zone R presents similar stratigraphic jumps from the top of the Slide U deposits to the *INU2* level, regardless of their different settings. Indeed, the ramp at the edge of Zone C does not reach more than a few meters in height (Fig. 6.2c) whereas the ramp at the edge of Zone R reaches almost 100 m (Fig. 6.2b) as a consequence of the sediment thickness variations within seismic unit VI. Additionally, these ramps are also associated to different styles of retrogressive development; whereas the sidewall collapse in Zone C quickly propagated to shallower stratigraphic levels (see Fig. 5.22) and the detachment surface in Zone R follows the *INU2* level beyond the study area. The preferential use of certain sedimentary units as sliding surfaces has already been described for some

Norwegian mass movement deposits by Solheim et al. (2005a) and Bull et al. (2009, p. 1139) has postulated that “switching between two or more preferred stratigraphic levels for the flat segments of the basal shear surface possibly reflects the availability of more than a single surface of low shear strength”. However, within the Storegga Slide region, the stratigraphic jumps occur usually between sedimentary units characterised by similar stratified seismic signatures (Solheim et al., 2005a), whereas on the ramps along the main Møre Slide sidewall the stratigraphic jumps occur between two seismic units with distinctive signatures, the top of Slide U deposits and the INU2 level that correspond to the top of a GDF’s sequence.

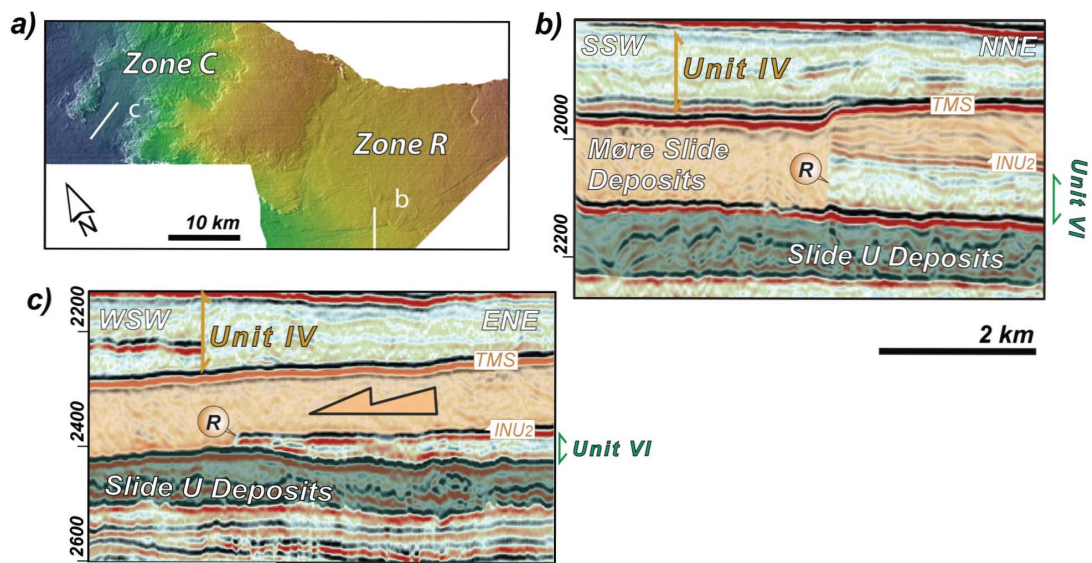


Figure 6.2: a) Shaded-relief map of the post-Møre surface DEM in ms (TWT), as displayed on fig. 5.18. b) Segment of seismic trace 2000 centred on the down-cutting ramp between Zone R and the main Møre Slide. c) Segment of an arbitrary seismic line centred on the down-cutting ramp between Zone C and the main Møre Slide. Location of both seismic lines is shown in a).

The three main ramps at the base of Slide U deposits do not present a preferential upper sliding surface or even a preferential lower sliding surface. This appears to reflect the irregular and complex geometry of the underlying stratigraphic sequence, comprised of debrites and spatial-constricted GDF deposits. They are possibly part of a complex and extensive head-scar development by retrogressive progression where the Ramp W and Ramp E, parallel to the main direction of transport, would correspond to the sidewall of adjacent lobes connected by Ramp N, perpendicular to the direction of transport. This type of orthogonal relation between headwall ramps has been already inferred by Trincardi and Argnani (1990), based on their study of the Gela Slide on the Sicily Channel, and more closely related, parallel, adjacent lobes of multi-failure are commonly observed on the northern flank of the Holocene Storegga Slide

headscar, specially along the Lower Headwalls described by Bryn et al. (2005a). However, due to the positional uncertainty of the study area in relation to the full geometry of the Slide U (see section 5.4), the exact development of these ramps is unclear, as it is also possible that these ramps resulted from down-cutting processes at the base of an initial sliding surface. Nevertheless, a development associated to retrogressive failure is favoured considering the regional sliding history and described geometry of the Ramp W and Ramp E, which independent of the complex geometry of the underlying material, present similar orientations consistent with parallel failure lobes development.

Down-cutting ramps unrelated to retrogressive development of a headscarp can result from incision and mobilisation of the underlying sediments induced by the shear stress generated along the sliding surface by the downslope mass movement. The location of these incisions and the consequent development of the down-cutting ramps can be controlled by factors related to lateral variations of the underlying material caused by the original depositional style of the sediments, which can affect the material strength or mechanical properties of the sliding surface, or by factors related with changes of shear intensity along the sliding surface (Rupke, 1976) that can generate localised erosion. A particular type of stratigraphic jump parallel to the direction of transport and an example of incision by increase in the shear intensity along the detachment surface was described for the offshore area of Trinidad by Moscardelli et al. (2006). MTC1, one of the slide deposits studied by these authors in that area, is characterised by the presence of deep, wide, erosional megascours with observed widths ranging from less than 2 km to more than 7 km, and observed lengths up to 60 km. These incisions are delimited by steep ramps that range from 33 m to less than 13 m deep (Fig.6.3) and are believed to be erosional features generated during a transitional state in which the flow was partly under confined conditions (Moscardelli et al., 2006).

Some of the controlling factors for the development of down-cutting ramps mentioned above will also control the development of up-cutting ramps. However, these ramps are mainly defined by the balance between the downslope driving stresses and the material resisting forces. The best described up-cutting ramps are the *frontal ramps*, which develop perpendicular to the main direction of transport where the material propagation along the detachment surface ceases as the downslope driving stresses become lower than the resisting forces (Varnes, 1978). At that point, dependent upon the remaining downslope inertial energy and the depth of the detachment surface, in the cases of *frontally confined* slides the displacement ceases, or in the

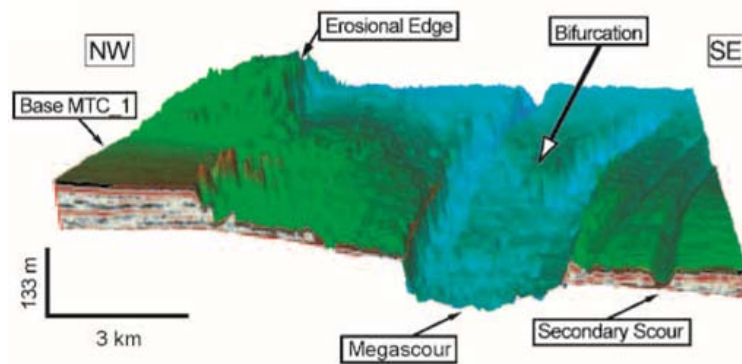


Figure 6.3: Backstripped image extracted from Moscardelli et al. (2006) showing several geomorphological elements in base of a mass movement deposit (MTC1), including the erosional edge on the west, megascours in the centre of the image, and secondary scours on the east side.

cases of *frontally emergent* slides the material over-thrust the frontal ramp and spread out over the downslope seabed. These two scenarios were proposed by Frey-Martinez et al. (2006) as being the end members of a continuum of mass movement types of evolution. Therefore, it is reasonable to think that up-cutting ramps which do not reach the seabed but truncate the stratigraphic sequence will correspond to an intermediate scenario where the presence of a shallower weak-layer or changes on material properties allowed the slide to progress only in its upper stratigraphic level.

The frontal ramps of the compression zones Ch^1 and Ch^2 (see Fig. 4.6) can be considered as good examples of *frontally confined* frontal ramps. Mainly because the mass movement did not abandon the detachment surface, the top of Tampen Slide deposits nor overcame these “formed barriers” in the frontal edge of Ch^2 and Ch^1 , respectively of ~ 185 m and ~ 165.5 m high (from the top of Tampen Slide to the undisturbed seabed). Whereas the compression zone C1 (see chapter 4, section 4.2.3) can be more likely considered as a segment of an intermediate case between *frontally confined* and *frontally emergent* slides since a major up-cutting ramp can be observed at the edge of Zone S where the Holocene Storegga deep failure abandoned the detachment surface at the top of the Slide U deposits and “climbed” up to the top of the Tampen Slide deposits (see Fig. 4.12). Then the energy associated to this movement was dissipated downslope by the deformation of sediment package of Unit I without emerging at the seabed. Færseth and Sætersmoen (2008) calculated that once the material overthrust this ramp of approximately 250 m, it propagated downslope for 1.5 km without forming a new ramp and emerging at the seabed.

6.3.2 Islands of undisturbed material

Within mass movement deposits and surrounded by deformed material, it is possible to find blocks of undisturbed, coherent sediment, which can be *in situ* or may have been transported over considerable distances. Depending of the distance and type of transport, translated blocks can be called *detached*, *rafted* or *outrunner* blocks, where *detached* blocks show minimal transport, *rafted* are transported along with the mass flow, and *outrunner* blocks can glide over long distances beyond the main failed mass (Fig. 6.4). Both *in situ* and transported blocks can normally be recognized by the contrast between areas of laterally concordant and continuous seismic facies and the often chaotic facies of the remoulded material, from which they can be isolated by steep flanks in seismic profile (e.g. Frey-Martinez et al., 2005; Gee et al., 2005). In modern deposits these blocks can also be recognised on sidescan sonar or bathymetric data as they tend to rise above the surrounding material (e.g. Masson et al., 1993, 2002b). However, with these last two methods, it is not always possible to make the distinction between *in situ* and *detached* blocks, since the definitive distinction lays in the fact that *in situ* blocks are coupled to the underlying, undeformed sedimentary succession whereas the *detached* blocks present a detachment surface.

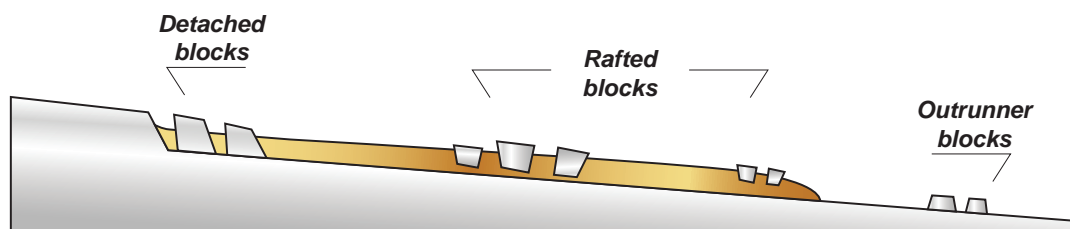


Figure 6.4: Schematic diagram showing the main location of detached, rafted or outrunner blocks relative to a slide deposit.

While the different types of translated blocks have been described and studied in several slides deposits that have contributed to a better understanding of these types of blocks (e.g. Nissen et al., 1999; Kuijpers et al., 2001; Iltad et al., 2004; Gee et al., 2005; Lastras et al., 2005; Vanneste et al., 2006), little is still known about how and why some material remain *in situ* and undisturbed within a large scale slide. Moscardelli et al. (2006) presented an interesting process of preservation of the material *in situ* above the surrounding detachment surface and highlighted the potential of such structures to act as stratigraphic traps. However, these *in situ* blocks, termed by Moscardelli et al. (2006) as “erosional shadow remnants” (Fig. 6.5), can only be formed in very particular settings since they depend on the presence of mud volcanoes

or another type of diapiric feature that could act as physiographic barriers that would prevent erosion by the passing material flow of the seabed behind it.

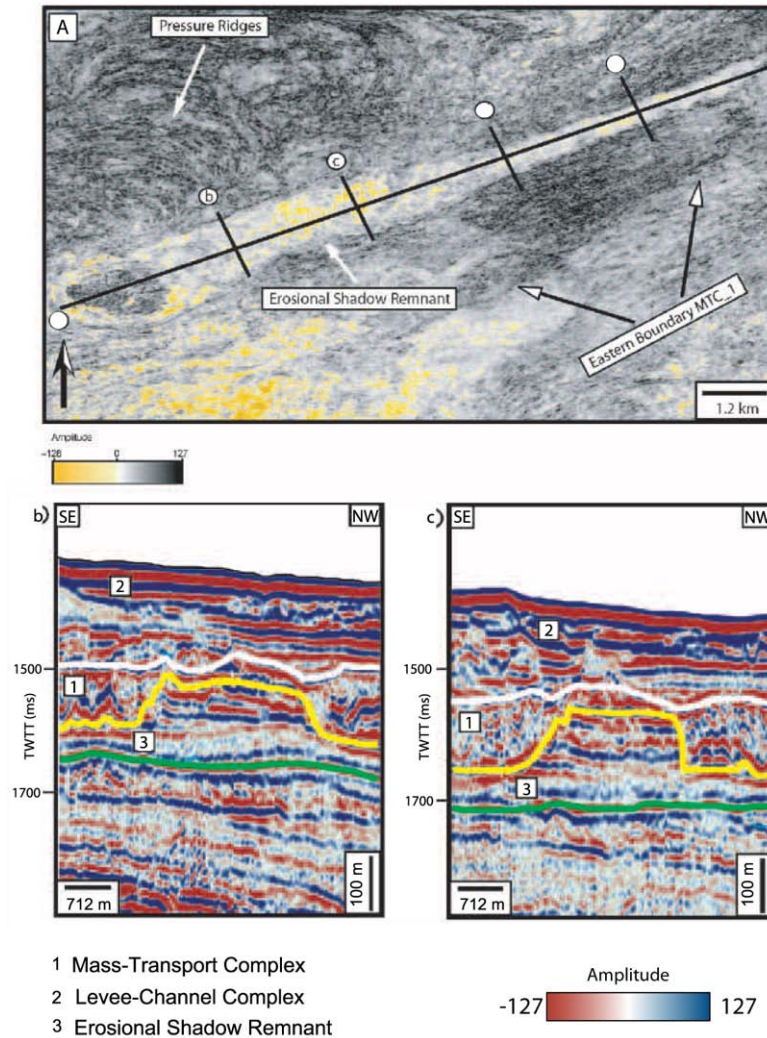


Figure 6.5: A) Coherency image showing triangular-shaped plan view geometry and high-amplitude character of a single erosional shadow remnant (ESR). B and C) Seismic lines across the ESR showing the sharp truncation along the edges. Location of the seismic lines is indicated in (A). Modified from Moscardelli et al. (2006).

Therefore it is necessary to consider other processes capable of explaining the preservation of what can be called an *island* of undistributed material within the geological settings of the studied area. The first and almost intuitive explanation would be to justify the preservation of these areas as the result of intrinsic differences in the physical properties of the sediment that could induce a local increase of the material strength. However that would not necessarily justify the cubic geometry presented by these features, neither would it be expected to have major localised variations within sedimentary packages mainly consisting of glacial debris

flow deposits. Two distinct models will be presented here that could explain respectively the isolated block of undistributed material found within Zone R of the Møre Slide Complex and the elongated area between compression zones Ch^1 and Ch^2 . Although both models assume an initial subtle lateral variation of material strength, the main processes responsible for their development are associated with the sliding events itself.

Model for the undisturbed block within Zone R

The conceptual model developed for the 1.8 km wide and 2.5 km long block of undisturbed material within Zone R of the Møre Slide Complex (see Fig. 5.26) was based on the observation of Zone C located further west on the same slide complex. Zone C is characterised by the presence of two headscars separated by a promontory that presents a narrower segment, 1 km wide (Fig. 6.6), which is also less prominent than the other segments of this ridge of undistributed material (see Fig. 5.23). This morphology is interpreted to be the result of two simultaneous retrogressive failures generated by the collapse of the main Møre Slide. However, if in Zone C the slope failure had not stopped when and where it did, it is possible to conceive that the propagation of the headwalls could induce the two headscars to merge into one. The model in figure 6.7 presents this scenario in which the propagation of two adjacent cauliflower-shaped headwall leads to the preservation of an isolated portion of the ridge which would originally have separated them (steps I to IV in Fig. 6.7). After a stage of erosion (step 1 and 2 in Fig. 6.7), this isolated block could have been sustained by the lateral support provided by the flowing remoulded material surrounding it.

This model is also supported by two additional observations. First, on seismic lines cutting through the promontory of undisturbed material, the material above the adjacent internal depositional areas shows an advanced stage of disaggregation whereas the material at depths lower than the top of the adjacent remoulded material presents steep flanks. Second, evidence of slope instability and material collapse were only found from the narrowest segment of the promontory (see Fig. 5.23b) to the upper headwall, indicating that when the mass movement ceased, the flanks of the distal area of this promontory were under relatively stable conditions.

According to this model, the isolated, remaining block would be more of a residual feature than a resistance feature. In other words, the undisturbed blocks found above the detachment surface could correspond to remains of the original sedimentary sequence mainly due to the local sliding evolution rather than a significant local increase of the sediment strength. Nevertheless,

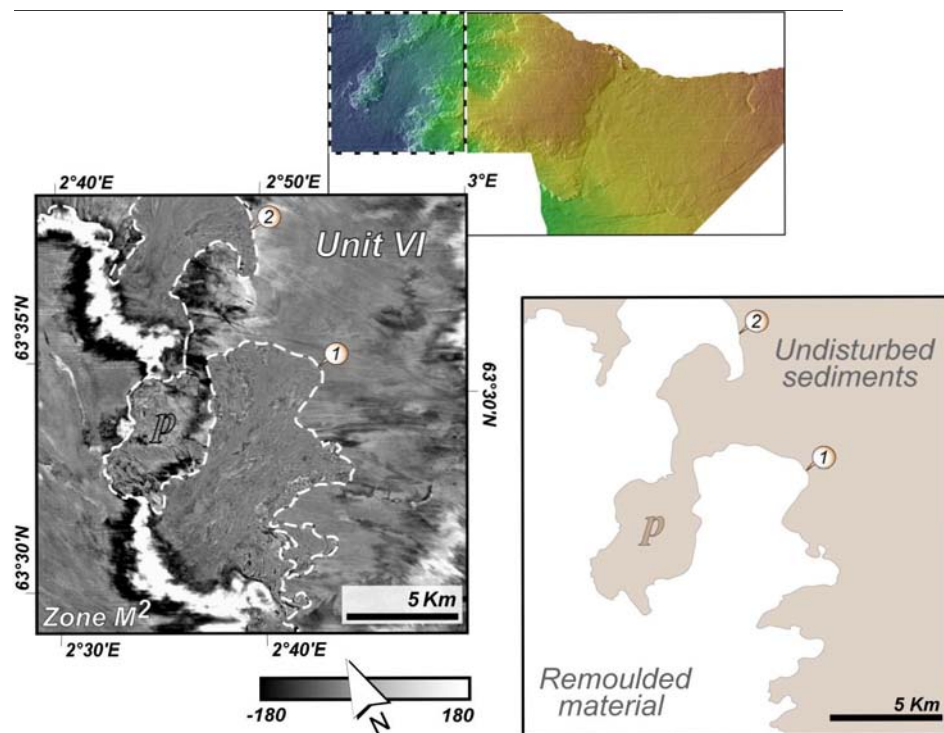


Figure 6.6: Morphology of adjacent headscars on Zone C of the Møre Slide complex. Above) Location map. Left) Time-slice at 2300 ms TWT cutting through the western edge of the MTH and the Møre Slide remoulded material. Right) Distribution map of undisturbed and remoulded material, from the 2300 ms time-slice, showing the promontory of undisturbed material (*p*) between the two retrogressive headscars (1 and 2).

this is still an hypothetical model and further work and experimental or numerical modelling would be required to properly validate this type of development of undisturbed blocks at the detachment surface.

Model for the undisturbed material around Ch^1

The conceptual model conceived for the development the elongated area of undisturbed material between the compression zones Ch^1 and Ch^2 was build upon the assumption that these two compressions, although part of the same event, occurred at different times. Compression zone Ch^1 is assumed to have developed first, followed by zone Ch^2 , this order of events would be consistent with the present and orientation of the second family of thrust observed on Ch^2 (see Fig. 4.8). Associated with the impact on the frontal ramp of the compression zone Ch^1 , a shock wave must have been formed and propagated through the surrounding material. Ground acceleration could have induced a local increase of the sediment strength around the area affected by the emplacement of Ch^1 . (REFERENCE to frequent earthquakes inducing increase

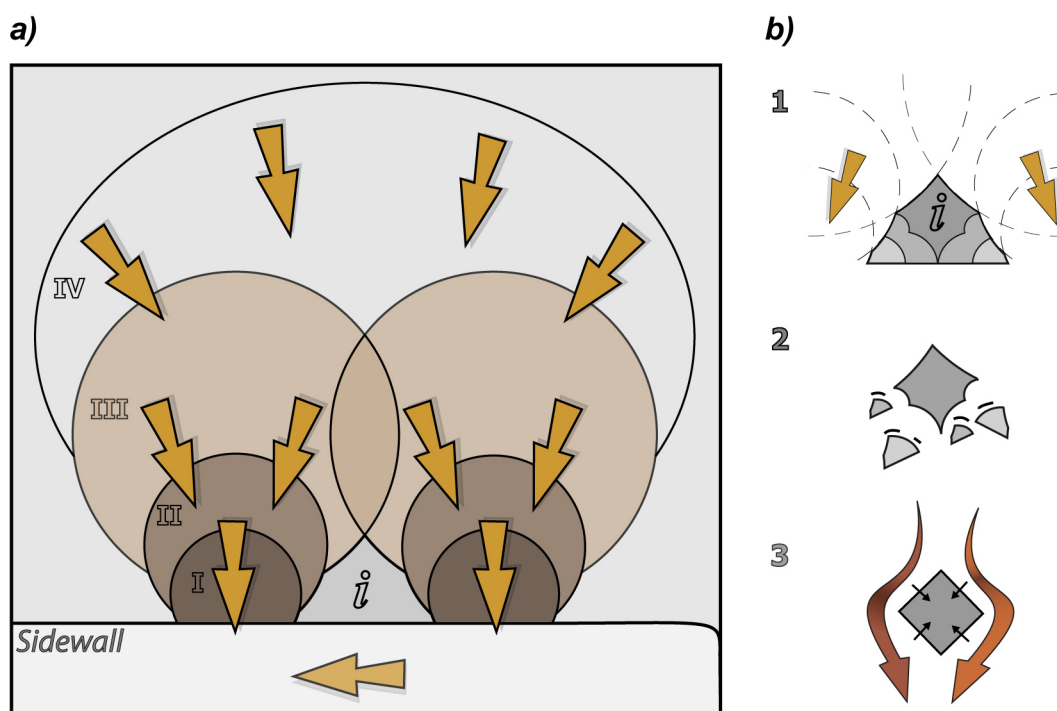


Figure 6.7: Conceptual model of development of isolated block as result of adjacent retrogressive failures. a) Retrogressive evolution of two simultaneous and adjacent cauliflower-shaped headwall, resulting of sidewall collapse (stage I), and joining into a single headwall at a final stage (stage IV). Note: the isolated block left by this process (i). b) Detail view of the evolution of the isolated block (i) marked by a stage of evolution, shown in 1 and 2, and stage 3 where that lateral support by the material. Brown arrows show main direction of transport.

of strength). This strength increase is thought to be what prevented the deformation of the material between the compression zones. This model is consistent by two further observations 1) the observed presence of an area of undisturbed material between Zone Ch^1 and Zone S (see Figs 4.5 and 4.10), and 2) Zone B, interpreted as the result of slope instability, does not reach the frontal escarpment of Ch^1 while it is reaching the frontal escarpment of Ch^2 (see Fig 4.14).

The *islands* of undisturbed material that have not experienced failure can present wide range of sizes. To some extent, the MTH could be considered as an extreme case of an *island* of undisturbed material that persisted through several slide events (Møre Slide, Tampen Slide and even Storegga Slide). And formed by buttressed remains of Unit VI material, characterised by glacial debris flow deposits but it may also have fine-grained glacial marine, hemipelagic and contouritic sediments deposited during interglacial periods. However, with the data available and the degree of deformation caused by the Holocene Storegga Slide, it is impossible to define if the MTH is indeed an *island* or if it is a large scale promontory shaped by retrogressive sliding

events along the sidewall of the Møre Slide. Regardless of being a *island* or a promontory, MTH provides an important indication of the original thickness and sediment nature in an area intensely affected by slope instability. It is quite intriguing that this massive portion of mid-Pleistocene deposits remained between the North Sea Fan and the Storegga depression and may have had some implications on the development of the Holocene Storegga Slide.

6.4 Structures of Internal deformation

Studying the internal deformation of mass movements can provide crucial information to understand the physical characteristics of the material and its kinematics. The distribution of internal deformation is one of the principal controls on the external morphology of a mass movement deposit. The internal deformation itself is dependent on the stress regime, on the mechanical properties of the sediment, on the failure style and on the morphology of the underlying surface (Strachan, 2003; Lucente and Pini, 2003). Therefore the external morphology of the final mass movement deposit depends on a combination of several factors related to (1) the dynamics of the movement (velocity, runout, coupling with the substrate), (2) variations in the lithofacies of the mass including variations in porosity, permeability, fluid saturations and fluid type (water, saltwater, gas, etc.), and (3) the morphology of the paleo-seabed (slope, roughness).

As observed in terrestrial landslides, different types of internal deformation are found in submarine mass movement deposits. Each type of deformation preferentially occurs in specific domains of the slide: extensional structures are typical close to the headwalls and above down-cutting ramps, compressional structures are mainly found at the toe region of the slide and above up-cutting ramps, and shear structures are common along the sidewalls and within the main body of the slide deposits.

Any of these three types of deformation can generate structures whose size may range from less than a few centimetres to several kilometres. However, due to the resolution of the data used in this study, only structures whose characteristic dimension are larger than 100 m are likely to be well imaged on 3D seismic. As the spatial extension of the data available for this study is mainly covering the main body of the three studied slide deposits (Tampen Slide, Møre Slide and Slide S), the main types of internal deformation observed are compressional and shear structures. They are further discussed in the following subsections.

6.4.1 Compression structures

Lateral compression conditions are typically found at the toe region of some mass movement deposit (e.g. Gawthorpe and Clemmey, 1985; Martinsen and Bakken, 1990; Trincardi and Argnani, 1990; Frey-Martinez et al., 2006; Hjelstuen et al., 2007). Farrell (1984) suggested that this compression results from the motion ceasing first at the mass movement's downslope margin, generating a compressional strain wave which propagates from the front to the rear of the unit. However, deformation by compression can also be found within other regions of the *zone of accumulation* or even further upslope, and resulting from processes other than that presented by Farrell (1984). Compressional deformation structures can be observed on the remoulded material above up-cutting ramps to accommodate the change in gradient of the sliding surface (Gawthorpe and Clemmey, 1985; Trincardi and Argnani, 1990), for example, Dykstra (2005) describes the development of thrust faults above the frontal ramp. Trincardi and Argnani (1990), using 2D seismic data to map the Gela Slide on the Sicily Channel, attribute the observed frontal confinement and compressional deformation features to the presence of a positive topographic feature, which provided the necessary resisting forces to prevent further translation. Trincardi and Argnani (1990) suggested that the sliding material movement ceased abruptly and deformed due to a compressional strain wave that propagated from the topographic obstacle. Lindberg et al. (2004), employing a combination of high-resolution seismic data, side-scan sonar imagery, and gravity cores to analyse the late Weichselian Nyk Slide, observed that the deposits of this slide present "*somewhat anomalously*" compressional ridges in the upper slide area. Lindberg et al. (2004, p. 287) attribute the compressional ridges to "*particular large-scale funnel-shape morphology defined by the Vøring Plateau slope facing the continental slope*". Finally, Garziglia et al. (2008), studying mass movement deposits in the the Rosetta province of Nile Delta, attribute the development of imbricated thrusts to the presence of the uneven and hummocky texture and to subtle positive changes in gradient (less than 2°) of the underlying topography during their emplacement.

Although their distinction is not always very clear in the literature, two main types of compressional deformation associated with submarine mass movements can be distinguished: *pressure ridges* and *syndepositional thrusting*. According to Nissen et al. (1999), *pressure ridges* are regularly spaced undulations caused by compression within the main body of the debris flow at the terminal part of the slide. Prior et al. (1982) described *pressure ridges*, hundreds of metres or more across, occurring at the downslope end of a fjord debris flow and formed due to the

reduced motion near the slide margins accompanied by continued sediment supply from further upslope. Since then several other works have described evidence for this type of deformation, for example, Laberg and Vorren (2000a) described arcuate ridges on debris-flow deposits on the Bear Island TMF interpreted as *pressure ridges*, but in this case the authors favour the hypothesis that these ridges' development was associated with flow surge rather than the decelerating model proposed by Prior et al. (1982). Moscardelli et al. (2006) also describe *pressure ridges* on mass movement deposit offshore of Trinidad and Venezuela, however according to these authors their specific occurrence is most likely associated with debris-flow confinement between sea-floor mud volcanoes.

Syndepositional thrusting implies a certain degree of coherence in the sediments that allows the propagation of the thrust structures from the sliding surface towards the top of the deposit. These thrusts tend to present fault planes generally dipping towards the headscar but, in few cases of fault planes dipping in the direction of the transport it has been demonstrated that these structures can represent back-thrusts related to larger synthetic thrusts (Martinsen and Bakken, 1990). The syndepositional thrusts have been studied on outcropping ancient deposits (e.g. Gawthorpe and Clemmey, 1985; Martinsen and Bakken, 1990; Strachan, 2008) and modern slide deposits, where they can be viewed in seismic profiles as discontinuities that can be traced through the deposit, ramping up from the basal shear surface and steepening upwards to assume a listric morphology (e.g. Frey-Martinez et al., 2006; Garziglia et al., 2008). Generally organised in an arcuate way, associated with thickening of the mass deposit and with the creation of topography on the surface of the mass movement deposit, the syndepositional thrusting commonly forms imbrications of multiple thrusts separated by zones of chaotically deformed or coherently folded material (e.g. Frey-Martinez et al., 2006; Garziglia et al., 2008; Lonergan, 2008; Hjelstuen et al., 2007; Moscardelli et al., 2006). These thrust imbrications can be observed within the different sections of a mass movement deposit, from the toe of a slide unit to the upper section, and are particularly evident in zones of rapid change of gradient of the basal shear surface (Garziglia et al., 2008) and at the distal edge of *frontally confined* slides (Frey-Martinez et al., 2006). Additionally, in their study of the mass movement deposits offshore Trinidad and Venezuela, Moscardelli et al. (2006) present imbrications generated against the northern sidewall where the material encountered lateral barriers that caused it to overthrust due of a lack of space for accommodation.

The characteristics of Zone Ch resemble some of the syndepositional, imbricate thrusting ob-

served in the cases mentioned above and it is interpreted to be the result of the deformation associated with the cessation of the mass movement and the development of a frontal ramp due to the increase in thickness of the sedimentary package above the detachment surface (see chapter 4, section 4.2.2). This type of development of imbricate thrusting can be compared, regardless of the scale differences, to the development of fold-and-thrust belts or their submarine equivalent - accretionary wedges (Fig.6.8). As in the case of fold-and-thrust belts, the question of *what is the direction of propagation of the thrust development* (i.e. foreland, hinterland or out-of-sequence) can be raised. From the geometries observed, it is not possible to give a definitive answer, however it appears more likely to have been a *hinterland* development where a sequential thrusting took place from the frontal *frozen* ramp and propagated upslope.

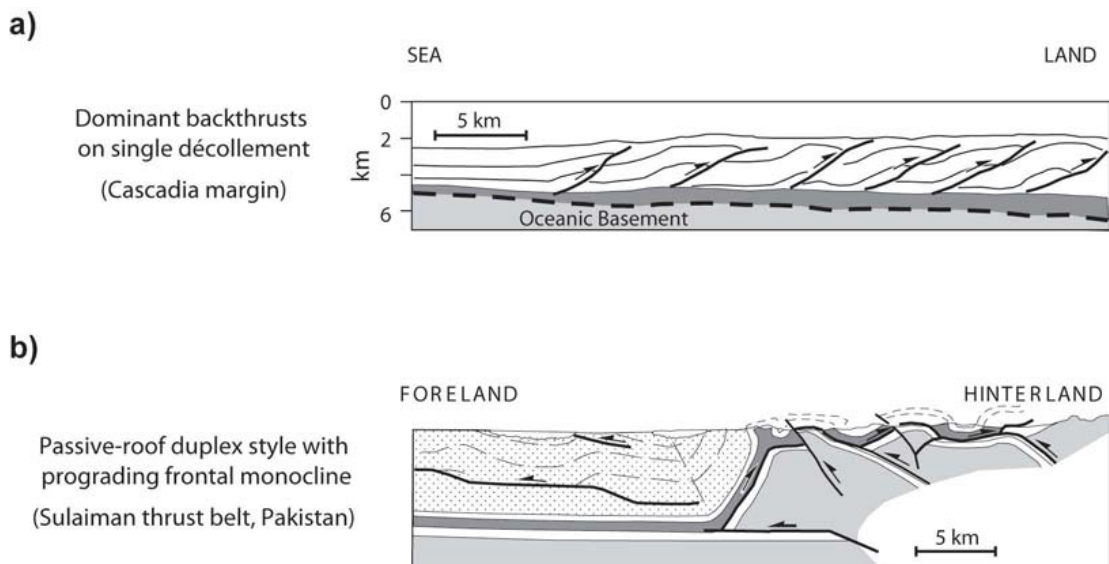


Figure 6.8: Example of main structural patterns in an accretionary prism and a fold-and-thrust belt, extracted from Bonini (2007). a) Cascadia margin. b) Sulaiman thrust belt, Pakistan.

The superficial geometry of the compression zone Ch also presents several similarities with the Nyk Slide's B-ridges described by Lindberg et al. (2004): ridges are parallel to the frontal escarpment and perpendicular to the sliding direction, and appear to die out away from the frontal edge. These similarities plus the similar nature of the remoulded material and the limited transport due to frontal confinement (on the case of Zone Ch due to the thickening of Unit I and on the case of Nyk Slide due to local seabed geomorphology) could suggest the possibility that the Nyk Slide's B-ridges were generated by internal syndepositional, imbricate thrusting. However, this hypothesis appears not be confirmed by the sparker profiles presented by Lindberg et al. (2004). Appropriate seismic profiles are required to assess the type of internal deformation present, and to assess the possibility that syndepositional, imbricate thrusting could be present

in other slide deposits previously described based only on sidescan sonar data or bathymetric data.

Although imbricate thrusting may be more common than previously thought, it is not the only style of *syndepositional thrusting* that can be found in the studied mass movement deposits. A more unusual style of deformation within mass movement, and to the author's knowledge not reported in any other described slide deposit, was presented in section 4.2.3 and 4.2.1. These two areas, which propagate beyond the study area, are characterised by symmetric thrusting that developed a series of pop-up blocks nucleated at the sliding surface and propagated upwards. Both present very similar angular relationship between conjugate thrusts but on a quite different scales. The structures on Zone S can affect a sediment package up to ~ 500 m thick, comprised of deposits of Unit VI to I (see Fig. 4.3). Further north within the same compression zone Færseth and Sætersmoen (2008) report maximum thickness of up to 700 m, whereas the structures observed on Zone Cl developed above the Tampen Slide deposits affect c. 150-350 m of sediment. This difference of thickness of the compressed sediment package appears to be a major control of the spacing between conjugate thrusts. Other differences are also observed on the deformation of the shallowest affected sediments: 1) *seabed relief* - on Zone Cl the superficial expression of the pop-up consist of parallel ridges at the edge of the blocks, whereas on Zone S the topographic relief is due to the different heights of emplacement of the individual blocks, and 2) *degree of disruption of the material* - on Zone Cl, except for the topography formed during compression there is no evidence of major changes in the characteristic of material, whereas in Zone S it is clear that there is the complete disruption of the material above the more coherent Tampen Slide deposits. Associated with the shallower material disruption, there is apparent loss of volume and it is possible that this material suffered liquefaction during the formation of the underlying pop-up blocks as the result of the enormous energy that must have been release during the compression of this thick and extensive area.

In addition to the thickness of the material affected, other factors may have controlled the main structural vergence and distribution of *syndepositional thrusting*. The previously mentioned analogy between the development of *syndepositional thrusting* and fold-and-thrust belts can help us to identify which are the main controlling factors. Scaled physical models studies, like the one presented by Bonini (2007), have shown the importance of factors like: the orientation of the principal stress (σ_1) axis, the basal friction and the displacement along the décollement. However, these factors appear to be insufficient to explain the marked differences between the

imbricate thrusting observed on the compression zone Ch and the pop-up block structure of the compression zone Cl since both cases shared similar settings, including the top of Tampen Slide deposits as the displacement/décollement surface. Factors like the rate of compression and lateral confinement may also constrain the kinematic structural development and induce *syndepositional thrusting* during collapse. Specific modelling would be required to properly assess the importance of the different factors and to quantify the energy required to develop such compression zones.

6.4.2 Longitudinal Shear Structures

Shear zones are common features of mass movements deposits. They are mainly found at the base of the deposits but they can also be observed along mass movement sidewalls or within the slide deposits between areas of remoulded material moving at different speeds, at different times, with different flow behaviour or with different material characteristics. The data used in this study did not allow the characterisation of the shear features at the sliding surface since the dimension of the shear structures formed at this interface are smaller than the data resolution. Those deformation structures are better studied from outcrop studies. However, it is possible to view and characterise some of the longitudinal shear structures using 3D seismic as they can occur on a larger scale. For these structures, 3D seismic provides the 3D geometry that can only be inferred using any other method.

Most of the shear deformation along the slide sidewalls tends to occur on a surface or in a thin shear zone at the flank of the slide. However strike-slip faults can be developed to accommodate differential motion within remoulded material on the lateral flanks of the deposits (Dykstra, 2004). In areas affected by strike-slip faulting, 3D seismic and outcrop studies reveal patterns made of sequences of en-echelon faults or faults parallel to the sidewall of the mass movement that can be mapped over several kilometres (Dykstra, 2005). Based on geophysical observations of the Slumgullion earthflow, Gombert et al. (1995) show that strike-slip faults involved in landslide faulting are analogous to those that operate in crustal-scale faulting.

In the study area, only one large scale shear zone is found in the north-western edge of the Zone R of the Møre Slide complex (see Fig. 5.31). As described in section 5.3.2 of chapter 5, the edge of the MTH corresponds to the sidewall of a retrogressive slide event and a horizon amplitude map coupled with an RMS amplitude reveal the presence of a shear zone consisting of a series of dextral strike-slip faults within an internal brittle zone developed between two ductile zones.

The blocks defined by strike-slip faults within the brittle zone show anti-clockwise rotation (see Fig. 5.32) suggesting an extensional regime. This is consistent with material removal towards the main Møre Slide and demonstrates that those structures can be used as kinematic indicators within mass movement.

Lateral variation between ductile and brittle regimes have been previously described in the literature. Factors such as material rheology, deformation rate, degree of coherence and material thickness are recognised as determining factors to define whether ductile or brittle deformation will develop in the material. Therefore, the division between ductile and brittle zones can be used, for example, to identify areas of contrasting rheology (Bull et al., 2009). As shown by Dykstra (2005) penetrative brittle deformation structures are more common in fine-grained succession. Additionally, the degree of displacement along the sidewall can also be a determining factors to define the type of deformation, with brittle deformation associated with areas of low displacement (Bull et al., 2009). In the case considered in this study, some of the factors enumerated above can be excluded: no significant lateral variation either in thickness nor in material nature is observed within the shear zone. This suggests that the rate of deformation and the degree of displacement are the main factors controlling the deformation partition in this shear zone.

It is interesting to note the similarities between the longitudinal structures described in this shear zone and the structure found in hand specimen from the base of a slide deposit presented by Yenes et al. (2009) in their study of the modern Peñalba landslide. As shown in figure 6.9, brittle deformation consisting of a sequence of dextral faults along Riedel planes, an extensional component and alternation between brittle and ductile shear are observed in both examples, independent of the major difference in dimensions and the fact that in the case of the hand specimen the observed section is perpendicular to the sliding surface while in the case described in this thesis the section is parallel. This is consistent with the fact that the same factors are controlling the development of shear zones in both settings within mass movement deposits.

Shear zones can also be observed within the main body of the mass movement in each slide of the study area. These shear zones mark the boundaries between portions of the flow with either different flow behaviour, different speeds of transport or different material properties. These boundaries can extend over several kilometres in length and through the entire thickness of the deposit. However, they present a very narrow width, quite distinct from the shear zone observed along the sidewall of the Møre Slide.

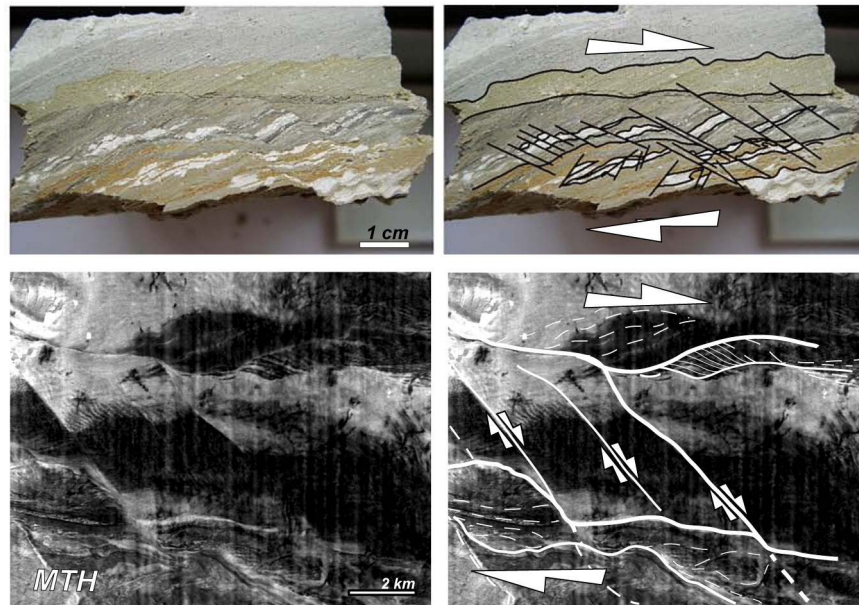


Figure 6.9: Comparison between shear zones recognised in a hand-sample and in the 3D dataset. Top row: Left) Hand-sample photograph from a cross-section showing the deformation features on the Peñalba landslide basal material. Right) Interpretation of the shear zone and its structures. Extracted from Yenes et al. (2009). Bottom row: Left) Amplitude map of the post-Møre Slide surface showing the shear zone found at the north-western edge of the Zone R. Right) Interaction of the shear zone and its structures.

Within the Tampen Slide and Slide U deposits, longitudinal shear zones extending for more than ten kilometres can be observed (see Figs. 5.17 and 5.49). In the Tampen Slide case, they are attributed to the presence of adjacent areas of material being transported at different speeds. In the case of Slide U, in addition to the difference in transport speeds, the adjacent zones also present marked differences in material properties (see section 5.4.2). Although both Tampen Slide and Slide U shear zones present similar dimensions, it should be noted that their traces in plan view are quite distinct. The Tampen Slide's shear zones are almost straight while the Slide U's shear zones present a curvilinear architecture. This is attributed to the deformation of the boundary between different types of material within Slide U.

As well as those shear zones where the sense of shear is well defined, other acoustic longitudinal lineations are also observed in this study. These lineations indicate the presence of boundaries between remoulded material, but it is not possible to infer their sense of shear. This can be due to the insufficient resolution to visualise determinative features. However, in some cases these boundaries are not believed to represent a separation between material flowing under different conditions but they most probably represent the legacy of previous separations, acting as inactive interface between two flow. The best example supporting this hypothesis is

the lineations found downslope of the block of undisturbed material in Zone R of the Møre Slide complex (see Fig. 5.26b). In this case, these lineations can be followed through several kilometres without any evidence of significant shear along their surface.

It is also observed that these lineations can be followed through changes of main direction of transport without evidence of transformation of their characteristics (see Figs. 5.27 and 5.47). This supports the supposition that these lineations are inactive interfaces as one would expect an active boundary to be affected by such changes. In extreme cases, these lineations can actually be folded as it is observed in the longitudinal folds within the Slide U deposits (see Figs. 5.46 and 5.49).

Both a) longitudinal shear zones along the sidewall and within the main body of slide deposits and b) other longitudinal lineations can provide key evidence to understand the kinematics of mass movement processes. However their interpretation must be proceed with care, since: 1) they tend to reflect local shear that may not be representative of the general trend, 2) the apparent differences in transport speed can be the result of either a effective difference in speed or from difference on the flow timing, i.e. the interface of two sections of the mass movement that ceased their motion at different times during the sliding event will resemble the interface between flow that were moving simultaneously but at different speeds, and 3) inactive boundaries can be transferred along the mass movement.

6.5 Implications of slide deposit's external geometry and internal structures

Repetitive instability

Several authors, such as Edwards et al. (1995); Lindberg et al. (2004); Wilson et al. (2004); Solheim et al. (2005a); Georgiopolou et al. (2007), have studied not only the superficial expression of modern submarine mass movement but also the underlying stratigraphic sequences, and have observed an apparent tendency to have localised repetitive failures. In other words, areas of the present-day seabed that were affected by slope instability commonly show pre-existing underlying slide deposits.

In some cases, there is strong evidence that the failure recurrence is mainly controlled 1) by trigger recurrence which may be recurrent seismicity (e.g. Adams, 1990) or 2) by the repetitive recreation of the failure preconditions, such as recurrent climatic changes (e.g. Nygård et al., 2005). However, in other cases there is an apparent absence of a particular and localised factor promoting submarine mass movement. One of the most intriguing examples of localised repetitive failure was found on the Farø-Shetland Channel. The relatively small Afen Slide, with 12 km x 4 km in size, *mimics* an older pre-existing buried slide (Long et al., 2003; Wilson et al., 2004). This almost perfect failure repetition (in location, style and dimensions; Figure 6.10) is particularly unexpected considering that very few slide deposits have been found along the sides of the Farø-Shetland Channel.

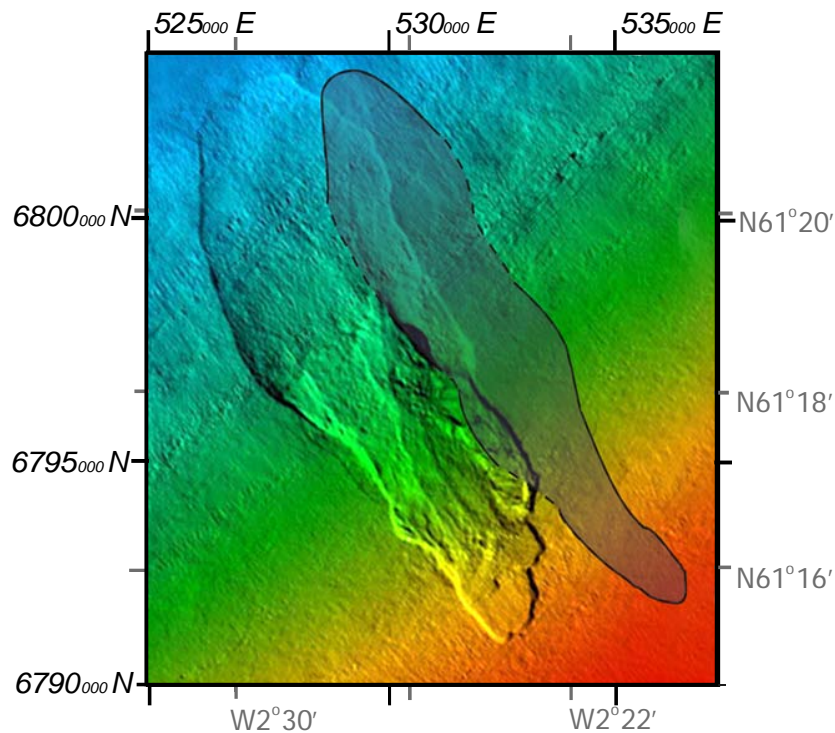


Figure 6.10: *The outline of the Palaeo-Afen Slide mimics that of the Afen Slide on the seabed. Extracted from Long et al. (2003).*

Georgiopoulou et al. (2007) presented a conceptual model of repeated slide generation due to differential sediment loading and compaction controlled by the geometry of previous slide buried escarpments. According with the proposed model, the generation of an accentuated anticline hinge lead to over-steepening and potential excess pore pressure which promoted repetitive instability . Other factors associated with pre-existing slide deposits could also promote recurrent events. Weak layers in the fine-grained sediments infilling of the slide scars can act as

detachment surfaces for younger slide (e.g. Rise et al., 2005). These examples are showing that failure re-occurrence through time on an specific location could be controlled by the external geometry of the initial slide event.

The repetitive slope instability of the North Sea Fan is believed to be mainly controlled by the recurrence of glacial periods, characterised by periods of sedimentation with high deposition rate and by ice sheets loading and unloading of the continental shelf edge (Nygård et al., 2005, see subsection 2.4.2). However the external geometry of the pre-existing slide deposits, at least on the study area, tend to play a key role on the development of the subsequent slides.

All the studied slides have used at some stage the top of a previous slide deposit as their detachment surface, as shown for example on figure 5.27c where the Møre Slide deposits directly overly the Slide U deposits. The use of the top of previous slide deposits as a preferential surface of sliding is particularly well demonstrated in the case of the southern margin of Holocene Storegga Slide at the transition from Zone S to Zone Cl, where the displacement *jumps* from a stratigraphic level set on the the top of Slide U to a stratigraphic level set on the top of the Tampen Slide (see Figs. 4.12 and 4.13). It is still unclear if the preferential use of the top of previous slide deposits is due to 1) the presence of a weak layer immediately above these deposits or to 2) the fact that previous slide deposits should present an higher internal strength than the overlying sequence of glaciogenic debris-flows deposits.

Slide deposits versus fluid migration

Discrete vertical disturbance, along which high-amplitude reflectors upward deflection and central amplitude decrease can occur, were found in seismic data used for this study (Fig. 6.11). This type of vertical disturbance on a sequence of seismic reflectors are normally referred to as *pipes* and interpreted as fluid pathways, formed by rapid migration of gas-charged pore fluids and its action may disrupt strata over a vertical section greater than 1000 m (Løseth et al., 2003). These pipe-shaped features are also reported further north in the Vøring margin (e.g. Evans et al., 1996; Bouriak et al., 2000; Bünz et al., 2003; Hustoft et al., 2007), where they tend to be more abundant and associated to fluid escape features at the seabed such as pockmarks. For example, Gay and Berndt (2007) reported 40 pockmarks craters within a area of 5000 km³ in the Vøring Plateau. However, in the case of the pipes observed in the present study, these features developed only up to the stratigraphic level of the Tampen Slide. Figure 6.11 shows one of the pipe-shaped features observed in the study area, where *up-pulling* of the *INS* and *TNS*

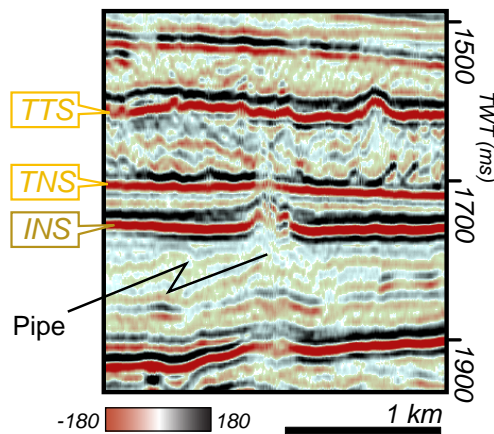


Figure 6.11: Seismic line from the 3D volume showing up-pulling and disruption of the INS and TNS reflectors due to fluid migration, which do not appear to propagate beyond the TTS stratigraphic level. INS Naust S internal reflector; TNS Top of Naust S reflector, which on this location corresponds to the base of the Tampen Slide deposits; TTS: Top of the Tampen Slide.

reflectors suggesting fast-flowing vertical movement rather than pure diffusive fluid migration processes. The *up-pulling* effect on the seismic velocity could also be caused by a seismic velocities increase as a result of consolidation due to the precipitation of carbonate precipitates within the pipe or gas hydrates (Gay and Berndt, 2007). On this figure a focus amplitude decrease can be seen downwards the TNS reflectors, whereas the reflectors above TNS do not show any significant evidence of disruption or alteration in their geometry or seismic character.

Although a single pipe may reflect several active periods, the timing of the most recent seep activity can be indicated by its upper termination (Hustoft et al., 2007). In the case of the study area, this would suggest three possible scenarios: 1) the pipes were active and pierced the seafloor before the Tampen Slide event during the Saalian glacial period; 2) the pipe structures are of post-Saalian age, but the excess pore pressure was dissipated when the pipes reached the stratigraphic level of the Tampen Slide deposits; or, 3) the pipes are of post-Saalian age, but the Tampen Slide deposits form a barrier to flow, preventing further advance of the fluid pressure front. In the last scenario, the internal structure of Tampen Slide deposits may have interfered with fluid migration through the sedimentary column and served as a barrier by diffusion of the fluid flow through interconnected discontinuities with the remoulded material. This third scenario would have to be favoured if it is shown that the fluid migration history in the study area mimics the fluid migration history observed on the northern flank of the Storegga Slide.

Chapter 7

Summary and Conclusions

7.1 Key points of the thesis

This study consists of the morphological characterisation of mass-movements processes that occurred from the Mid-Pleistocene to the Holocene on the northern flank of the North Sea Fan. This was made possible by the study of 3D seismic data that allowed the imaging and interpretation of the external geometry and internal structure of the buried slide deposits as well as the features at the seabed.

The most commonly used tool to describe and characterize buried, large-scale slide deposits has been 2D seismic profiling. This has led to these deposits commonly being described as chaotic or structureless in order to distinguish them from the reflector-rich sedimentary sequences from which they may be derived. However, interpretation of 3D seismic data reveals that slide deposits are far from having structureless or chaotic acoustic internal character.

This study involved both seismic interpretation of 3D seismic and spatial analysis of the extracted surfaces. Detailed and interactive picking of the key reflectors was followed by the extraction of horizon and window-based seismic attribute maps. The digital elevation models of the key reflectors and their seismic attribute maps were then transferred to a GIS environment where they could be interactively interpreted using the full visualisation potential of the software. The geomorphological interpretation was enhanced by the use of the software's spatial analysis tools.

Marked differences in external geometry and internal seismic character were observed between each slide deposit studied. Their main characteristics and observations are summarised below:

Seabed - The seabed of the study area was most-recently shaped by generation of compression zones associated with the Storegga Slide Complex. Several sequences of ridges found at the seabed, which are the superficial expressions of different systems of *syndepositional thrusting*.

Tampen Slide - The internal structure of the Tampen Slide deposits is characterised by penetrative acoustic discontinuities within the remoulded material defined by low-amplitude values.

These discontinuities define different fabrics recognisable in both horizon and windowed amplitudes maps and in spatial analysis maps generated from the top of the slide surface. The distribution of differing fabrics within the Tampen Slide deposits has been greatly influenced by the presence of the Møre Topographic High. *Møre Slide* - The Møre Slide presents a complex distribution of sidewall collapses showing a large variety of failure processes. This complex setting generated marked variations of deposits thickness, different flow behaviours and the development of several features along sliding surface (e.g. stratigraphic ramps and blocks of undisturbed material).

Slide U - Marked heterogeneities in the nature of the remobilised sediments can be observed in Slide U deposits. The transport of material during this mass movement was influenced by development ramps parallel and perpendicular to the direction of transport and by the interactions between the different types of remoulded material.

Assuming that the preconditions for these slides and the nature of the material affected were similar, the marked differences on the geometry and the internal features between the deposits these slides are thought to be primarily controlled by the relative position of the studied area in regard with their respective headscars. Although, the study area covers only small parts of any of the major slides, it does cover: 1) the toe area for the frontally confined slide and part of the southern sidewall of the Storegga Slide, 2) the Tampen Slide's main zone of material transport, 3) the sidewall of the Møre Slide and, possibly, 4) an area near the headwall of Slide U. Although the remoulded material probably presented relative similar initial characteristics, different amounts of displacement, levels of disaggregation and rates of deformation have induced the distinctive differences observed. Additionally, the distinct conditions under which each slide motion ceased is another aspect that leads towards the diversity observed.

The internal structure of a mass movement deposit depends on 1) the stress regime, 2) the mechanical properties of the remoulded sediment and 3) the morphology of the underlying surface. Therefore, the internal structure of a mass movement deposit results from the combination of various factors related to the dynamics of the mass movement (velocity, thickness, interaction with the underlying surface), variations in the nature of the mass flow (lithology, porosity, fluid saturation, cohesion) and the characteristics of the underlying morphology (slope, aspect, smoothness). The studied internal structures are thought to provide reliable new insights into mass flow behaviour and transport direction, for the final stages of the mass movement.

The mode of emplacement of slide deposits can be revealed by the architecture of some types of features described in this work. Features like flow lineations and longitudinal shear-zones can be considered reliable kinematic indicators. However, the observed complexity of the studied deposits highlights the risks associated with the use of such features as kinematic indicators if their geometry is not fully understood. The three-dimensional characterisation of some of these features is crucial to their interpretation, yet not always possible in other study approaches, such as the study of outcrop deposits.

The outcomes of this study highlight the importance of detailed horizon picking and interactive interpretation followed by spatial analysis and visualisation in GIS environment. The identification of acoustic patterns within deposits that are normally described from 2D seismic as chaotic or acoustically transparent highlight the potential of detailed analysis of 3D seismic data. This gives an example of how this type of data can provide new insights into the mechanisms and processes associated with mass movements. In particular, amplitude and RMS amplitude maps provided remarkable detailed information of internal deformation structures whereas slope, shaded-relief and thickness maps allowed detailed characterisation of the external geometry. Various types of kinematic indicators can be recognized within the mass movement deposits through combined seismic analysis and detailed morphological mapping. Finally, the use of 3D seismic can enhance the conceptual model of mass movements.

7.2 Further work

Potential research routes for the study of submarine mass movements and the better understanding of these processes include the following:

- The North Sea Fan is mainly comprised of sequences of glacial debris-flows and slide deposits. This study provides several detailed analysis of these slide deposits. A natural continuation of this work would be to apply the same approach to the study glacial debris flows deposits. The ability given by the 3D seismic to extract information from the base of these deposits can reveal impressive insight to the transport mechanisms acting

during these mass movements as shown, for example, by the amplitude map of INS on figure 7.1. The study of the glacial debris-flow deposits would also provide a better understanding of how these different submarine mass movements interacted and contributed to the evolution of the North Sea Fan.

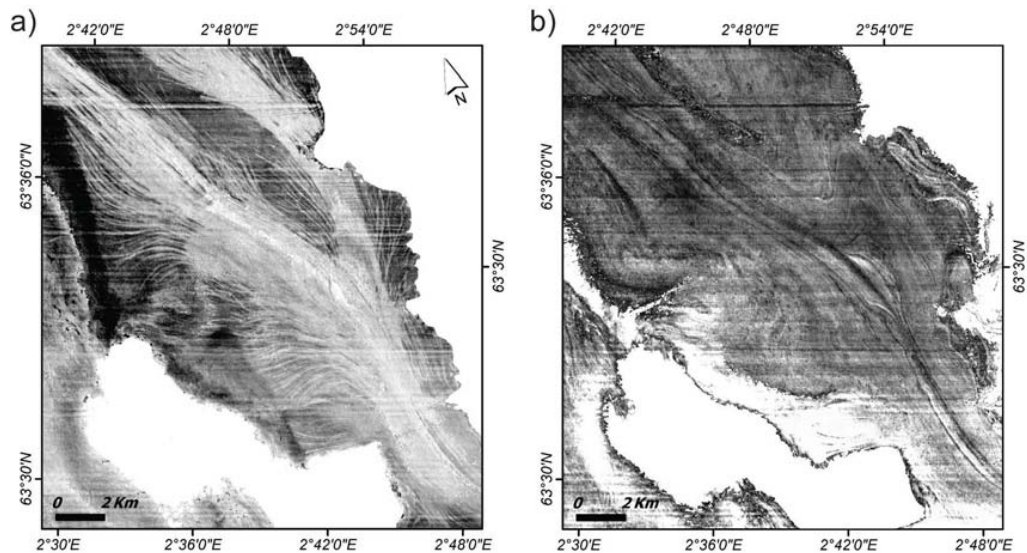


Figure 7.1: Amplitude maps of the **a)** base and **b)** top of the glacial debris-flow deposits Unit III. Amplitude variations show a textbf feather-like pattern at the base of the glacial debris-flow deposits, which can be flow lineations displayed at the top of those deposits. White: low amplitudes, black: high amplitudes. Areas totally in white correspond to textbf no data areas due to the absence of those deposits.

- The North Sea Fan has experienced repetitive and cyclic large-scale events of slope instability since the Mid-Pleistocene. However, the thick sequence of late Weichselian debris-flow deposits that accumulated on this region has not been affected by any large scale failure at the end of the last glacial maximum. It is not understood how the slope instability during the Holocene Storegga Slide did not propagate across the North Sea Fan, which only disrupted its northern flank. This stability is in contrast to the earlier major slides that are seen on the North Sea Fan which clearly extended into the Storegga region, although it is not known how far they once extended. Further investigation could assess if the presence of large undisturbed area of material more consolidated than the above material like the Møre Topographic High could have contributed to the slope stability of the fan.
- Better understanding of the development of the compression zone Ch is required to re-

assess the model of the Holocene Storegga Slide. The observations presented in this work are apparently inconsistent with the retrogressive models presented by Haffidason et al. (2004) and Bryn et al. (2005a). In their study, this compression zone is the result of either the impact due to failure within the Ormen Lange area or to lateral compression associated with a later retrogressive collapse of the southern edge of the Storegga inner slide escarpment. However, this thesis' observations support the hypothesis of a source of material located upslope of the study area. Further investigation is needed to constrain more precisely the origin of the compression zone.

- The detailed analysis of the 3D seismic data has proven to be a powerful tool to study mass movement deposits, but not without its limitation. This method is best suited for viewing large-scale structures (larger than 100 meters), can be subject to ambiguity of interpretation and cannot identify sedimentary variations that are not translated into different acoustic properties. By contrast, outcrops field studies of ancient submarine mass movement deposits (normally done at metric to centimetric scale) provide a direct and detailed source of information on internal structures and depositional processes. However, most of the outcrop studies only provide a discontinuous record along scattered vertical cuts. Therefore, it is difficult to relate the lateral and vertical changes in the internal deformation to the overall geometry of the bodies. As the 3D seismic studies' main advantages are complementary to the field study approach, the comparison between similar observations provided by both methods could improve the understanding of mass movement deposits and their processes.
- Through this thesis, several examples have demonstrated that detailed study of 3D seismic data from buried slide deposits can greatly contribute to the understanding of mass movement processes. An increasing number of 3D seismic survey have been acquired in recent years, providing a larger number of datasets potentially available for the study of slide deposits in other geological settings. Since those datasets are mainly acquired by the oil and gas companies, collaboration between academia and the industry on the model of this thesis should be continuously promoted.

Appendix A

Tulipan Survey Header

C01 CLIENT= STATOIL, PROCESSED BY=CGG NORGE, OSLO PROC.CENTRE, CREW 103N1GK
C02 INLINE: 2000 SURVEY: ST0105
C03 AREA: PL 251 NOCS BLOCKS 6302/6,9 AND 6303/7,8 MOERE WEST
C04 DATA FORMAT: SEG-Y DATE:09/01-2002 TAPE: 4755
C05 DATA TYPE: FULL OFFSET VOLUME FINAL 3D MIGRATED STACK
C06 GEODETIC DATUM: ED 1950 SPHEROID: INTERNAT. PROJECTION: UTM
C07 CENTR. MERID.: 03 UTM ZONE: 31 N, FALSE EASTING: 500000
C08 FIRST SAMPLE= 4 MS LAST SAMPLE= 6996 MS SAMPLE INTERVAL 4 MS
C09 DISTANCE BETWEEN INLINES=12.5M,CROSSLINES=12.5M BIN SIZE:12.5m x 12.5m
C10 INLINE DIRECTION (GRID): 296.0000000 DEGREES (CLOCKWISE FROM NORTH)
C11 CROSSLINE DIRECTION (GRID): 26.0000000 DEGREES (CLOCKWISE FROM NORTH)
C12 ORIGO(1.1): UTM-X AT: 521811.04 M UTM-Y AT: 6975712.41 M
C13 DATA RANGE: INLINES=(2000-4546) (INC 1), CROSSLINES=(0498-5670) (INC 1)
C14 CORNER1:3D INLINE 2000,3D CROSSLINE 0498,UTM-X 527181.09,UTM-Y 7000894.40
C15 CORNER2:3D INLINE 2000,3D CROSSLINE 5670,UTM-X 469074.05,UTM-Y 7029235.10
C16 CORNER3:3D INLINE 4546,3D CROSSLINE 5670,UTM-X 483025.21,UTM-Y 7057839.22
C17 CORNER4:3D INLINE 4546,3D CROSSLINE 0498,UTM-X 541132.25,UTM-Y 7029498.52
C18 LIVE DATA POLYGON: (DESCRIPTION WITH CELL ID (INLINE#,CROSSLINE#)
C19 (4546,0498), (4546,5670), (2956,5670), (2956,3385), (2512,3272),
C20 (2280,3272), (2098,3205), (2000,3205), (2000,1580), (3077,0498)
C21.
C22 NAVIGATION SOURCE: P1/90 UKOOA BIN CENTER CELL GRID
C23 PROCESSING SEQUENCE:REFORMAT & RESAMPLE FROM 2MS TO 4MS & SEISMIC/NAV.MERGE&
C24 EDITS & LOW CUT FILTER & ZERO PHASE CONVERSION & SPHERICAL DIVERGENCE
C25 CORRECTION & IMPULSIVE NOISE ATTENUATION & INV PHASE Q185 & NORMAL MOVEOUT CORR &
C26 (REGIONAL FUNCTION) & FK ANTIALIAS FILTER & ALTERNATE TRACE DROP &
C27 RVS NORMAL MOVEOUT CORRECTION & 2D CMP SORT & NORMAL MOVEOUT CORRECTION (1KM) &
C28 PARABOLIC RADON DEMULTIPLE & SORT TO 50 OFFSET CLASSES & INTELLIGENT BINNING

Tulipan Survey Header

C29 FLEX: CLASS 1 - 100%; CLASS 50 - 200%) & 3D DMO & FX-INTERPOLATION
C30 (INTERPOLATING 1 INL.) & PSTM & RVS NORMAL MOVEOUT CORRECTION & NORMAL MOVEOUT
C31 CORRECTION (250M)& AMPLITUDE VS OFFSET CORRECTION & OUTER AND INNER MUTE &
C32 STACK & DEMIGRATION& DECONVOLUTION AFTER STACK & 3D FX TIME MIGRATION &
C33 GLOBAL EXPONENTIAL SCALING & TIME VARIANT FILTER & OUTPUT RAW MIGRATION SEG-Y
C34.
C35 HEADER WORD POSITIONS:
C36 3D INLINE IN BYTES 005-008. 3D CROSSLINE IN BYTES 021-024
C37 BIN CENTER UTM-X IN BYTES 181-184. BIN CENTER UTM-Y IN BYTES 185-188
C38 POLARITY:NEG ZERO PHASE DATA - A NEGATIVE SAMPLE CORRESPONDS TO AN INCREASE
C39 IN ACOUSTIC IMPEDANCE AND DISPLAYS AS A TROUGH (WHITE)
C40 END EBCDIC

Bibliography

- Adams, J. (1990). Paleoseismicity of the Cascadia subduction zone: Evidence from turbidites off the Oregon-Washington margin. *Tectonics*, 9:569–583. 10, 164
- Assier-Rzadkiewic, S., Heinrich, P., Sabatier, P. C., Savoye, B., and Bourillet, J. F. (2000). Numerical modelling of a landslide-generated tsunami: The 1979 Nice event. *Pure and Applied Geophysics*, 157:1707–1727. 7
- Atakan, K. and Ojeda, A. (2005). Stress transfer in the Storegga area, offshore Mid-Norway. *Marine and Petroleum Geology*, 22:161–170. 37
- Atigh, E. and Byrne, P. M. (2003). *Flow liquefaction of submarine slopes due to monotonic loadings-an effective stress approach*, volume 19 of *Advances in the Natural and Technological Hazards Research*, pages 3–10. Kluwer Academic Publishers, Dordrecht, Netherlands, 1st edition. 7
- Ayers, S. (2007). White Paper: Some observations related to submarine slides and a basic approach for event-based seismostratigraphic interpretation of slide affected sequences on passive margins. In *Addressing Geologic Hazards Through Ocean Drilling Workshop*, pages 1–7, Portland. IODP. 6, 143
- Badley, M. E., Price, J. D., Rambech, D., and Agdestein, T. (1988). The structural evolution of the northern Viking Graben and its bearing upon extensional modes of basin formation. *Journal Geological Society*, 145:455–472. 16
- Barnes, A. E. (2006). Too many seismic attributes? *CSEG Recorder*, 31:40–45. 44
- Barnes, A. E. (2007). Redundant and useless seismic attributes. *Geophysics*, 72:P33. 44
- Batson, R., Edwards, K., and Eliason, E. (1975). Computer generated shaded relief images. *US Geol. Sur. Res*, 3:401–408. 47
- Bea, R., Wright, S. G., Sircar, P., and Niedoroda, A. W. (1983). Wave-induced slides in South Pass Block 70, Mississippi Delta. *Journal of Geotechnical Engineering*, 109:619–644. 7
- Berger, W. and Jansen, E. (1994). Mid-Pleistocene climate shift-the Nansen connection. *Geophysical Monograph - American Geophysical Union*, 85:295–295. 18

- Blystad, P., Brekke, H., Færseth, R., and Larsen, B. (1995). Structural elements of the Norwegian continental shelf. Part II: The Norwegian Sea region. *Norwegian Petroleum Directorate Bulletin*, 8. 16
- Bonini, M. (2007). Deformation patterns and structural vergence in brittle-ductile thrust wedges: An additional analogue modelling perspective. *Journal of Structural Geology*, 29:141–158. xiii, 158, 159
- Booth, J. S., O’Leary, D. W., Popenoe, P., and Danforth, W. W. (1993). US Atlantic continental slope landslides; their distribution, general attributes, and implications. *USGS Bulletin*, 2002:14–22. 1
- Bouriak, S., Vanneste, M., and Saoutkine, A. (2000). Inferred gas hydrates and clay diapirs near the Storegga Slide on the southern edge of the Vøring Plateau, offshore Norway. *Marine Geology*, 163:125–148. 165
- Brown, A. R. (1996). *Interpretation of three-dimensional seismic data*, volume Memoir 42. AAPG, Tulsa, Oklahoma, USA. 42, 44
- Brown, A. R. (2005). Pitfalls in 3D seismic interpretation. *The Leading Edge*, 24:716–717. 44, 46
- Brune, S. (2009). *Landslide generated tsunamis: numerical modeling and real-time prediction*. Phd, University of Potsdam. 9
- Brunsdon, D. and Prior, D. B. (1984). *Slope instability*. Wiley. 2
- Bryn, P., Berg, K., Forsberg, C. F., Solheim, A., and Kvalstad, T. J. (2005a). Explaining the Storegga Slide. *Marine and Petroleum Geology*, 22:11–19. ix, 10, 36, 67, 148, 171
- Bryn, P., Berg, K., Stoker, M. S., Hafliðason, H., and Solheim, A. (2005b). Contourites and their relevance for mass wasting along the Mid-Norwegian Margin. *Marine and Petroleum Geology*, 22:85–96. 34
- Bryn, P., Solheim, A., Berg, K., Lien, R., Forsberg, C. F., Hafliðason, H., Ottesen, D., and Rise, L. (2003). The Storegga Slide complex; Repeated large scale sliding in response to climatic cyclicity. In Locat, J. and Mienert, J., editors, *Submarine Mass Movements and Their Consequences: 1st International Symposium*, volume 19 of *Advances in the Natural and Technological Hazards Research*, pages 215–222. Kluwer Academic Publishers, Dordrecht, Netherlands, 1st edition. 29, 31, 34, 137

- Bugge, T. (1983). *Submarine Slides on the Norwegian Continental Margin with Special Emphasis on the Storegga Area*. PhD thesis, Norwegian University of Science and Technology. 34, 53
- Bugge, T., Befring, S., Belderson, R. H., Eidvin, T., Jansen, E., Kenyon, N. H., Holtedahl, H., and Sejrup, H. P. (1987). A Giant Three-Stage Submarine Slide Off Norway. *Geo-Marine Letters*, 7:191–198. 143
- Bugge, T., Belderson, R. H., and Kenyon, N. H. (1988). The Storegga slide. *Phil. Transact. R. Soc. London*, 325:357–388. 34
- Bulat, J. and Long, D. (2001). Images of the seabed in the Faroe-Shetland Channel from commercial 3D seismic data. *Marine Geophysical Researches*, 22:345–367. 49
- Bulat, J. and Long, D. (2007). Recommended operating guidelines (ROG) for 3D. 48
- Bull, S., Cartwright, J., and Huuse, M. (2009). A review of kinematic indicators from mass-transport complexes using 3D seismic data. *Marine and Petroleum Geology*, 26:11321151. 92, 147, 161
- Bünz, S., Mienert, J., and Berndt, C. (2003). Geological controls on the Storegga gas-hydrate system of the mid-Norwegian continental margin. *Earth and Planetary Science Letters*, 209:291–307. 165
- Canals, M., Lastras, G., Urgeles, R., Casamor, J. L., Mienert, J., Cattaneo, A., De Batist, M., Hafidason, H., Imbo, Y., and Laberg, J. S. (2004). Slope failure dynamics and impacts from seafloor and shallow sub-seafloor geophysical data: case studies from the COSTA project. *Marine Geology*, 213:9–72. 4, 5, 8
- Cartwright, J. A. and Dewhurst, D. N. (1998). Layer-bound compaction faults in fine-grained sediments. *GSA Bulletin*, 110:1242–1257. 41
- Cashman, K. V. and Popenoe, P. (1985). Slumping and shallow faulting related to the presence of salt on the Continental Slope and Rise off North Carolina. *Marine and Petroleum Geology*, 2:260–271. 7
- Chopra, S. and Marfurt, K. J. (2005). Seismic attributes - a historical perspective. *Geophysics*, 70:3SO—28SO. 44

- Coleman, J. M. and Prior, D. B. (1988). Mass Wasting on Continental Margins. *Annual Review of Earth and Planetary Sciences*, 16:101–119. 53
- Coleman, J. M., Prior, D. B., Garrison, L. E., and Lee, H. J. (1993). Slope failures in an area of high sedimentation rate: offshore Mississippi River Delta. In Schwab, W. C., Lee, H. J., and Twichell, D. C., editors, *Submarine Landslides: Selected Studies in the U.S. exclusive economic zone*, Bulletin, pages 79–91. U.S. Dept. of the Interior, U.S. Geological Survey, 2002 edition. viii, 4, 7
- Corporation, L. G. (2004). ZAP! Technical report, Landmark Graphics Corporation, Building 1, Suite 200, 2101 CityWest, Houston, Texas 77042, USA. 42, 43
- Dahlgren, K. I. T., Vorren, T. O., Stoker, M. S., Nielsen, T., Nygård, A., and Sejrup, H. P. (2005). Late Cenozoic prograding wedges on the NW European continental margin: their formation and relationship to tectonics and climate. *Marine and Petroleum Geology*, 22:1089–1110. viii, 14, 15, 23
- Dalland, A., Worsley, D., and Ofstad, K. (1988). A lithostratigraphic scheme for the Mesozoic and Cenozoic succession offshore mid-and northern Norway. *Norwegian Petroleum Directorate Bulletin*, 4:65. 22
- Dalley, R. M., Gevers, E. C. A., Stampfli, G. M., Davies, D. J., Gastaldi, C. N., Ruijtenberg, P. A., and Vermeer, G. J. O. (1989). Dip and azimuth displays for 3D seismic interpretation. *First Break*, 7:86–95. 44
- Dan, G., Sultan, N., and Savoye, B. (2007). The 1979 Nice harbour catastrophe revisited: Trigger mechanism inferred from geotechnical measurements and numerical modelling. *Marine Geology*, 245(1-4):40–64. 9
- Davies, R. J. and Posamentier, H. W. (2005). Geologic processes in sedimentary basins inferred from three-dimensional seismic imaging. *GSA Today*, 15:4–9. 41
- Davies, R. J., Stewart, S. A., Cartwright, J. A., Lappin, M., Johnston, R., and Fraser, S. I. (2004). 3D Seismic Technology: Are We Realising Its Full Potential? *Geological Society, London, Memoirs*, 29:1–10. 41
- Deplus, C., Le Friant, A., Boudon, G., Komorowski, J. C., Villemant, B., Harford, C., Ségoufin, J., and Cheminée, J. L. (2001). Submarine evidence for large-scale debris avalanches in the Lesser Antilles Arc. *Earth and Planetary Science Letters*, 192:145–157. 1

- Doré, A. G., Lundin, E., Fichler, C., and Olesen, O. (1997). Patterns of basement structure and reactivation along the NE Atlantic margin. *Journal of the Geological Society*, 154:85–92. 16
- Doré, A. G., Lundin, E., Jensen, L. N., Birkeland, O., Eliassen, P. E., and Fichler, C. (1999). Principal tectonic events in the evolution of the northwest European Atlantic margin. In Fleet, A. J. and Boldy, S. A. R., editors, *Petroleum Geology of Northwest Europe: Proceedings of the 5th Conference*, pages 41–61, Bath. Geological Society, London. viii, 15, 16, 17
- Dorn, G. A. (1998). Modern 3-D seismic interpretation. *The Leading Edge*, 17:1262–1272. ix, 42, 43, 45
- Dott, R. (1963). Dynamics of subaqueous gravity depositional processes. *AAPG Bulletin*, 47:104–128. 3, 4
- Dowdeswell, J. A., Elverhøi, A., and Spielhagen, R. (1998). Glacimarine sedimentary processes and facies on the Polar North Atlantic margins. *Quaternary Science Reviews*, 17:243–272. 18
- Dowdeswell, J. A., Kenyon, N. H., Elverhøi, A., Laberg, J. S., Hollender, F.-J., Mienert, J., and Siegert, M. J. (1996). Large-scale sedimentation on the glacier-influenced Polar North Atlantic margins: Long-range side-scan sonar evidence. *Geophysical Research Letters*, 23:3535–3538. 1, 18
- Dugan, B. and Flemings, P. B. (2000). Overpressure and Fluid Flow in the New Jersey Continental Slope: Implications for Slope Failure and Cold Seeps. *Science*, 289:288–291. 7
- Dykstra, M. (2004). Review of mass-transport: processes and products. 2, 160
- Dykstra, M. (2005). *Dynamics of submarine sediment mass-transport, from the shelf to the deep sea*. Phd, University of California - Santa Barbara. 1, 139, 144, 156, 160, 161
- Edwards, B. D., Lee, H. J., and Field, M. E. (1995). Mudflow generated by retrogressive slope failure, Santa Barbara Basin, California continental borderland. *Journal of Sedimentary Research*, 65:57–68. 163
- Erismann, T. H. and Abele, G. (2001). *Dynamics of rockslides and rockfalls*. Springer Verlag. 2
- Evans, D., Harrison, Z., Shannon, P. M., Laberg, J. S., Nielsen, T., Ayers, S., Holmes, R., Hoult, R. J., Lindberg, B., and Hafliðason, H. (2005). Palaeoslides and other mass failures

- of Pliocene to Pleistocene age along the Atlantic continental margin of NW Europe. *Marine and Petroleum Geology*, 22:1131–1148. 1, 31, 34
- Evans, D., King, E. L., Kenyon, N. H., Brett, C., and Wallis, D. (1996). Evidence for long-term instability in the Storegga Slide region off western Norway. *Marine Geology*, 130:281–292. 18, 27, 29, 31, 34, 81, 98, 165
- Færseth, R. B. and Sætersmoen, B. H. (2008). Geometry of a major slump structure in the Storegga slide region offshore western Norway. *Norwegian Journal of Geology*, 88:1–11. 68, 149, 159
- Farrell, S. G. (1984). A dislocation model applied to slump structures, Ainsa Basin, South Central Pyrenees. *Journal of Structural Geology*, 6:727–736. 156
- Frey-Martinez, J. (2005). *3D Seismic interpretation of Soft-sediment deformational processes offshore Israel: Implications for Hydrocarbon Prospectivity*. Phd, Cardiff University. 9, 53
- Frey-Martinez, J., Cartwright, J. A., and Hall, B. (2005). 3D seismic interpretation of slump complexes: examples from the continental margin of Israel. *Basin Research*, 17:83–108. 112, 115, 137, 145, 150
- Frey-Martinez, J., Cartwright, J. A., and James, D. (2006). Frontally confined versus frontally emergent submarine landslides: A 3D seismic characterisation. *Marine and Petroleum Geology*, 23:585–604. 41, 62, 64, 93, 144, 145, 149, 156, 157
- Fryer, G. J., Watts, P., and Pratson, L. F. (2004). Source of the great tsunami of 1 April 1946: a landslide in the upper Aleutian forearc. *Marine Geology*, 203:201–218. 9
- Funder, S., Hjort, C., Landvik, J., Nam, S., Reeh, N., and Stein, R. (1998). History of a stable ice margin East Greenland during the Middle and Upper Pleistocene. *Quaternary Science Reviews*, 17(1-3):77–123. viii, 23
- Gafeira, J., Bulat, J., and Evans, D. (2007). The Southern Flank Of The Storegga Slide: Imaging And Geomorphological Analyses Using 3D Seismic. In Lykousis, V., Sakellariou, D., and Locat, J., editors, *Submarine Mass Movements and Their Consequences: 3rd International Symposium*, volume 27 of *Advances in Natural and Technological Hazards Research*, pages 57–65. Springer, Dordrecht, Netherlands. 55

- Garziglia, S., Migeon, S., Ducassou, E., Loncke, L., and Mascle, J. (2008). Mass-transport deposits on the Rosetta province (NW Nile deep-sea turbidite system, Egyptian margin): Characteristics, distribution, and potential causal processes. *Marine Geology*, 250:180–198. 115, 145, 146, 156, 157
- Gawthorpe, R. L. and Clemmey, H. (1985). Geometry of submarine slides in the Bowland Basin (Dinantian) and their relation to debris flows. *Journal of the Geological Society*, 142:555–565. 145, 146, 156, 157
- Gay, A. and Berndt, C. (2007). Cessation/reactivation of polygonal faulting and effects on fluid flow in the Voring Basin, Norwegian Margin. *Journal of the Geological Society*, 164:129–141. 165, 166
- Gee, M. J. R., Gawthorpe, R. L., and Friedmann, J. S. (2005). Giant striations at the base of a submarine landslide. *Marine Geology*, 214:287–294. 72, 115, 144, 145, 150
- Gee, M. J. R., Gawthorpe, R. L., and Friedmann, S. J. (2006). Triggering and Evolution of a Giant Submarine Landslide, Offshore Angola, Revealed by 3D Seismic Stratigraphy and Geomorphology. *Journal of Sedimentary Research*, 76:9–19. 144
- Gee, M. J. R., Watts, A. B., Masson, D. G., and Mitchell, N. C. (2001). Landslides and the evolution of El Hierro in Canary Islands. *Marine Geology*, 177:271–293. 7
- Georgiopoulou, A., Krastel, S., Masson, D. G., and Wynn, R. B. (2007). Repeated instability of the NW African margin related to buried landslide scarps. In Lykousis, V., Sakellariou, D., and Locat, J., editors, *Submarine Mass Movements and Their Consequences: 3rd International Symposium*, volume 27 of *Advances in Natural and Technological Hazards Research*, pages 29–36. Springer, Dordrecht, Netherlands. 163, 164
- Goldfinger, C., La Verne, D. K., Mc Neill, L. C., and Watts, P. (2000). Super-scale failure of the southern Oregon Cascadia margin. *Pure and Applied Geophysics*, 157:1189–1226. 1
- Gomberg, J., Bodin, P., Savage, W., and Jackson, M. (1995). Landslide faults and tectonic faults, analogs?: The Slumgullion earthflow, Colorado. *Geology*, 23(1):41. 160
- Greene, H. G., Murai, L. Y., Watts, P., Maher, N. A., Fisher, M. A., Paull, C. E., and Eichhubl, P. (2006). Submarine landslides in the Santa Barbara Channel as potential tsunami sources. *Natural Hazards And Earth System Sciences*, 6:63–88. 1, 143

- Hafliðason, H., Lien, R., Sejrup, H. P., Forsberg, C. F., and Bryn, P. (2005). The dating and morphometry of the Storegga Slide. *Marine and Petroleum Geology*, 22:123–136. 34, 56
- Hafliðason, H., Sejrup, H. P., Nygård, A., Mienert, J., Bryn, P., Lien, R., Forsberg, C. F., Berg, K., and Masson, D. G. (2004). The Storegga Slide: architecture, geometry and slide development. *Marine Geology*, 213:201–234. 26, 34, 36, 56, 171
- Hampton, M. A., Lee, H. J., and Locat, J. (1996). Submarine landslides. *Reviews of Geophysics*, 34:33–59. 2, 5, 53
- Hart, B. S. (1999). Definition of subsurface stratigraphy, structure and rock properties from 3-D seismic data. *Earth-Science Reviews*, 47:189–218. 41
- Herron, D. A. (2000). Horizon autopicking. *The Leading Edge*, 19:491. 42
- Hjelstuen, B. O., Eldholm, O., and Faleide, J. I. (2007). Recurrent Pleistocene mega-failures on the SW Barents Sea margin. *Earth and Planetary Science Letters*, 258:605–618. viii, 20, 156, 157
- Hjelstuen, B. O., Sejrup, H. P., Hafliðason, H., Berg, K., and Bryn, P. (2004). Neogene and Quaternary depositional environments on the Norwegian continental margin, 62°N–68°N. *Marine Geology*, 213:257–276. 18
- Hjelstuen, B. O., Sejrup, H. P., Hafliðason, H., Nygård, A., Ceramicola, S., and Bryn, P. (2005). Late Cenozoic glacial history and evolution of the Storegga Slide area and adjacent slide flank regions, Norwegian continental margin. *Marine and Petroleum Geology*, 22:57–69. 31, 98
- Howard, K. A. (1973). Avalanche Mode of Motion: Implications from Lunar Examples. *Science*, 180:1052–1055. 2
- Hustoft, S., Mienert, J., Büinz, S., and Nouze, H. (2007). High-resolution 3D-seismic data indicate focussed fluid migration pathways above polygonal fault systems of the mid-Norwegian margin. *Marine Geology*, 245:89–106. 165, 166
- Huvenne, V. A. I., Croker, P. F., and Henriët, J.-P. (2002). A refreshing 3D view of an ancient sediment collapse and slope failure. *Terra Nova*, 14:33–40. 65, 72, 92, 93
- Ilstad, T., De Blasio, F. V., Elverhøi, A., Harbitz, C. B., Engvik, L., Longva, O., and Marr, J. G. (2004). On the frontal dynamics and morphology of submarine debris flows. *Marine Geology*, 213:481–497. 150

- Imbo, Y., De Batist, M., Canals, M., Prieto, M. J., and Baraza, J. (2003). The Gebra Slide: a submarine slide on the Trinity Peninsula Margin, Antarctica. *Marine Geology*, 193:235–252. 142
- Kayen, R. E. and Lee, H. J. (1993). *Slope stability in regions of sea-floor gas hydrate: Beaufort Sea continental slope*, pages 97–103. Bulletin. U.S. Dept. of the Interior, U.S. Geological Survey, 2002 edition. 7
- Keating, B. H., Helsley, C. E., and Karogodina, I. (2000). Sonar Studies of Submarine Mass Wasting and Volcanic structures off Savaii Island, Samoa. *Pure and Applied Geophysics*, 157:1285–1313. 115
- King, E. L., Hafliðason, H., Sejrup, H. P., and Løvlie, R. (1998). Glacigenic debris flows on the North Sea Trough Mouth Fan during ice stream maxima. *Marine Geology*, 152:217–246. 23, 75
- King, E. L., Sejrup, H. P., Hafliðason, H., Elverhøi, A., and Aarseth, I. (1996). Quaternary seismic stratigraphy of the North Sea Fan: glacially-fed gravity flow aprons, hemipelagic sediments, and large submarine slides. *Marine Geology*, 130:293–315. viii, 18, 23, 26, 27, 29, 31, 98, 121
- Knott, S., Burchell, M., Jolley, E., and Fraser, A. (1993). Mesozoic to Cenozoic plate reconstructions of the North Atlantic and hydrocarbon plays of the Atlantic margins. In *Geological Society, London, Petroleum Geology Conference series*, volume 4, pages 953–974. Geological Society of London. 14, 15, 16
- Krastel, S., Wynn, R. B., Hanebuth, T. J. J., Henrich, R., Holz, C., Meggers, H., Kuhlmann, H., Georgiopoulou, A., and Schulz, H. D. (2006). Mapping of seabed morphology and shallow sediment structure of the Mauritania continental margin, North-west Africa: some implications for geohazard potential. *Norwegian Journal of Geology*, 86:163–176. 7
- Kuijpers, A. H., Nielsen, T., Alexanderson, H., De Haas, H., Kenyon, N. H., and Van Weering, T. C. E. (2001). Late Quaternary slope instability on the Faeroe margin: mass flow features and timing of events. *Geo-Marine Letters*, 20:149–159. 150
- Kvalstad, T. J., Andresen, L., Forsberg, C. F., Berg, K., Bryn, P., and Wangen, M. (2005). The Storegga slide: evaluation of triggering sources and slide mechanics. *Marine and Petroleum Geology*, 22:245–256. 143

- Labazuy, P. (1996). Recurrent landslides events on the submarine flank of Piton de la Fournaise volcano (Reunion Island). *Geological Society London Special Publications*, 110:295–306. 1
- Laberg, J. S. and Andreassen, K. (2007). *Submarine Paleo-Failure Morphology On A Glaciated Continental Margin From 3d Seismic Data*, volume 27 of *Advances in Natural and Technological Hazards Research*, pages 11 – 18. Springer Netherlands, section 1 edition. 144
- Laberg, J. S. and Vorren, T. O. (1995). Late Weichselian submarine debris flow deposits on the Bear Island Trough Mouth Fan. *Marine Geology*, 127:45–72. 18
- Laberg, J. S. and Vorren, T. O. (2000a). Flow behaviour of the submarine glacial debris flows on the Bear Island Trough Mouth Fan, western Barents Sea. *Sedimentology*, 47:1105–1117. 157
- Laberg, J. S. and Vorren, T. O. (2000b). The Trænadjupet Slide, offshore Norway - morphology, evacuation and triggering mechanisms. *Marine Geology*, 171:95–114. 137, 143, 144, 145
- Lastras, G., Canals, M., Urgeles, R., De Batist, M., Calafat, A. M., and Casamor, J. L. (2004a). Characterisation of the recent BIG'95 debris flow deposit on the Ebro margin, Western Mediterranean Sea, after a variety of seismic reflection data. *Marine Geology*, 213:235–255. 65
- Lastras, G., Canals, M., Urgeles, R., Hughes-Clarke, J. E., and Acosta, J. (2004b). Shallow slides and pockmark swarms in the Eivissa Channel, western Mediterranean Sea. *Sedimentology*, 51:837–850. 144
- Lastras, G., De Blasio, F. V., Canals, M., and Elverhøi, A. (2005). Conceptual and Numerical Modeling of the BIG'95 Debris Flow, Western Mediterranean Sea. *Journal of Sedimentary Research*, 75:784–797. 115, 150
- Lee, H. J., Schwab, W. C., and Booth, J. S. (1991). Submarine Landslides: An Introduction. In Schwab, W. C., Lee, H. J., and Twichell, D. C., editors, *Submarine Landslides: Selected studies in the U. S. exclusive economic zone*. US Geological Survey. 8, 53
- Leynaud, D., Mienert, J., and Vanneste, M. (2009). Submarine mass movements on glaciated and non-glaciated European continental margins: A review of triggering mechanisms and preconditions to failure. *Marine and Petroleum Geology*, 26:618–632. xiv, 10, 20, 21
- Ligtenberg, J. H. (2005). Detection and fluid migration pathways in seismic data: implications for fault sea analysis. *Basin Research*, 17:10–13. 41

- Lindberg, B., Laberg, J. S., and Vorren, T. O. (2004). The Nyk Slide—morphology, progression, and age of a partly buried submarine slide offshore northern Norway. *Marine Geology*, 213:277–289. 1, 7, 156, 158, 163
- Lindseth, R. O. (2005). Seismic attributes - Some recollections. *Geophysicists Recorder*, 30:16–17. 44
- Locat, J. (2001). Instabilities along ocean margins: a geomorphological and geotechnical perspective. *Marine and Petroleum Geology*, 18:503–512. 8
- Locat, J. and Lee, H. J. (2002). Submarine landslides: advances and challenges. *Canadian Geotechnical Journal*, 39:193–212. xiv, 2, 5, 6, 8
- Locat, J. and Mienert, J. (2003). *Foreword*, volume 19 of *Advances in the Natural and Technological Hazards Research*, pages 1–2. Kluwer Academic Publishers, Dordrecht, Netherlands, 1st edition. 1
- Lonergan, L. (2008). Structure of a near-recent giant submarine landslide on the continental slope of the NE Gulf of Mexico. In Turner, J., editor, *Gravitational Collapse at Continental Margins*, page 6, London, UK. GSL. 157
- Long, D., Bulat, J., and Stoker, M. S. (2004). *Seabed morphology of the Faroe-Shetland Channel derived from 3D seismic data sets*, volume 3D Seismic, pages 53–61. Geological Society. 49
- Long, D., Stevenson, A. G., Wilson, C. K., and Bulat, J. (2003). *Slope failures in the Faroe-Shetland Channel*, volume 19 of *Advances in the Natural and Technological Hazards Research*, pages 281–289. Kluwer Academic Publishers, Dordrecht, Netherlands. xiii, 164
- Løseth, H., Wensaas, L., Arntsen, B., Hanken, N., Christophe, B., and Gaue, K. (2003). 1000 Meter Long Gas Blow-Out Pipes. In *AAPG Annual Convention, Expanded Abstracts*, volume 3, page 109, Salt Lake City, Utah. American Association of Petroleum. 165
- Lucchitta, B. K. (1978). A large landslide on Mars. *Bulletin of the Geological Society of America*, 89:1601–1609. 2
- Lucente, C. C. and Pini, G. A. (2003). Anatomy and emplacement mechanism of a large submarine slide within a Miocene foredeep in the northern Apennines, Italy: A field perspective. *American Journal of Science*, 3:32. 155

- Lundin, E. and Doré, A. G. (2002). Mid-Cenozoic post-breakup deformation in the 'passive' margins bordering the Norwegian-Greenland Sea. *Marine and Petroleum Geology*, 19:79–93. 15, 16
- Lykousis, V., Roussakis, G., Alexandri, M., Pavlakis, P., and Papoulia, I. (2002). Sliding and regional slope stability in active margins: North Aegean Trough (Mediterranean). *Marine Geology*, 186:281–298. 7
- Lynch, S., Townsley, J., Dennis, M., and Gibson, C. (2005). Enhancing Fault Visibility Using Bump Mapped Seismic Attributes. In *2005 CSEG National Convention*, volume Evolving G, pages 243–246. 47
- Malin, M. C. (1992). Mass movements on Venus: Preliminary results from Magellan cycle 1 observations. *Journal of Geophysical Research*, 97:16337–16352. 2
- Marfurt, K. J., Kirilin, R. L., Farmer, S. L., and Bahorich, M. S. (1998). 3D seismic attributes using a semblance-based coherency algorithm. *Geophysics*, 63:1150–1165. 49
- Martel, S. J. (2004). Mechanics of landslide initiation as a shear fracture phenomenon. *Marine Geology*, 203:319–339. 144
- Martinsen, O. J. and Bakken, B. (1990). Extensional and compressional zones in slumps and slides in the Namurian of County Clare, Ireland. *Journal of the Geological Society*, 147:153164. 1, 156, 157
- Maslin, M., Owen, M., Day, S., and Long, D. (2004). Linking continental-slope failures and climate change: Testing the clathrate gun hypothesis. *Geology*, 32:5356. 7
- Masson, D., Huggett, Q., and Brunsden, D. (1993). The surface texture of the Saharan Debris Flow deposit and some speculations on submarine debris flow processes. *Sedimentology*, 40:583–598. 150
- Masson, D. G. (1996). Catastrophic collapse of the volcanic island of Hierro 15 ka ago and the history of landslides in the Canary Islands. *Geology*, 24:231–234. 1
- Masson, D. G., Canals, M., Alonso, B., Urgeles, R., and Hühnerbach, V. (1998). The Canary Debris Flow: source area morphology and failure mechanisms. *Sedimentology*, 45:411–432. 115

- Masson, D. G., Le Bas, T., and Holmes, R. (2002a). Kommandor Jack Cruise Leg 1, 1 Jul-23 Jul 2002. MULTIBEAM survey of the UKCS north of Shetland. Technical report, National Oceanography Centre Research. 29, 34
- Masson, D. G., Watts, A. B., Gee, M. J. R., Urgeles, R., Mitchell, N. C., Le Bas, T., and Canals, M. (2002b). Slope failures on the flanks of the western Canary Islands. *Earth-Science Reviews*, 57:1–35. 150
- McAdoo, B. G., Pratson, L. F., and Orange, D. L. (2000). Submarine landslide geomorphology, US continental slope. *Marine Geology*, 169:103–136. 1, 7, 115
- McGregor, B. A. (1977). Geophysical assessment of submarine slide northeast of Wilmington Canyon. *Marine Georesources & Geotechnology*, 2:229244. 144
- Micallef, A., Berndt, C., Masson, D. G., and Stow, D. A. V. (2008). Scale invariant characteristics of the Storegga Slide and implications for large-scale submarine mass movements. *Marine Geology*, 247:46–60. 34, 112
- Micallef, A., Masson, D. G., Berndt, C., and Stow, D. A. V. (2007). Morphology and mechanics of submarine spreading: A case study from the Storegga Slide. *Journal of Geophysical Research*, 112:1–21. ix, 35, 36
- Middleton, G. V. and Hampton, M. A. (1973). *Sediment gravity flows: mechanics of flow and deposition*, page 138. Pacific Section SEPM. 3
- Mienert, J., Vanneste, M., Bünz, S., Andreassen, K., Haffidason, H., and Sejrup, H. P. (2005). Ocean warming and gas hydrate stability on the mid-Norwegian margin at the Storegga Slide. *Marine and Petroleum Geology*, 22:233–244. 37
- Moore, J. G., Normark, W. R., and Holcomb, R. T. (1994). Giant Hawaiian landslides. *Annual Review of Earth and Planetary Sciences*, 22:119–144. 1
- Moore, J. G., Normark, W. R., and Holcomb, R. T. (2008). Giant Hawaiian Underwater Landslides. *Science*, 264:46–47. 7
- Moore, J. M., Asphaug, E., Morrison, D., Spencer, J. R., Chapman, C. R., Bierhaus, B., Sullivan, R. J., Chuang, F. C., Klemaszewski, J. E., Greeley, R., and Others (1999). Mass movement and landform degradation on the icy Galilean satellites: results of the Galileo nominal mission. *Icarus*, 140:294–312. 2

- Moscardelli, L. and Wood, L. (2008). New classification system for mass transport complexes in offshore Trinidad. *Basin Research*, 20:73–98. viii, 4, 7, 53, 144
- Moscardelli, L., Wood, L., and Mann, P. (2006). Mass-transport complexes and associated processes in the offshore area of Trinidad and Venezuela. *AAPG bulletin*, 90:1059–1088. xii, 148, 149, 150, 151, 157
- Mulder, T. and Alexander, J. (2001). The physical character of subaqueous sedimentary density flows and their deposits. *Sedimentology*, 48:269–299. 3
- Mulder, T. and Cochonat, P. (1996). Classification of offshore mass movements. *Journal of Sedimentary Research*, 66:43–57. 3, 53
- Mulder, T. and Moran, K. (1995). Relationship Among Submarine Instabilities, Sea Level Variations, and the Presence of an Ice Sheet on the Continental Shelf: An Example from the Verrill Canyon Area, Scotian Shelf. *Paleoceanography*, 10:137154. 7
- Nadim, F. (2006). Challenges to geo-scientists in risk assessment for submarine slides. *Norwegian Journal of Geology*, 86:351–362. 9
- Nardin, T. R., Hein, F. J., Gorsline, D. S., and Edwards, B. D. (1979). A review of mass movement processes, sediment and acoustic characteristics, and contrasts in slope and base-of-slope systems versus canyon-fan-basin floor systems. *Special Publications - Society of Economic Paleontologists and Mineralogists*, 27:61–73. 3, 4
- Nemec, W. (1990). Aspects of sediment movement on steep delta slopes. In Prior, D. B., editor, *Coarse-Grained Deltas*, pages p. 29—73. International Association of Sedimentologists. 53
- Newton, C., Shipp, R., Mosher, D. C., and Wach, G. (2004). Importance of mass transport complexes in the Quaternary development of the Nile fan, Egypt. In *Offshore Technology Conference*, page 10, Houston, Texas. 8
- Newton, R., Cunningham, R., and Schubert, C. (1980). Mud volcanoes and pockmarks: seafloor engineering hazards or geological curiosities? In *Offshore Technology Conference, 5-8 May 1980*, Houston, Texas. 7
- Nissen, S. E., Haskell, N. L., Steiner, C. T., and Coterill, K. L. (1999). Debris flow outrunner blocks, glide tracks, and pressure ridges identified on the Nigerian continental slope using 3-D seismic coherency. *The Leading Edge*, 18:595–599. 150, 156

- Normark, W. R. and Piper, D. J. W. (1991). Initiation processes and flow evolution of turbidity currents: implications for the depositional record. *From Shoreline to Abyss: contributions in marine geology in honor of Francis Parker Shepard*, 46:207–230. 4
- Norwegian Deepwater Programme (2004). Mid- to Late Cenozoic Geomodel of the Mid-Norwegian Continental Margin. Model Volume. Seabed Project Phase II. Technical report, Seabed Project. viii, 22, 23, 25, 80, 121
- Nye, J. F. (1952). The mechanics of glacier flow. *Journal of Glaciology*, 2:82–93. x, 94
- Nygård, A., Sejrup, H. P., Hafliðason, H., and Bryn, P. (2005). The glacial North Sea Fan, southern Norwegian Margin: architecture and evolution from the upper continental slope to the deep-sea basin. *Marine and Petroleum Geology*, 22:71–84. viii, 23, 26, 27, 28, 29, 31, 32, 33, 81, 93, 98, 121, 164, 165
- Nygård, A., Sejrup, H. P., Hafliðason, H., Lekens, W. A. H., Clark, C. D., and Bigg, G. R. (2007). Extreme sediment and ice discharge from marine-based ice streams: New evidence from the North Sea. *Geology*, 35:395. 29
- Ottesen, D. (2006). *Ice-sheet dynamics and glacial development of the Norwegian continental margin during the last 3 million years*. Phd, University of Bergen, Norway. 24
- Ottesen, D., Rise, L., Rokoengen, K., and Sttem, J. (2001). Glacial processes and large-scale morphology on the mid-Norwegian continental shelf. In Martinsen, O. J. and Dreyer, T., editors, *Sedimentary Environments Offshore Norway Palaeozoic to Recent*, volume 10 of *Norwegian Petroleum Society Special Publication*, pages 441–449. Elsevier, Bergen, Norway. 15
- Papadopoulos, G. A., Daskalaki, E., and Fokaefs, A. (2007). Tsunamis generated by coastal and submarine landslides in the Mediterranean Sea. *Submarine Mass Movements and Their Consequences: 3rd International Symposium*, 27:327–336. 9
- Paterson, W. S. B. (1994). *The physics of glaciers*. Pergamon. 94
- Piper, D. J. W. and Macdonald, A. (2001). Timing and position of Late Wisconsinan ice-margins on the upper slope seaward of Laurentian Channel. *Géographie physique et Quaternaire*, 55:131–140. 7

- Piper, D. J. W., Shor, A. N., and Clarke, J. E. H. (1988). The 1929 Grand Banks earthquake, slump, and turbidity current. *Geological Society of America - Special Paper*, 229:177–182. 7, 9
- Prior, D. B., Coleman, J. M., and Bornhold, B. D. (1982). Results of a known seafloor instability event. *Geo-Marine Letters*, 2:153164. 156, 157
- Prior, D. B. and Doyle, E. H. (1993). Submarine landslides: the value of high resolution geophysical survey for engineering. In *The Royal Academy of Engineering Conference on Landslide Mitigation with particular reference to Developing Countries*, page 6782, London, UK. 7
- Prior, D. B. and Hooper, J. R. (1999). Sea floor engineering geomorphology: recent achievements and future directions. *Geomorphology*, 31:411–439. 7
- Rise, L., Ottesen, D., Berg, K., and Lundin, E. (2005). Large-scale development of the mid-Norwegian margin during the last 3 million years. *Marine and Petroleum Geology*, 22:33–44. ix, 14, 15, 22, 37, 164
- Rupke, N. A. (1976). Large-scale slumping in a flysch basin, southwestern Pyrenees. *Journal of the Geological Society*, 132:121–130. 148
- Schwab, W. C., Lee, H. J., and Twichell, D. C. (1993). Submarine landslides; selected studies in the US Exclusive Economic Zone. Technical report. 2
- Sejrup, H. P., Hafliðason, H., Hjelstuen, B. O., Nygård, A., Bryn, P., and Lien, R. (2004). Pleistocene development of the SE Nordic Seas margin. *Marine Geology*, 213:169–200. 26, 31, 81
- Sejrup, H. P., Hjelstuen, B. O., Dahlgren, K. I. T., Hafliðason, H., Kuijpers, A. H., Nygård, A., Praeg, D., Stoker, M. S., and Vorren, T. O. (2005). Pleistocene glacial history of the NW European continental margin. *Marine and Petroleum Geology*, 22:1111–1129. viii, 23
- Sejrup, H. P., Larsen, E., Hafliðason, H., Berstad, I. M., Hjelstuen, B. O., Jonsdottir, H. E., King, E. L., Landvik, J. Y., Longva, O., Nygård, A., and Others (2003). Configuration, history and impact of the Norwegian Channel Ice Stream. *Boreas*, 32:18–36. 26
- Sejrup, H. P., Larsen, E., Landvik, J. Y., King, E. L., Hafliðason, H., and Nesje, A. (2000). Quaternary glaciations in southern Fennoscandia: evidence from southwestern Norway and the northern North Sea region. *Quaternary Science Reviews*, 19:667–685. viii, 18, 19

- Shanmugam, G. (2000). 50 Years of the Turbidite Paradigm (1950s-1990s): Deep-Water Processes and Facies Models - A Critical Perspective. *Marine and Petroleum Geology*, 17:285–342. 3
- Skogseid, J., Planke, S., Faleide, J. I., Pedersen, T., Eldholm, O., and Neverdal, F. (2000). NE Atlantic continental rifting and volcanic margin formation. *Geological Society, London, Special Publications*, 167(1):295–326. 16
- Solheim, A., Berg, K., Forsberg, C. F., and Bryn, P. (2005a). The Storegga Slide complex: repetitive large scale sliding with similar cause and development. *Marine and Petroleum Geology*, 22:97–107. 29, 34, 37, 80, 98, 112, 115, 121, 137, 145, 146, 147, 163
- Solheim, A., Bryn, P., Sejrup, H. P., Mienert, J., and Berg, K. (2005b). Ormen Lange - an integrated study for the safe development of a deep-water gas field within the Storegga Slide Complex, NE Atlantic continental margin; executive summary. *Marine and Petroleum Geology*, 22:1–9. 41
- Stoker, M., Praeg, D., Shannon, P., Hjelstuen, B., Laberg, J., Nielsen, T., Van Weering, T., Sejrup, H., and Evans, D. (2005a). Neogene evolution of the Atlantic continental margin of NW Europe (Lofoten Islands to SW Ireland): anything but passive. In *Geological Society, London, Petroleum Geology Conference series*, volume 6, page 1057. Geological Society of London. 14, 15
- Stoker, M. S., Praeg, D., Hjelstuen, B. O., Laberg, J. S., Nielsen, T., and Shannon, P. M. (2005b). Neogene stratigraphy and the sedimentary and oceanographic development of the NW European Atlantic margin. *Marine and Petroleum Geology*, 22:977–1005. 22
- Strachan, L. J. (2002). Slump-initiated and controlled syndepositional sandstone remobilization: an example from the Namurian of County Clare, Ireland. *Sedimentology*, 49:25–42. 62
- Strachan, L. J. (2003). *Geometry to genesis: a comparative field study of slump deposits and their modes of formation*. Phd, Cardiff University. 155
- Strachan, L. J. (2008). Flow transformations in slumps: a case study from the Waitemata Basin, New Zealand. *Sedimentology*, 55:1311–1332. 157
- Sultan, N., Cochonat, P., Canals, M., Cattaneo, A., Dennielou, B., Hafliðason, H., Laberg, J. S., Long, D., Mienert, J., Trincardi, F., Urgeles, R., Vorren, T. O., and Wilson, C. K. (2004).

- Triggering Mechanisms of slope instability processes and sediment failures on continental margins: a geotechnical approach. *Marine Geology*, 213:291–321. 5
- Tappin, D. R., Watts, P., McMurtry, G. M., Lafoy, Y., and Matsumoto, T. (2001). The Sissano, Papua New Guinea tsunami of July 1998 - offshore evidence on the source mechanism. *Marine Geology*, 175:1–23. 7, 9
- Taylor, J., Dowdeswell, J. A., and Siegert, M. J. (2002). Late Weichselian depositional processes, fluxes, and sediment volumes on the margins of the Norwegian Sea (62-75N). *Marine Geology*, 188:61–77. 18
- Terzaghi, K. (1956). Varieties of submarine slope failures. In *Proceedings of the 8th Texas Conference on Soil Mechanics and Foundation Engineering, Special Publication*, volume 29, pages 1–41. 7
- Trincardi, F. and Argnani, A. (1990). Gela submarine slide: A major basin-wide event in the plio-quadernary foredeep of Sicily. *Geo-Marine Letters*, 10:1321. 1, 65, 145, 146, 147, 156
- Tripsanas, E. K., Piper, D. J. W., and Campbell, D. (2008). Evolution and depositional structure of earthquake-induced mass movements and gravity flows: Southwest Orphan Basin, Labrador Sea. *Marine and Petroleum Geology*, 25:645–662. 144
- Vanneste, M., Mienert, J., and Bünz, S. (2006). The Hinlopen Slide: A giant, submarine slope failure on the northern Svalbard margin, Arctic Ocean. *Earth and Planetary Science Letters*, 245:373–388. 115, 137, 142, 143, 150
- Varnes, D. J. (1978). Slope movement types and processes. In Schuster, R. L. and Krizek, R. J., editors, *Landslides, analysis and control*, pages 11–33. Nat. Acad. of Sciences. 3, 53, 64, 144, 148
- Vorren, T. O. and Laberg, J. S. (1997). Though Mouth Fans - Palaeoclimate and Ice-Sheet monitors. *Quaternary Science Reviews*, 16:865–881. viii, 18, 26, 27
- Watts, A. B. and Masson, D. G. (1995). A giant landslide on the north flank of Tenerife, Canary Islands. *Journal of Geophysical Research*, 100:24,48724,498. 7
- Weaver, P. P. E. and Kuijpers, A. H. (1983). Climatic control of turbidite deposition on the Madeira Abyssal Plain. *Nature*, 306:360. 7

- Weaver, P. P. E., Wynn, R. B., Kenyon, N. H., and Evans, J. (2000). Continental margin sedimentation, with special reference to the north-east Atlantic margin. *Sedimentology*, 47:239–256. 10
- White, N. and Lovell, B. (1997). Measuring the pulse of a plume with the sedimentary record. *Nature*, 387(6636):888–891. 16
- White, R. (1988). A hot-spot model for early Tertiary volcanism in the N Atlantic. *Geological Society London Special Publications*, 39(1):3–13. 16
- Widess, M. B. (1973). How Thin Is a Thin Bed? *Geophysics*, 38:1176–1180. 45
- Wilson, C. K., Long, D., and Bulat, J. (2004). The morphology, setting and processes of the Afen Slide. *Marine Geology*, 213:149–167. 142, 145, 146, 163, 164
- Woodcock, N. and Strachan, R. (2000). *Geological history of Britain and Ireland*. Blackwell Pub. 16
- Woodcock, N. H. (1976). Structural style in slump sheets: Ludlow Series, Powys, Wales. *Journal of the Geological Society*, 132:399–415. 53
- Wright, A. and Flower, B. (2002). Surface and deep ocean circulation in the subpolar North Atlantic during the mid-Pleistocene revolution. *Paleoceanography*, 17(4):1068. 18
- Yang, S., Solheim, A., Kvalstad, T. J., Forsberg, C. F., and Schnellmann, M. (2006). Behaviour of the sediments in the Sloregga Slide interpreted by the steady state concept. *Norwegian Journal of Geology*, 86:243–253. 34
- Yenes, M., Monterrubio, S., Nespereira, J., and Santos, G. (2009). Geometry and kinematics of a landslide surface in tertiary clays from the Duero Basin (Spain). *Engineering Geology*, 104:41–54. xiii, 1, 161, 162
- Ziegler, P. A. (1988). *Evolution of the Arctic-North Atlantic and the Western Tethys*, volume AAPG Memoi. Association of Petroleum Geologists. 15